1991

Oceanographic and topographic interactions in underwater acoustic propagation, with regional applications.

Carman, Jessie Caton

Oceanographic and Topographic Interactions in Underwater Acoustic Propagation, with Regional Applications

A thesis presented

by

Jessie Caton Carman

to

The Division of Applied Sciences

in partial fulfillment of the requirements

for the degree of

Doctor of Philosophy

in the subject of

Applied Physics

Harvard University

Cambridge, Massachusetts

May, 1991

Abstract

Accurate range dependent underwater acoustic propagation using a parabolic approximation to the Helmholtz equation, and including sediment interactions, can be calculated in any part of the world ocean using sound speed fields generated by the Harvard Open Ocean Modeling system. The resulting acoustic predictions can be valid at any time for which oceanographic mesoscale environmental fields can be forecast.

A thorough study is conducted of the effects of inclusion of a fluid sediment model with variable topographic depth on underwater acoustic propagation at low frequencies (25–100 Hz). Source depth and frequency dependencies of propagation patterns in the presence of such a sediment model are delineated in two realistic Gulf Stream region sound speed profiles. Effects of source depth and frequency on sensitivity to values of model parameters are determined. Fundamental physical reasons for these sediment interaction effects are given. Unusual propagation regimes occurring when source sound speed exceeds bottom sound speed, and the extreme sensitivity of these propagation regimes to sediment parametrization, are documented. Propagation effects are separately determined for topographic variations such as monotonic increase or decrease of depth, and oceanographic variations such as frontal crossing from Slope to Sargasso water or vice versa. Interaction effects when both physical conditions vary are detailed.

With the sediment, topographic, and oceanographic interactions thus described, acoustic propagation is studied in two other Atlantic regions, the North Atlantic Drift Current and the Iceland-Faeroes front. Distinct oceanographic surface boundary layer effects at frequencies too low for duct trapping are documented in the North Atlantic Drift Current region: the surface boundary layer prevents sound from deep sources from penetrating the shallow regions for certain frequency ranges. Shallow-to-deep water propagation with strong oceanographic variations is demonstrated in the Iceland-Faeroes front. Two propagation transects are studied; propagation through a developing eddy and across the Iceland-Faeroes front. Strong dependence of propagation on source depth, frequency, topography, and oceanography is described in detail.

Acknowledgements

I would like to thank the many people who have helped me during the course of my graduate studies. My advisor, Professor Robinson, originally introduced me to the field of physical oceanography as an undergraduate and inspired me to gain a greater understanding of geophysical fluid dynamics, both oceanography and meteorology. I am grateful to Professor Frederic Abernathy, Professor George Carrier, Professor William Siegmann of Renssalaer Polytechnic Institute, and Professor George Frisk of Woods Hole Oceanographic Institute for their careful reading of my thesis and many helpful comments. Additionally, discussions with Professors Siegmann and Frisk provided many helpful insights into acoustic phenomena and interpretations.

I have enjoyed working with the research group at Harvard, both past and present. All the members have provided help and support; a few have stood out. In particular, I must thank Dr. Don Denbo for his helpful guidance in efficient and defensive programming strategies. Dr. Denbo wrote the Plot-Plus Graphics software used in this work. Ms. Gerry Gardner provided considerable advice in creating the specific plotting software. Mr. Wayne Leslie also provided a great deal of computational and system assistance in obtaining the forecast acoustic fields.

At Naval Underwater Systems Command, New London, Mr. George Botseas provided untold amounts of help in troubleshooting acoustic code problems between various machines. Dr. Ding Lee also gave me much support and encouragement. At the Navy Research Laboratory in Washington, D.C., Mr. John Collier provided assistance above and beyond the call of duty in designing computational strategies that would permit me to fulfill my intensive calculation requirements while simultaneously remaining within system rules and etiquette.

I want to thank Ms. Marsha Cormier for all her helpful assistance in resolving the everyday problems before they became crises, and Ms. Pauline Mitchell for all her support and help in managing the bureaucracy. Quang Ha spent untold hours of prodigious, painstaking labor in preparing plots. I especially want to thank my friend and officemate Maryam Golnaraghi for the many times she provided emotional support through the crises and comic relief, and Dr. Mike Montgomery for his continued encouragement.

Finally, I want to thank my parents for always stressing highly the value of education and encouraging me to continue in my studies.

This work was conducted under a Secretary of the Navy Graduate Fellowship in Oceanography, with partial support by the Office of Naval Research under grant N00014-90-J-1593 to Harvard University.

in memoriam

Чёрная Кошка

Contents

Chapter 1

Introduction

1.1 The Physical Problem

The ocean is essentially opaque to electromagnetic waves, due to scattering by dense sea life and properties of the water; another means of remote sensing is necessary to determine locations of objects within the ocean, its properties, and those of its boundaries. The low amount of attenuation and large value of sound speed mean that acoustic methods can be used for long-range sensing in the ocean over reasonable time periods. Acoustic propagation in the ocean is not a simple straight propagation line problem, however, because sound speed depends strongly on the temperature, pressure, and salinity within the water. The increase in sound speed with depth due to pressure and the increase toward the surface due primarily to temperature result in formation of a waveguide within the ocean, in which sound can propagate to extremely long ranges (range to depth ratios of 100 or greater) without interacting with either the surface or bottom, where losses occur. Within this waveguide, the sound undergoes local focusing and defocusing phenomena (convergence zones) whose form, location, and strength depend crucially on source location and properties of the waveguide. The ocean is primarily horizontally stratified, and the formation of this deep sound channel is a principal facet of the underwater acoustic environment.

Superimposed upon this generally horizontally stratified environment are the ocean currents and their associated properties of pressure, temperature, and

salinity, which vary horizontally throughout the ocean. These variations (the oceanic mesoscale) contain more energy than any other form of motion in the sea and have dominant spatial scales of tens to hundreds of kilometers and dominant temporal scales of weeks to months (Robinson, 1983). Furthermore, the changes in the oceanic mesoscale occur intermittently, frequently as distinct events, and significant changes to the ocean's properties and currents can occur on the order of days. The strong dependence of sound speed on these varying properties of the mesoscale environment means that the magnitude of sound speed will also change horizontally and with time. These changes will have a strong effect on the shape of the acoustic waveguide, which thus changes shape with location and time, modifying patterns of propagation within the sound channel. The impact of range-dependent mesoscale oceanographic effects on acoustic prediction has been documented many times since such model studies began in the 1970s (for examples, see Spindel and Desaubies, 1983; Lee et al., 1989; Chiu and Ehret, 1990; Mellberg et al., 1990) and shown to have profound effects on the radii and magnitudes of convergence zone focusing phenomena, as well as other phenomena such as shadow zones. In order to predict correctly the locations and strengths of these acoustic features, we must have an accurate representation of the mesoscale oceanographic features, their locations and strengths.

Additionally, the mesoscale oceanographic environment constantly evolves with time, and acoustic predictions based on a single accurate realization of the oceanographic fields will have transient validity, frequently less than four days (Mellberg et al., 1990). Thus we must additionally have the ability to forecast the changing location and intensity of these mesoscale features to obtain acoustic predictions useful for an increased period of time.

The underwater acoustic problem is not completely determined by describing just the range- and time-varying oceanographic environment; choice of surface and bottom boundary conditions have a profound effect on propagation patterns within a waveguide. Local transient weather patterns can modify the surface boundary condition by changing the sea state, introducing bubbles, or changing the physical properties of the water in the upper portion of the ocean. Scales of these surface phenomena are known, and certain of them such as roughness and bubble effects can be neglected in lower frequency ranges; the acoustic effects of others such as the oceanographic surface boundary layer have yet to

be fully studied. An accurate description of the sediment layer is also necessary to describe the acoustic waveguide; in general, both sediment depth and properties vary from region to region within the ocean, and will affect oceanographic propagation patterns via bottom reflections, refractions within the sediment, and losses from various causes.

1.2 Present Opportunity

Underwater acoustics presently stands at a threshold where tools are just becoming available to assess the separate effects of the above phenomena. For instance, dynamical oceanographic modeling has progressed to the point where timely analyses and forecasts of mesoscale oceanographic environmental fields are available, often in real time by shipboard systems (Robinson et al., 1986; Robinson and Walstad, 1987). A procedure has been developed at Harvard to model oceanic mesoscale variability which consists of four components: a) the observational system, b) the statistical model, c) the dynamical model, and d) an energy and vorticity analysis package (Robinson and Leslie, 1985; Pinardi and Robinson, 1986). The observational system collects data on the mesoscale flow, using both *in-situ* measurements and remote sensing. Expendable bathythermographs (XBTs), conductivity-temperature-depth devices (CTDs), moored current meters, and drifting floats provide useful data about the ocean interior; satellite information such as infra-red (IR) images and sea-surface height provides data about the ocean's surface, from which certain properties of the interior may be deduced. Each data source provides useful information, which will generally be irregular in both space and time, and the data will consist of multiple variables (temperature, salinity, density, x-velocity, y-velocity, etc.) which will be valid at different times. Additionally, each data source alone will usually be insufficient to describe fully the mesoscale oceanographic fields. The statistical model maps these multivariate data sets onto a uniform spatial grid of a single variable at a single time (Carter and Robinson, 1987). This model currently uses objective analysis techniques and statistical models about the correlation function to do the mapping. The fields thus generated provide both initial and boundary conditions for the dynamical model.

The dynamical model evolves the numerical fields forward in time consistent with the dynamics of the particular governing equations. Two dynamical

models currently exist at Harvard for calculating oceanographic forecasts: first, the quasigeostrophic model uses the quasigeostrophic approximation to the dynamical equations. This model has been used in several regions of the open ocean and is capable of providing forecasts of environmental fields with high resolution and accuracy (Robinson et al. 1986; Glenn and Robinson, 1990). A surface boundary layer model can optionally be used with the quasigeostrophic model, and is capable of providing range dependent, time-evolving information about environmental properties within the thin surface boundary layer of the ocean (Walstad and Robinson, submitted manuscript). Second, the primitive equation model includes physics not included in the quasigeostrophic approximation, such as high topography, strong currents, and coasts (Spall and Robinson, 1989). Interpretation and analysis of the dynamical model forecast is aided by an energy and vorticity package consistent with the particular dynamical model used; analysis packages exist for both the quasigeostrophic and primitive equation models. Chapter 2 of this work describes the statistical and dynamical models in more detail; since energy and vorticity analysis is not pertinent to this work, it was not included.

Acoustic propagation models capable of handling range dependent propagation problems have been developed using several methods; examples of recent versions of these models include a ray approximation (Jones et al., 1986; Newhall et al., 1990), a normal mode approach (Chiu and Ehret, 1990), and a parabolic approximation model in both two (IFD) and three (FOR3D) dimensions developed at NUSC New London (Lee and Botseas, 1982; Botseas et al. 1983; Botseas et al. 1989). A parabolic approximation to the Helmholtz equation was selected for the following work for reasons of both speed and accuracy. Model coupling between the range-dependent oceanographic output fields and the parabolic approximation models has been conducted (Botseas et al., 1989; Lee et al. 1989). The recent inclusion of a fluid sediment layer in the coupling (Siegmann et al. 1990) increases the utility of the parabolic approximation to study the interacting effects of range-varying oceanography, range-varying topography, and sediment properties on underwater acoustic propagation. As a result, the coupled modeling system can be used to predict realistic acoustic propagation in any region of the world ocean for which data exist. Chapter 2 also contains a more detailed description of the acoustic propagation model used. This work contains no comparisons with data since there is no data yet of the appropriate quality or

quantity. Many other studies have used a parabolic approximation to model data; for instance, Dosso and Chapman (1987) showed that a parabolic approximation model with similar sediment parametrization provided excellent agreement with data taken on a region of continental slope off Vancouver Island.

1.3 Method of Approach

Specific propagation changes due to the range varying oceanography and range varying topography, in the presence of a fluid sediment layer, have not previously been studied in a systematic manner. This work investigates these questions via the modern concept of numerical simulation, which provides the power to examine propagation patterns in the realistic environment as well as under careful choices of simplified or artificial conditions. Varying environmental parameters around the "best" choices for a region reveals the effects those "best" parameters produce. Additionally, varying the physical oceanographic and topographic fields reveals the effects the realistic environmental fields produce.

Using the environmental sound speed fields provided by the Harvard oceanographic modeling system and the variable depth fluid sediment layer included in the acoustic propagation model, realistic propagation patterns including bottom interactions can easily be calculated in a fully range dependent oceanographic and topographic environment. To separate the effects of varying topography from the effects of varying oceanography, it is useful to additionally calculate propagation in a) a range-independent oceanographic, flat bottom environment; b) a range-dependent oceanographic, flat bottom environment; and c) a range-independent oceanographic, realistic topographic environment. Intercomparisons between propagation in these selected artificial conditions and with the full realistic case can reveal the specific effects that topographic and oceanographic variations separately have on the propagation patterns as well as their interacting effects. Thus the tool of numerical simulation permits us to conduct experiments under conditions more carefully controlled and possibly more widely varying than those found in nature. Such simulations do not obviate the need for data collection, as comparisons between data and calculation reveal how realistic a particular prediction may be; however, numerical simulation greatly increases the amount of knowledge that can be obtained from a single realization of data.

The following work applies this technique to the problem of dependence of range-dependent underwater acoustic propagation phenomena on the interacting effects of oceanographic variations and of topographic variations, all in the presence of a realistic sediment parametrization. Fundamental to an understanding of the full propagation interaction problem is a thorough understanding of sediment interactions through the realistic range of sediment properties, and the dependence of these interactions on frequency and source depth. From a knowledge of the sediment interactions we can then develop an understanding of the separate effects of oceanographic variations in the presence of this flat sediment, or of variations in the depth of the sediment when the oceanographic sound speeds are unchanging with range. The types and magnitudes of these effects will determine the form of effect that the interaction between oceanography and topography will have on underwater acoustic propagation.

The strong oceanographic variations in the Gulf Stream region and the existence of highly accurate sound speed fields output from the Harvard quasi-geostrophic model made it an excellent laboratory for exploring these various effects. A sensitivity and parameter study of these interactions was conducted via numerical simulation using both realistic and artificial oceanographic sound speed fields, as well as realistic and artificial topographic variations. Chapter 3 contains an extensive discussion of acoustic propagation under these various artificial conditions, first using range-independent oceanographic fields and flat topography to test the results of various forms of sediment parametrizations. Then the effects of variable topography alone are documented, and of range-dependent oceanography alone. Finally, the effects are combined and interactions delineated. Some interesting mid- to long-range forms of propagation, involving sound in bottom-glancing paths, appeared that could only be discerned by modeling lower frequencies and including a bottom parametrization; these propagation patterns are affected by the oceanographic and topographic variations more critically than standard water-propagating sound.

Using the knowledge of oceanographic and topographic interactions gained from the Gulf Stream region, we can move with some confidence to other parts of the ocean, to demonstrate the realistic propagation properties typical within each region. Chapter 4 discusses acoustic propagation in two other North Atlantic regions in detail.

An experiment performed in the North Atlantic near 52.5 N 25.5 W by the French Navy in 1988, with three Harvard personnel on board the vessel, provided an excellent source of data to study the mesoscale oceanographic effects on acoustic propagation of the eddies in the North Atlantic Drift region. Additionally, the excellent data set provided sufficient information to study the effect of including the oceanographic surface boundary layer on acoustic propagation patterns. It will be shown that even for frequencies too low to show trapping within a particular surface duct, inclusion of that duct can have a strong effect on propagation patterns by both changing the shape of the upper portion of the sound speed profile, and by effectively barring certain frequency ranges from the near surface regions.

The Iceland-UK Gap region near 64 N 11 W provided an excellent example of the combination of steep topography and strong frontal interactions. The Iceland-Faeroes front forms the boundary between the North Atlantic water and colder Norwegian Sea water; the front is topographically tied to the sharp ridge of continental shelf extending between Iceland and Britain, although its exact position varies as meanders and eddies form. The work of Jensen, Dreini, and Prior (1990) showed that the dominant factor determining acoustic propagation patterns in this region is the topography; this work supports that conclusion while demonstrating the lesser but very significant effects oceanography has on the propagation.

The results shown in chapter 3 of the general form of deep-water sediment interaction could equally well be applied elsewhere in the deep ocean. The methodology of analyzing the oceanographic and topographic interactions on propagation patterns could also be applied elsewhere, although in different regions with different oceanographic sound speed profiles, sediment and topographic conditions, the exact results will differ. The examples provided in chapter 4 demonstrate the efficacy of the acoustic prediction system to model sound propagation in widely differing regions of the ocean. With a proper set of sound speed fields, topography, and sediment type information, accurate and timely acoustic propagation predictions valid at present or future times can be calculated in any region of the ocean.

Chapter 2

Numerical Models and Model Coupling Methods

In this chapter the statistical model, the open ocean dynamical models, and the acoustic prediction model will be described. The first section describes the statistical model used for analysis of the data and initialization of the dynamical oceanographic models. In the second section, the quasigeostrophic model is developed and the nature of its approximations discussed. In the third section the surface boundary layer model is described, and the nature of its coupling to the quasigeostrophic model. The primitive equation oceanographic model is discussed in the fourth section, and the fifth section describes the methods used to calculate range-dependent sound speed fields from the various oceanographic model outputs, and the different methods used in the different oceanic regions. The sixth section discusses the parabolic approximation acoustic propagation model used to calculate the acoustic fields.

2.1 Oceanographic Model Initialization

The ocean is difficult to sample, due to its breadth, environmental conditions, and opacity. In addition, measurements must be taken on a smaller horizontal scale in the ocean (order ten kilometers) than in the atmosphere. Thus a variety of ways must be exploited to gain a complete set of fields to initialize the computational models. Among these methods are a full water column CTD (conductivity, temperature, and depth; the device measures salinity,

temperature, and pressure), XBT (expendable bathythermograph, to measure temperature and depth), AXBT (airborne expendable bathythermograph), and current meters to measure local velocities. Additionally, drifting floats provide a Lagrangian measure of the flow. Remote sensing is greatly expanding the amount and synopticity of data, by providing both infra-red (IR) surface temperatures and satellite altimetric sea-surface heights valid at a point in time.

All these data, of course, are irregularly spaced and noisy; in order to be assimilated into the computational models, an objective analysis procedure is used to place them on a regular grid while minimizing the expected error. Robinson and Leslie (1985) and Carter and Robinson (1987) discuss the method in detail; this summary follows Robinson and Walstad (1987). To summarize, the procedure assumes stationary homogeneous fields of scalar, vector, or multivariate data. We assume a measurement ϕ_r at position r can be expressed $\phi_r = \theta_r + e_r$, where θ_r is the true value and e_r is random noise. If the error is uncorrelated with both the measured values and with the error at other locations s, the expected values $E[e_r\phi_s] = 0$ and $E[e_re_s] = \epsilon^2\delta_{rs}$ where ϵ^2 is the error variance. Then the least squares optimal estimator of θ is

$$\hat{\theta}_x = \sum_{r=1}^{n} B_{xr}\Big(\sum_{s=1}^{n} A_{rs}^{-1}\phi_s\Big),$$

where A is the observation autocorrelation matrix: $A_{rs} = E[\phi_r\phi_s] = C(x_r - x_s) + \epsilon^2\delta_{rs}$ and C is the correlation for the field ϕ. The cross-correlation matrix between estimations and observations is $B_{xr} = C(x - x_r)$.

The correlation function C can be calculated from the data, if the data set is sufficiently large. However, in regions of limited data an analytical correlation function can be used, given reasonable estimates of the length and time scales in the region. Frequently, either the first Rossby radius or a typical eddy radius for the region serve for length scales, and a phase speed or decorrelation time serve for time scales. The usual form of correlation function used is

$$C = \Big(1 - (\frac{r}{a})^2\Big)\exp\Big(-\frac{1}{2}(\frac{r}{b})^2\Big),$$

where

$$r^2 = \Big(\frac{\Delta x}{L}\Big)^2 + \Big(\frac{\Delta y}{L}\Big)^2 + \Big(\frac{\Delta t}{T}\Big)^2.$$

and a, b are parameters controlling the zero crossing and decay scale of the correlation. Varying the space and time scale parameters L and T within the limits imposed by the data will generally provide a sufficiently accurate estimate of the oceanographic input fields (Robinson and Walstad, 1987).

2.2 Quasigeostrophic Model

The Harvard Open Ocean Model has been described in Miller, et al. (1981); dynamical model performance has been evaluated in experiments in the California Current (Robinson et al. 1986), the POLYMODE region (Walstad and Robinson, 1990), and the Gulf Stream (Robinson et al, 1988). A brief summary of model equations is given here; the derivation follows Robinson and Walstad (1987).

The Harvard Open Ocean Model is a regional eddy-resolving model which uses the quasigeostrophic approximation to the hydrostatic, incompressible Boussinesq equations of motion on the beta plane. This approximation was first applied in the atmosphere to study mid-latitude cyclones (Charney and Flierl, 1981) and consists of an expansion around the Rossby number ε. The approximation is even more appropriate in the ocean, where the Rossby number is an order of magnitude smaller. Thus flows with spatial scales of tens to hundreds of kilometers and temporal scales of weeks to months can be described.

Traditionally, $\varepsilon = V_0/f_0 D$, where V_0 and D are characteristic horizontal velocity and length scales and f_0 is the Coriolis parameter for the region. Instead, we will use a more general definition $\varepsilon = (f_0 t_0)^{-1}$, where t_0 is a characteristic time scale for the problem, generally the least of D/V_0, $(\beta D)^{-1}$, or an external forcing time. This definition allows us to approach more general problems from a single derivation.

Using conservation of momentum for a fluid element we can derive the x, y, and z momentum equations (Phillips, 1969; Spall and Robinson, 1989)

$$\frac{\partial u}{\partial t} + u\frac{\partial u}{\partial x} + v\frac{\partial u}{\partial y} + w\frac{\partial u}{\partial z} + \frac{1}{\rho}\frac{\partial P}{\partial x} - 2\Omega v \sin\Theta = F_m, \qquad (2.2.1a)$$

$$\frac{\partial v}{\partial t} + u\frac{\partial v}{\partial x} + v\frac{\partial v}{\partial y} + w\frac{\partial v}{\partial z} + \frac{1}{\rho}\frac{\partial P}{\partial y} - 2\Omega u \sin\Theta = F_m, \qquad (2.2.1b)$$

$$\frac{\partial P}{\partial z} - g = 0, \tag{2.2.1c}$$

where u, v, and w are the velocities in the zonal, meridional and vertical directions. Ω is the rotation rate of the earth, Θ is the latitude, F_m is a parameterization for the viscous force in the fluid. P is the pressure, ρ is the density, and g is gravitational acceleration. The hydrostatic approximation applies to the z-momentum equation, since this is a thin fluid on a β-plane, with $H/D \ll 1$ where H is the vertical length scale, rendering the time derivative Dw/Dt negligible (von Schwind, 1980). Additionally, since density variations are very small ($\sim 0.1\%$) we will use the Boussinesq approximation: that $\rho = \rho_0$ except in the hydrostatic equation where buoyancy accelerations are important. Temperature and salinity variations are combined in terms of their effects on density, as molecular diffusion processes are not treated.

Conservation of mass gives us the local time change of density,

$$\frac{\partial \rho}{\partial t} + \nabla \cdot \rho \vec{u} = 0$$

which for an incompressible fluid reduces to

$$\nabla \cdot \vec{u} = 0. \tag{2.2.1d}$$

Energy conservation for an incompressible fluid without energy sources, sinks, or conduction can be written in terms of the temperature (T) and salinity (S) as

$$\frac{\partial T}{\partial t} + u\frac{\partial T}{\partial x} + v\frac{\partial T}{\partial y} + w\frac{\partial T}{\partial z} = F_{h_T}$$

$$\frac{\partial S}{\partial t} + u\frac{\partial S}{\partial x} + v\frac{\partial S}{\partial y} + w\frac{\partial S}{\partial z} = F_{h_S}$$

with an equation of state $\rho = \rho(T, S, P)$ to close the system, and the Fs parameterize viscous diffusion for each variable. If the temperature and salinity mixing properties are similar enough, we can combine these expressions into a single one for density,

$$\frac{\partial \rho}{\partial t} + u\frac{\partial \rho}{\partial x} + v\frac{\partial \rho}{\partial y} + w\frac{\partial \rho}{\partial z} = F_h. \tag{2.2.1e}$$

This states that the local time change of density ρ is balanced by net advection of density and by a viscous diffusion F_h. Equations (2.2.1) represent five equations for the five unknowns u, v, w, P, and ρ.

The equations are nondimensionalized using the following definitions

$$x = Dx', \qquad y = Dy', \qquad z = Hz', \qquad t = t_0 t',$$
$$u = V_0 u', \qquad v = V_0 v', \qquad w = V_0 (H/D) w',$$

where D is the characteristic length scale for phenomena (eddy radius, etc.), and H is the characteristic depth related to the main thermocline depth. Beta plane coordinates are used, where we expand the actual Coriolis parameter $2\Omega \sin \Theta$ in a Taylor series about the central latitude Θ_0 as

$$f = f_0 + \left(\frac{\partial f}{\partial y}\right)_{\Theta=\Theta_0} (y - y_0) + \frac{1}{2}\left(\frac{\partial^2 f}{\partial y^2}\right)_{\Theta=\Theta_0} (y - y_0)^2 + \ldots$$

If the meridional scale of flow is small compared to the radius of the earth ($D \ll a$, where a is the earth's radius) the higher order terms may be neglected and we obtain the traditional β-plane approximation

$$f = f_0 f' = f_0 (1 + \epsilon \beta y)$$

where $\beta = (\partial f / \partial y)_{\Theta=\Theta_0}$. The modeling region has physical extent $\hat{X}$, $\hat{Y}$, and mean depth $\hat{Z}$, where the mean ocean surface is at $z = 0$ and bottom at $z = b(x, y) = \epsilon H b'(x, y) - \hat{Z}$. Note that the bottom must have variations only of order ϵ from the mean depth $\hat{Z}$.

The structure of the quasigeostrophic approximation depends crucially on the decomposition of the pressure and density fields. We let s represent the horizontally- and time-averaged non-dimensional stratification of the chosen region and $\tilde{\rho}$ represent the local density

$$s(z) = \frac{1}{\rho_0}(\tilde{\rho}(x, y, z, t) - \rho_0)$$

where

$$\rho_0 = \frac{1}{\hat{z}} \int \tilde{\rho}\, dz.$$

An essential physical restriction to this approximation is that displacements from the basic state be small. Then

$$\rho = \rho_0\Big(1 + s(z) - \frac{f_0 V_0 D}{Hg}\delta(x,y,z,t)\Big)$$

and

$$P = -\rho_0 g \int_0^z (1+s)\,dz + \rho_0 f_0 V_0 D P'(x,y,z,t)$$

where

$$P' = P_0' + \int_0^{z'} \delta\,dz'.$$

Here P' and δ represent variations from the mean state due to the motion, and P_0 is the variation due to surface height.

Thus defined, the non-dimensional equations of motion (with the primes dropped) become

$$\varepsilon\Big(\frac{\partial u}{\partial t} + \alpha\Big(u\frac{\partial u}{\partial x} + v\frac{\partial u}{\partial y} + w\frac{\partial u}{\partial z}\Big)\Big) - (1+\varepsilon\beta y)v + \frac{\partial P}{\partial x} = F_u, \tag{2.2.2a}$$

$$\varepsilon\Big(\frac{\partial v}{\partial t} + \alpha\Big(u\frac{\partial v}{\partial x} + v\frac{\partial v}{\partial y} + w\frac{\partial v}{\partial z}\Big)\Big) - (1+\varepsilon\beta y)u + \frac{\partial P}{\partial y} = F_v, \tag{2.2.2b}$$

$$\delta - \frac{\partial P}{\partial z} = 0, \tag{2.2.2c}$$

$$\frac{\partial u}{\partial x} + \frac{\partial v}{\partial y} + \frac{\partial w}{\partial z} = 0, \tag{2.2.2d}$$

$$\varepsilon\Big(\frac{\partial \delta}{\partial t} + \alpha\Big(u\frac{\partial \delta}{\partial x} + v\frac{\partial \delta}{\partial y} + w\frac{\partial \delta}{\partial z}\Big)\Big) + \frac{w}{\Gamma^2\sigma} = 0. \tag{2.2.2e}$$

The non-dimensional constant parameters used above are

$$\alpha = \frac{V_0 t_0}{D}, \qquad \beta = \beta_0 D t_0, \qquad \Gamma^2 = \frac{f_0^2 D^2}{N_0^2 H^2}, \qquad \varepsilon = \frac{1}{f_0 t_0},$$

$$f_0 = 2\Omega\sin\Theta_0, \qquad \beta_0 = \frac{\partial f}{\partial y} = \frac{2\Omega}{a}\cos\Theta_0$$

and the non-dimensional function is

$$\sigma(z) = \frac{N_0^2}{N^2} \qquad \text{where} \qquad N^2 = -\frac{g}{\rho}\frac{\partial \rho}{\partial z} \approx -\frac{g}{H}\frac{\partial s}{\partial z'}$$

where Θ_0 is the latitude of the domain central point, and N_0 is a typical main thermocline Brunt–Väisälä frequency. F_u and F_v represent frictional terms which will be assumed to be small at horizontal and vertical length scales used. These terms will be modeled with a filter.

Note that if we choose $\alpha = 1$, then $t_0 = D/V_0$, the advective time scale, and we recover $\varepsilon = V_0/f_0 D$, the historical Rossby number. If we instead choose $\beta = 1$, then $t_0 = 1/\beta_0 D$, the planetary wave time scale, and $\varepsilon = \beta_0 D/f_0$. We can additionally chose t_0 equal to an external forcing time.

In order to obtain the quasi-geostrophic approximation and a prognostic equation for the fields, we let $\varepsilon \ll 1$, $H/D \ll 1$, $\Gamma^2 \sim 1$. Then if we write all the variables as perturbation expansions in ε (for instance, $u = u^0 + \varepsilon u^1 + \cdots$) we see that the zero-order equations are

$$v^0 = \psi_x, \qquad u^0 = -\psi_y, \qquad w^0 = 0, \qquad u^0_x + v^0_y = 0,$$

where

$$\psi = P^0, \qquad \psi_z = \delta^0.$$

These are the geostrophic relations; to zeroth-order the motion is both horizontally non-divergent and has no vertical component. This approximation is valid for flows in which Coriolis accelerations and pressure gradients are in equilibrium. The strong geostrophic constraint that $\nabla_H \cdot \vec{u} = 0$ leads to a vertical velocity even smaller than that due to the thin fluid hydrostatic approximation ($O(\varepsilon)$ smaller). Additionally, to zeroth-order there are no prognostic equations for the evolution of the fields. It is the small deviations from pure geostrophic balance that allow the fields to evolve in time.

To examine the first small but important deviations from geostrophy, we look at the first-order components of the variables, where we do find a set of prognostic equations.

$$\frac{\partial u^0}{\partial t} + \alpha\left(u^0 \frac{\partial u^0}{\partial x} + v^0 \frac{\partial u^0}{\partial y}\right) - v^1 - \beta v^0 + P^1_x = F_u, \tag{2.2.3a}$$

$$\frac{\partial v^0}{\partial t} + \alpha\left(u^0 \frac{\partial v^0}{\partial x} + v^0 \frac{\partial v^0}{\partial y}\right) + u^1 + \beta u^0 + P^1_y = F_v, \tag{2.2.3b}$$

$$u^1_x + v^1_y + w^1_z = 0, \tag{2.2.3c}$$

$$\frac{\partial \delta^0}{\partial t} + \alpha\left(u^0 \frac{\partial \delta^0}{\partial x} + v^0 \frac{\partial \delta^0}{\partial y}\right) + \frac{w^1}{\Gamma^2 \sigma} = 0. \qquad (2.2.3d)$$

To this order we do see horizontally divergent flow, balanced with a vertical velocity determined from density conservation, where w advects the mean stratification and balances the horizontal density advection and local time derivitive. In light of the approximations used, we see that this QG approximation is important and valid for flows having a horizontal scale much larger than the vertical scale and less than the planetary scale, a vertical scale comparable to the basin depth, and time scale long compared to a day.

If we cross-differentiate the horizontal velocity equations and apply the divergence and density anomaly equations, we can remove the velocity variables to obtain the pseudo-potential vorticity equation

$$\frac{\partial \zeta}{\partial t} + \alpha J(\psi, \zeta) + \beta \psi_x = F_{pqr}, \qquad (2.2.4)$$

where

$$\zeta = \nabla_H^2 \psi + \Gamma^2 (\sigma \psi_z)_z \qquad (2.2.5)$$

and the Jacobian $J(\psi, \zeta) = \psi_x \zeta_y - \psi_y \zeta_x$. Equation (2.2.4) can be written as

$$\left(\frac{\partial}{\partial t} + \alpha \vec{u} \cdot \nabla_H\right)\left(\nabla_H^2 \psi + \Gamma^2 (\sigma \psi_z)_z + \beta y\right) = F_{pqr},$$

which states that the pseudo-potential vorticity $q = \zeta + \frac{\beta}{\alpha} y$ is conserved at the projection of a particle in a horizontal plane, rather than at the particle (Charney and Flierl, 1981).

The filter F_{pqr} models frictional losses by removing small-scale vorticity which cascades from larger scales in nonlinear flows. This removal is necessary since small scales are not included in the quasigeostrophic scaling; and computationally, if two-gridpoint scale vorticity accumulates, numerical instability will result (Robinson and Walstad, 1987).

The boundary conditions required are ζ specified at side boundary inflow points, ψ specified on all sides, and ψ_z specified at top and bottom (Charney, Fjortoft, and von Neumann, 1950). These surface and bottom conditions on ψ_z are found by considering the Ekman layers. At the surface, wind-forcing

may occur in which the curl of the wind stress causes a divergent horizontal velocity field. Consistent with the scaling of the pressure field, we can use a rigid lid approximation which gives $w^{QG} + w^E = 0$ at $z = 0$, where $w^{QG} = \varepsilon V_0(H/D)w'$ is the quasi-geostrophic part of the vertical velocity and w^E is the Ekman layer contribution. At the bottom, an Ekman layer develops due to the no-slip boundary condition. Since the net transport is to the left of the geostrophic flow, the non-divergent geostrophic flow drives a divergent boundary flow. Additionally, the condition of no normal flow through the bottom causes a vertical flow on sloping topography. We therefore obtain prognostic equations for density at the surface and bottom

$$\frac{\partial \Gamma^2 \sigma \psi_z}{\partial t} + \alpha J(\psi, \Gamma^2 \sigma \psi_z) = \begin{cases} -\hat{k} \cdot \nabla \times \tau & \text{at} \quad z = 0 \\ -\kappa \nabla_H^2 \psi - J(\psi, b) & \text{at} \quad z = -Z. \end{cases}$$

where $\tau = \varepsilon \rho_0 f_0 V_0 (H/D)\tau'$ is the non-dimensionalized stress at the sea surface and $\kappa = (1/\varepsilon H)\sqrt{A_V/2f_0}$ is the non-dimensionalized vertical eddy viscosity at the bottom. Frequently, internal dynamics alone evolve the flow field with local wind stress of negligible importance. Bottom friction effects are only important for integrations of several months.

The numerical model uses separation of variables such that the equation for ζ is solved in the horizontal by the finite element method. The new vorticity ζ in general contains small scales which are removed by a filter (Shapiro, 1971) which acts on the small scales and does not produce aliasing errors. In the vertical, the ζ equation is solved by finding solutions to a sequence of uncoupled Helmholtz equations

$$(\nabla_H^2 - \lambda_j^2)\Psi_j = \zeta_j, \qquad j = 0, 1, \ldots, (l-1)$$

where

$$\Gamma^2 (\sigma \Psi_{jz})_z = -\lambda_j^2 \Psi_j, \qquad \sigma \Psi_{jz} = 0 \quad \text{at} \quad z = 0, -Z,$$

and l is the number of modes represented. A finite difference scheme is used in the vertical, which will give l eigenvectors which approximate the corresponding eigenfunctions (Miller, Robinson, and Haidvogel, 1981). These eigenfunctions are the barotropic ($j = 0$) and baroclinic modes ($j = 1, 2, \ldots$). This approach permits the use of fast 2D Helmholtz solvers.

2.3 Coupled Quasigeostrophic-Surface Boundary Layer Model

A three dimensional model of the mesoscale surface boundary layer of the ocean has been coupled to the QG model discussed above, as described in Walstad and Robinson (submitted manuscript). A summary of the model principles is given below.

The essential nature of the coupling is to use quasigeostrophic dynamics away from the mixed layer and an arbitrary mixing model within the layer. The QG approximation applies to vertical scales on the order of the thermocline depth, whereas the thickness of the surface boundary layer is generally only tens of meters deep. The coupling method therefore exploits the scale differences between the two types of dynamics, separating each dependent variable into an interior and a boundary layer component (e.g. $u = u^I + u^S$), where the superscripts refer to interior and surface boundary layer respectively. Instead of using a matching requirement, the boundary layer fields are required to approach zero as depth increases. At the surface, the sum of the fields is required to satisfy the appropriate boundary conditions.

The hydrostatic Boussinesq β-plane equations of motion including conservation of potential temperature and salinity are as follows (ibid.):

$$u_t + uu_x + vu_y + wu_z - fv + \frac{P_x}{\rho_0} = F_u + \frac{\partial M_u}{\partial z}, \tag{2.3.1a}$$

$$v_t + uv_x + vv_y + wv_z + fu + \frac{P_y}{\rho_0} = F_v + \frac{\partial M_v}{\partial z}, \tag{2.3.1b}$$

$$P_z + \rho g = 0, \tag{2.3.1c}$$

$$u_x + v_y + w_z = 0, \tag{2.3.1d}$$

$$\rho_t + u\rho_x + v\rho_y + w\rho_z = F_\rho + \frac{\partial}{\partial z} M_\rho - \frac{\alpha_T}{c_p}\frac{\partial I}{\partial z}, \tag{2.3.1e}$$

$$\rho = \rho(T, S), \tag{2.3.1f}$$

$$\eta_t + u\eta_x + v\eta_y - w = 0, \tag{2.3.1g}$$

$$T_t + uT_x + vT_y + wT_z = F_T + \frac{\partial M_T}{\partial z} + \frac{1}{\rho_0 c_p}\frac{\partial I}{\partial z}, \tag{2.3.1h}$$

$$S_t + uS_x + vS_y + wS_z = F_S + \frac{\partial M_S}{\partial z}. \tag{2.3.1i}$$

In the above expressions, the potential density equation (2.3.1e) has been derived from the potential temperature and salinity equations assuming that differential diffusion of heat and salinity is not significant. The other equations represent eight equations for the eight unknowns u, v, w, P, ρ, T, S, and η.

In the β-plane approximation, the Coriolis parameter f is expressed by the first two terms of the Taylor expansion of the actual Coriolis parameter $f = 2\Omega \sin\Theta \simeq f_0 + \beta y$. The potential temperature equation includes the penetrative solar radiation, $I = I_0 \exp \gamma z$. Equation (2.3.1g) describes surface elevation η, although the rigid lid approximation is valid for flows in question.

Boundary conditions for the ocean surface are for heat, salinity, buoyancy, and momentum fluxes. These quantities are parameterized as M_T, M_S, M_ρ, M_u, and M_v. The heat, salinity, and density fluxes are not independent; the density flux may be determined from the heat and salinity fluxes and the equation of state for seawater. Vertical mixing of momentum, mass, heat, and salt is expressed in the vertical derivatives of the M quantities, and the Garwood mixing model (Garwood, 1977) parameterizes this mixing within the surface boundary layer. The Garwood model is a bulk mixed layer model; in other words, it assumes that the mean momentum, salinity, and temperature are vertically homogeneous above the mixed layer depth h. This introduces an additional equation for the mixed layer depth

$$h_t + uh_x + vh_y + w = e \qquad (2.3.1j)$$

where the entrainment rate e is the cross surface flux (Garwood, 1977). Garwood assumes that the source of turbulent kinetic energy for entrainment of less buoyant water beneath the mixed layer is vertically transported energy generated by surface buoyancy and turbulent kinetic energy fluxes.

The surface boundary layer model applies a scale separation to the variables in the equations, in which the interior components are expected to vary on the scale of the depth of the main thermocline or the depth of the basin, and the SBL terms are expected to vary on scales comparable to the mixed layer depth. Then terms which contain small vertical scales are assigned to the boundary layer equations, while terms with large vertical scales are assigned to the interior equations. The resulting interior equations then lead to the quasi-geostrophic equations, through the development summarized in section 2.2. The

surface boundary layer equations are as follows:

$$\mu_t + \mu\mu_x + \nu\mu_y + \omega\mu_z + \mu u_x + \nu u_y + \omega u_z + u\mu_x + v\mu_y + w\mu_z - f\nu + \frac{\pi_x}{\rho_0}$$
$$= F_\mu + \frac{\partial}{\partial z}(M_u + M_\mu); \tag{2.3.2a}$$

$$\nu_t + \mu\nu_x + \nu\nu_y + \omega\nu_z + \mu v_x + \nu v_y + \omega v_z + u\nu_x + v\nu_y + w\nu_z + f\mu + \frac{\pi_y}{\rho_0}$$
$$= F_\nu + \frac{\partial}{\partial z}(M_v + M_\nu); \tag{2.3.2b}$$

$$\pi_z + \rho_0 g\varrho = 0; \tag{2.3.2c}$$

$$\mu_x + \nu_y + \omega_z = 0; \tag{2.3.2d}$$

$$\rho_0(\varrho_t + \mu\varrho_x + \nu\varrho_y + \omega\varrho_z - \mu\delta_x - \nu\delta_y - \omega(\delta_z + S_z) + u\varrho_x + v\varrho_y + w\varrho_z)$$
$$= F_\varrho + \rho_0 \frac{\partial}{\partial z}(-M_s - M_\delta + M_\varrho) + \frac{\alpha_T}{c_p}\frac{\partial I}{\partial z}; \tag{2.3.2e}$$

$$T_0(T_t^S + \mu T_x^S + \nu T_y^S + \omega T_z^S + \mu T_x + \nu T_y + \omega(T_z + \chi_z) + uT_x^S + vT_y^S + wT_z^S)$$
$$= T_0 F_{T^S} + T_0 \frac{\partial}{\partial z}(M_{S_T} + M_{T^I} + M_{T^S}) + \frac{1}{\rho_0 c_p}\frac{\partial I}{\partial z}; \tag{2.3.2f}$$

$$h_t + \mu h_x + \nu h_y + uh_x + vh_y + w + \omega = e. \tag{2.3.2h}$$

In these expressions, μ, ν, ω, ϱ, and π are equivalent to u^S, v^S, w^S, $-\delta^S$, and P^S. In the advective equations we see three groups of terms; the first expresses advection of the SBL field by the SBL field; the second expresses advection of the SBL field by the interior flow; the third expresses transfer of interior quantities to the SBL due to advection by the boundary layer velocity field.

Disregarding sea state, the equation for the free surface is

$$\eta_t + (u + \mu)\eta_x + (v + \nu)\eta_y - (w + \omega) = 0. \tag{2.3.3}$$

The surface elevation is neither an interior nor a surface boundary layer field since it has no vertical length scale.

Walstad and Robinson (submitted manuscript) provides an extensive discussion of non-dimensionalization of these surface boundary layer equations to

identify the magnitudes of various terms and to determine which are of fundamental importance to the behavior of the surface boundary layer. After considering several parameter ranges appropriate for the oceanic mesoscale under various atmospheric forcing conditions, the terms most important to surface boundary layer dynamics (in dimensional form) are

$$\mu = \frac{1}{f_0 h}\hat{j}\cdot\vec{\tau}, \qquad \nu = \frac{-1}{f_0 h}\hat{i}\cdot\vec{\tau}, \tag{2.3.4a}$$

$$\omega_{z=0} = \frac{h}{f_0}(\mu\nabla_H^2\psi_x + \nu\nabla_H^2\psi_y + \beta\nu) - \frac{\hat{k}}{f_0}\cdot\nabla\times\vec{\tau}, \tag{2.3.4b}$$

$$\begin{aligned}\varrho_t + \mu\varrho_x + \nu\varrho_y - \rho_0(\mu\delta_x + \nu\delta_y) + J(\psi,\varrho)\\ = -\frac{\alpha_T}{h\rho_0 c_p}(Q_0 + I_{z=0} - I_{z=-h}),\end{aligned} \tag{2.3.4c}$$

$$\begin{aligned}T_t^S + \mu T_x^S + \nu T_y^S + (\mu T_x + \nu T_y) + J(\psi,T^S)\\ = \frac{1}{\rho_0 c_p}(Q_0 + I_{z=0} - I_{z=-h}),\end{aligned} \tag{2.3.4d}$$

$$h_t + J(\psi,h) + w = e, \tag{2.3.4e}$$

In the above expressions $\vec{\tau}$ is the surface wind stress, and Q_0 is the surface heat flux. Below the surface boundary layer, the SBL velocity fields are zero; however, vertical advection of the SBL density and temperature gradients must be considered.

$$\varrho_t + J(\psi,\varrho) + w\rho_z = \kappa_\varrho\frac{\partial^2\varrho}{\partial z^2} - \frac{\alpha_T}{\rho_0 c_p}\frac{\partial I}{\partial z}, \tag{2.3.4f}$$

$$T_t^S + J(\psi,T^S) + wT_z^S = \kappa_T\frac{\partial^2 T^S}{\partial z^2} + \frac{1}{\rho_0 c_p}\frac{\partial I}{\partial z} \tag{2.3.4g}$$

for $z < -h$. We note that these relations require calculations from the quasi-geostrophic interior fields of

$$\psi = VD\psi', \qquad \nabla_H^2\psi = \frac{V}{D}\nabla_H^2\psi', \qquad \delta = \frac{f_0 VD}{gH}\delta',$$

$$T = \chi\varepsilon\alpha H\Gamma^2\sigma\delta', \qquad w = -\omega|_{z=0} - z\frac{\varepsilon V}{D}\frac{D}{Dt}\Gamma^2(\sigma\psi_z')_z|_{z=0}.$$

The expressions use the traditional Jacobian

$$J(a,b) = \frac{\partial a}{\partial x}\frac{\partial b}{\partial y} - \frac{\partial a}{\partial y}\frac{\partial b}{\partial x}.$$

The boundary conditions for the surface boundary layer model are the same CFvN conditions described for the QG model and values for surface forcing must be given. A Shapiro filter is again used to remove small-scale flows.

The QG portion of the model is solved by the method described briefly in the previous section and in more depth in Robinson and Walstad (1987). The SBL equations are solved on the same horizontal grid as the QG model.

The SBL model is calculated on a vertical grid with intervals defined as

$$\Delta z_k^s = \Delta z_1^s \alpha_g^{(k-1)}, \qquad \text{where} \quad k = 1, \ldots, l_s$$

and α_g is the grid expansion parameter. Levels must be defined such that the mixing layer is always deeper than the first vertical layer and shallower than the last layer. This formulation permits very high resolution in the near-surface regions without excessive computational cost.

2.4 Primitive Equation Oceanographic Model

The quasigeostrophic model described above has the benefit that for most mid-latitude mesoscale flows the QG equations are a good approximation, and they are generally less costly for computation. There are also certain conceptual and interpretational benefits to using the simplest dynamical equations necessary to determine the dominant flow processes. Other phenomena such as gravity waves, steep topography, and strong currents are contained in the primitive equations, however, and may be desirable to incorporate under certain circumstances. An intercomparison of quasigeostrophic and primitive equation models in a particular region can validate or invalidate the quasigeostrophic model for that problem, determining whether the QG model can be used with confidence or whether the primitive equations are required to characterize the flow.

The primitive equation model developed at Harvard Oceanography group is well-documented as is its performance in the Gulf Stream region (Spall and

Robinson, 1990). A short summary of the model equations is given below; development follows Spall and Robinson (1989).

As in the discussion of the quasigeostrophic model, we begin with the x, y, and z momentum equations given before and restated here:

$$\frac{\partial u}{\partial t} + u\frac{\partial u}{\partial x} + v\frac{\partial u}{\partial y} + w\frac{\partial u}{\partial z} + \frac{1}{\rho}\frac{\partial P}{\partial x} - 2\Omega v \sin\Theta = F_m, \tag{2.4.1a}$$

$$\frac{\partial v}{\partial t} + u\frac{\partial v}{\partial x} + v\frac{\partial v}{\partial y} + w\frac{\partial v}{\partial z} + \frac{1}{\rho}\frac{\partial P}{\partial y} - 2\Omega u \sin\Theta = F_m, \tag{2.4.1b}$$

$$\frac{\partial P}{\partial z} - g = 0, \tag{2.4.1c}$$

$$\nabla \cdot \vec{u} = 0. \tag{2.4.1e}$$

Conservation of energy for an incompressible fluid without energy sources or sinks can be written in terms of the temperature (T) and salinity (S), using an equation of state to close the system:

$$\frac{\partial T}{\partial t} + u\frac{\partial T}{\partial x} + v\frac{\partial T}{\partial y} + w\frac{\partial T}{\partial z} = F_h \tag{2.4.1f}$$

$$\frac{\partial S}{\partial t} + u\frac{\partial S}{\partial x} + v\frac{\partial S}{\partial y} + w\frac{\partial S}{\partial z} = F_h \tag{2.4.1g}$$

$$\rho = \rho(T, S, P) \tag{2.4.1h}$$

where F_h represents viscous diffusion, taken to be equal for T and S in this development. These equations constitute the primitive equations in cartesian coordinates. The integration is based on an original code developed in the 1960s (Bryan and Cox, 1967) with modifications made for both physical and practical reasons, to facilitate comparisons with the open ocean quasigeostrophic model. The modifications include 1) open boundary conditions, 2) hybrid coordinates in the vertical, 3) the Shapiro filter in the horizontal to parameterize the subgrid-scale processes in the numerical representation, and 4) a rotated model domain.

Regional modeling often involves topographic interactions on fine spatial scales. Use of highly resolved bottom topography in the standard form of oceanographic model would require that many levels be placed near the bottom.

Addition of these levels would cause two problems; first, the computational cost would increase, and second, the topography would be resolved only as a staircase instead being smoothly sloping. To avoid these difficulties, hybrid coordinates were implemented, with levels that follow the terrain in the deep ocean.

Hybrid coordinates involve a simple transformation of coordinates for all model levels below a prescribed depth z_c:

$$\sigma(x,y,z) = \frac{z - z_c}{H'} \tag{2.4.2}$$

$$H' = H(x,y) - z_c \qquad \text{for} \quad z_c \le z \le H(x,y).$$

This transformation allows the model surfaces to follow the topography smoothly over the entire domain below z_c; all levels shallower than z_c remain horizontal. The vertical resolution below z_c increases above shallow regions such as seamounts or coasts and decreases in deeper basins. Since the surfaces on which the prognostic variables are calculated are not horizontal, cross terms must be included in the equations of motion. Differences can be minimized by defining the sigma coordinate vertical velocity ω as

$$\omega = \frac{1}{H'}(w - \sigma(uH'_x + vH'_y)). \tag{2.4.3}$$

With this definition, the primitive equations become

$$u_t + \frac{u}{H'}(H'u)_x + \frac{v}{H'}(H'u)_y + \omega(u)_\sigma - fv = -\frac{1}{\rho_0}(P_x - g\sigma H'_x\rho) + F_m, \tag{2.4.4a}$$

$$v_t + \frac{u}{H'}(H'v)_x + \frac{v}{H'}(H'v)_y + \omega(v)_\sigma + fu = -\frac{1}{\rho_0}(P_y - g\sigma H'_y\rho) + F_m, \tag{2.4.4b}$$

$$P = H' \int_0^\sigma \rho \, d\sigma, \tag{2.4.4c}$$

$$\frac{1}{H'}(H'u)_x + \frac{1}{H'}(H'v)_y + \omega_\sigma = 0, \tag{2.4.4d}$$

$$T_t + \frac{u}{H'}(H'T)_x + \frac{v}{H'}(H'T)_y + \omega(T)_\sigma = F_h, \tag{2.4.4e}$$

$$S_t + \frac{u}{H'}(H'S)_x + \frac{v}{H'}(H'S)_y + \omega(S)_\sigma = F_h, \tag{2.4.4f}$$

$$\rho = \rho(T,S,P). \tag{2.4.4g}$$

For levels above the critical depth we take $H' = z_c$ to recover the standard primitive equations.

The integration procedure follows the method of Bryan and Cox (1967), which eliminates surface pressure from the equations by decomposing the horizontal velocity field into an internal mode $\hat{\mathbf{u}}$ and an external mode $\bar{\mathbf{u}}$ such that

$$\mathbf{u} = \hat{\mathbf{u}} + \bar{\mathbf{u}},$$

where, for any variable μ,

$$\bar{\mu} = \frac{1}{H} \int_{-H}^{0} \mu \, dz$$

and H is the depth of the ocean. We can then obtain the internal mode from

$$u_t = -\left(\frac{1}{H'} \frac{\partial (H'uu)}{\partial x} + \frac{1}{H'} \frac{\partial (H'vu)}{\partial y} + \frac{\partial (wu)}{\partial \sigma} \right) + fv - g\left(H' \int_0^\sigma \rho \, d\sigma \right)_x$$
$$-g\sigma H'_x \rho + F_{mh} + F_{mz}, \qquad (2.4.5a)$$

$$v_t = -\left(\frac{1}{H'} \frac{\partial (H'uv)}{\partial x} + \frac{1}{H'} \frac{\partial (H'vv)}{\partial y} + \frac{\partial (wv)}{\partial \sigma} \right) - fu - g\left(H' \int_0^\sigma \rho \, d\sigma \right)_y$$
$$-g\sigma H'_y \rho + F_{mh} + F_{mz}. \qquad (2.4.5b)$$

These expressions combine the continuity equation with the advection terms and divide the viscous diffusion into horizontal and vertical components (F_{mh}) and (F_{mz}).

The following relations define a volume transport streamfunction Ψ:

$$\bar{u} = -\frac{1}{H} \frac{\partial \Psi}{\partial y},$$

$$\bar{v} = -\frac{1}{H} \frac{\partial \Psi}{\partial x}.$$

Neglecting viscosity, equations 2.4.1a and 2.4.1b are cross differentiated and integrated in the vertical to yield a prognostic equation for Ψ_t

$$\frac{\partial}{\partial x}\left(\frac{1}{H} \frac{\partial \Psi_t}{\partial x} \right) - \frac{\partial}{\partial y}\left(\frac{1}{H} \frac{\partial \Psi_t}{\partial y} \right) = \frac{\partial \bar{v}_t}{\partial x} - \frac{\partial \bar{u}_t}{\partial y}.$$

Similarly, the prognostic equations for temperature and salinity can be written as

$$T_t + \frac{1}{H'}(H'uT)_x + \frac{1}{H'}(H'vT)_y + (\omega T)_\sigma = F_{hh} + F_{hz},$$

$$S_t + \frac{1}{H'}(H'uS)_x + \frac{1}{H'}(H'vS)_y + (\omega S)_\sigma = F_{hh} + F_{hz},$$

which combines the continuity equation with the prognostic equations for temperature and salinity, and separates the viscous diffusion of temperature and salinity into horizontal and vertical components (F_{hh}) and (F_{hz}).

The boundary conditions used are analogous to the open boundary conditions discussed for the quasigeostrophic model (Charney et al., 1950). The primitive equation equivalent to specification of streamfunction at all boundary points and vorticity at inflow points is specification of density and normal velocity at all boundary points and tangential velocity at inflow points.

2.5 Model Coupling: Oceanographic Outputs to Acoustic Inputs

2.5.1 Oceanographic Model Regions, Vertical and Horizontal Resolution

In the following studies acoustic propagation calculations will be conducted in three major regions of the ocean, and major interactions compared. The regions used were the Gulf Stream region, a region in the vicinity 52.5 N 25.5 W (AthenA), and the Iceland-UK Gap region. Various dynamical models were used in the different regions, and results of acoustic propagation in the different fields compared.

The Harvard University Gulfcast system is an environmental prediction system for the Gulf Stream region that uses dynamical and statistical models, an ocean observation network, and a data assimilation scheme to provide an optimal forecast of the 3-D environmental fields. The forecast system is well-documented (Robinson et al., 1988) and is routinely used to provide 7-day forecasts in real time (Glenn et al., 1987). Coupling of model outputs to acoustic prediction systems has been described by Robinson (1987) and Botseas et al. (1989); the system has been used in a number of underwater acoustic studies (Lee et al., 1989;

Chiu and Ehret, 1990; Mellberg et al., 1990; Newhall et al., 1990; Siegmann et al., 1990). The particular Gulfcast used in the upcoming studies was a 7-day forecast running from 6–13 May 1987 with 12 levels in the vertical (plus top and bottom) and a horizontal grid spacing of 15 km. The model adequately reproduces the characteristics of the temperature profile in the deep thermocline, but does not include surface boundary layer effects.

Another region of study is the central North Atlantic in the vicinity of 52.5 N 25.5 W, the location of an oceanographic experiment carried out during July and August of 1988 by the French Navy on board their naval research vessel *B.O. D'Entrecasteaux* with three Harvard scientific personnel on board. The experimental region was known as AthenA (Acquisition de données de Topographie de surface et d'Hydrologie dans l'Est Nord Atlantique) and was selected in view of its relatively flat bathymetry, presence of mesoscale eddies of the North Atlantic Drift current, and excellent satellite altimetric coverage (le Squere, 1989). The experiment consisted of two separate realizations of the hydrographic fields completed with CTD and XBT stations, three moorings for current meters and a meteorological buoy for the acquisition of air-sea interaction data. Two Maresonde GT drifting buoys provided confirmation of the hydrographic fields. Satellite altimetric data received onboard the *D'Entrecasteaux* provided further information on frontal strength and location. The Harvard Open Ocean (QG) Model was run in the resulting fields, as was the coupled QG-SBL model to provide greater resolution of the surface boundary layer.

QG oceanographic runs have been conducted in the Iceland-UK Gap region, initialized by AXBT and GEOSAT altimetric data (Robinson et al., 1989) Additionally, primitive equation model calculations have been conducted in this region.

The coupling methods used to provide inputs to the IFD acoustic propagation model yield sound speed fields of the same vertical and horizontal resolution as the particular oceanographic run; typically, profiles with between 6 and 14 points were provided to the acoustic model. Sensitivity studies have been done in the Gulf Stream region which showed that 11 points was sufficient in that region at 25 Hz, but 14 points were necessary at 100 Hz (Robinson et al., 1991). Careful choice of oceanographic model levels to meet both oceanographic dynamic requirements and acoustic resolution requirements can be made to improve the

quality of sound speed profile without too much computing cost.

Similar sensitivity studies were done on horizontal grid spacing in the Gulf Stream region comparing model runs with 10 km and 15 km horizontal spacing. These studies showed that the 15 km grid spacing was sufficient, provided the IFD model updated its own profile with each range step (Robinson et al., 1991).

The QG model used in the Gulf Stream region has been carefully tuned to meet acoustic requirements; fields obtained for the AthenA and Gap regions did not undergo such careful scrutiny. Clearly, the sensitivity of acoustic propagation to the horizontal and vertical spacing in these other regions needs to be addressed; however, the results of the Gulf Stream sensitivity studies are a preliminary indication that the dynamical model output data sets have satisfactory resolution, and certainly meaningful physical interpretations can be made.

2.5.2 QG and QG-SBL Model Outputs to Sound Speed Fields

Sound speed fields can be obtained from streamfunction fields output by the quasigeostrophic model using the relationship (equation 2.2.2c)

$$\delta = \psi_z$$

where ψ is the streamfunction and δ is the density anomaly. Assuming that the density anomaly δ is due to the vertical displacement of the mean density gradient $\partial\bar{\rho}/\partial z$, a local vertical displacement Δz from the prescribed QG model level can be calculated from

$$-\left(\frac{f_0 V_0 D}{Hg}\right)\psi_z(x,y,z,t) = \Delta z \frac{ds}{dz}$$

With the depth thus calculated, a realistic profile of temperature and salinity vs. depth provide a temperature and salinity value for that gridpoint; from knowledge of local temperature, salinity, and depth a value for sound speed is calculated according to Fofonoff and Millard (1983). Realistic temperature and salinity profiles can be obtained from data if it is available, or from climatology if not.

Sound speed fields were obtained from the QG model run in the AthenA region using the above algorithm. The temperature and salinity profiles used in

this case were averaged from the CTD data taken on the cruise. The QG model run used a horizontal grid spacing of 6.6 km and 6 levels in the vertical.

The coupled QG-SBL model was also run for comparisons with the QG model outputs alone; the coupled QG-SBL model provides fields of temperature and salinity at the SBL levels, and streamfunction at the QG levels. Sound speed fields were calculated directly from the temperature and salinity fields in the surface boundary layer, and from streamfunction for those QG levels below the lowest SBL level. QG levels above the lowest SBL level were discarded. To compare the differences in acoustic propagation between fields calculated from QG model outputs and QG-SBL model outputs, parallel calculations were performed in each data set and will be discussed in chapter 4.

In the Gap region the QG model is run with analytic topography and model levels extending to 850 m depth; with the algorithm given in section 2.5.2 we can obtain dynamically evolving sound speed fields in the upper portion of the ocean. The temperature and salinity profiles used to obtain these fields came from the Levitus climatological data set. Since the sound speed profiles are primarily downward-refracting to 850 m depth, information on the deep profile was required to properly characterize the sound speed increase with pressure in the deep regions. All of the deeper locations within the Gap model domain fall on the northeastern side of the ridge and thus within the Arctic water mass; therefore, Levitus climatology for that region provided the necessary deep temperature and salinity values for calculations of sound speed (Levitus, 1982).

2.5.3 PE Model Outputs to Sound Speed Fields

The PE model is also run in the Gap region, and sound speed fields can be calculated directly from PE model output temperature, salinity, and depth fields. The sound speeds thus obtained will be free of the errors due to the use of climatological profiles in the QG streamfunction to sound speed algorithm and the PE model sigma level formulation will reduce problems of vertical discretization. The current method of PE model initialization takes the QG model initialization streamfunction fields and assigns a temperature and salinity to each point by the method outlined above. Sound speed fields can then be calculated directly from PE model output temperature and salinity fields. A complication devel-

oped in that the local value of the analytical bottom depth used for historical reasons in the QG model frequently differs considerably from the local value of the real bottom depth, causing distortions in the resulting sound speed profiles. In shallow regions the differences are minor (of order 20 to 40 m) and the sound speed profiles closely match expected climatology; in deeper regions the topography differences can be as much as 1000 m in the vertical causing significant distortions in the sound speed profiles. Profiles were improved by reducing the amplitude of the analytical bottom and applying the same climatological deep profile used to add depth to the QG model outputs, although some distortion is still apparent in deeper regions. Work continues on the coupling of PE outputs to acoustic input fields.

2.5.4 Gulf Stream Acoustic Fields

Due to the strong differences in temperature and salinity relationships between the Slope and Sargasso water masses, the algorithm described above for obtaining sound speed from quasigeostrophic streamfunction yielded profiles that matched the data only poorly. A more accurate method was developed in Glenn and Robinson (1990) that provided more accurate profiles of sound speed in the two water masses and a more realistic gradient across the Gulf Stream. The method uses separate climatological profiles of T and S with depth for Slope, Stream, and Sargasso water. From these profiles, values of the streamfunction characteristic of each water type are calculated at each model level depth; values of model-output streamfunction at each gridpoint are then compared to these characteristic values. The appropriate temperature and salinity at each point and level is determined by linear interpolation or extrapolation from the two closest characteristic streamfunction values at that level. Sound speeds are then given by Fofonoff and Millard (1983). Acoustic propagation in the Gulf Stream region will be discussed in detail in chapter 3.

2.6 Implicit Finite Difference Model

Many acoustic models exist to calculate propagation in a horizontally stratified ocean; however, the variations in sound speed with range have been shown to have significant effect on propagation results (Mellberg, Robinson, and

Botseas, 1990; Lee et al., 1989). The most promising approach to computing acoustic propagation in a range-dependent ocean seems to be a parabolic equation method, due to its accuracy and capabilities within a feasible computation time. The acoustic propagation model used in this work is the Implicit Finite Difference (IFD) model developed at NUSC New London, CT (Lee and Botseas, 1982; Botseas et al., 1983; Lee and McDaniel, 1988; Botseas et al., 1989). Details concerning the theoretical development of the model and the stability, consistency, and convergence of the IFD formula have been documented (Lee, Botseas, and Papadakis 1981; Lee and Papadakis, 1979). Recent work has shown that inclusion of a realistic sediment model has a greater effect on propagation results than does inclusion of three-dimensional angular coupling, except in regions of strong azimuthal topographic variations (Siegmann et al., 1990). Thus the two-dimensional version of the model, which includes a sediment layer, was used for the upcoming propagation calculations.

Assuming a harmonic time dependence ($e^{-i\omega t}$), the spatial part of the acoustic pressure wave $p(r,\theta,z)$ satisfies the Helmholtz equation

$$\nabla^2 p + k_0^2 n^2 p = 0. \tag{2.6.1}$$

Here we have defined a reference wavenumber $k_0 = \omega/c_0$ and the index of refraction $n(r,\theta,z) = c_0/c(r,\theta,z)$. The difficulty in solving this equation in a general oceanic environment arises from the dependence on $c(r,\theta,z)$. In cylindrical coordinates, we can write the Helmholtz equation as

$$\frac{\partial^2 p}{\partial r^2} + \frac{1}{r}\frac{\partial p}{\partial r} + \frac{1}{r^2}\frac{\partial p}{\partial \theta^2} + \frac{\partial^2 p}{\partial z^2} + k_0^2 n^2(r,\theta,z)p = 0. \tag{2.6.2}$$

In the parabolic decomposition technique, we write pressure as the product of two functions, where $u(r,\theta,z)$ is slowly varying in r:

$$p(r,\theta,z) = v(r)u(r,\theta,z) \qquad \text{where} \quad \frac{dv}{dr} \gg \frac{\partial u}{\partial r}. \tag{2.6.3}$$

Substituting this expression into the Helmholtz equation, we get

$$u\left[\frac{d^2 v}{dr^2} + \frac{1}{r}\frac{dv}{dr}\right] + v\left[\frac{\partial^2 u}{\partial r^2} + \left(\frac{1}{r} + \frac{2}{v}\frac{dv}{dr}\right)\frac{\partial u}{\partial r} + \frac{1}{r^2}\frac{\partial^2 u}{\partial \theta^2} + \frac{\partial^2 u}{\partial z^2} + k_0^2 n^2 u\right] = 0$$

Using k_0^2 as a separation parameter, we obtain

$$\frac{d^2 v}{dr^2} + \frac{1}{r}\frac{dv}{dr} + k_0^2 v = 0$$

$$\frac{\partial^2 u}{\partial r^2} + \left(\frac{1}{r} + \frac{2}{v}\frac{dv}{dr}\right)\frac{\partial u}{\partial r} + \frac{1}{r^2}\frac{\partial^2 u}{\partial \theta^2} + \frac{\partial^2 u}{\partial z^2} + k_0^2(n^2 - 1)u = 0.$$

The solution for $v(r)$ for an outgoing wave is the zeroth order Hankel function of the first kind

$$v(r) = H_0^{(1)}(k_0 r)$$

which can be approximated as

$$v(r) \simeq \sqrt{\frac{2}{\pi k_0 r}}\, e^{i(k_0 r - \pi/4)} \tag{2.6.4}$$

for $k_0 r \gg 1$. We note that at 25 Hz this condition is met for $r \gg 10$ m, and at 100 Hz it is met for $r \gg 2.5$ m. Using this approximation, we can calculate

$$\frac{1}{r} + \frac{2}{v}\frac{dv}{dr} = 2ik_0$$

which we substitute into the equation for u to obtain

$$\frac{\partial^2 u}{\partial r^2} + 2ik_0\frac{\partial u}{\partial r} + \frac{1}{r^2}\frac{\partial^2 u}{\partial \theta^2} + \frac{\partial^2 u}{\partial z^2} + k_0^2(n^2 - 1)u = 0. \tag{2.6.5}$$

Assuming the operators $\partial/\partial r$, $\partial/\partial\theta$, and $\partial/\partial z$ commute, we can factor the equation as

$$\left[\frac{\partial}{\partial r} + ik_0 - ik_0\sqrt{1 + (n^2 - 1) + \frac{1}{k_0^2}\frac{\partial^2}{\partial z^2} + \frac{1}{(k_0 r)^2}\frac{\partial^2}{\partial \theta^2}}\right]$$
$$\times\left[\frac{\partial}{\partial r} + ik_0 + ik_0\sqrt{1 + (n^2 - 1) + \frac{1}{k_0^2}\frac{\partial^2}{\partial z^2} + \frac{1}{(k_0 r)^2}\frac{\partial^2}{\partial \theta^2}}\right] u = 0.$$

The first operator in brackets represents an outgoing wave; the second represents the incoming wave. If we neglect the incoming wave (i.e. neglect backscatter) then we are left with

$$\left[\frac{\partial}{\partial r} + ik_0 - ik_0\sqrt{1 + (n^2 - 1) + \frac{1}{k_0^2}\frac{\partial^2}{\partial z^2} + \frac{1}{(k_0 r)^2}\frac{\partial^2}{\partial \theta^2}}\right] u = 0. \tag{2.6.6}$$

We define the operators

$$x = (n^2(r, \theta, z) - 1) + \frac{1}{k_0^2}\frac{\partial^2}{\partial z^2}$$

$$y = \frac{1}{(k_0 r)^2}\frac{\partial^2}{\partial \theta^2}$$

which allow us to write the equation as

$$\left[\frac{\partial}{\partial r} + ik_0 - ik_0\sqrt{1+x+y}\right]u = 0$$

In the wide angle IFD model, we reduce this equation to two dimensions by letting $y = 0$, which removes all angular coupling from the propagation solution. We then take a rational function approximation to the square root operator in the form of

$$\sqrt{1+x} = \frac{A+Bx}{C+Dx}$$

which yields

$$\frac{\partial u}{\partial r} = ik_0\left(\frac{A+Bx}{C+Dx} - 1\right)u.$$

A good choice of coefficients for the rational function is

$$A = 1. \qquad B = .75 \qquad C = 1. \qquad D = .25$$

which yield results for propagation angles of approximately 40 deg from the horizontal (Lee and McDaniel, 1988). For cases in which losses due to interaction with the sea floor are so great that no energy interacting with the bottom reaches the receiver, from Snell's Law we can approximate the propagation angle as

$$\Theta = \cos^{-1}\left(\frac{c_{min}}{c_{max}}\right) \approx \sqrt{\frac{2\Delta c}{c_0}}$$

and note that for the Gulf Stream region, $\Theta \approx \sqrt{\frac{2\cdot 35}{1500}} = 12.4^o$ within the water column waveguide, well within the range of angles permitted. We note, however, that the bottom plays a significant role in propagation patterns; a greater range of propagation angles is necessary.

The initial field for computations is specified with a Gaussian function, which must asymptotically match the solution to the reduced wave equation for a point source. The parameters defining the Gaussian beam are

G_W = beam width, measured 3 dB downward on the main lobe
W_a = average wavenumber
G_a = amplitude of the Gaussian beam function.

These parameters can be related by

$$G_a = \frac{1}{G_W}\sqrt{\frac{2}{W_a}}.$$

We define

Δz = mesh point in the depth direction

z_s = source depth measured from the surface.

Then the matching condition gives a starting Gaussian field

$$\Re(u_0) = G_a \left(\exp\left[-\left(\frac{\Delta z - z_s}{G_W} \right)^2 \right] - \exp\left[-\left(\frac{-\Delta z - z_s}{G_W} \right)^2 \right] \right) \qquad (2.6.7)$$

with the imaginary part $\Im(u_0)$ set to zero (Lee and McDaniel, 1988). This form for the starting field has been confirmed to be a good representative of a point source in the parabolic approximation in the presence of a bottom (Jensen and Kuperman, 1980).

The IFD model is capable of obtaining sound speed profiles from fields output by the Harvard oceanographic modeling system (Botseas et al., 1989), and calculates a new sound speed profile for each range step by linearly interpolating in the horizontal between the four nearest points in the input sound speed fields. In the vertical, Harvard oceanographic model resolution yields a sparse sound speed profile; if surface and bottom values of sound speed are not given, the model linearly extrapolates, and care must be used that the extrapolations not extend over physically unreasonable distances. After the IFD model reads this sparse profile and determines surface and bottom values of sound speed, a spline fitting routine (Akima, 1970) is used to interpolate the profile to the vertical grid spacing. This particular spline fitting routine was specifically chosen for its lack of unnatural oscillations.

The upper boundary condition used for these calculations was a perfectly reflecting, or pressure-release surface: $u(r, z = 0) = (0, 0)$. At the frequencies considered (25 to 100 Hz) wavelengths vary between 15 and 60 m, so sea surface roughness effects would be minimal except in conditions of high sea state.

At the water-sediment interface, the IFD model maintains continuity of sound pressure and normal particle velocity (Lee and McDaniel, 1988); the former condition requires that

$$p_1(r, z_{bot}) = p_2(r, z_{bot})$$

where the water is medium 1 and the bottom is medium 2. Substituting in equation 2.6.3 yields

$$u_1(r, z_{bot}) = u_2(r, z_{bot}). \tag{2.6.8}$$

We can obtain the requirement for normal particle velocity by considering these waves in terms of a velocity potential Φ, where particle velocity $\vec{V} = -\nabla\Phi$. From momentum balance, we see that

$$\rho\nabla\left(\frac{\partial\Phi}{\partial t}\right) = \nabla p$$

which for a harmonic source implies that $p = -i\omega\rho\Phi$. Continuity of normal particle velocity at a sediment interface of angle φ from the horizontal then requires that

$$\frac{1}{\rho_1}\frac{\partial p_1}{\partial n}\Big|_{z_{bot}} = \frac{1}{\rho_2}\frac{\partial p_2}{\partial n}\Big|_{z_{bot}} \tag{2.6.9}$$

where $\partial/\partial n$ is the outward normal derivative operator,

$$\frac{\partial}{\partial n} = \cos\varphi\frac{\partial}{\partial z} - \sin\varphi\frac{\partial}{\partial r}. \tag{2.6.10}$$

Substituting equation 2.6.3 into 2.6.9 and using equation 2.6.10, we obtain the general two-dimensional expression for continuity of normal particle velocity at the interface,

$$\begin{aligned}\rho_2\left[\frac{\partial u_1}{\partial z}v\cos\varphi - \frac{\partial u_1}{\partial r}v\sin\varphi\right]\Big|_{z_{bot}} - \rho_2 u_1\frac{dv}{dr}\sin\varphi\Big|_{z_{bot}} \\ = \rho_1\left[\frac{\partial u_2}{\partial z}v\cos\varphi - \frac{\partial u_2}{\partial r}v\sin\varphi\right]\Big|_{z_{bot}} - \rho_1 u_2\frac{dv}{dr}\sin\varphi\Big|_{z_{bot}}.\end{aligned} \tag{2.6.11}$$

At a locally flat interface, $\varphi = 0$, and equation 2.6.11 reduces to

$$\rho_2\frac{\partial u_1}{\partial z}\Big|_{z_{bot}} = \rho_1\frac{\partial u_2}{\partial z}\Big|_{z_{bot}}. \tag{2.6.12}$$

The current version of the IFD model is capable of handling a variable topography, although such variations are modeled in "staircase" fashion satisfying equation (2.6.12) on the flat stairs; there is no bottom roughness. Topography values were obtained from the ETOPO 5 data set from the National Oceanographic Data Center; the data set has 5 minute resolution in latitude and longitude.

Depth values were updated in the horizontal at each range step in an identical manner to the sound speed profile.

A fluid sediment layer is imposed below the water column, for which values of various parameters can be chosen: density ρ, sound speed discontinuity at the water-sediment interface c_w/c_b, constant sound speed gradient within the sediment layer $\partial c/\partial z$ (to model the effect of pressure within the sediment), an effective attenuation within the sediment, and the depth z_{sed} of the layer, which is uniform and follows the topography. Within the sediment, attenuation (β, hereafter) is modeled by inserting units of loss into the imaginary part of the index of refraction as

$$n^2 = \left(\frac{c_0}{c_i}\right)^2 + i\left(\frac{c_0}{c_i}\right)^2 \frac{\beta}{20\pi \log_{10} e}$$

where β is given in dB per wavelength and c_i is the speed of sound at the point (Lee and Botseas, 1982). Figure 2.1 schematizes the sediment model. Note that for some values of c_w/c_b, $\partial c/\partial z$, and z_{sed} there will be a duct in the sediment layer. Below the sediment layer is an artificial absorbing basement, with a perfectly transmitting interface between the two layers. In the absorbing basement, the sound speed, density, and attenuation are maintained constant to the bottom of the computational array to prevent reflections or refractions back to the water column, and an exponential damping is imposed on the complex sound field to permit use of a zero boundary condition at the bottom of the computational array.

In realistic sediments density gradients are small (usually less than .002 $gm/cm^3/m$); Rutherford and Hawker (1978) showed that inclusion of sediment density gradients increased bottom loss by approximately 2 dB in a narrow range of angles near incidence, and had negligible effect at other angles. Additionally, the sound speed in the top of the sediment maintains a constant ratio with the sound speed in the bottom of the water column (Hamilton and Bachman, 1982). Sound speed increases with depth in the sediment; the increase is primarily linear with a smaller quadratic component which increases the gradient with depth (Hamilton, 1985).

The sediment model described above specifically characterizes a fluid layer as the current version of the IFD model does not include a capability to model

shear waves. The mismatch in shear and compressional wave speeds causes conversion from compressional to shear waves to be small; furthermore, the typically high value of shear wave attenuation results in reconversion from shear to compressional waves to be negligible (Knobles and Vidmar, 1986). Thus shear wave excitation within the sediment acts primarily as a sink for acoustic energy. The ocean floor typically consists of a surface layer of unconsolidated sediment, which may contain multiple layers of different particle types and sizes. Consolidation and structural strength increase with depth (overburden pressure) in this layer, which would thus support shear waves. Below the sediment layer lies a solid basement. It has been shown that shear-wave excitation by compressional waves is negligible within the sediment layer for frequencies above 3 Hz (Vidmar and Foreman, 1979), and additionally that the mechanism for sediment shear wave excitation is primarily through conversion at the sediment-basement interface (Vidmar, 1980). Consequently, for acoustically thick sediments in which very little of the compressional wave energy reaches the substrate, shear wave excitation will be a negligible loss mechanism and the sediment may be treated as a fluid. For acoustically thin sediments, a large portion of the compressional wave energy interacts with the substrate and the sediment must be treated as a solid. In view of the loss associated with shear wave excitation, in this work it was modeled using a high value of compressional wave attenuation in the Iceland-UK Gap region, due to the extremely shallow sediment layer found on the ridge. In other cases, the sediment layer was thick enough to preclude shear wave excitation and the attenuation was not used to parameterize shear wave excitation losses. Hamilton (1976) showed that compressional wave attenuation decreases slowly within the sediment; within the upper 250 m the scatter among values is far greater than any trend with depth. Throughout this work compressional wave attenuation values have been chosen as the highest realistic values for the particular sediment, to model losses due to multiple layering within the sediments.

The IFD model calculates values of the complex sound pressure, which can be turned into the more familiar propagation loss by the expression $PL = -20 \log_{10} |p|$. In order to view the frequency-dependent propagation patterns in the entire water column, contour plots of propagation loss were created. Magnitudes can still be compared using the more familiar line plots of a receiver at a particular depth. Contours of propagation loss are beneficial in assisting an overall physical understanding of the frequency-dependent propagation patterns.

Figure 2.2 (after Tappert, 1977) shows a ray calculation and matching parabolic approximation sound field contours, calculated at 25, 50, and 100 Hz; contour levels given in Tappert (1977) are uncertain. The sound speed profile used in all cases was an idealized bilinear duct, with depth 4876.8 m and sound channel axis at 1219.2 m; a highly lossy bottom was used to eliminate bottom reflections. The source, at left, was at 609.6 m depth; axis tics on the vertical axes of the acoustic plots are at 1000 m intervals.

Interpretation of sound magnitude contours yields more quantitative information than does interpretation of ray diagrams. In the ray trace (top) we can see caustics at the convergence zones at the source depth, near 63 and 125 km range; also at the reciprocal of the source depth (2438.4 m) near 32 and 95 km range. These features appear in the propagation loss contours as local maxima of intensity at the same ranges and depths. Note that at 25 Hz the maxima associated with caustic structures are much more broad and diffuse; additionally, at lower frequencies the shadow zones between convergence maxima are increasingly filled in by diffraction, particularly at 25 Hz near 700 m depth and 120 km range. These contour plots allow us to see both interference and diffraction effects that are included in the parabolic equation but are absent from the ray approximation.

Figure Captions, Chapter 2

Figure 2.1) IFD fluid sediment model.

Figure 2.2) Acoustic propagation through an idealized bilinear sound speed profile. a. Ray calculation. b. Parabolic approximation, 25 Hz. c. Parabolic approximation, 50 Hz. d. Parabolic approximation, 100 Hz (after Tappert, 1977).

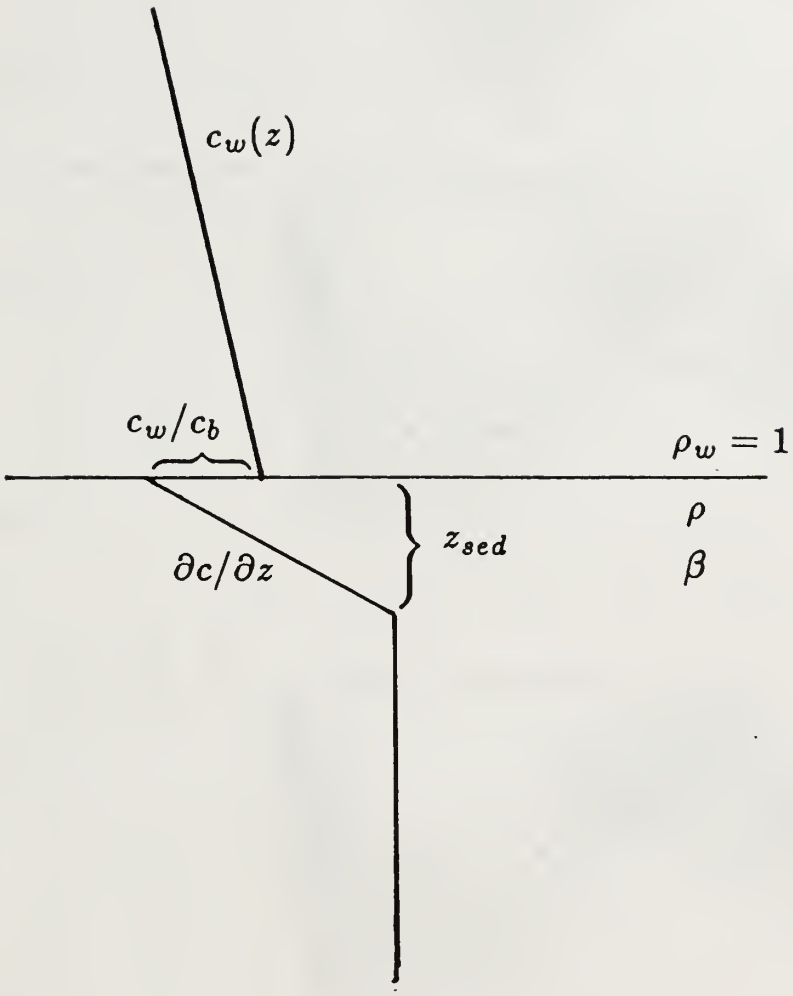

Figure 2.1) IFD fluid sediment model.

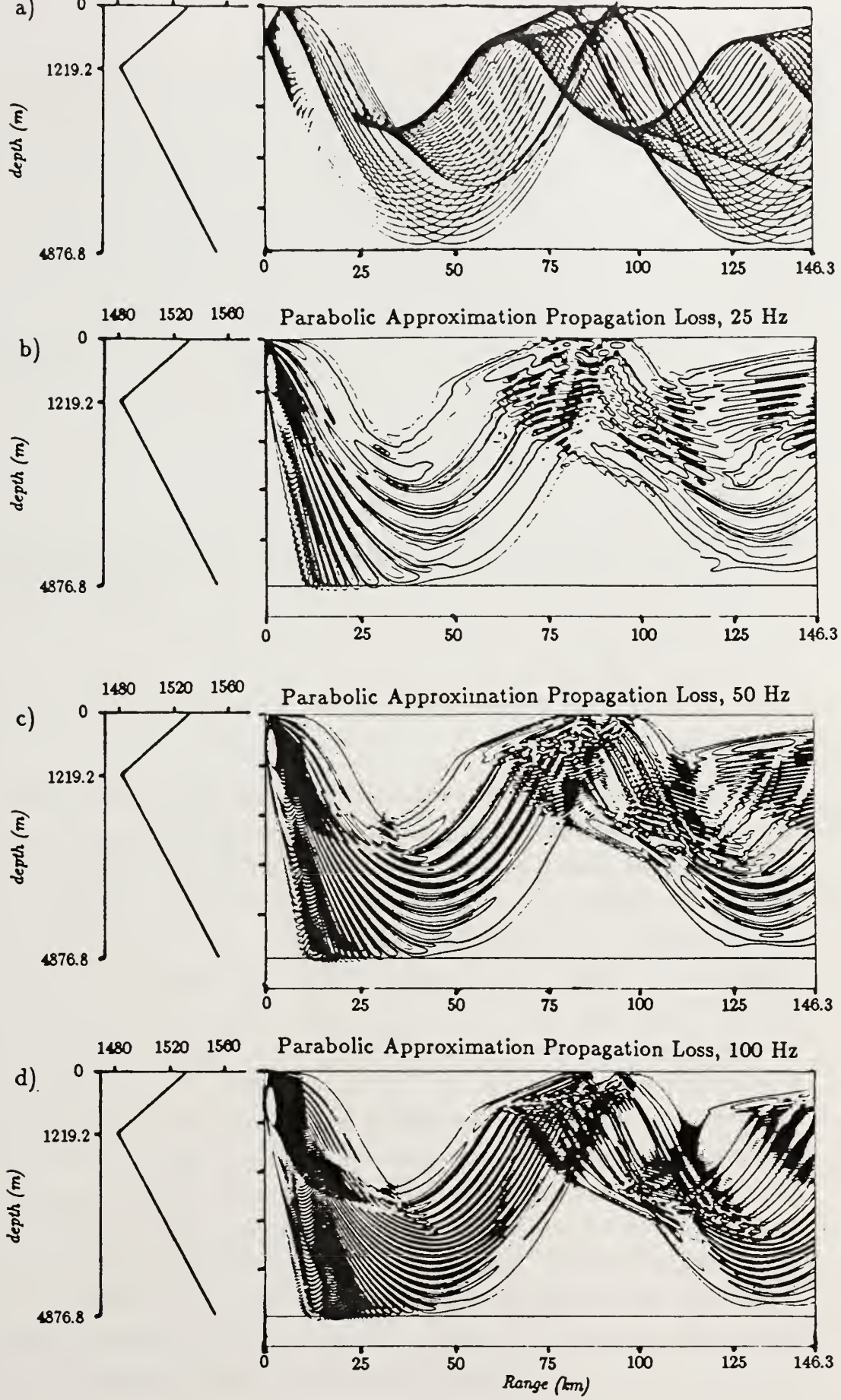

Figure 2.2) Acoustic propagation through an idealized bilinear sound speed profile. a. Ray calculation. b. Parabolic approximation, 25 Hz. c. Parabolic approximation, 50 Hz. d. Parabolic approximation, 100 Hz (after Tappert, 1977).

Chapter 3

Oceanographic and Topographic Interactions in the Gulf Stream Region

The Harvard Open Ocean Model outputs have been coupled to the finite difference parabolic approximation model and the resulting calculations of acoustic propagation through range-dependent oceanographic fields have been reported (Robinson, 1987; Lee et al., 1989; Mellberg et al., 1990). The addition of both variable topography and a fluid sediment layer to the acoustic propagation model has also been documented (Siegmann et al., 1990). This sediment layer changes the nature of the acoustic waveguide by changing both its depth and the boundary condition at that depth, with resultant dramatic changes to the propagation patterns within the water. The addition of the variable-depth sediment layer had a stronger effect on propagation patterns than did azimuthal coupling, except in regions of extremely strong azimuthal water-column effects near a seamount (Siegmann et al., 1990). The exact nature of these topographic modifications to the water column propagation patterns was not known, however, nor was the specific effect of the sediment layer itself. A systematic analysis is necessary to determine the magnitude and nature of the changes in underwater acoustic propagation due to changing properties of the water column, the underlying topography depth, and sediment character.

3.1 Parameter Study Design

In order to study these interactions in a controlled fashion, a parameter study was developed in a section of the Gulf Stream region, designed to include strong oceanographic effects and monotonic topographic effects (sloping either upward or downward). A pair of reciprocal points on either side of the Gulf Stream was selected in the continental slope region, and acoustic propagation was calculated from the Slope water to the Sargasso water (with realistic downsloping topography) and from Sargasso water to Slope water (with realistic upsloping topography). Figure 3.1a shows a horizontal map of the dynamically adjusted oceanographic streamfunction fields valid at model time $t = 0$ used for acoustic propagation, with the the reciprocal pair of points added. Figures 3.1b and 3.1c show the sound speed profiles at the two points. The Slope water profile shows a sound speed channel axis near 500 m depth with a rapid increase in sound speed toward the surface; the Sargasso water profile shows a much deeper sound channel axis near 1275 m depth and a more gradual increase in sound speed toward the surface. Note the weak secondary duct near 370 m; its magnitude is less than .5 m/sec.

In the study, the effects of the oceanography were assessed by comparing acoustic propagation through realistic oceanographic fields with calculations through range-independent oceanographic fields; the effects of the monotonically increasing or decreasing topography were likewise determined by comparing acoustic propagation over the range-dependent bottom with acoustic propagation over a flat bottom. Thus a set of four environmental conditions were considered for each source location: a) range dependent oceanography/range dependent topography, b) range dependent oceanography/flat bottom, c) range independent oceanography/range dependent topography, and d) range independent oceanography/flat bottom. Additionally, to study the dependence of interaction effects on source depth, four different source depths were considered for each configuration of environmental fields. Sources were located at 10, 100, 750, and 3000 m depth; the 10 m source was chosen to be near the surface, the 100 m source to be slightly farther away and to match other studies, the 750 m source to be between the sound channel axes of the Slope and Sargasso water profiles, and the 3000 m source to be in the deep part of the profile. Table 3.1 summarizes the physical design of the study; figure 3.2 demonstrates the combinations of oceano-

graphic sound speed and topographic configurations used, for the two reciprocal propagation transects. Asterisks along the left axes denote source depths for the 100, 750, and 3000 m sources; the 10 m source was left off the figures due to the scale. Range independent oceanographic fields are on the left and range dependent on the right in each case. Sound speed contour intervals are 5 m/sec. Note that the runs with range independent oceanography and flat bottom were conducted with different sound speed profiles and bottom depths, to match the starting conditions for the appropriate comparison run: calculations from Slope to Sargasso water are compared with range independent Slope water runs, and calculations with bottom topography starting at 3170 m deepening to 4440 m were compared with flat bottom runs with depth 3170 m. A similar system of comparisons was used for the Sargasso to Slope water calculations. Most runs were conducted at frequencies of 25 and 100 Hz; it became necessary to make some calculations at 50 Hz to clarify certain phenomena. In all these cases, the form of the acoustic interaction with the sediment could be analyzed by varying the sediment parameters.

Parameter Study Experimental Design

Slope to Sargasso Propagation

Range Dependent Oceanog.		Range Ind. Oceanog. (Slope)	
Downslope source depth	Flat (3170 m) source depth	Downslope source depth	Flat (3170 m) source depth
10	10	10	10
100	100	100	100
750	750	750	750
3000	3000	3000	3000

Sargasso to Slope Propagation

Range Dependent Oceanog.		Range Ind. Oceanog. (Sargasso)	
Upslope source depth	Flat (4440 m) source depth	Upslope source depth	Flat (4440 m) source depth
10	10	10	10
100	100	100	100
750	750	750	750
3000	3000	3000	3000

Table 3.1

3.1.1 Examples of Realistic Propagation

Figures 3.3 through 3.6 show representative cases of propagation from Slope water to Sargasso water and from Sargasso to Slope water for sources at 100 m depth and frequencies of 25 and 100 Hz. These figures include plots of sound speed contours, propagation loss at a 100 m receiver, propagation loss contours, and propagation loss at a 1000 m receiver. All propagation loss values are obtained by averaging computed results over a 1 km window centered at each plotted range value. Contour intervals on the propagation loss plots are every 5 dB with a dark contour every 20 dB (80, 100, 120, etc.). Contour intervals remain the same in all the upcoming plots; however, the starting and ending contours occasionally differ in order to delineate areas of lesser ensonification. The calculations include effects of the varying oceanography and topography, as well as the sediment layer. We see the formation of a shadow zone after 125 km range in the Slope to Sargasso water case (figures 3.3 at 25 Hz and 3.4 at 100 Hz); this greatly reduces postfrontal ensonification at the 100 m receiver. The frontal interaction has also disrupted the convergence zone pattern at the 1000 m receiver. This effect is far more dramatic at 100 Hz than at 25 Hz; at 100 Hz it results in a general increase in post-frontal ensonification at that 1000 m receiver. Turning to the Sargasso to Slope case (figures 3.5 at 25 Hz, 3.6 at 100 Hz) we see that the propagation pattern changes dramatically as frequency increases two octaves. At 25 Hz, the frontal interaction produced a convergence zone pattern for both the 100 m and 1000 m receivers beyond 150 km. At 100 Hz, bottom reflections seem to dominate the propagation pattern throughout the range, with some sort of modification by the oceanography seen between 125–175 km in the propagation loss contours. We see these bottom-reflection maxima in the 100 m receiver near 100, 183, and 228 km range. It is unclear what features of these propagation patterns, specifically, are due to the oceanographic variations, and what features are due to the topographic variations, or perhaps due to an interaction of both physical variations. Additionally, it is not known how the propagation patterns will change as the nature of the sediment changes, nor is it known how all these propagation interaction effects depend on source depth and frequency.

The type of effect the oceanography and topography interactions have on the propagation patterns depends on the properties of the sediment itself.

Therefore, to build a clear understanding of the propagation properties of any particular acoustic waveguide, we must start first from the basics and clarify the source and frequency dependence of propagation sensitivity to the sediment parameter values; from this knowledge we will be able to build an understanding of the effects of varying sediment depth with range, varying the form of the oceanographic waveguide with range, and the interactions when both vary.

3.2 Bottom Sediment Effects on Waveguide Propagation

3.2.1 Source Depth, Frequency Dependence of Sediment Interactions

The source depth dependence of propagation is related to the relationship between the sound speeds at the surface, source, and sediment interface. In the present work we deal with a two-dimensional ocean without angular dependence; additionally, the strong horizontal stratification of the ocean means we can think of sound speed as a function of depth alone for this discussion of sediment interactions. Range dependence of sound speed will be discussed in later sections.

It is a fundamental principle of refraction (Snell's law) that propagating sound in a range independent waveguide will maintain a constant value of $(\sin\theta)/c$, where θ is the propagation direction (normal to the wavefronts) measured from the vertical. It must be noted that Snell's law is a high frequency result; it can break down at lower frequencies.

For a general sound speed profile containing a deep sound channel and no surface duct, there will exist two possibilities: either the sound speed at the surface is less than that at the bottom, or it is greater. If the sound speed at the surface is less than that at the bottom, the profile is said to have "depth excess" and any sound that grazes the surface as it refracts will again refract with depth before reaching the sediment. There will additionally exist propagation paths that refract with depth before reaching the sediment, but which reflect off the surface; the sound in all these paths will reinforce to produce convergence zones at the surface. In this type of profile, the existence of propagation paths which refract before reaching the bottom is not altered, whether $c_{bot} > c_{surf} > c_{src}$ or $c_{bot} > c_{src} > c_{surf}$, where c_{surf}, c_{src}, and c_{bot} are the sound speeds at the surface, source, and water side of the water-sediment interface, respectively. Since there

are no sediment losses along these depth-refracting paths, they will dominate the propagation pattern.

If, on the other hand, the sound speed at the surface is greater than that at the bottom, then there are two possibilities for sound speed relationships and propagation patterns differ strongly between the two cases. First, suppose that $c_{surf} > c_{bot} > c_{src}$, that the sound speed at the bottom of the water column exceeds that at the source. In this case there will exist sound propagation paths departing from the source that refract with depth before encountering the sediment; these paths will not reach the surface. Since sound in these paths will undergo no bottom losses, it will dominate long-range propagation patterns.

Alternatively, suppose that $c_{surf} > c_{src} > c_{bot}$, that the sound speed at the source exceeds that at the bottom of the water column (a bottom-limited case). Then all sound propagation paths departing from the source impact the bottom before refracting with depth; there will be no paths that leave the source and subsequently refract entirely within the water column. We can expect bottom interactions to have a much greater effect in these cases.

Sound Speed Values at Surface, Source Depths, and Sediment

	Slope	Sargasso
z	$c(z)$	$c(z)$
0	1535.5	1543.5
10	1530.2	1543.3
100	1501.6	1539.6
750	1481.5	1516.6
3000	1511.4	1512.2
3170	1514.0	
4440		1534.1

Table 3.2

Table 3.2 shows values of sound speeds at the surface, four source depths, and sediment depth in the Slope and Sargasso water profiles. We see that for both these profiles the sound speed at the surface exceeds that at the bottom; neither has depth excess. Furthermore, in the Slope profile for $z_s = 10$ m and the

Sargasso profile for $z_s = 10$ and 100 m, the sound speed at the source is greater than that at the sediment; for these cases we can expect bottom interactions to be very important in the propagation patterns, which would show strong sensitivity to the values of the sediment model parameters. We might expect the deeper three sources in the Slope profile and the deeper two in the Sargasso profile to be comparatively insensitive to bottom interactions.

In fact, low-frequency interference effects modify this line of reasoning, and we must examine the propagation properties in the water column in the first 50 km. For a source in the presence of a reflecting surface, an interference pattern forms between sound radiating from the source and its reflected image source an equal distance above the surface. For general spherical waves, this can be written as

$$\Psi = \Psi_1 \frac{e^{ikr_1 - i\omega t}}{r_1} + \Psi_2 \frac{e^{ikr_2 - i\omega t}}{r_2}$$

$$= e^{-i\omega t} e^{ikr_1} e^{i\phi_1} \left[\frac{|\Psi_1|}{r_1} + \frac{|\Psi_2|}{r_2} e^{ik(r_2 - r_1)} e^{i(\phi_2 - \phi_1)} \right]$$

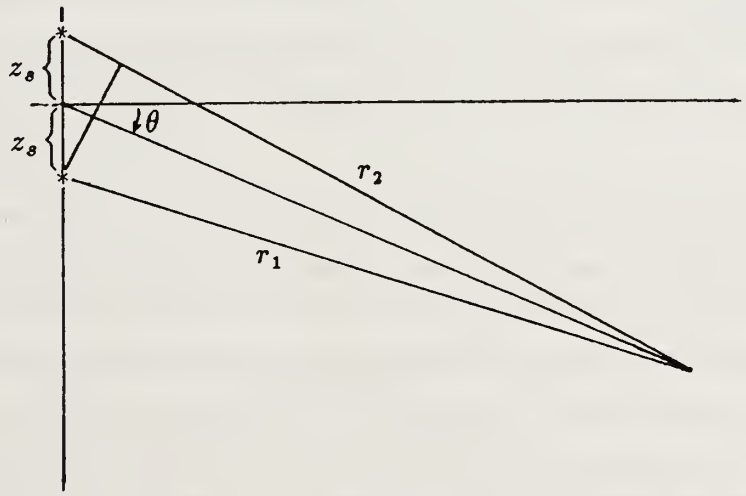

where r_1 and r_2 are distance from each source to the observer, θ is the angle from the origin to the observer, Ψ_1 and Ψ_2 are the (possibly complex) pressures of each source, with phases of ϕ. In the case of the reflecting surface, the magnitudes will be equal and the phase difference between them $\phi_2 - \phi_1 = \pi$. Calculating intensity $|\Psi|^2 = \Psi^* \cdot \Psi$, we get

$$|\Psi|^2 = \frac{|\Psi_1|^2}{r_1^2} + \frac{|\Psi_1|^2}{r_2^2} + 2\frac{|\Psi_1|^2}{r_1 r_2} \cos\left(k(r_2 - r_1) + \pi\right).$$

We take the Fraunhofer approximation, by which we assume the observer at a great distance from the source; in amplitudes, $r_1 \approx r_2 \approx r$ and in wave phase, $r_1 - r_2 = 2z_s \sin\theta$. Then the intensity becomes

$$\begin{aligned} |\Psi|^2 &= \frac{2|\Psi_1|^2}{r^2}\left[1 - \cos(2kz_s \sin\theta)\right] \\ &= \frac{4|\Psi_1|^2}{r^2}\sin^2(kz_s \sin\theta) \end{aligned}$$

We see that if $kz_s > \pi$ (i.e., $2z_s/\lambda > 1$), then the argument of the squared sine goes through more than one period of π as $0 < \theta < \pi$ and the intensity field will have more than one lobe of sound maxima. If $kz_s < \pi$ (i.e., $2z_s/\lambda < 1$), the argument does not go through any complete cycles of $n\pi$ as $0 < \theta < \pi$, and the intensity field will have a single maximum around $\theta = \pi/2$ (the vertical), whose form depends on kz_s. The interference patterns described here are known as Lloyd's Mirror. In our case of underwater acoustic propagation, if the source is greater than one wavelength from the surface, the interference patterns separate the sound into distinct energy maxima. If the source is less than one wavelength from the surface, a single lobe of energy will form, centered around the vertical. Since sound speed varies with depth in this duct, refraction of the individual paths causes a distortion of the beam pattern and the lobes will propagate with different angles at depth.

The acoustic propagation patterns and their dependencies on frequency, profile shape, source depth, and local bottom depth have a profound effect on the amount and type of sediment interaction that occurs in each instance. Figures 3.7 and 3.8 show the short-range propagation patterns for the range independent Slope profile and flat bottom at 3170 m. Figure 3.7 shows sources at 10 m depth on the left and 100 m depth on the right, and frequencies from 25, 50 and 100 Hz from the top to bottom of the page. Figure 3.8 shows sources at 750 and 3000 m depth for the same profile and frequencies. Figures 3.9 and 3.10 show the same sequence of source depths 10, 100, 750, and 3000 m, and frequencies for the Sargasso profile and bottom depth of 4440 m. In order to focus only on water column propagation patterns with no confusion from bottom reflecting or refracting propagation paths, these particular figures show calculations done with the so-called "absorbing" bottom: where density $\rho = 1.0$, attenuation $\beta = 0.0$, interface sound speed ratio $c_w/c_b = 1.0$, sediment gradient $\partial c/\partial z = 0.0$, and sediment thickness $z_{sed} = 0$ m. With these parameter choices, all sound

that strikes the bottom propagates straight into it away from the water column; the artificial absorbing basement described in chapter 2 decreases the sound magnitude with depth.

The calculations were all done with a perfectly reflecting surface, and in these plots we see the Lloyd's Mirror interference pattern formed by the source and its reflected image above the surface. Note when $z_s = 10$ m at 25 and 50 Hz ($\lambda \sim 60$ and 30 m, respectively) that we do not resolve separate Lloyd's Mirror interference lobes; when $f = 100$ Hz ($\lambda \sim 15$ m) we do. As an aside, note when $z_s = 3000$ m that the Fraunhofer approximation is breaking down; we do not begin to resolve separate interference lobes until after 20 km range, if at all.

In these calculations, we see that the primary lobe containing the largest amount of sound energy is the one that propagates with shallowest angle, although for sources farther from the surface or higher frequencies the distinction decreases. Since sound speed within the water column is not constant with depth, these interference lobes will refract; we may infer that there will be some configuration of sound speed profile, source depth, and bottom depth for which the primary lobe of sound strikes the sediment at 25 Hz but refracts within the water column at 100 Hz. This is in fact the case for the Slope profile with source at 100 m and bottom at 3170 m as shown on the right side of figure 3.7. At 25 Hz, the primary beam of sound strikes the sediment approximately 16 km from the source, at 50 Hz it grazes the sediment, and at 100 Hz it refracts entirely within the water column.

The sensitivities of water column propagation to all the bottom sediment parameters can be related to the properties outlined above. In frequency and source depth cases where the primary lobe of sound interacted with the bottom, the values of the sediment parameters had a strong effect on water column propagation; in cases where the majority of the sound refracted entirely within the water, propagation was relatively insensitive to the bottom properties. From this we could expect Slope water propagation with the source at 100 m to behave as if it had $c_{bot} > c_{src}$ and be relatively insensitive to bottom parameters for the highest frequency used (100 Hz) and to be strongly bottom-interacting as if $c_{src} > c_{bot}$ at the lowest frequency (25 Hz); this was in fact the case. An example of this phenomenon will be shown below.

Looking again at the cases where $c_{src} > c_{bot}$, i.e., figure 3.7 for $z_s = 10$ m (left) and figure 3.9 for both $z_s = 10$ m and 100 m, we see that we do nevertheless get sound that refracts totally within the water column. In figure 3.7 for $z_s = 10$ that water-refracted return appears near the surface at 50 km range, and in figure 3.9 for both $z_s = 10$ and 100 m it appears near 3000 m depth at 50 km. In the Snell's law interpretation, sound in these paths must have left the source with complex propagation angle. According to Brekhovskikh (1980, section 26.3), complex propagation angles are physical and can be shown to be the result of representing a spherical source as the superposition of plane waves. Alternatively, the existence of sound in these paths can be explained through the normal mode formulation.

One method of solution of the Helmholtz equation in a range-invariant environment is by separation of variables, which yields separate expressions for the range dependence and depth dependence of the acoustic field. The depth dependence is represented as a sum of normal modes, whose shapes depend on the form of the sound speed profile. In a range-dependent environment, the shapes of these modes will change with location as the local sound speed profile $c(r, z)$ changes. The local normal modes of the sound field are eigenfunctions Z_n with eigenvalues k_n of the equation (Clay and Medwin, 1977, section 9.1.1)

$$\frac{d^2 Z_n}{dz^2} + \left[\left(\frac{\omega}{c(z)} \right)^2 - k_n^2 \right] Z_n = 0;$$

solutions are exponentials which oscillate for

$$\left(\frac{\omega}{c(z)} \right)^2 - k_n^2 > 0$$

and attenuate for

$$\left(\frac{\omega}{c(z)} \right)^2 - k_n^2 < 0.$$

The exponential will attenuate more rapidly at higher frequencies, so lower frequencies will show more sound penetration into regions of higher sound speed. Particular modes can be excited by a source located anywhere they have non-zero amplitude, and the amount of such excitation will depend on the magnitude of the mode at that depth. Thus a source in higher sound speed water can excite a mode via its exponential tail from the lower sound speed water; since

the magnitude of that exponential tail will be higher at lower frequencies, such modes will be more strongly excited at lower frequencies; they will also be more strongly excited for sources closer to the lower sound speed water. The equivalent ray-angle θ_n of a normal mode is defined as $k_n = (\omega/c_0)\sin\theta_n$, where c_0 is the minimum sound speed in the profile and θ_n is measured from the vertical. This is equivalent to Snell's law since k_n is constant throughout the waveguide, so

$$k_n = \frac{\omega}{c}\sin\theta$$

Modes which propagate entirely within the water column are referred to as "trapped" modes, as they are trapped within the waveguide. Modes that interact with the lossy sediment are referred to as "leaky" modes as their magnitude decreases with range. Tindle and Guthrie (1974) showed that ray propagation paths are duplicated by summing modes in groups; each group of neighboring modes manifests as energy traveling along the ray path corresponding to the central mode. These ray propagation paths can be thought of as "equivalent" or "fuzzy" rays whose full width at half-maximum γ goes as $\gamma \propto (r/\omega)^{1/2}$ (Guthrie and Tindle, 1976). The expression demonstrates that ray width increases with range and tends to zero at infinite frequency.

Returning to figure 3.7 for $z_s = 10$ m (left column) and figure 3.9 for both $z_s = 10$ and 100 m, we can conclude that the water-refracted sound consists of modes that have been excited via their exponential tails into the higher sound speed water at the source. For instance, in the Slope water profile, the sound speed at the bottom is 1514.0 m/sec (table 3.2). Sound which refracts at this depth would also refract near 50 m depth, where the sound speed is also 1514.0 m/sec in this profile. According to the mode formulation and the "equivalent" ray connection of Tindle and Guthrie (1974), the group of normal modes that comprises the sound in this equivalent ray path would have exponentially decaying tails that extend into the higher sound speed water; the strength of their excitation would depend on the magnitude of the mode at the source location. That magnitude depends both on frequency and on position of the source. In figure 3.7 for the Slope water profile with $z_s = 10$ m (left column), we can see this frequency dependence. At 25 Hz (top left), the sound magnitude in the propagating path reaches a maximum of 105 dB near the surface by 50 km range; at 50 Hz (middle left), the magnitude is between 105–110 dB; and at 100 Hz (lower left), it is 110–115 dB. As frequency increased, excitation of the modes comprising that refracted sound decreased.

The same principles can be used to explain magnitudes in the refracted sound paths in the Sargasso profile, for z_s = 10 and 100 m (figure 3.9). The refracted returns appear near 3000 m depth at 50 km range. In the Sargasso profile, the sound speed at the 4440 m bottom is 1534.1 m/sec (table 3.2). Sound which refracts at this depth would also refract near 165 m depth, where the sound speed has the same value. We note in these cases that both the 10 and 100 m sources excite the same group of trapped modes; excitation is stronger for the 100 m source than the 10 m source, and stronger at 25 Hz than at 100 Hz. These sources would also excite groups of trapped modes with shallower equivalent ray-angles which would propagate much closer to the axis of the waveguide; the strength of excitation of these groups of modes will depend on source depth and frequency in the same manner. Their magnitudes will be sufficiently weaker than those of the modes propagating between 165 and 4440 m that they are not seen here, but their effect will become apparent in section 3.5.

These cases also demonstrate another phenomenon; in the 100 Hz cases (figure 3.9, bottom) we see beams propagating back from the sediment which reach the surface near 40 km range for the 10 m source, and near 25, 33, 41, and 50 km range for the 100 m source. Due to the angles of propagation and thicknesses of these beams, they appear to be reflections off the sound speed gradient discontinuity at 4440 m depth; Brekhovskikh (1980, section 20.5) discusses such reflections in the case of normal incidence, after Rayleigh (1945, Vol. I, section 148b). Tests were conducted with a negative sound speed gradient, to increase the magnitude of the discontinuity while not refracting sound from greater depths back to the water column; the sound magnitudes in these paths increased with the change in magnitude of sound speed discontinuity, as indicated by the theory. These test cases are included in appendix A.

In the upcoming discussions of bottom interaction phenomena we will refer frequently to the form of the water-sediment Rayleigh reflection coefficient due to discontinuities between the media, which has been calculated for each case. The Rayleigh reflection coefficient is given by

$$R_{12} = \frac{\rho_2 c_2 cos\theta_1 - \rho_1 c_1 cos\theta_2}{\rho_2 c_2 cos\theta_1 + \rho_1 c_1 cos\theta_2}$$

where c_1 is the sound speed on the water side of the interface and c_2 is the sound

speed on the sediment side of the interface (Clay and Medwin, 1977, section 2.9). Angles θ_1 and θ_2 are normal to the sound pressure wave-fronts and are measured from the vertical on the water and sediment sides of the interface respectively; sound which approaches the bottom with grazing incidence will have $\theta_1 \rightarrow 90°$. Values for θ_2 can be obtained from Snell's Law

$$\frac{sin\theta_1}{c_1} = \frac{sin\theta_2}{c_2}$$

For cases of interest here, the magnitudes of such reflections will generally be larger than the magnitudes of reflections from the discontinuity in sound speed gradient (Brekhovskikh, 1980, section 20.5). Attenuation in medium 2 is modeled by (Lee and Botseas, 1982)

$$n^2 = \left(\frac{c_0^2}{c_2^2}\right) + i\left(\frac{c_0^2}{c_2^2}\right)\frac{\beta}{\gamma}$$

where c_0 is the reference sound speed for the calculation, β is the attenuation in dB/λ and $\gamma = 20\pi log_{10}e$. Using this index of refraction $n(z) = c/c(z)$ in the Rayleigh reflection coefficient is mathematically equivalent to the reflection coefficient obtained when sound speed in the attenuating medium is a complex number (Mackenzie, 1960). This interface form of the reflection coefficent was selected over an integrated form (Williams and MacAyeal, 1979), which includes the effect of a sound speed gradient in the bottom, because the bottom-reflected and refracted sound returns can frequently be distinguished from one another within the water column. Additionally, propagation paths which include bottom reflections near grazing incidence were seen to be extremely important in certain cases, and the integrated form of the reflection coefficient is only valid for angles $10° \leq \theta \leq 70°$. The interaction of the angular distribution of incident sound energy with the reflection coefficient's dependence on incident angle frequently explains many observed propagation effects.

3.2.2 Effects of Individual Sediment Parameters

To study the effects of the sediment in isolation from any modifications by the oceanography or topography variations, we will discuss for the present only

calculations performed with range independent oceanography and flat topography. The particular cases used as reference examples for most of the sediment discussion will be the Slope profile with $z_s = 10$ m and the Sargasso profile with $z_s = 100$ m, and the "realistic" set of sediment parameters: $\rho = 1.352$ gm/cm^3, $\beta = .9$ dB/λ, $c_w/c_b = 1.017$, $\partial c/\partial z = 1.227$ sec^{-1}, and $z_{sed} = 100$ m. In the upcoming discussions we will vary these values one at a time and compare the results with these reference cases. Figures 3.11 through 3.14 show the reference cases at 25 and 100 Hz; figure 3.11 shows propagation in the Slope water profile for a source at $z_s = 10$ m and frequency 25 Hz; figure 3.12 shows the same case but at 100 Hz. In figure 3.13 we have propagation in the Sargasso profile with $z_s = 100$ m at 25 Hz, and in figure 3.14 we have the same case at 100 Hz. These figures contain a plot of the magnitude (solid) and phase (dashed) of the Rayleigh reflection coefficient at the water-sediment interface, a contour plot of propagation loss, and propagation loss for receivers at 100 and 3000 m depth for magnitude comparisons. The plots of reflection coefficient show a spurious jump in phase as $\theta \rightarrow 90°$; this was an artifact of the numerical code and not present in the limiting behavior of the analytical expression. In the upcoming examples the values of each of these parameters will be varied alone, to determine its effect on the propagation. These cases were chosen to have source sound speed greater than the sediment sound speed in order to demonstrate strong bottom interactions in each profile; the primary lobe of the Lloyd's Mirror interference pattern strikes the sediment at all frequencies tested. This implies that long-range propagation patterns in these cases will consist of sound which left the source with complex propagation angle. These cases were also chosen to be illustrative of particular different phenomena. Readers interested in seeing these phenomena in the other source depths are referred to appendix A.

The Slope water cases are fairly representative of convergence zone propagation, whether consisting of sound with real or complex initial angle. In figures 3.11 and 3.12, we see an interesting frequency effect: the convergence zone radius (r_{cz}) with which sound refracting within the water column returns to the surface is slightly longer at 100 Hz than at 25 Hz; for example, at 25 Hz with the 3170 m bottom, r_{cz}=49.5 km while at 100 Hz, r_{cz}=52 km. For instance, in figure 3.11 we see the fourth convergence zone maximum near the surface at 198 km range; in figure 3.12 at 100 Hz the same convergence zone maximum appears near 208 km range. The change can be explained by referring to the "equivalent" ray con-

cept of Guthrie and Tindle (1976); recall that the full width at half-maximum of these equivalent rays decreases with increasing frequency as $\gamma \propto (r/\omega)^{1/2}$. At 25 Hz, the "ray" whose center just grazes the bottom also extends some distance into the sediment, interacts, and thus attenuates away; the first non-interacting "ray" has a center less deep and thus r_{cz} is shorter. At 100 Hz, the "ray" whose center just grazes the bottom extends a lesser distance into the sediment; the first non-interacting "ray" has a center deeper than in the 25 Hz case and thus r_{cz} is slightly longer. Notice in the plots of the 3000 m receivers not only are the convergence zone maxima at greater ranges in the 100 Hz case than in the 25 Hz case, they have 2–3 dB greater magnitude. This is not due to greater energy in the convergence zone path; at the 100 m receiver the 100 Hz case has 2–3 dB less sound in the maxima than the 25 Hz case. At 100 Hz the deep sound maxima are closer to the sediment, since the deepest non-sediment interacting "ray" has a deeper center, and the 3000 m receiver cuts closer to this deep center.

The Sargasso water examples show an unusual form of propagation. At 25 Hz (figure 3.13), we see a great deal of interference nearly obscuring convergence zone propagation. At 100 Hz (figure 3.14), we see a large number of sound beams reflecting off the bottom. Referring back to figure 3.9 for the early propagation patterns for this configuration, we see that at 100 Hz several interference lobes interact with the sediment near grazing incidence. From the plots of reflection coefficient, $|R_{12}| \rightarrow 1$ for sound approaching grazing incidence; therefore we can expect sound to propagate for mid- to long-ranges along a path that refracts through the water, strikes the sediment with glancing incidence and undergoes significant reflection, then refracts again through the water. Successive bottom interactions will cause the sound in this path to weaken with range, but the loss will be slow. Eventually, sound propagating entirely within the water column will dominate. In figure 3.14 for 100 Hz we see the shift in which propagation path is most important between 125 and 175 km range. In the 100 m receiver, the maxima near 100 and 150 km range represent the bottom-reflected sound; the maximum near 205 km represents water-propagating sound. This can be determined by comparison with the contour plot. The 3000 m receiver cuts through bottom-reflecting maxima until 125 km range; subsequent maxima at 150, 180, 220, and 250 km represent water-propagating sound. Since these mid- to long-range bottom "glancing" paths depend strongly on the functional form of the reflection coefficient near grazing incidence, and since they dominate the

propagation pattern so extensively, the entire water column propagation pattern will be extremely sensitive to the form of the reflection coefficient and thus to the parameters that determine its shape.

3.2.2.1 Density

Figure 3.15 shows the propagation patterns in Slope water for source $z_s = 10$ m and frequency $f = 100$ Hz, with bottom density $\rho = 1.0$ (density continuous with the water). The plots of 100 and 3000 m receivers show this case overlaid with the reference case in figure 3.11; results with $\rho = 1.0$ are in bold. We see that the primary effect of bottom sediment density on the reflection coefficient is to decrease $|R_{12}|$ for steep angles of incidence and to increase $|R_{12}|$ for grazing angles ($> 75^o$ from vertical). In the propagation fields, removing the density discontinuity has reduced by 20 dB the steep bottom-reflected return seen in the 100 m receiver plots between 2 and 5 km from the source. As an aside, we note that the IFD model does not accurately handle these steep returns; we could probably expect a larger return in short ranges than calculated here. Recall that the wide-angle approximation to the parabolic equation permits propagation at angles up to 40^o from the vertical. Considering propagation at steep angles to be nearly straight-line, for a profile of depth 3170 and source at 10 m, the code will incorrectly handle sound that strikes the bottom closer than 3.8 km range; sound striking the bottom the first time at greater ranges will be propagated correctly. These early returns appear near the surface at 7.6 km range. The relatively small $|R_{12}|$ at steep angles for realistic sediments means these returns do not survive many bottom reflections.

On the other hand, the increase in $|R_{12}|$ near grazing has increased the sound magnitude by about 7 dB in the returns near 30 km and 75 km. These latter returns thus represent sound which hit the bottom with near grazing incidence and had a large percentage reflect. These reflections propagate down the channel and can be seen in the 100 m depth convergence zone minima near 125, 170, and 225 km, and as an increase in magnitude at the 3000 m receiver near 105, 155, and 200 km range. Since each bottom interaction causes some percentage of the sound to be lost, the magnitude of this reflecting/refracting sound decreases leaving the purely water-propagating sound in the channel. This example is representative of the fairly standard form of bottom density effect found

in other cases.

Figure 3.16 shows the propagation patterns for the Sargasso water example with $z_s = 100$ m and $f = 100$ Hz, and a bottom density $\rho = 1.0$. The plots of the receivers show values for this case overlaid with values from the reference case figure 3.14; results with $\rho = 1.0$ are again in bold. In the 100 m receiver, we see the same decrease of 20 dB in the steep reflected return near 5 to 10 km, and an increase in sound magnitude of 10 to 15 dB for the rest of the propagation range. In this case the increase in $|R_{12}|$ near grazing incidence has caused a great deal more sound to propagate on that bottom-glancing path down the waveguide; the contours of propagation loss show that the water-refracting sound does not begin to observably dominate the propagation pattern until after 225 km range or further. Note in the 3000 m receiver that the increased bottom reflections obscure the regular water-propagation maxima seen past 125 km in the reference case (figure 3.14d). It is unusual to have the bottom density affect the mid- to long-range propagation pattern, but under certain conditions, quite physical.

3.2.2.2 Attenuation

The effect of bottom attenuation is to decrease the sound magnitude that refracts through the sediment layer back toward the water column. With no attenuation, the sound that transmits into the sediment refracts around and back into the water column, with a phase shift dependent upon the path length travelled through the sediment. Without attenuation, the propagation pattern is one of maximal interference between sound on these different propagation paths. Gradually increasing β will slowly filter out sound in deep sediment propagation paths, while decreasing the sound magnitude returning from shallower propagation paths.

The frequency dependence of propagation sensitivity to the value of β will be due to two effects: first, the attenuation is given in dB/λ, which is nearly constant over frequency (Hamilton, 1980) although recent work suggests that the relationship may not hold at low frequencies (Kibblewhite, 1989). At 25 Hz, $\lambda \simeq 60$ m; and at 100 Hz, $\lambda \simeq 15$ m, so higher frequency sound will undergo more attenuation per meter within the sediment. In figures 3.17 and 3.18 for 25 and 100 Hz respectively we see propagation for the Slope example with attenuation

$\beta = .25$ dB/λ. Note that the magnitude of R_{12} is slightly less for all values of θ when β is smaller; less sound reflects, more sound propagates into the sediment. The receivers in figure 3.17 are overlaid with those in figure 3.11, and the receivers in figure 3.18 are overlaid with those in figure 3.12. Each time, the case $\beta = .25$ is in bold. Note how much more quickly the water column propagation is resolved from the interfering sediment returns at 100 Hz than at 25 Hz.

Additionally, in figure 3.18 at the 100 m receiver, we see an increase in sound magnitude near 30, 65, and 125 km range; since we know that less of the sediment-refracting sound attenuates with $\beta = .25$, we can identify these returns as traveling a path within the sediment. The receiver at 3000 m shows similar increases near 35 km range and increases in interference patterns in the convergence zone minima further down range.

We see that β affects the same parts of the 100 m and 3000 m returns as did the ρ decrease; this is to be expected. With the decrease in ρ came an increase in reflection for sound with grazing angle incidence, and with the decrease in β came an increase in sediment propagation for sound with grazing incidence.

3.2.2.3 Sediment Sound Speed Gradient

The sound speed gradient within the sediment controls the rate at which the sound refracts back toward the water column—in other words, the path length it travels through the sediment before returning to the water. We can infer that for small values of $\partial c/\partial z$, less sound will return from the sediment since it will have travelled over a longer path with attenuation. Additionally, focusing effects may occur. Realistic values of $\partial c/\partial z$ vary from .5 $\sec^{-1}$ to 1.5 $\sec^{-1}$ (Hamilton, 1980). Since these values are much greater than the sound speed gradient in the deep portion of the water column (typically .016 $\sec^{-1}$), the sediment-refracted sound returns to the interface relatively close to its point of entry.

Figure 3.19 shows propagation for the Slope water case at 100 Hz with $\partial c/\partial z = 0$; the receivers overlaid with those from figure 3.12 with $\partial c/\partial z = 0$ in bold. In this case, no sound is refracted back into the water column from the sediment. Comparing sound magnitudes at the 100 m receiver, however, the case $\partial c/\partial z = 0$ shows an increase in sound magnitude of 3 dB at 35 km range,

and 5 dB at 75 km range over the reference case, which has $\partial c/\partial z = 1.227$. Other differences less than 3 dB can be determined in the convergence zone minima further down the calculation. Therefore in the Slope profile at 100 Hz, the bottom-refracted sound in the reference case interferes destructively with the reflected and water-propagating returns to decrease the sound magnitude, but the effects are only significant within 100 km of the source. Other values of c_w/c_b (.75, 1.5) for 25 and 100 Hz are shown in appendix A. Sometimes the refracted sound interfered constructively with the bottom-reflected and water-propagating returns, and sometimes destructively. Figure 3.20 shows the Sargasso example at 25 Hz for $\partial c/\partial z = 0$; receivers overlaid with those from figure 3.13. With no sound refracting back from the sediment, figure 3.21 shows a decrease of 5–7 dB at 100 m depth near 40 and 80 km range and a shift in interference patterns throughout the range. At 3000 m depths, removing the bottom-refracted sound decreases the ensonification near 35 km by 3–5 dB. Thus, in the realistic case, the sediment-refracted sound interferes constructively in this profile to cause an increase in the sound level at certain locations. Another value of $\partial c/\partial z$ might cause destructive interference; in the Sargasso example at 25 Hz with $\partial c/\partial z = .75$ (figure 3.21), we see a decrease of 10–15 dB in the magnitude of those refracted returns near 40 and 80 km range in the 100 m receiver, and a dramatic change in the small-scale interference patterns resulting in increased resolution of convergence zone phenomena. At 3000 m we simply see a shift in the interference patterns. Since the water-propagating sound is more easily resolved with $\partial c/\partial z = .75$, one might think that the sediment-refracted returns cause the homogeneity of the propagation field in the realistic case. Figure 3.20 with $\partial c/\partial z = 0$ indicates otherwise, however, since the sound field was relatively homogeneous in that case and no sound was returning to the water column from the sediment. Some other factor obscures the water-propagating sound, and will be discussed below in the section on interface sound speed discontinuity.

3.2.2.4 Sediment Thickness

The effect of sediment thickness will be to control the value of sound speed at the base of the sediment layer, by truncating the sediment gradient at some point. It has been shown (Williams, 1976) that it is not necessary to model the bottom below the sound's turning point in a sediment. Attenuation will further

decrease the depth necessary to describe since sound travelling along deep paths will undergo enough attenuation that no energy will return to the water column. Referring back to the sediment model shown in figure 2.1, we see that for certain choices of the bottom parameters c_w/c_b and $\partial c/\partial z$ there will be a sound speed duct within the sediment; if the sediment depth is set less than a certain critical depth (which will depend on values of c_w/c_b and $\partial c/\partial z$) then the sound speed at the bottom of the duct will be less than the sound speed at the bottom of the water column; the duct will fail to have a significant trapping effect on the sound. On the other hand, if the values of c_w/c_b and $\partial c/\partial z$ are such that even a complete duct has vertical extent small compared to the wavelength of the sound, the duct will still fail to effectively trap sound (Williams, 1981). In the Gulf Stream "realistic" parameter set we have a sediment duct with thickness 20.4 m. This depth is certainly small with respect to the 60 m acoustic wavelength at 25 Hz, but not necessarily small with respect to the 15 m wavelength at 100 Hz. At 100 Hz, however, attenuation will have a greater effect. It is not clear, a priori, what the frequency dependence of sediment depth sensitivity will be.

Calculations performed in the Slope profile with decreasing values of z_{sed} at frequencies of 25, 50, and 100 Hz showed that for each frequency, decreasing the value of z_{sed} from its "excess" value of 100 m has no effect, until a certain critical value is reached, where small increases in the refracted return (frequently of order 1–2 dB) become perceptible. Since we saw in the previous section that for the reference set of sediment parameters the bottom-refracted return interferes destructively with the other sound, this increase in magnitude as the sediment is truncated is believable. Further decrease in z_{sed} past this critical value results in more change in magnitude of the refracted return, slight decreases in the sound levels in the convergence zone nulls, and shifts in the small-scale interference patterns along the edges of the convergence zones. Critical values of z_{sed} of course depend on frequency; at 25 Hz, differences of 1–2 dB became perceptible for $z_{sed} = 50$ m; at 50 Hz, for $z_{sed} = 30$ m; and at 100 Hz, for $z_{sed} = 10$ m. A sufficient depth to model the sediment seems to be approximately one wavelength, for this set of parameters. For 100 Hz, the effect of the sediment was very small throughout; figure 3.22 shows propagation in the Slope water at 100 Hz with $z_{sed} = 0$, receivers overlaid with those from figure 3.12. We see an increase in sound magnitude of only 3 to 4 dB near 70 km range in the 100 m receiver and a similar increase in the convergence zone nulls of the 3000 m receiver. Note

that this example is one where all the sound from the source interacted with the sediment; for the source depths with $c_{sed} > c_{src}$ the magnitude of these effects were less.

3.2.2.5 Sound Speed Discontinuity

Realistic values of the sound speed discontinuity at the water-sediment interface range between $.98 \leq c_w/c_b \leq 1.1$ (Hamilton, 1980). Therefore a series of tests were performed for $c_w/c_b = .98$, 1.0, and 1.1 and compared with the reference cases with $c_w/c_b = 1.017$. The effects of the interface sound speed discontinuity on the water column propagation patterns proved to be a complicated interaction between two underlying phenomena: the change in angular dependence of the reflection coefficient as c_w/c_b changes, and the change in angular distribution of the sound energy interacting with the bottom as frequency and source depth change within each sound speed profile.

Figure 3.23 shows the form of the reflection coefficient for the "realistic" density $\rho = 1.352$ gm/cm^3 and attenuation $\beta = .9$ dB/λ, and the above values of c_w/c_b in the right column. The reflection coefficients for the same density and c_w/c_b but without attenuation appear in the left column for comparison. At the top, with $c_w/c_b = .98$, the sediment has an angle of total reflection near $\theta = 78^o$ beyond which $|R_{12}| = 1.0$; all sound impacting the sediment with angle greater than this reflects totally, with some phase shift. The presence of attenuation greatly decreases the amount of sound reflecting near grazing incidence, but the magnitude of the reflection coefficient for large θ remains larger than in the other cases. Similarly, for $c_w/c_b = 1.0$, the reflection coefficient would depend on density alone and would be constant for all θ, except that the presence of attenuation causes $|R_{12}| \rightarrow 1$ as θ approaches 90^o. When $c_w/c_b > 0$, the reflection coefficient develops a Brewster's angle of total transmission, the value of which depends on the value of c_w/c_b. For $c_w/c_b = 1.017$, total transmission occurs near 78.4^o and for $c_w/c_b = 1.1$ near 59.7^o; in both cases attenuation increases reflection near Brewster's angle. For $c_w/c_b = 1.1$, note that $|R_{12}|$ increases considerably for angles near grazing, although for all θ it remains smaller than $|R_{12}|$ for $c_w/c_b = .98$.

Figure 3.24 shows the Slope profile case of $z_s = 10$ m at 100 Hz, for values

of c_w/c_b = .98, 1.0, 1.017, and 1.1. With c_w/c_b = .98 (upper left), interference patterns increase drastically due to the increase of sound reflecting near grazing incidence for this form of $|R_{12}|$. The interference patterns overwhelm the sound in water-refracting paths; since attenuation decreases reflections near grazing incidence from unity, the interference does die away. We can begin to resolve some water-propagating sound after 200 km range; outside the calculation range resolution would continue to improve. Calculations done with c_w/c_b = 1.0 (upper right) and c_w/c_b = 1.017 (lower left) showed progressively less interference phenomena, due to the relative magnitudes of the reflection coefficients. Additionally, calculations done with c_w/c_b = 1.1 (lower right) showed an increase in interference patterns, although considerably less than the cases with c_w/c_b = .98. The increase in $|R_{12}|$ as $\theta \rightarrow 90^o$ accounts for the effect.

Figures 3.25 and 3.26 illustrate the frequency and source depth interaction of the strength of this effect. This time, we see Slope water propagation for z_s = 100 m; figure 3.25 shows propagation patterns at 25 Hz for all four values of c_w/c_b; figure 3.26 shows the same examples at 100 Hz. Recall that for the Slope water profile with 3170 m bottom depth, when z_s = 100 m, at 25 Hz the primary beam formed by the Lloyd's Mirror pattern interacts with the sediment, whereas at 100 Hz that primary beam refracts entirely within the water column. In figure 3.25 at 25 Hz the propagation patterns depend fairly strongly on the value of c_w/c_b in the manner outlined above, while in figure 3.26 at 100 Hz the propagation patterns are relatively insensitive to this parameter. This insensitivity is typical of cases in which water-refracting sound rapidly dominated over bottom-interacting sound.

In the Sargasso profile, calculations with z_s = 750 and 3000 m showed the same pattern of sensitivity to the value of c_w/c_b outlined above. The cases with z_s = 10 and 100 m, however, contained those mid- to long-range bottom glancing propagation paths due to the large amount of energy striking the bottom near grazing incidence; these cases proved extremely sensitive to the precise functional form of R_{12} for near-horizontal sound. Table 3.3 shows values of the incident angles at which sound struck the sediment for the Slope and Sargasso profiles with z_s = 10 and 100 m at all frequencies used, in the flat-bottom case. Values were obtained graphically and thus are approximate. Note that we cannot obtain values for z_s = 10 m at 25 and 50 Hz; the Lloyd's Mirror pattern does not resolve interference beams if the source-image distance is less than the

wavelength. Additionally, for the 10 m source, at all frequencies used the beam strikes the sediment with wide angular spread and should be interpreted as a continuum. With values for the incident sound angles, we can use $|R_{12}(\theta)|$ to predict the amount of reflected sound.

Incident Angles of Sound Maxima

	Slope Profile		Sargasso Profile	
	$z_s = 10$	$z_s = 100$	$z_s = 10$	$z_s = 100$
25 Hz	—	79.3	—	80.3
		62.3		63.7
		46.7		48.6
50 Hz	—	89.5	—	83.7
		77.3		76.0
		68.4		67.4
		60.7		58.3
		50.8		50.5
100 Hz	60.5	refracts	63.7	84.0
	28.7	82.3	22.2	81.6
		78.0		77.5
		74.9		73.9
		69.6		69.8
		65.8		64.2
		60.3		58.8
				55.1
				50.8

Table 3.3

Figure 3.27 demonstrates this sediment interaction for source depth 100 m, $c_w/c_b = 1.017$, and frequencies of 25, 50, and 100 Hz from top to bottom. In this case, the reflection coefficient has a minimum near 78°. At 25 Hz, the primary lobe of sound strikes the bottom with angle 80° from the vertical; a certain percent (approximately 15%) reflects, producing interference patterns with the long-range water-propagating sound. Additionally, the beam has such wide angular spread that a wide spread of sound reflects; note the broad fan of

sound in the reflected return between 30 and 75 km range near the surface, 40 and 100 km range near the bottom. This wide angular spread of reflected sound causes the relative homogeneity of the sound field.

At 50 Hz, the primary lobe is narrower, and strikes the bottom with angle 84°; approximately 30% will reflect in a more coherent beam, resulting in the observed pattern where bottom-glancing sound propagates to middle ranges before enough is lost that the emphasis shifts to water-refracting sound. The shift in dominant propagation path occurs between 75 and 125 km at this frequency. Note that at 50 Hz the second lobe of sound strikes the bottom with angle 76°, near the minimum of $|R_{12}|$. Only 9% reflects; sound in this path is quickly lost.

At 100 Hz, the first lobe also strikes the bottom with angle 84° and 30% reflects; the second lobe strikes the bottom with angle 82° and 21% reflects. The third lobe strikes the bottom with angle 77.5°, again very close to the minimum in $|R_{12}|$ for this set of sediment parameters. Subsequent, steeper lobes undergo approximately 13% reflection; since sound with steep angle has a large number of bottom interactions in a small horizontal distance, these lobes can be disregarded. The contours of propagation loss at the bottom of figure 3.26 show the importance of the first two beams in the propagation patterns; the first beam hits the sediment its second time near 75 km range, and the second beam likewise near 63 km range. The larger $|R_{12}|$ for the first beam causes it to rapidly dominate over the other; sound in this path dominates propagation patterns until enough magnitude is lost to permit resolution of the water-propagating sound.

The shift in dominant propagation path from bottom reflection to water propagation occurs between 125 and 170 km range at 100 Hz; note that the shift occurs at a greater range than in the 50 Hz case in spite of the fact that the primary beams for 50 and 100 Hz reflect the same amount. At 100 Hz the trapped modes are less strongly excited than at 50 Hz and more bottom-glancing sound must be lost for sound in the water-propagating path to predominate. At 50 Hz, sound levels in the water-propagating path vary between 110 and 120 dB by 250 km range; at 100 Hz, the sound levels in that path vary between 125 and 130 dB at the same range.

These same ideas explain propagation patterns for the other tested values of c_w/c_b for the sources at 10 and 100 m depth at all frequencies. For instance,

figure 3.28 shows propagation patterns for the 10 m source in the same profile and with the same sediment conditions at the three frequencies used. Recall that when the source is at 10 m, the sound hits the bottom in a broad, smooth angular spread rather than in discrete lobes at 25 and 50 Hz; even at 100 Hz the primary interference beam has greater width than it did for $z_s = 100$ m. Additionally, the 10 m source will not excite the trapped modes as strongly as did the 100 m source. At 25 Hz (top) a bottom reflection fans out in a broad spread near the surface between 30 and 75 km range. We can resolve the trapped modes with difficulty between 125 and 175 km range, and with ease by 200 km. Notice that the sound levels in the water-propagating path at 200 km range run between 130–135 dB when $z_s = 10$ m, and between 110–115 dB at the same range when $z_s = 100$ m; the modes comprising the water-propagating path are excited less strongly at $z_s = 10$ m.

At 50 Hz (middle), we still do not resolve separate lobes from the source, but a greater sound intensity hits the bottom near grazing incidence where $|R_{12}|$ is larger. We see the reflected portion of the incident sound near the surface at 50 km range and near the bottom at 75 km. By 130 km the water-propagating sound dominates the propagation pattern; again this path contains less energy when $z_s = 10$ (140–145 dB) than $z_s = 100$ m (110–120 dB).

At 100 Hz (bottom), we resolve a broad interference lobe that strikes the sediment with angle 64°; in that region $|R_{12}|$ is nearly flat and approximately 12% of the beam reflects all across its angular spread. We see a pattern of bottom reflecting returns, each with nearly constant sound magnitude across its horizontal range; by 200 and 225 km enough sound has been lost into the sediment that the water-refracting propagation can be resolved. Again, this path has less magnitude when $z_s = 10$ m (160–165 dB) than when $z_s = 100$ m (125–125 dB).

The above ideas also suggest that with a suitable choice of source depth, sediment parameters, and bottom depth, a waveguide showing these bottom-glancing propagation paths could be "tuned" to quickly filter out the interference patterns from the bottom-reflecting sound and make the water-propagating sound dominate earlier. A reflection coefficient chosen to reflect the minimum amount of total sound for that source depth and frequency will most quickly remove the bottom-reflecting sound from the propagation pattern, leaving only the water-borne sound. Because of the change in angular distribution of incident

sound with frequency, an R_{12} that is most efficient for one frequency would not be for another. The "best" form of R_{12} for any water column would be found by calculating the magnitude of energy incident upon the sediment as a function of θ, multiplying by $|R_{12}(\theta)|$, and minimizing the integral over θ. A useful experiment to empirically test this hypothesis would be to test different values of c_w/c_b, thus controlling the shape of R_{12}, to see if it is indeed possible to selectively remove the interfering sound.

This experiment was conducted in the Sargasso profile for $z_s = 100$ m at 25 and 50 Hz, testing values of c_w/c_b ranging from 1.01 to 1.05; the results for $c_w/c_b = 1.01$, 1.02, 1.03, and 1.04 are shown in figures 3.29 and 3.30. Figure 3.29 contains the results at 25 Hz; the case with $c_w/c_b = 1.03$ (lower left) provided the best filtering effect, permitting the water-propagating sound to predominate by 70 km from the source. The filtering effect is seen most dramatically in the contour plot at 30 km range, 3000 m depth, where there is a pronounced sound minimum. To the left of the minimum we see steep bottom reflecting propagation that is quickly lost with range; to the right we see the water-refracting sound emerging from the early propagation patterns. Note we have not lost all the bottom reflecting beam, since $|R_{12}|$ is non-zero, but we have greatly reduced its magnitude over the neighboring cases. Figure 3.30 contains results at 50 Hz, where $c_w/c_b = 1.02$ provided better filtering (upper right), through the same mechanism of decreasing the amount of energy in the reflected beam. With less energy reflected, the trapped modes are resolved more quickly. From these two studies, we can see how extremely sensitive the large-scale propagation patterns will be to the parameters that determine the reflection coefficient when bottom-glancing propagation paths are important.

More complete plots of these experiments, including magnitudes for 100 and 1000 m receivers and an expanded plot of the first 50 km, are included in appendix A.

Another useful experiment would be to test the Slope sound speed profile with different source or bottom depths, to see if these bottom reflection/refraction propagation paths can be found in that profile when significant sound energy strikes the sediment with large θ, and confirm or disprove the above results. Note in table 3.3 that when $z_s = 100$ m and $f = 50$ Hz, the primary beam of sound grazes the sediment, but we did not see these unusual propagation

paths. This could be the result of one of two possibilities: first, that in the Slope profile when $z_s = 100$ m there do exist water-propagation paths that leave the source with real θ; they would contain more sound energy (modes making up these paths would be more strongly excited) and they would overwhelm the propagation pattern. The other possible explanation is that the appearance of these unusual propagation patterns is in some way an interaction of the shape of the entire sound speed profile with the sediment layer; the Slope profile has a relatively shallow sound channel axis and sound speed increases rapidly toward the surface. The Sargasso profile has a relatively deep sound channel and sound speed increases more slowly toward the surface, with a secondary duct. The shape of the upper portion of the profile will affect the strength of excitation of modes in water-propagating paths that have complex angle at the source.

3.2.3 Summary of Sediment Parameter Effects

In the above subsections we have seen that under these conditions of deep-water propagation where the sound speed profiles had no depth excess, the propagation patterns formed two major regimes. One regime occurs when large sound intensity propagates within the oceanic waveguide and most of the bottom-interacting sound strikes the sediment with steep angle and is relatively quickly lost through one or both of the following causes: 1) the small magnitude of $|R_{12}|$ for steep-angle sound, and 2) losses due to refraction along a steep path through the attenuating bottom. Figures 3.31a and 3.31b depict propagation in this regime. The lines represent paths of primary energy propagation; in figure 3.31a the principal interference lobe refracts entirely within the waveguide, while in figure 3.31b the principal lobe (bold) interacts with the bottom at steep angle, with a portion of its width refracting within the water column (light). The second regime occurs when relatively smaller sound intensity propagates within the oceanic waveguide, and the bottom-interacting sound strikes the sediment near grazing incidence, where the magnitude of $|R_{12}|$ is fairly large. Figure 3.31c schematizes propagation in this regime; the bold line represents the propagation path of the primary interference lobe which strikes the bottom near grazing incidence and survives several bottom interactions. The light line shows the propagation path of the equivalent ray consisting of the trapped modes. These two propagation regimes show very different patterns of sensitivity to the sediment

parametrization.

3.2.3.1 Water Column Propagation Dominant over Bottom Reflections

The first major regime, in which water-propagating sound dominated the acoustic fields, was made up of the Slope water cases for all tested source depths whether $c_{src} > c_{bot}$ or $c_{bot} > c_{src}$, and the Sargasso water cases for the deeper two source depths $z_s = 750$ and 3000 m where $c_{bot} > c_{src}$. This propagation regime can be subdivided further; not into cases bounded by the relative magnitudes of sound speed at the source and bottom as we would for ray physics, but by the low-frequency behavior of the propagation pattern within one deep cycle distance of the source. If the physical conditions (frequency, source depth, profile form, and bottom depth) caused a large amount of sound from the original Lloyd's Mirror source-image interference pattern to refract with depth before interacting with the sediment, then the water column propagation proved fairly insensitive to the form of sediment parameterization. This condition can be achieved by either a deep source with a broad spread of propagation angles in the center of the sound channel, or by a shallower source with the primary interference lobe refracting before reaching the bottom. Cases with $c_{bot} > c_{src}$, where sound refracts with depth at high frequencies, might fail this condition at low frequencies. Figure 3.31a schematizes this case; the bold line representing the primary interference beam propagates to long range within the water.

If instead the physical conditions caused the primary interference lobe to interact with the sediment, then the water column propagation pattern was more sensitive to the form of sediment parameterization. This condition occured with $c_{src} > c_{bot}$ and with $c_{bot} > c_{src}$ for lower frequencies. Figure 3.31b shows this case, where the bold line representing the primary interference beam strikes the sediment steeply and has relatively little effect on long-range patterns. It is important to note that the types of effects caused by the sediment in these two sub-cases were similar; the difference lies in the sensitivity of the propagation patterns to the form of bottom. In this major regime with the water-propagating sound dominating the acoustic fields, the specific effects of each sediment parameter can be summarized as follows:

a) Density ρ: decreases the magnitude of the first steep bottom-reflecting returns

by 20 or more dB for density decreases of .5 gm/cm^3 or less in the realistic range of densities, by decreasing $|R_{12}|$ for steep incidence. These changes take place within the first 20–40 km, depending on water depth. Density decreases cause increases of 3–7 dB to the bottom-grazing propagation seen in convergence zone minima by increasing $|R_{12}|$ for sound with shallow incidence; these differences decrease with range as reflection is not complete.

b) Attenuation β: filters out interfering sound from the sediment-refracted paths and filters out deep paths more than shallow; affects the entire range of calculation.

c) Sediment sound speed gradient: controls the magnitude and phase of interfering sound returning to the water from sediment-refracting paths. The primary effect is up to 5–7 dB magnitude for a gradient change of 1.3 sec^{-1} in the first refracted return; the range of this change from the source depends on the sound speed profile and water depth via the horizontal distance travelled for one bottom interaction and return. Effects decrease with range as sediment attenuation acts on multiply-refracting sound.

d) Sediment thickness: below a certain critical value determined by the interaction of the other parameters (f, β, $\partial c/\partial z$, c_w/c_b), reducing the sediment thickness reduces the amount of sound returned from the sediment by selectively truncating the deep sediment paths. This will have a different effect on the sediment returns than loss of deep propagation paths due to an increase in β, since by truncating the sediment depth we do not affect the magnitude of shallow sediment returns. Frequency and attenuation control the magnitude of this effect by altering the amount of sound returning from the sediment along any one bottom-refracting propagation path.

e) Sound speed discontinuity: strongly affects the angular dependence of the reflection coefficient for large angles from the vertical, with modifications by ρ and β. Thus c_w/c_b has a strong effect on the magnitude of bottom-glancing sound propagation that appears in convergence zone minima and interferes with regular maxima.

3.2.3.2 Bottom Reflections Dominant over Water Column Propagation

The second major regime showed a large amount of sound propagating in bottom glancing paths relative to the amount of sound in purely water-refracting paths, and consisted of propagation in the Sargasso profile for source depths $z_s = 10$ and 100 m at all tested frequencies. Figure 3.31c shows this case, with the bottom-reflecting sound persisting to mid ranges. Due to the relative importance of these reflected paths to the entire sound field, propagation in this regime showed an extreme sensitivity to the angular dependence of the reflection coefficient around the incident angles of that sound. Due to the different nature of this propagation pattern, the effects of the sediment parameters frequently differed in kind from those given above; those parameters which most strongly modify the form of $|R_{12}|$ had the greatest effect on propagation. For this bottom-interacting regime, the following effects were seen:

a) Density ρ: increases the sound magnitude by 7–10 dB throughout the range of calculation, for density decreases of .5 gm/cm^3 or less, by increasing the magnitude of $|R_{12}|$ for those critical bottom-reflecting paths. This increase causes the sound in these paths to dominate propagation for longer ranges.

b) Attenuation β: as above, β filters out interfering sound from the sediment-refracted paths and affects the entire range of calculation. Attenuation does modify the magnitude of $|R_{12}|$, but the interference effects from sediment-refracting sound overwhelmed such changes.

c) Sediment sound speed gradient: again, this parameter controls the magnitude and phase of sediment returns without modifying the reflection coefficient. In some cases this sediment return could interfere destructively with the bottom-reflected sound, to resolve the water-propagating sound at earlier ranges and modify local sound magnitudes by as much as 25 dB for changes of .5 sec^{-1} or less in $\partial c/\partial z$. In other cases the sediment return simply shifted interference patterns. Effects again decrease with range as attenuation acts on multiply-refracting sound.

d) Sediment thickness: truncates the deep sediment paths. Propagation was relatively insensitive to this parameter, in view of the dominance of bottom reflecting sound.

e) Sound speed discontinuity: greatly affects the angular dependence of the reflection coefficient, which governs the important bottom-glancing paths. Under certain conditions determined by source depth, frequency, profile shape, and bottom depth, the sediment surface will reflect a minimum amount of the incident sound, causing these paths to collapse and leave only water-propagating sound in the waveguide. Alternatively, the bottom-glancing paths can become considerably more important, if $|R_{12}(\theta)|$ has increased for the particular incident angles θ of the bottom-glancing paths, as they are determined by source-image interference patterns.

It must be noted that in the realistic ocean, bottom sediment properties change with range, and these strongly sediment-dependent propagation patterns would be significantly altered by a range-dependent sediment model. We could expect the bottom-glancing paths to have greater or lesser importance with range; however, since the magnitude of the reflection coefficient always increases to 1 as angles approach grazing for realistic sediments having any attenuation, it is reasonable to expect sound with glancing incidence to reflect for all such cases. Range dependence of the sediment properties would modify the relative importance of such propagation paths, and could be an important improvement to the sediment model.

3.3 Topographic Effects: Range Independent Oceanography

3.3.1 Downward Topography

In general, downward topography decreases sediment interaction effects. Sound that reflects off the bottom the first time it hits the sediment may later refract with depth within the deeper water column. A source depth and frequency dependence occurs that is similar to the one discussed in the previous section on sediment parameters.

Sources positioned such that most energy refracted within the water column, in the flat-bottom case, showed little to no change in surface convergence zone radius as topography deepened, although some secondary differences appeared in the deeper propagation patterns. The clearest example of such effects appears in figure 3.32, which shows propagation in the Slope profile at 100 Hz

with $z_s = 100$ m; top figures are contours of propagation loss and propagation loss at a 3000 m deep receiver for the flat-bottom case, bottom figures are the same for the downsloping case. Note from figure 3.32a that the primary lobe of sound refracts with depth in the flat-bottom case; comparing this example to figure 3.32c we see that the propagation patterns in the upper water are nearly the same. From the plots of the 3000 m receivers we see that the main convergence zone locations at that depth are the same at 77, 128, 180, and 230 km. Their form changes slightly, and in the downsloping case we see secondary maxima at 57, 113, 170, and 223 km. In the downsloping contour plot we can trace this return back to the surface near 35 km, and thence to the second Lloyd's Mirror interference lobe which strikes the sediment near 20 km range. The deepening topography has permitted greater amounts of this sound to propagate to long ranges by two mechanisms.

First, the sound initially strikes the bottom at greater depth and range; while propagating this additional depth, the sound continues to refract and strikes the bottom at 84° from the vertical. This angle was again calculated graphically, including the effects of greater depth, range, and additional refraction, but treating the deeper bottom as locally flat. From the reflection coefficient, sound striking the bottom with this angle will undergo 28% reflection; in the flat-bottom case, where this sound strikes the bottom at 82° angle, 21% reflects. We can see the change in magnitude and range in the 3000 m receivers: the flat-bottom case has a maximum of 100 dB near 53 km range, and the downsloping case has a maximum of 97 dB near 58 km range. Secondly and more effectively, as the sound continues to propagate the bottom continues to deepen, and by 120 km range this sound refracts entirely within the water column, permitting long-range propagation without bottom losses. Thus we see these secondary propagation maxima propagating to long ranges in the downsloping case; in the flat bottom case these returns appear as modifications to the sides of the primary convergence zone maxima near 113 and 155 km range, whose magnitudes decrease with range.

For sources near the surface, with the primary lobe of sound interacting with the bottom, the deepening topography permitted more sound to refract within the water column, extending the convergence zone radius. Figure 3.33 shows propagation at 25 Hz in the Slope water profile with the source at 10 m. Receiver depths shown are 10 and 3000 m, overlaid with the corresponding flat-

bottom example receivers (from figure 3.11); downsloping topography receivers in bold. With the downsloping topography, we see an increase in convergence zone radius at both 10 and 3000 m receivers as deeper propagation paths are included in the sound field. The flat bottom case shows convergence zone maxima just short of 150 and 200 km range in the 100 m receiver; the downsloping case shows these same maxima near 155 and 210 km range. Comparing receivers at 3000 m depth additionally shows this phenomenon; the flat-bottom case has maxima near 125, 175, and 225 km; in the downsloping case, these maxima occur near 130, 183, and 235. Both receivers show an increase in magnitude, which demonstrates that sound in deeper propagation paths now remains in the water column.

For deeper sources (near the bottom) the convergence zone radii again increased in the downsloping topography cases, since the location of long-range maxima is influenced by the sound that travels down from the source, refracts before getting to the bottom, and then travels up to the surface. The depth of the bottom will affect the range at which that sound reaches the surface. Figure 3.34 shows contours of propagation loss and loss at a 100 m reciever in the case of Slope water propagation with the source at 3000 m; the flat-bottom case is on top and the downsloping case is on the bottom. Note that the flat-bottom case shows surface convergence zone maxima near 175 and 225 km, whereas in the downsloping topography case these maxima are extended to 180 and 233 km respectively.

In the Sargasso sound speed profile, cases with most of the sound refracting within the water column behaved as above: downsloping topography caused no change to the primary water-propagating sound, but modifications to propagation patterns by sound in deeper sound paths. However, the cases with large amounts of bottom-interacting sound ($z_s = 10$ and 100 m) showed mid- to long-range bottom glancing propagation for the flat bottom cases; with a downsloping topography, these bottom reflecting paths became entirely water-refracting with depth. Figure 3.35 shows propagation in the Sargasso profile with $z_s = 10$ m at 25 Hz for both the flat and downward cases. In this example the deepening topography has not extended the convergence zone radius, but has permitted sound in bottom glancing paths to refract entirely within the water column, and reinforce the flat-bottom trapped modes. In the 100 m receiver, figure 3.35d, these convergence zones emerge from the interference patterns near 190 and 250

km range.

We note a change in ensonification within the sediment with the addition of a sloping bottom; a large number of unusually shaped maxima seem to propagate into the sediment layer. The example of the Sargasso water profile and downward topography with constant slope offered an opportunity to test the relationship of these propagation patterns to bottom slope. A series of calculations with the Sargasso profile, $z_s = 10$ m, $f = 25$ Hz, and several bottom slopes showed that these maxima occur at specific depths, independent of range. Figure 3.36 shows propagation loss for the Sargasso profile and bottom slopes of $\Delta z/\Delta r = .004$ (top) and $\Delta z/\Delta r = .005$ (bottom). When the bottom slope is .004, we see a maximum propagating into the sediment near 200 km range where the bottom depth is 5240 m. When the bottom slope is .005, the bottom has depth 5240 m at 160 km range; we see a maximum propagating into the sediment there, as well. Other cases of this phenomenon can be found in appendix A. Since these maxima appear to be a function of water column depth rather than range from the source, they may represent adiabatic compensation of the propagating modes to the change in profile depth. In other words, modes would have different shapes in profiles of different depths, and adjust to the change in depth by interacting with the sediment rather than with neighboring modes. Jensen and Kuperman (1980a) showed that for propagation over constant downward slopes, modes adapt adiabatically to the changes in depth; mode coupling seemed to be associated with abrupt changes in bottom slope. Comparison of propagation loss at 100 m shows significant modifications in the small-scale interference patterns, but not in the larger-scale convergence zone propagation.

3.3.2 Upward Topography

In general, upward topography increases the sediment interaction effects. Sound that refracts with depth at one range may encounter the sediment at further range. With a primarily lossy bottom, this will have the effect of eliminating sound from deep propagation paths. Figure 3.37 shows this phenomenon for Sargasso water at 100 Hz, with source $z_s = 750$ m. By the end of the computation, the upwardly sloping topography has removed the propagation paths that extend between the surface and 4440 m depth, leaving only those in the main sound channel between 600 and 3600 m depth; further upward topography will

progressively filter out the deeper paths within that sound channel. This effect causes a sound level reduction of 5–10 dB at the 100 m receiver by the end of the calculation. Small-scale phase shifts appear in propagation patterns at this receiver, which could be due either to loss of sound in those deep paths, or to reflections from the shallower sediment surface.

In the Sargasso profile, the sources at 10 and 100 m again show unusual propagation patterns; after the initial bottom-reflecting signal is lost at near- to mid-ranges from interactions with the upsloping bottom, sound beams propagate at odd angles to long ranges and obey surface reflection properties but do not refract with sound speed. Calculations at 50 and 100 Hz showed these beams, calculations at 25 Hz did not. When traced back through the near- to mid-range field, these beams appear to fan out from the location where the primary sound lobe struck the sediment. They do not simply represent a low sound level remnant field left over after the primary pattern has been lost, since they show local maxima that are comparable to or higher than sound levels present when the primary propagation pattern is retained; instead, they seem to represent a different form of propagation.

Figure 3.38 illustrates the effect at 100 Hz for a source at 10 m, with propagation loss contours and propagation loss at a 1000 m receiver for the flat bottom case (top) and the upsloping case (bottom). The flat bottom propagation loss contours show the purely bottom-reflecting propagation pattern of a beam of sound striking the sediment at steep incident angle. The upsloping propagation loss contours show these anomalous beams. At the 1000 m receivers, note that in the flat bottom case (top) sound levels show interference patterns overlaying a step pattern of broad flat areas with relatively constant sound. In section 3.2.2.5 we saw that for this sound speed profile, source depth, and frequency, the primary lobe of sound is broad and strikes the sediment with angle 64° from the vertical; $|R_{12}|$ is nearly constant over θ in this region and 12% of the beam reflects over its entire angular spread, causing the step functions in sound magnitude. Each step down represents one more bottom reflection. In the upsloping bottom case, the step functions become disrupted near 125 km; by 250 km we see a general increase in ensonification of 10–15 dB over the flat-bottom example, similar to the shallow-water work of Collins et. al. (1988) for propagation in an upsloping wedge with an upward-refracting sediment layer. Note that with the shallower

source we see an increase in water column ensonification as the bottom slopes upward, whereas with the deeper source we saw a decrease in water column ensonification as the bottom sloped upward.

Note also in figure 3.38 that the sound patterns interacting with the sediment again show local maxima within the sediment, usually where some of these beams strike the bottom. These maxima are similar in form to the results of Jensen and Kuperman (1980) and Collins et. al. (1988), who modeled low-frequency sound propagation in upsloping wedges with various bottom sediment conditions. They found that when the water column shallowed past the cut-off depth of any particular vertical mode, a beam of sound propagated away from the water column within the sediment; the angle of that propagation within the sediment depended on sediment parameters. In other words, a mode past cut-off interacted with the sediment rather than with other modes. The cases they studied were in shallow water and contained only a small number of vertical modes, whereas the current realistic profile and deep water column support a large number of vertical modes. To determine if the phenomena seen in these shallow source calculations were related to mode cut-off, a series of calculations were performed with the Sargasso profile and upward topography of various slopes at 50 and 100 Hz. If mode cut-off is causing these sound maxima to propagate into the sediment, we can expect them to occur at a particular sediment depth independent of the range from the source or the bottom slope. This was in fact the case; figure 3.39 shows calculations at 100 Hz for the Sargasso profile with bottom slope $\Delta z/\Delta r = -.002$ and $\Delta z/\Delta r = -.003$. On top, the calculation with slope $-.002$ shows a characteristic triple beam striking the bottom at 225 km range, where the bottom depth is 3990 m. The lower calculation with slope $-.003$ reaches bottom depth 3990 m at 150 km range; we see a similar but narrower triple beam propagating into the bottom at that range. Many other examples were noted; other cases are shown in Appendix A.

A series of calculations with the Slope sound speed profile and upward topography at 50 Hz showed the same phenomenon of beams propagating into the sediment at specific depths; figure 3.40 shows cases with slopes $\Delta z/\Delta r = -.003$ and $\Delta z/\Delta r = -.004$. With the Slope profile we do not see the pattern of beams propagating at odd angles within the water column; the convergence zone propagation signal persists although radii are shortened and magnitudes decrease

as deep propagation paths are lost. We do, however, see beams propagating into the sediment at fixed bottom depths. The top case in figure 3.40, with slope $-.003$, shows a beam in the sediment at 210 km range where the bottom depth is 2540 m. The lower case, with slope $-.004$, reaches bottom depth 2540 m at 157 km range; we see a similar beam propagate into the bottom at that range.

Thus the beams propagating into the sediment do seem to represent mode cut-off in a wedge; the beams propagating in the water in the Sargasso profile case may be in some way related to superpositions of these modes. The appearance of these beams in the water column was related to the values of the sediment parameters; the reader can verify in appendix A that in the cases where $\rho = 1.0$ and $c_w/c_b = .98$, they do not appear whereas when $\partial c/\partial z = 0$, $c_w/c_b = 1$, and $c_w/c_b = 1.1$ they do (barely, in the case of $c_w/c_b = 1.1$). Of course, changing the sediment properties changes the shapes of the water column modes.

The appearance of these mode cut-off phenomena in the upsloping case with similarities to work done elsewhere under more carefully controlled conditions of fewer modes in an ideal, shallow profile (Jensen and Kuperman, 1980a, 1980b; Collins et. al. 1988) seems to support the hypothesis that the maxima seen within the sediment with the downsloping bottom as well are related to adiabatic compensation of the modes to changes in depth.

3.3.3 Summary of Topographic Effects

3.3.3.1 Downsloping Topography

As we saw above, the primary effect of downward topography is to decrease bottom interactions and permit sound to refract with depth that did not, in the flat-bottom case. This principle had slightly different effects in different propagation regimes.

First, when the primary Lloyd's Mirror interference lobe refracted with depth in the flat-bottom case, the increasing depth had no effect on propagation in that path and thus the main convergence zones were unchanged. The increasing depth did, however, modify the lesser interference maxima which interacted with the sediment. Figure 3.41a demonstrates this change; the solid lines represent the downsloping case while the dashed lines represent the flat bottom case.

Again the bold line represents sound in the primary interference lobe; this time the light line shows the secondary lobe. We can see that the topography permits the secondary lobe to propagate deeper and refract more before striking the bottom the first time; on the second deep excursion it refracts with depth. Thus energy in this path propagates to longer ranges by two mechanisms: a) a greater percent of sound reflects off the bottom with the first interaction, and b) fewer sediment interactions. This phenomenon did not affect the shallow receiver; the deep receiver, however, showed local changes of 10–15 dB due to this deep path. In general, whenever the major interference lobe refracts with depth in the flat-bottom case, the downsloping topography will only modify the lesser maxima. The exact form and magnitude of this effect will depend on the propagation conditions.

When instead the primary Lloyd's Mirror interference lobe interacts with the bottom at steep angle (figure 3.41b, bold) we saw that the deepening topography increased the convergence zone radius by permitting a larger portion of that energy to refract with depth, without undergoing sediment losses. The amount of change this effect had on propagation patterns was a change of 3 km in convergence zone radius; by the fourth convergence zone, the accumulated difference displaced the surface maximum 12 km. In general, initial propagation conditions (frequency, source depth, profile) and local topography will govern the magnitude of this change. Convergence zone maxima increased magnitude 7–10 dB due to the inclusion of these deep paths; topographic slope will again determine the magnitude of this effect.

The cases having bottom glancing paths dominate propagation showed a different effect with the increase in deeper propagation paths. Figure 3.41c demonstrates this case; we see that the downward topography has permitted the previously bottom-glancing sound to refract entirely within the deeper water column. In the case we studied, this sound reflects once and then refracts within the water column on its next deep excursion; that reflection reduced the range at which it first returned to the surface, but its greater propagation extent gave it greater skip distance, so it gradually came into phase with the narrower-angle convergence pattern.

3.3.3.2 Upsloping Topography

The primary effects of upsloping topography were to truncate the deep propagation paths and cause increased interactions with the sediment. This fundamental principle caused two different effects, depending on propagation regime.

First, when sound refracting entirely within the water column dominates propagation patterns, the shallowing bottom caused sound that previously refracted to strike the bottom and have some portion reflect. Figure 3.42a schematizes this case; the solid lines represent two demonstrative propagation paths in the upsloping case while the dashed lines show the continuations of these paths in the flat-bottom case. Note that the path with greater angular excursion strikes the shallowing sediment first and reflects; this shortens its convergence radius and decreases its magnitude approximately 10 dB.

Insufficient tests were conducted with the Slope water profile and upsloping topography to determine what change, if any, to propagation patterns might result whether the primary Lloyd's Mirror interference lobe refracted with depth or interacted with the sediment. However, the case shown in section 3.3.2 would indicate that propagation with the main lobe interacting with the sediment could show the same shortening of convergence zone radius and magnitude decrease due to loss of deep propagation paths.

The propagation regime in which the bottom-glancing sound dominated the water column showed an unusual transformation with the addition of upsloping topography. Truncation of the deep sound paths and their subsequent reflections at shallower depths caused an unusual interference pattern which is not completely understood but is be related to mode-cutoff phenomena. Figure 3.42b schematizes this case, where the dashed lines represent the flat-bottom case and the solid lines represent the upsloping case, with bold solid lines the bottom reflecting paths and crossing lighter solid lines at right the interference maxima due to the odd beam pattern. Instead of showing a decrease in waveguide ensonification due to the topography, as in the previous regime, this propagation condition resulted in a 10–15 dB increase in waveguide ensonification.

3.4 Oceanographic Effects: Flat Topography

3.4.1 Slope to Sargasso Water Propagation

Propagation from Slope to Sargasso water has several interrelated effects on the sound speed profile, the most obvious of which is a deepening of the sound speed channel axis from approximately 500 m in the Slope water to about 1250 m in the Sargasso water. Additionally, the surface sound speed increases as we move from the Slope to the warmer, saltier Sargasso water.

The deepening sound channel axis has the effect of refracting the sound deeper within the water column. Figure 3.43 shows the effects of the water mass transition on propagation. The left example shows propagation from the Slope to Sargasso water mass, with 3170 m flat bottom; the right case shows the corresponding range-independent case with source at 100 m and frequency 100 Hz. As the sound passes the oceanographic frontal zone between 75 and 175 km range, it refracts deeper in the water column around the deepening sound channel axis. After the frontal interaction, most of the sound in the water column is confined between 600 m and the 3170 m flat bottom. As it refracts more deeply, it strikes the sediment and undergoes reflections, transmissions and loss within the sediment.

Figure 3.44 shows propagation loss at the 1000 m receiver for the same pair of cases. In the range-independent case (figure 3.44d) the convergence zone width gradually increases with range, due to the different refracting radii of the various sound paths. In the range dependent case, the frontal interaction disrupts this pattern and causes a pattern of maxima near 150, 190, and 235 km associated with the downward refraction of the surface sound. Note that for the first one to two cycles following the beginning of the frontal interaction, a great deal of sound propagates in bottom reflecting paths which undergo loss with each interaction. We see this effect in the contours of propagation loss, figure 3.43c, which show a sharp angle in the sound maxima at the bottom near 125 and 175 km range. This effect causes the distance between post-frontal maxima at the 1000 m receiver to increase with range as the sound in bottom-reflecting paths is lost, leaving the water-propagating paths to become more important.

The other major effect of the frontal interaction is to increase the sound

speed near the surface in the Sargasso water mass. In the classic ray interpretation, this increase will cause a shadow zone; it is well-known that at lower frequencies, some sound will penetrate into the shadow zone. This set of runs offers an opportunity to measure the effect of frequency on shadow zone ensonification.

Figure 3.45 shows contours of sound speed and of propagation loss at 25, 50, and 100 Hz for a source at 100 m and sound propagating on the transect from Slope to Sargasso water masses. In the upper right corner of each of the propagation loss contours we see the sudden drop in sound levels that is the low-frequency representation of a shadow zone; at 25 Hz more sound reaches into the shadow zone than at 100 Hz. To get a quantitative idea of this frequency dependence, figure 3.46 shows propagation loss at 100 m receivers for the same cases. Note that the vertical axes cover different ranges, but are on the same scale. By the end of the calculation, sound values decrease approximately 50 dB from their pre-frontal convergence zone values at 25 Hz; 100 dB at 50 Hz; and 125 dB at 100 Hz.

In order to study the dependence of the propagation pattern on the distance from the source to the front, propagation calculations were conducted along the same source-receiver line as the above runs, with various source locations along the line. These calculations were performed with the same flat bottom depth, at frequencies of 25 and 50 Hz.

To choose the source locations, cycle distances for propagation in each of the water masses were calculated by looking at the range-independent propagation calculations; measuring the distance to the nth convergence zone, and dividing by the number of convergence zones. Cycle distances were thus determined at 25 Hz to be approximately 49.5 km for slope water and 65 km for Sargasso water. Source positions were found up close to the Gulf Stream on each side, as well as .75 cycle distance away in each water mass. These runs were compared with the corresponding original parameter study runs, which have the source located 1.5 cycle distance away from the Stream in the slope water case and 1.3 cycle distance away in the Sargasso water case. It must be noted that for acoustic purposes the effective width of the Gulf Stream is approximately 100 km.

In view of the relative horizontal scales of the sound propagation and the frontal interaction, it is not surprising that the amount of loss at any one location depends most greatly on the distance past the front, rather than on the distance from the source to the front. Sound intensity after frontal interaction falls off within the same envelope for each source depth and frequency case. The downward-refracted convergence zone maxima, at greater depths due to the frontal interaction, show some low-frequency penetration into the shallower water and cause local maxima whose magnitudes remain within this envelope. Figure 3.47 shows propagation loss at the 100 m receiver for the 100 m deep source at 50 Hz. Starting positions of the calculations are those given above, and the plots are overlaid so as to align the geographic locations of the sources, thus aligning the Gulf Stream. Within the shadow zone, loss depends most greatly on geographic distance from the observer to the front, rather than on the source-frontal distance. Included in figure 3.47 are the full sound fields for these same cases, aligned on the page to similarly geographically line up on the Gulf Stream. We see that once the sound refracts more deeply within the water column, forming new convergence zone maxima near 750 m depth, the propagation patterns thus established continue in the new regime.

3.4.2 Sargasso to Slope Water Propagation

Propagation across the Gulf Stream from Sargasso to Slope side primarily involves a shallowing of the sound speed channel and a decrease in the value of sound speed in the axis. The surface sound speeds also decrease in the colder Slope water. These waveguide properties combine to refract the sound more shallowly than in the Sargasso water mass, resulting in an increase in surface ensonification and decrease in bottom interactions.

Figure 3.48 provides an example of the oceanographic effect when propagation patterns are dominated by the water-refracting sound; it compares propagation from Sargasso to Slope water with propagation in range independent Sargasso water, at 50 Hz and with a source at 750 m. The change in propagation patterns is apparent between 100 and 175 km range in figure 3.48c, where sound that had oscillated between 500 and 3500 m depth shifts higher in the water to reflect off the surface and refract near 3000 m depth. Note that we do still retain some deep propagation paths near the sediment. Also, the sound that refracted

more shallowly did not interfere constructively with the sound in deep propagation paths, so the surface ensonification did not form coherent convergence zone patterns. Figure 3.49 shows propagation loss at the 100 m receiver for the same cases in figure 3.48; we see that the convergence zone pattern in the range independent case (formed by sound in deep-to-shallow propagation paths) has been obscured in the range dependent case by the sound that has been refracted higher in the water column. The effect has caused a general increase in surface ensonification of 10 dB over the pre-frontal convergence zone maxima, and was relatively independent of frequency.

When the source is located such that the range independent propagation patterns were dominated by sound in the bottom-glancing paths, the upward refraction of the sound channel change lifts those very deep sediment-interacting paths away from the bottom. The results of this phenomenon were strongly dependent on frequency, via both the angular dependence of sound interacting with the bottom and the strength of excitation of trapped modes. Figure 3.50 shows propagation patterns from the Sargasso to Slope water for a source at 100 m and frequencies of 25, 50, and 100 Hz. In each case we can see the deep portion of the sound energy lifting away from the bottom between 135 and 175 km range with the frontal interaction.

Figure 3.51 shows propagation loss at the 100 m receiver for these same cases; raising the sediment-interacting paths off the bottom has resulted in the formation of convergence zone patterns. Note that the shape of the convergence zone peaks modifies with range, even past the frontal zone: the trailing portions weaken. At 25 Hz, where the sound struck the sediment in a broad spread, the upward refraction quickly decreased the smooth interference pattern and focused the sound into convergence zones whose magnitudes are approximately 20 dB higher than the smooth interference patterns. At 50 Hz, where the specific form of reflection coefficient caused the water-propagating path to dominate by 100 km range, the frontal interaction increased the magnitudes of convergence zone maxima by approximately 10 dB by moving the maxima closer to the surface. At 100 Hz, a great deal of sound remained in the bottom-glancing paths which subsequently refracted upward, causing a greater width of surface maxima. While the frontal interaction has increased the amount of sound refracting in the water, there is still sound in bottom-glancing paths, undergoing incomplete reflections,

that causes the trailing portion of the maxima to decrease with range. Calculations performed with the source closer to the front showed that once the sound sets up its convergence zone propagation pattern in the Slope water mass, it simply continues that propagation pattern. The bottom-glancing paths disappear with range due to reflection losses, leaving only water-propagating sound.

The same frequency and range-dependent effects occur for the source at 10 m; in figure 3.52 we see the contours of propagation loss at 25, 50, and 100 Hz and in figure 3.53 we see sound levels at the 100 m receiver depth. Overall we have the same pattern of the oceanography refracting the sound away from the bottom between 135 and 175 km range, forming convergence zone propagation. Recall that the amount of excitation of the trapped modes is weaker for the 10 m than the 100 m source; also the amount of excitation of these modes becomes weaker as frequency increases. By $z_s = 10$ m and $f = 100$ Hz, the amount of sound in the water-refracting paths was sufficiently small relative to the bottom reflecting sound that steep-angle bottom reflections were still dominating the range-independent propagation pattern out to 200 km in the range-independent case, figure 3.28 (bottom). In figure 3.52d at 100 Hz the upward refraction of the oceanography at 125 km has modified the range-independent pattern of bottom reflections by refracting the weaker water-propagating sound upward as well as the more shallow-angle bottom reflections; due to the weakness of the original trapped modes, the original bottom reflecting sound remains a dominant part of the propagation pattern even after the front, and is refracted away from the bottom to propagate for long ranges. In figure 3.53d we see this effect in the square shapes of the post-frontal maxima; the weaker sound from those pre-frontal water modes does not dominate the post-frontal pattern.

3.4.3 Summary of Oceanographic Effects

As we saw above, the primary effect of propagation from Slope to Sargasso water was to refract sound deeper within the water column, away from the surface. This downward refraction had two results: to cause an increase in bottom interactions and thus loss, and a decrease in surface ensonification (a shadow zone). Figure 3.54a schematizes this case, with the solid line representing the frontal interaction and the dashed line showing the range independent propagation. The increased bottom interactions occurred because the sound strikes

the sediment after the front, and the greater depth of refraction away from the surface results in a shadow zone. Due to low-frequency effects, some sound did penetrate into the shadow zone; we saw a greater ensonification decrease at 100 Hz (125 dB) than at 25 Hz (50 dB). But at any one frequency, shadow zone ensonification depended more on the distance of the observer from the front than on the distance from the source to the front.

Propagation from Sargasso to Slope water involves upward refraction of sound within the waveguide. This property had a markedly different effect on propagation patterns in the two regimes, where either water-refracting paths or bottom-glancing paths dominated the pre-frontal propagation patterns. In both cases, though, surface ensonification increased.

Figure 3.54b schematizes the first case where water-propagating sound dominated the waveguide; the solid lines show the results of the frontal interaction and the dashed lines show the range independent case. Past the front, sound which refracted below the surface now reflects off the surface, accounting for the increased ensonification of about 10 dB. The broad convergence zones seen in the range-independent case were overwhelmed by the increase in sound paths reaching the surface out of horizontal phase with the convergence zone paths. This effect was largely independent of frequency.

The propagation regime dominated by sound in the bottom-glancing paths showed a much greater dependence on frequency, due to the relative strengths of bottom-glancing and water-propagating sound. Figure 3.54c schematizes this case, with the dashed lines representing range-independent propagation and the solid lines representing the frontal interaction. The bold lines show the water-propagating sound and the lighter lines represent the pre-frontal bottom-glancing sound. The upward refraction of the frontal interaction permits the water-propagating sound to reach the surface, forming convergence zones with magnitudes approximately 10–20 dB higher than the range independent cases. Some of the bottom-glancing sound also reaches the surface after the frontal interaction. We saw that the magnitudes of sound in this path will vary with frequency and sediment type: at 100 Hz it is approximately 20 dB greater than at 50 Hz.

3.5 Oceanographic and Topographic Interactions

In the realistic ocean, both range-dependent oceanography and varying topography interact to affect the acoustic propagation patterns. With the understanding gained above of the effects that oceanography and topography separately have on acoustic propagation patterns, we are equipped to put them together and build up the realistic cases.

3.5.1 Slope to Sargasso Water Propagation

Propagation southeast across the Gulf Stream involves both a transition from Slope to Sargasso water and a deepening of topography. The change of water masses will cause a deepening of the sound channel axis, refracting the sound deeper within the water column, and the deepening of the topography will permit sound to refract with depth rather than interacting with the bottom.

The four source depths and three frequencies tested followed the same general pattern; we will look closely at the case with $z_s = 100$ m at 100 Hz, building from flat-bottom, range independent propagation up to variable topography, range dependent propagation. Figure 3.55 shows the matrix sound speed fields used for the comparison: range-independent oceanographic fields on the left and range-dependent fields on the right; flat topography on top and realistic downsloping topography on the bottom. In figure 3.56 we have the propagation loss contours for the four cases, arranged in the same fashion, and in figure 3.57 we have propagation loss at the 100 m receiver, likewise arranged in the same fashion. Henceforth the y-axes of the 100 m receiver plots are all the same, for comparison of the magnitudes of the interaction effects.

We can see in figure 3.56 each of the separate effects of oceanography and topography; starting with the range-independent, flat-bottom case at upper left, adding deepening topography (lower left) permits sound in deeper propagation paths to refract with depth. Alternatively, starting from the range-independent, flat-bottom case, adding oceanography variation (upper right) has caused sound to refract away from the surface and deeper into the water as discussed before. Adding the topography variation to that case results in increased amounts of sound refracting with depth rather than interacting with the lossy bottom. In the

lower right corner of figure 3.56 we see that this combination of effects has resulted in the expected refraction away from the surface; there is a surface shadow zone past 125 km. The frontal transition has refracted sound downward away from the surface toward the bottom; the downward topography has permitted the deeper propagation paths to refract within the water column instead of encountering the bottom with its reflections and losses. With the inclusion of these deeper paths, the propagation patterns in the deeper water have changed dramatically; the deeper convergence zones near 750 m depth are not nearly so well in phase due to interfering sound in deep propagation paths which the deeper topography permits.

In figure 3.57 we see the effect of these changes on the sound levels at 100 m depth. Starting from the range independent, flat-bottom case (upper left), adding deepening topography (lower left) had very little effect on the long-range propagation pattern. The only significant effect of realistic topography was to modify the bottom-reflected returns that appear near 35 and 70 km range in the flat-bottom case; with downsloping topography, these returns appear near 38 km and merged with the second water-refracting convergence zone maximum near 100 km. This is the same modification of the secondary Lloyd's Mirror sound lobe discussed in section 3.3.1, as it appears in the 100 m receiver.

Alternatively, starting from the range independent oceanographic, flat bottom example and adding oceanography (upper right) caused a drastic decrease in surface ensonification as we saw in section 3.4.1, down to 210 dB by 250 km range in this 100 Hz case. Adding the topography variation permits sound in deep propagation paths to refract within the water rather than interact with the bottom; thus less bottom loss occurs. The decrease in loss raises the sound levels in the shadow zone; sound levels stabilize around 140 dB after the frontal interaction.

In other sections we have found indications that mode compensation to changes in the water column depth can occur through sediment interactions; note that in changing from one water mass to another the vertical modes must change as well, yet in the range-dependent oceanographic, flat-bottom case (figure 3.56b) we see no evidence of interactions with the sediment. However, between the range-independent oceanographic case with realistic topography (figure 3.56c) and the range-dependent oceanographic case with realistic topography (figure

3.56d), only the oceanography changes, and we do see some very small changes in the sound maxima within the sediment. Note particularly the maximum near 235 km range, 4400 m depth in both cases; other slight changes in magnitude appear. With this set of sediment parameters, the relative size of these changes in sediment maxima with respect to the changes due to topography alone shows why we see no sediment patterns in the realistic-oceanography, flat-bottom case; with the flat bottom they are too small to pick out from the sediment contours.

Propagation at the other frequencies shows the same general effects of refracting sound deeper in the water column and permitting deep refraction paths, as we see in figures 3.58 and 3.59 of the range-dependent oceanographic, variable topographic case at 25, 50, and 100 Hz. The frequency effects on shadow zone ensonification are twofold; first, at lower frequencies, more sound penetrates into the shadow zone as discussed earlier. In figure 3.59 in the 25 Hz case, shadow zone ensonification has maxima of approximately 112 dB. In the 50 Hz case, we see shadow zone maxima of 123 dB, and in the 100 Hz case, 138 dB. Note that in the 100 Hz case, these maxima appear in different locations that at the lower frequencies; the second effect of frequency on shadow zone ensonification relates to the frequency dependence of propagation patterns within the first 50 km and the modification of this pattern due to deepening topography, as discussed above and in section 3.3.1.

Recall that this is the example with primary lobe of sound striking the bottom at 25 Hz, grazing the bottom at 50 Hz, and totally refracting within the water column at 100 Hz. The secondary sound lobes also strike the bottom at different angles, as shown in table 3.3. At 25 Hz, the secondary lobe strikes the (flat) bottom at 62^o from the vertical to have 12% reflect; at 50 Hz, at 77^o, to have 10% reflect; and at 100 Hz, at 82^o, to have 22% reflect. With downward topography, these beams will strike the bottom slightly deeper and thus with angle slightly closer to grazing. At 25 Hz, the secondary lobe strikes the (downward) bottom at 64^o, to have 12% reflect; at 50 Hz, at 77^o, to have 10% reflect, and at 100 Hz, at 84^o, to have 28% reflect, an increase of 6% over the flat-bottom case. The angle of the bottom topography will affect only the depth of incidence and thus the amount of water-column refraction that occurred, since the IFD model treats the bottom as locally flat. From the above numbers, we see that at 100 Hz, the secondary lobe is propagating with shallow enough angle

by 3170 m depth that refraction through the additional depth makes perceptible change to its angle of incidence at the sediment; the rapid increase in $|R_{12}|$ for angles past 80° causes a slight increase in the amount of sound reflected in this path at 100 Hz, while the other two frequencies remain unchanged. Thus at 100 Hz, with the downsloping bottom, sound in that secondary path will affect the propagation patterns more greatly than in the flat-bottom case or at the lower frequencies. In figure 3.58, lower right, we see this return near the bottom at 20, 70, 120, and 170 km range. Sound in this path appears near the surface at 155 and 225 km range; in figure 3.59 these are the maxima in the 100 m receiver at these ranges. We do not see these returns in the 25 and 50 Hz cases because the magnitude of any sound from this secondary beam is so much less at those frequencies.

3.5.2 Sargasso to Slope Water Propagation

Propagation northwest across the Gulf Stream involves a transition from the Sargasso water mass with its deep sound channel and weak secondary duct to the Slope water mass with its single shallower sound channel axis. The change in water masses will refract the sound upward and closer to the surface. Additionally, the topography slopes upward, truncating the deep portion of the water column with range.

Propagation patterns for all source depths and frequencies tested did not follow the same general pattern as they did above; the sources at $z_s = 750$ and 3000 m showed fairly simple, predictable oceanographic and topographic effects, but the sources at $z_s = 10$ and 100 m continued to display unusual interaction effects due to both frequency effects and their strong bottom-glancing propagation patterns. We will discuss the simpler cases of the deeper sources before moving on to the shallower ones.

Figure 3.60 shows the same matrix of sound speed fields as they appear for propagation in this direction: the range-independent oceanographic fields are on the left and the range-dependent oceanographic fields are on the right; the flat-bottom cases are on the top and the variable topographic fields are on the bottom. In figure 3.61 we have the contours of propagation loss at 100 Hz for a source at 750 m for the four cases, arranged in the same fashion; the

range-dependent oceanographic flat-bottom case (figure 3.61b) has the upsloping topography overlaid on the plot to show explicitly which sound paths will become bottom-interacting. Figure 3.62 shows propagation loss at the 100 m receiver arranged similarly.

In figure 3.61 we can see the separate effects of oceanography and topography. Starting with the range-independent, flat-bottom case (upper left), addition of upsloping topography (lower left) truncates the deep propagation paths. Alternatively, starting from the range-independent, flat-bottom case and adding realistic oceanography (upper right) causes an upward refraction toward the surface of the sound in the deeper sound channel. Adding the upsloping topography (lower right) then truncates the deep propagation paths.

We see the effects of these phenomena on a receiver at 100 m depth in figure 3.62; starting from the range-independent oceanography, flat bottom case (upper left) and adding upsloping topography (lower left) truncated deep propagation paths and caused a decrease of 5–10 dB; alternatively, starting from the range-independent, flat-bottom case and adding realistic oceanography (upper right), caused an increase in surface ensonification of 35–40 dB after the front. Adding the realistic, upsloping topography (lower right) caused some shifts in the small-scale propagation patterns but no major changes in magnitude. The effects of the range-dependent oceanography seems to dominate over the effects of the upsloping topography.

Propagation at the other frequencies for these two deeper sources showed the same general pattern outlined for the 100 Hz, $z_s = 750$ m case; in figure 3.63 we have propagation patterns for this source at all three frequencies tested and in figure 3.64, the propagation loss at the 100 m receiver. The qualitative propagation patterns are the same at all the frequencies, as are the sound levels at the 100 m receiver. Thus realistic propagation upslope from Sargasso to Slope water increases ensonification at a shallow receiver, and the effect is largely independent of frequency in the 25–100 Hz range.

For the two shallower sources, the interactions of oceanography and topography depend strongly on frequency and source depth, via the strength of excitation of the trapped modes relative to the amount of sound in bottom-glancing paths. Recall that the trapped modes will be excited more strongly by

sources nearer the sound channel, and for any one source, the trapped modes will be excited more strongly at lower frequencies. Additionally, the form of the bottom interaction depends on both source depth and frequency via the angular distribution of sound striking the sediment and the angular dependence of the reflection coefficient. In general, the stronger the relative excitation of the water column modes, the more the final propagation patterns will depend on the oceanography, and the more closely the final propagation patterns will resemble the range-dependent oceanographic, flat-bottom case. Likewise, the weaker the relative excitation of these trapped modes, the more the propagation will be dominated by topographic effects and the more closely the final propagation patterns will resemble the range-independent oceanographic, variable topographic case.

Figure 3.65 shows contours of propagation loss when $z_s = 100$ m and $f = 25$ Hz; the plots are arranged on the page to correspond to the sound speed fields given in figure 3.60. Again, the range-dependent oceanographic, flat-bottom case has the upward topography added, to show explicitly the sound paths which will become bottom-interacting. In the flat-bottom, range-independent oceanography case (upper left), we see a relatively homogeneous propagation field with weak convergence zone propagation in water-propagating paths emerging from a bottom-reflecting interference pattern by 200 km range. Sound magnitudes range between 110 and 115 dB in the water-propagating paths. Adding upsloping topography (lower left) truncates the bottom of the water-propagating paths, leaving a pattern of bottom reflecting sound. Leaving the topography flat and instead adding oceanographic variations (upper right) refracts the water-propagating and some of the bottom-reflecting sound away from the bottom, to form convergence zone propagation with sound levels ranging between 105 and 110 dB in the convergence zones. The increase in magnitude is due to sound in the pre-frontal bottom-reflecting paths coming into focus with the sound in the pre-frontal water-propagating paths. Adding upsloping topography (lower right) truncates the deep paths; however, because of the upward refraction of sound due to the front, convergence zone propagation patterns persist although the sound magnitude in the convergence zone maxima is somewhat decreased to 110 to 115 dB, due to the bottom losses from those deeper paths which encountered the sediment.

Figure 3.66 shows the same configuration of four cases at 50 Hz. In the flat-bottom, range-independent oceanography case (upper left) we see the quickly-resolved pattern of convergence zones which form the dominant propagation pattern by 100 km range; sound magnitudes range between 115 and 120 dB in these paths by the end of the calculation. Adding upsloping topography (lower left) again truncates the bottom of the water-propagation paths, leaving a pattern of bottom reflecting sound. Leaving the topography flat and instead adding the frontal transition (upper right) refracts the water-propagating, and some of the bottom-propagating, sound away from the bottom, to form convergence zones with magnitudes between 110 and 115 dB. Note that at this frequency, we explicitly see the sound maximum near 3700 m depth and 220 km range below the realistic topography. Adding that upsloping topography (lower right) truncates these deep paths; the sound remaining in the weakened convergence zones (120–125 dB by 250 km) consists of more weakly excited trapped modes that had lesser equivalent ray angles and propagated closer to the axis of the sound channel. In the flat bottom cases sound in these paths was overwhelmed by the greater sound magniutde in the main trapped propagation paths; in the range-independent oceanographic, upward topography case, these modes were not refracted upward and thus were lost from interactions with the bottom. The frontal interaction shifts the trapped modes upward enough that water-borne propagation paths continue to dominate the sound fields in spite of the increased topographic interactions.

In figure 3.67 we have the same set of four cases at 100 Hz; in the flat-bottom, range-independent oceanography case (upper left) the propagation pattern begins with a large number of bottom reflecting beams which gradually weaken through reflection losses; water-propagating sound dominates the propagation patterns by 175 km with magnitudes ranging between 120 and 125 dB. Adding upward topography (lower left) truncates these water-propagating paths, leaving a pattern of bottom-reflecting beams that weakens due to bottom losses. By 250 km range we see the pattern of anomalous beams discussed in section 3.3.2 above. Alternatively, keeping the topography flat and adding the frontal transition (upper right) refracts the water-propagating and some of the bottom-propagating sound upward in the water column, forming convergence zones with magnitudes between 115 and 120 dB by 250 km. These convergence zones show broad maxima due to the large amount of bottom interacting sound still dominant

in the propagation pattern during the frontal interaction. Adding the upsloping topography disrupts the convergence zone patterns; we see the bottom-reflecting beams dominating through 125 km range; from 125 to 175 km range the upward-refracted water-propagating sound appears, but at subsequent ranges the continuing upward topography truncates the water-propagating sound paths and we see a pattern of bottom-reflections again with magnitudes between 135–140 dB by 250 km range. The final, combined case shows a series of bottom reflections before and after the frontal interaction, with a modification to the reflections in the frontal region. The propagation patterns resemble neither the range-independent oceanographic, upsloping bottom case nor the range-dependent oceanographic, flat bottom case. With the higher frequency we can infer that excitation of the trapped modes closer to the sound channel axis was enough weaker that reflections from the upward topography prevented their being detected, even with the upward refraction of the frontal interaction.

Figure 3.68 shows the four cases for the shallower source $z_s = 10$ m and $f = 25$ Hz; this case is similar to the case of $z_s = 100$ m and $f = 25$ Hz except that the sound magnitudes in the trapped modes are less due to weaker excitation of these modes. Nevertheless, the convergence zone pattern persists in the final case (lower right), with sound magnitudes between 135–140 dB by the end of the calculation.

In figure 3.69 we have these cases for $z_s = 10$ m and $f = 50$ Hz; in the flat-bottom, range-independent oceanography case (upper left) we resolve the water-propagating sound by 125 km; it has magnitudes between 140–145 dB by 250 km. In the range-independent oceanography, upsloping bottom case (lower left), the anomalous pattern of beams appears; the beams are wider at 50 Hz than at 100 Hz. With the upward-refracting oceanography but flat bottom (upper right) we again see the convergence zones, with magnitudes ranging between 135–140 dB by 250 km. The final combined case (lower right) does not resemble either of the two previous cases, with just the oceanographic variations or just the topographic variations. With the shallower source, excitation of the trapped modes closer to the sound channel axis seems to have been sufficiently weaker that they cannot be perceived through the bottom interaction effects at 50 Hz; recall that this state was reached at 100 Hz when the source was at 100 m depth.

Finally, in figure 3.70 we see these cases at $f = 100$ Hz. The range-

independent oceanographic case with the flat bottom (upper left) shows the more weakly excited trapped modes only barely resolved by 225 km, containing sound magnitudes of 160–165 dB. With upsloping topography alone (lower left), we see the pattern of anomalous beams; with flat topography but varying oceanography (upper right), we see the previously bottom-reflecting sound refracting upward in the water, with slight modifications by the original water-propagating sound. The final combined case (lower right) almost exactly resembles the range-independent oceanographic, upsloping bottom case; the excitation of any trapped modes seems to be weak enough at this source depth and frequency for topography to entirely dominate propagation, with little modification by oceanographic variations.

To summarize the above six cases, we saw that for the source at 100 m, where there is relatively strong excitation of trapped modes due to the deeper source location, but the excitation decreases with increasing frequency, the cases 25 and 50 Hz had oceanography dominating propagation patterns. The 100 Hz case seemed to represent a transition case, where the oceanographic and topographic patterns seemed to balance. With the source at 10 m, where there is weaker excitation of trapped modes due to source location and the excitation again decreases with increasing frequency as well as a different pattern of topographic interactions, at 25 Hz oceanography dominated propagation patterns. The 50 Hz case seemed to represent the transition state, and at 100 Hz topography dominated propagation patterns.

It would be interesting to compare these interactions with a different set of sediment parameters, to see how the type of underlying sediment affects the interaction between oceanography and topography. Figure 3.71 shows the same matrix of cases for $z_s = 100$ m, $f = 25$ Hz, with the sediment parameters as follows: $\rho = 1.352$ gm/cm^3, $\beta = .9$ dB/λ, $c_w/c_b = 1.0$, $\partial c/\partial z = 1.227$ sec^{-1}, and $z_{sed} = 100$ m. In other words, the only change from the so-called realistic set of parameters is that $c_w/c_b = 1.0$. Recall that in this case the magnitude of R_{12} was increased for all values of θ over R_{12} with the realistic set of parameters; thus we can expect an increase in bottom reflections in all cases. In the range-independent oceanographic, flat-bottom example (upper left) we see a pattern of multiple bottom reflections overwhelming any water-propagating sound; the same condition obtains in the range-independent oceanographic, upsloping example (lower left). Returning to the flat topography but adding upward-refracting oceanog-

raphy (upper right), we can detect the upward refraction of water-propagating sound, but the bottom reflections still dominate the sound channel. Combining the oceanography and topography (lower right) continues to produce patterns of bottom reflections overwhelming the water-propagating sound.

Figure 3.72 shows the same matrix of cases with the same source depth and sediment parameters as figure 3.71, at $f = 100$ Hz. In the range-independent oceanographic, flat bottom case (upper left) we see a pattern of bottom reflecting beams with the water-propagating sound perhaps becoming discernable by 250 km. We can compare this case with figure 3.67, the realistic bottom case corresponding in source depth and frequency to this example, where we see reflections from the primary lobe of sound strike the sediment near 25, 75, and 125 km range. In the present case with $c_w/c_b = 1.0$ we see reflections from that primary lobe of sound striking the sediment near 25, 75, 125, and 175 km; more sound is reflecting with each interaction, increasing ensonification in the water column to the point where it overwhelms any water-propagating sound. Note magnitudes in that weakly discernable water-propagating path near 250 km vary between 120 and 125 dB in this case, the same as in the realistic case, but that interference from bottom reflections make that path difficult to resolve. In the range-independent oceanographic case with upsloping topography (lower left), we see a pattern of bottom reflections throughout the computation. With the flat bottom and upward-refracting oceanography, we see the upward-refracted sound past the frontal interaction. Note the broad flat form of these surface maxima near 170 and 225 km range, indicating the increased magnitude of previously bottom-reflected sound, whereas in figure 3.67 (upper right) the post-frontal maxima form sharper peaks near the surface at 185 km and 245 km. Addition of the upsloping topography again serves to increase bottom interactions, truncating the sound in upward-refracted water-propagating paths.

Thus from figures 3.65–3.72 we have seen that when the trapped modes are excited strongly enough to dominate over bottom reflections, the oceanographic effects will dominate over the topographic effects in the combined realistic case. In other words, with strong excitation of water propagation patterns relative to the bottom-interacting patterns, these shallow sources behave similarly to the deeper sources in this profile, which had water-trapped propagation paths that left the source with real propagation angle.

On the other hand, when the trapped modes are excited so weakly relative to bottom interacting sound that the bottom-reflecting sound still predominates well past the region of oceanographic frontal interaction, then the final combined case is entirely dominated by topographic effects. Additionally, there seems to be a transition state in which the final combined propagation patterns do not closely resemble either the flat bottom, variable oceanography case or the variable topography, range independent oceanography case but may appear totally different from either due to the combination of effects. The relative balance between water-propagating sound magnitudes and bottom-reflected sound magnitudes determines whether the oceanography or topography will have the greatest effect on propagation in these cases.

3.5.3 Summary of Oceanographic and Topographic Interactions

As we have seen propagation from Slope to Sargasso water involved both downward refraction of the sound away from the surface and deepening topographic depth. These two conditions have opposing effects; the oceanography acts to increase sediment interacitons, while the topography acts to decrease them. Propagation patterns showed the effects of both these conditions; figure 3.73a schematizes the case, with dashed lines representing range-independent, flat-bottom propagation and solid lines representing realistic propagation. The bold lines represent the primary interference path, while the lighter lines depict a secondary path. We can see the downward refraction of the primary path with the frontal interaction, as well as its excursion below the flat bottom depth. The downward refraction decreases ensonification near the surface, while the deeper bottom permits more sound to persist in the water column. As a result of the interaction, sound levels in the shadow zone are higher than thay were with flat topography: a decrease of only 20–25 dB at 25 Hz, 30–35 dB at 50 Hz, and 40–50 dB at 100 Hz, as opposed to the flat bottom case where shadow zone magnitude decreases were 50, 100, and 125 dB respectively.

Shadow zone ensonification with frequency also displayed lesser effects of the oceanographic and topographic interactions; other initial propagation paths may become more important in the realistic conditions due to 1) an increase in magnitude reflected with frequency and topographic variation, and 2) decrease in loss with the deeper range of water propagation. Figure 3.73a shows one such

path, which reflects closer to grazing at higher frequency, and thus with greater magnitude; at lower frequency, such a path would have less magnitude due to its initial bottom interaction and any possible subsequent bottom interactions. With their greater vertical extent, sound in these paths will increase shadow zone ensonification at higher frequencies. The form and magnitude of this effect would be strongly dependent on frequency, source depth, profile shape, and bottom topography via the angular distribution of sound incident on the bottom and the angular dependence of the reflection coefficient.

Propagation from Sargasso to Slope water involves both upward refraction of sound within the sound channel and upsloping topography. These physical conditions again have opposing effects: the topography acts to increase sediment interactions, while the oceanography acts to decrease them. The form of balance achieved between these conditions depends on the propagation regime.

For deep sources, having $c_{bot} > c_{src}$ and thus water propagation paths that left the source with real angle, the upward refraction from the frontal interaction increased surface ensonification without forming coherent convergence zone phenomena. Figure 3.73b schematizes this case, with dashed lines lines representing range-independent, flat bottom propagation and solid lines representing realistic propagation. This surface ensonification increase overwhelmed losses due to topographic truncation of deep sound paths; the topography merely modified locations of small-scale magnitude fluctuations.

For the shallower sources, in which bottom-glancing propagation was important, the upward refraction of the oceanography caused the sound in trapped modes and the bottom-glancing paths to reinforce and form regular convergence zones. The addition of upsloping topography, however, caused a variety of effects and these cases must be further divided due to the relative strengths of sound in water column modes and bottom interaction effects. The trapped water column modes are more strongly excited for lower frequencies and sources nearer the sound channel, while the form and magnitude of bottom reflection effects also depends strongly on source depth and frequency.

Cases with sufficient sound magnitude in trapped water-column modes to dominate topographic interaction effects are schematized in figure 3.73c. Dashed lines show range-independent propagation paths and solid lines depict realistic

propagation. Upward refraction of oceanography increases the amount of energy in shallower regions, but the topography interrupts the sound path at every deep excursion. Less-strongly excited modes then become more important to the propagation pattern. The lesser excitation of these modes was revealed in the decreased magnitudes of the convergence zones, which showed decreases of 10–15 dB due to this effect. These cases are similar to those with deeper sources, in that the oceanographic effects dominated over the topographic effects, although the topographic modification to propagation was larger.

If the excitation of the trapped modes is insufficient to overwhelm the bottom interactions, as schematized in figure 3.73d, then the topographically induced propagation patterns dominated the oceanographic patterns and the final combined case either resembled the case with topographic variations alone or resembled neither of its predecessor cases. The cases in which final propagation patterns resembled neither range-independent oceanographic propagation with upsloping topography or frontal propagation with a flat bottom seem to represent a transition between the propagation dominated by oceanography and propagation dominated by topography.

3.6 Summary of Gulf Stream Propagation Study

Through this intensive study of sediment, topographic, and oceanographic interactions in the Gulf Stream Region, an important point has emerged that deep water propagation patterns at these frequencies depend critically on low-frequency source-image interference patterns in the range of the first bottom interactions. Propagation proved to be very heavily influenced by the manner in which the angular distribution of sound striking the sediment interacts with the angular dependence of the Rayleigh reflection coefficient. We can classify all the cases into three groups, based on the behavior of the Lloyd's Mirror interference pattern.

The first group consists of cases in which the primary interference lobe refracts with depth in a flat bottom waveguide. This group also contains cases with source-image separation so great that the Lloyd's Mirror interference maxima are nearly unresolvable; in realistic oceanic waveguides at these frequencies, such cases have most of those minor maxima refract within the water column. As

such, this group consists of cases with $c_{surf} > c_{bot} > c_{src}$, when the frequency was great enough that the interference pattern fit the criterion. No examples with depth excess ($c_{bot} > c_{surf}$) were tested in this study, but according to Snell's law, propagation in profiles with depth excess is guaranteed real propagation angles leaving the source and refracting within the water. Propagation with depth excess will probably also fit into this group if the frequency is sufficient to cause the primary interference maximum to clear the bottom. In the parameter study just analyzed, this group consists of the following profile/source depth/frequency combinations: Sargasso water profile, $z_s = 750$ and 3000 m, all frequencies; Slope water profile, $z_s = 750$ and 3000 m, all frequencies; and Slope water profile, $z_s = 100$ m, $f = 100$ Hz. Propagation for cases in this group possessed the same general properties.

Cases within this group proved least sensitive to values of the sediment parameters, as sound propagated in the oceanic waveguide with enough magnitude to overwhelm modification caused by the relatively small total sound intensity interacting with the bottom. Certain values of the sediment parameters can have dramatic effects on propagation in this group, such as low values of attenuation β that permit large amounts of sound to return from within the sediment and propagate for long ranges in the waveguide, but even so, such effects were less than those obtained by the same parameter value on an example outside this group.

Topographic effects took the same forms for cases within this group. Since the main interference maximum refracts within the flat-bottomed waveguide, then downward topography only affects the lesser interference maxima, and the convergence zone patterns formed by the primary Lloyd's Mirror lobe remain unchanged. The form and magnitude of the secondary propagation modifications would depend on the exact propagation conditions of source depth, profile shape, and topographic slope. Alterations of 5–7 dB were noted in regions of lower ensonification. Upward topography served to truncate deeper propagation paths and thus decrease convergence zone radii by 1–3 km; the magnitude of change would depend on topographic slope. Truncation of the deep paths also decreased convergence zone maxima by 15–20 dB, depending on topographic slope.

Oceanographic variability effects were also similar for cases within this group. An upward refraction of sound within the waveguide increases surface

ensonification by 20–25 dB; downward refraction of waveguide sound decreases surface ensonification and results in a shadow zone. Sound levels in the shadow zones (for flat-bottom cases) decreased between 50 and 125 dB from their range-independent values, depending on frequency. This downward refraction also caused an increase in bottom interactions, where losses occurred.

The second major group of propagation cases consists of those in which the primary Lloyd's Mirror interference lobe interacts with the sediment, but the interaction either took place either at relatively steep angle, or when trapped water column modes were so strongly excited as to rapidly overwhelm any bottom interaction effects. This group consists of Slope profile propagation with $z_s = 10$ m, all frequencies tested, and $z_s = 100$ m, $f = 25$ and 50 Hz. Propagation patterns for these cases again followed certain general properties. They were considerably more sensitive to the values of sediment parameters, due to the larger relative sound magnitude interacting with the bottom compared with the amount of sound contained within the oceanic waveguide. All sediment parameter variations had a stronger effect on propagation patterns for these cases than those in the previous group.

Topographic effects took the same general forms for cases within this group, but downward topographic effects differed from those seen in the previous classification. Downsloping topography increased the convergence zone radius by including more deep sound paths in the main energy beam; adding this deeper sound to the propagation pattern increased convergence zone magnitudes 7–10 dB and increased convergence zone radii by 1–3 km. Upsloping topography again decreased the convergence zone radius by truncating deep sound paths, and therefore decreased water column ensonification as discussed above.

Oceanographic variations had a similar effect on cases within this group as in the first; downward refraction of sound within the waveguide resulted in a surface shadow zone and an increase in topographic interactions. Shadow zone sound magnitude decreases for flat-bottom propagation ranged between 60–150 dB, depending on frequency. Upward refraction of waveguide sound was not tested for this group, but through a knowledge of the physics one can predict an increase in surface ensonification and decrease in bottom interactions.

From comparisons of the above properties, we can see that these two

major classifications of propagation types are very similar. They differ due to the effects caused by the main Lloyd's Mirror interference lobe interacting with the sediment: if more energy interacts with the sediment, then sediment changes affect a greater percentage of the total waveguide sound. Additionally, with downsloping topography, the additional sound refracting within the water column greatly affects convergence zone radius if the convergence zones are not already strongly determined by the large sound magnitude in the primary Lloyd's Mirror lobe.

A third classification of cases appeared, in which the primary lobe of sound struck the sediment near grazing incidence, where the magnitude of R_{12} is large, and for which excitation of trapped water column modes was relatively weak. This group consisted of propagation in the Sargasso profile with source depths $z_s = 10$ and 100 m, all frequencies tested. These conditions permitted the imperfectly-reflected bottom glancing sound to dominate propagation for mid to long ranges, before reflection losses were sufficient to shift the balance of propagation patterns to the trapped water column modes. In view of the great importance of bottom-glancing sound in this propagation regime, these cases proved extremely sensitive to the values of the parameters which determine the angular dependence of the reflection coefficient for shallow-angle sound (ρ, c_w/c_b). Sensitivity to the parameters describing sediment with depth was considerably less.

Topographic effects on propagation within this regime differed markedly from those in the groups described above. Downward topography permits sound in that primary interference lobe to refract within the water column, increasing convergence zone coherence, radius by 2–4 km, and ensonification by approximately 20 dB in the cases studied. The magnitude of this effect depends on topographic slope and the angles of incident sound maxima; the interference lobe may not refract in the water on its first deep excursion but on its second or third.

Upward topography again causes unusual effects for propagation within this regime. Upsloping topography still truncates deep propagation paths, but when the deep paths consist of weakly excited trapped modes, truncation of those modes results in unusual propagation patterns containing interference maxima which point in odd directions and do not follow Snell's law refraction princi-

ples, but do reflect from the surface. These interference maxima are not fully understood but are thought to be related to mode cut-off phenomena in a wedge.

Oceanographic refraction upward in these profiles served to shift propagation patterns away from the bottom and toward the surface; thus bottom interactions decreased and surface ensonification increased due to: 1) shifting the trapped water column modes closer to the surface, and 2) decreasing the sediment interactions of the sound in bottom-glancing paths, which then reinforce the convergence zone patterns. These phenomena caused an increase in surface ensonification of 10–20 dB; magnitudes of this effect will depend on the strength of the upward refraction and on the amount of sound remaining in those bottom-glancing propagation paths when the frontal interaction occurs.

Oceanographic refraction downward away from the surface was not tested for these cases; it is difficult to say what the exact results would be. Such a condition would shift the weakly-excited trapped modes closer to the bottom and truncate them, increasing sediment losses. Insufficient information is contained in this study to predict the result.

Not all combinations of oceanographic and topographic conditions were tested this interaction study; only the two cases in which the oceanographic effects balanced the topographic effects were conducted. With the oceanography refracting downward and the topography deepening, the reduction of bottom losses weakened shadow zone ensonification decreases, so magnitude decreases remained in the 20–40 dB range (dependent upon frequency) from values seen in the flat, range independent oceanographic cases. Upward oceanographic refraction, combined with upward topography, resulted in a general increase in surface ensonification of 25–30 dB when bottom glancing propagation is not important to the propagation patterns; even when bottom-glancing regimes are important, a lesser increase in post-frontal surface ensonification is seen if trapped mode excitation was strong enough to overwhelm sediment interaction effects (e.g., the case with $z_s = 100$ m, $f = 25$ Hz showed a 5–10 dB increase in post-frontal ensonification, in coherent convergence zone maxima).

The two physical combinations in which the oceanographic effects would increase the topographic effects, i.e. downward refraction with upward topography or upward refraction with downward topography were not tested. Little can

be said of these cases except to note that upward topography would increase the sediment losses caused by the downward refraction, and we can expect shadow zone ensonification to weaken. Downward topography in conjunction with upward sound channel refraction would have no effect on the sound shifted upward in the profile; it could be expected to modify only the lesser Lloyd's Mirror interference maxima.

Thus we have seen three major deep water propagation regimes, of which the first two are quite similar and the third differs strongly from the other two. The major difference seems to lie in the sound magnitudes in bottom-reflecting paths relative to sound in trapped modes, since these propagation patterns were not observed in the Slope profile with $z_s = 100$ m and $f = 50$ Hz. It would be interesting to calculate modes for these profiles and determine relative magnitudes of excitation of the trapped modes.

It must be noted further that extensive propagation in bottom-glancing propagation regimes will depend on the sediment parameters, which were held constant here but will vary with range. However, for all realistic sediments, the magnitude of the reflection coefficient approaches unity for incident angles approaching grazing. Changes in the functional form of the reflection coefficient could cause these propagation regimes to either quickly collapse or extend their ranges due to variations in sediment composition.

By including low-frequency effects, we have expanded the types of classically permissible long range, water-refracting propagation regimes beyond those cases where the sound speed profile possessed depth excess for refraction within the water column. Excitation of trapped modes via the magnitudes of their exponential tail near the source in higher sound speed water can cause coherent convergence zone phenomena which propagate to long ranges within the water column, and interact with the oceanographic and topographic variations in a regular way. Low-frequency sediment interaction effects can have an extremely important effect on propagation patterns, however, and must be included for accurate acoustic prediction.

Figure 3.1) a. Gulf Stream region streamfunction fields, time = 0. b. Slope water sound speed profile. c. Sargasso water sound speed profile.

Figure 3.2) a. Range independent Slope water sound speed fields, z_{bot} = 3170 m. b. Range dependent Slope to Sargasso water sound speed fields, z_{bot} = 3170 m. c. Range independent Slope water sound speed fields, downsloping topography. d. Range dependent Slope to Sargasso water sound speed fields, downsloping topography. e. Range independent Sargasso water sound speed fields, z_{bot} = 4440 m. f. Range dependent Sargasso to Slope water sound speed fields, upsloping topography. g. Range independent Sargasso water sound speed fields, z_{bot} = 4440 m. h. Range dependent Sargasso to Slope water sound speed fields, upsloping topography.

Figure 3.3) Propagation from Slope to Sargasso water, z_s = 10 m, f = 25 Hz. a. Sound speed contours. b. Propagation loss at 100 m. c. Propagation loss contours. d. Propagation loss at 1000 m.

Figure 3.4) Propagation from Slope to Sargasso water, z_s = 10 m, f = 100 Hz. a. Sound speed contours. b. Propagation loss at 100 m. c. Propagation loss contours. d. Propagation loss at 1000 m.

Figure 3.5) Propagation from Sargasso to Slope water, z_s = 100 m, f = 25 Hz. a. Sound speed contours. b. Propagation loss at 100 m. c. Propagation loss contours. d. Propagation loss at 1000 m.

Figure 3.6) Propagation from Sargasso to Slope water, z_s = 100 m, f = 100 Hz. a. Sound speed contours. b. Propagation loss at 100 m. c. Propagation loss contours. d. Propagation loss at 1000 m.

Figure 3.7) Range-independent oceanography, flat bottom Slope water acoustic propagation, first 50 km. a. z_s = 10 m, f = 25 Hz. b. z_s = 100 m, f = 25 Hz. c. z_s = 10 m, f = 50 Hz. d. z_s = 100 m, f = 50 Hz. e. z_s = 10 m, f = 100 Hz. f. z_s = 100 m, f = 100 Hz.

Figure 3.8) Range-independent oceanography, flat bottom Slope water acoustic propagation, first 50 km. a. z_s = 750 m, f = 25 Hz. b. z_s = 3000 m, f = 25 Hz. c. z_s = 750 m, f = 50 Hz. d. z_s = 3000 m, f = 50 Hz. e. z_s = 750 m, f = 100 Hz. f. z_s = 3000 m, f = 100 Hz.

Figure 3.9) Range-independent oceanography, flat bottom Sargasso water acoustic propagation, first 50 km. a. z_s = 10 m, f = 25 Hz. b. z_s = 100 m, f = 25 Hz. c. z_s = 10 m, f = 50 Hz. d. z_s = 100 m, f = 50 Hz. e. z_s = 10 m, f = 100 Hz. f. z_s = 100 m, f = 100 Hz. Note the weak sound trapping near 400 m depth from the secondary sound speed duct.

Figure 3.10) Range-independent oceanography, flat bottom Sargasso water acoustic propagation, first 50 km. a. z_s = 750 m, f = 25 Hz. b. z_s = 3000 m, f = 25 Hz. c. z_s = 750 m, f = 50 Hz. d. z_s = 3000 m, f = 50 Hz. e. z_s = 750 m, f = 100 Hz. f. z_s = 3000 m, f = 100 Hz.

Figure 3.11) Range-independent oceanography, flat bottom Slope water propagation. $z_s = 10$ m, $f = 25$ Hz. "Realistic bottom:" $\rho = 1.352$ gm/cm^3, $\beta = .9$ dB/λ, $c_w/c_b = 1.017$, $\partial c/\partial z = 1.227$ sec^{-1}, $z_{sed} = 100$ m. a. Propagation loss contours. b. R_{12}. c. Propagation loss at 100 m receiver. d. Propagation loss at 3000 m receiver.

Figure 3.12) Range-independent oceanography, flat bottom Slope water propagation. $z_s = 10$ m, $f = 100$ Hz. Realistic bottom. a. Propagation loss contours. b. R_{12}. c. Propagation loss at 100 m receiver. d. Propagation loss at 3000 m receiver.

Figure 3.13) Range-independent oceanography, flat bottom Sargasso water propagation. $z_s = 100$ m, $f = 25$ Hz. Realistic bottom. a. Propagation loss contours. b. R_{12}. c. Propagation loss at 100 m receiver. d. Propagation loss at 3000 m receiver.

Figure 3.14) Range-independent oceanography, flat bottom Sargasso water propagation. $z_s = 100$ m, $f = 100$ Hz. Realistic bottom. a. Propagation loss contours. b. R_{12}. c. Propagation loss at 100 m receiver. d. Propagation loss at 3000 m receiver.

Figure 3.15) Range-independent oceanography, flat bottom Slope water propagation. $z_s = 10$ m, $f = 100$ Hz. $\rho = 1.0$ gm/cm^3, $\beta = .9$ dB/λ, $c_w/c_b = 1.017$, $\partial c/\partial z = 1.227$ sec^{-1}, $z_{sed} = 100$ m. Receiver plots overlaid with corresponding receivers from figure 3.11, present case bold. a. Propagation loss contours. b. R_{12}. c. Propagation loss at 100 m receivers. d. Propagation loss at 3000 m receivers.

Figure 3.16) Range-independent oceanography, flat bottom Sargasso water propagation. $z_s = 100$ m, $f = 100$ Hz. $\rho = 1.0$ gm/cm^3, $\beta = .9$ dB/λ, $c_w/c_b = 1.017$, $\partial c/\partial z = 1.227$ sec^{-1}, $z_{sed} = 100$ m. Receiver plots overlaid with corresponding receivers from figure 3.13, present case bold. a. Propagation loss contours. b. R_{12}. c. Propagation loss at 100 m receivers. d. Propagation loss at 3000 m receivers.

Figure 3.17) Range-independent oceanography, flat bottom Slope water propagation. $z_s = 10$ m, $f = 25$ Hz. $\rho = 1.352$ gm/cm^3, $\beta = .25$ dB/λ, $c_w/c_b = 1.017$, $\partial c/\partial z = 1.227$ sec^{-1}, $z_{sed} = 100$ m. Receiver plots overlaid with corresponding receivers from figure 3.10, present case bold. a. Propagation loss contours. b. R_{12}. c. Propagation loss at 100 m receivers. d. Propagation loss at 3000 m receivers.

Figure 3.18) Range-independent oceanography, flat bottom Slope water propagation. $z_s = 10$ m, $f = 100$ Hz. $\rho = 1.352$ gm/cm^3, $\beta = .25$ dB/λ, $c_w/c_b = 1.017$, $\partial c/\partial z = 1.227$ sec^{-1}, $z_{sed} = 100$ m. Receiver plots overlaid with corresponding receivers from figure 3.11, present case bold. a. Propagation loss contours. b. R_{12}. c. Propagation loss at 100 m receivers. d. Propagation loss at 3000 m receivers.

Figure 3.19) Range-independent oceanography, flat bottom Slope water propagation. $z_s = 10$ m, $f = 100$ Hz. $\rho = 1.352$ gm/cm^3, $\beta = .9$ dB/λ, $c_w/c_b = 1.017$, $\partial c/\partial z = 0.0$ sec^{-1}, $z_{sed} = 100$ m. Receiver plots overlaid with corresponding

receivers from figure 3.11, present case bold. a. Propagation loss contours. b. R_{12}. c. Propagation loss at 100 m receivers. d. Propagation loss at 3000 m receivers.

Figure 3.20) Range-independent oceanography, flat bottom Sargasso water propagation. $z_s = 100$ m, $f = 25$ Hz. $\rho = 1.352$ gm/cm^3, $\beta = .9$ dB/λ, $c_w/c_b = 1.017$, $\partial c/\partial z = 0.0$ sec^{-1}, $z_{sed} = 100$ m. Receiver plots overlaid with corresponding receivers from figure 3.12, present case bold. a. Propagation loss contours. b. R_{12}. c. Propagation loss at 100 m receivers. d. Propagation loss at 3000 m receivers.

Figure 3.21) Range-independent oceanography, flat bottom Sargasso water propagation. $z_s = 100$ m, $f = 25$ Hz. $\rho = 1.352$ gm/cm^3, $\beta = .9$ dB/λ, $c_w/c_b = 1.017$, $\partial c/\partial z = 0.75$ sec^{-1}, $z_{sed} = 100$ m. Receiver plots overlaid with corresponding receivers from figure 3.12, present case bold. a. Propagation loss contours. b. R_{12}. c. Propagation loss at 100 m receivers. d. Propagation loss at 3000 m receivers.

Figure 3.22) Range-independent oceanography, flat bottom Slope water propagation. $z_s = 10$ m, $f = 100$ Hz. $\rho = 1.352$ gm/cm^3, $\beta = .9$ dB/λ, $c_w/c_b = 1.017$, $\partial c/\partial z = 1.227$ sec^{-1}, $z_{sed} = 0$ m. Receiver plots overlaid with corresponding receivers from figure 3.11, present case bold. a. Propagation loss contours. b. R_{12}. c. Propagation loss at 100 m receivers. d. Propagation loss at 3000 m receivers.

Figure 3.23) Rayleigh reflection coefficient R_{12}. a. $\rho = 1.352$ gm/cm^3, $\beta = 0$ dB/λ, $c_w/c_b = .98$. b. $\rho = 1.352$ gm/cm^3, $\beta = 0.9$ dB/λ, $c_w/c_b = .98$. c. $\rho = 1.352$ gm/cm^3, $\beta = 0$ dB/λ, $c_w/c_b = 1.000$. d. $\rho = 1.352$ gm/cm^3, $\beta = 0.9$ dB/λ, $c_w/c_b = 1.000$. e. $\rho = 1.352$ gm/cm^3, $\beta = 0$ dB/λ, $c_w/c_b = 1.017$. f. $\rho = 1.352$ gm/cm^3, $\beta = 0.9$ dB/λ, $c_w/c_b = 1.017$. g. $\rho = 1.352$ gm/cm^3, $\beta = 0$ dB/λ, $c_w/c_b = 1.1$. h. $\rho = 1.352$ gm/cm^3, $\beta = 0.9$ dB/λ, $c_w/c_b = 1.1$.

Figure 3.24) Range-independent oceanography, flat bottom Slope water propagation. Propagation loss contours. $z_s = 10$ m, $f = 100$ Hz. $\rho = 1.352$ gm/cm^3, $\beta = .9$ dB/λ, $\partial c/\partial z = 1.227$ sec^{-1}, $z_{sed} = 100$ m. a. $c_w/c_b = .98$. b. $c_w/c_b = 1.0$. c. $c_w/c_b = 1.017$. d. $c_w/c_b = 1.1$.

Figure 3.25) Range-independent oceanography, flat bottom Slope water propagation. Propagation loss contours. $z_s = 100$ m, $f = 25$ Hz. $\rho = 1.352$ gm/cm^3, $\beta = .9$ dB/λ, $\partial c/\partial z = 1.227$ sec^{-1}, $z_{sed} = 100$ m. a. $c_w/c_b = .98$. b. $c_w/c_b = 1.0$. c. $c_w/c_b = 1.017$. d. $c_w/c_b = 1.1$.

Figure 3.26) Range-independent oceanography, flat bottom Slope water propagation. Propagation loss contours. $z_s = 100$ m, $f = 100$ Hz. $\rho = 1.352$ gm/cm^3, $\beta = .9$ dB/λ, $\partial c/\partial z = 1.227$ sec^{-1}, $z_{sed} = 100$ m. a. $c_w/c_b = .98$. b. $c_w/c_b = 1.0$. c. $c_w/c_b = 1.017$. d. $c_w/c_b = 1.1$.

Figure 3.27) Range-independent oceanography, flat bottom Sargasso water propagation. Propagation loss contours. $z_s = 100$ m, $\rho = 1.352$ gm/cm^3, $\beta = .9$ dB/λ, $c_w/c_b = 1.017$, $\partial c/\partial z = 1.227$ sec^{-1}, $z_{sed} = 100$ m. a. $f = 25$ Hz. b. $f = 50$ Hz. c. $f = 100$ Hz.

Figure 3.28) Range-independent oceanography, flat bottom Sargasso water propagation. Propagation loss contours. $z_s = 10$ m, $\rho = 1.352$ gm/cm^3, $\beta = .9$ dB/λ, $c_w/c_b = 1.017$, $\partial c/\partial z = 1.227$ sec^{-1}, $z_{sed} = 100$ m. a. $f = 25$ Hz. b. $f = 50$ Hz. c. $f = 100$ Hz.

Figure 3.29) Range-independent oceanography, flat bottom Sargasso water propagation. Propagation loss contours. $z_s = 100$ m, $f = 25$ Hz, $\rho = 1.352$ gm/cm^3, $\beta = .9$ dB/λ, $\partial c/\partial z = 1.227$ sec^{-1}, $z_{sed} = 100$ m. a. $c_w/c_b = 1.01$. b. $c_w/c_b = 1.02$. c. $c_w/c_b = 1.03$. d. $c_w/c_b = 1.04$.

Figure 3.30) Range-independent oceanography, flat bottom Sargasso water propagation. Propagation loss contours. $z_s = 100$ m, $f = 50$ Hz, $\rho = 1.352$ gm/cm^3, $\beta = .9$ dB/λ, $\partial c/\partial z = 1.227$ sec^{-1}, $z_{sed} = 100$ m. a. $c_w/c_b = 1.01$. b. $c_w/c_b = 1.02$. c. $c_w/c_b = 1.03$. d. $c_w/c_b = 1.04$.

Figure 3.31) Schematic of Sediment Interaction Effects. a. Principal sound path refracts with depth. b. Principal sound path interacts with sediment. c. Bottom glancing paths important.

Figure 3.32) Range-independent oceanography, flat bottom vs. downsloping Slope water propagation. $z_s = 100$ m, $f = 100$ Hz. a. Flat bottom propagation loss contours. b. Flat bottom propagation loss at 3000 m receiver. c. Downsloping propagation loss contours. d. Downsloping propagation loss at 3000 m receiver.

Figure 3.33) Range-independent oceanography, downsloping Slope water propagation. $z_s = 10$ m, $f = 25$ Hz. Receivers overlaid with corresponding receivers from figure 3.10. a. Sound speed contours. b. Propagation loss at 100 m receivers. c. Propagation loss contours. d. Propagation loss at 3000 m receivers.

Figure 3.34) Range-independent oceanography, flat bottom vs. downsloping Slope water propagation. $z_s = 3000$ m, $f = 25$ Hz. a. Flat bottom propagation loss contours. b. Flat bottom propagation loss at 100 m receiver. c. Downsloping propagation loss contours. d. Downsloping propagation loss at 100 m receiver.

Figure 3.35) Range-independent oceanography, flat bottom vs. downsloping Sargasso water propagation, bottom slope $\Delta z/\Delta r = .005$. $z_s = 10$ m, $f = 25$ Hz. a. Flat bottom propagation loss contours. b. Flat bottom propagation loss at 100 m receiver. c. Downsloping propagation loss contours. d. Downsloping propagation loss at 100 m receiver.

Figure 3.36) Range-independent oceanography, Sargasso water profile, bottom slope $\Delta z/\Delta r = .004$ vs. $\Delta z/\Delta r = .005$. $z_s = 10$ m, $f = 25$ Hz. a. Flat bottom propagation loss contours. b. Flat bottom propagation loss at 100 m receiver. c. Downsloping propagation loss contours. d. Downsloping propagation loss at 100 m receiver.

Figure 3.37) Range-independent oceanography, flat bottom vs. upsloping Sargasso water propagation. $z_s = 750$ m, $f = 100$ Hz. a. Flat bottom propagation loss contours. b. Flat bottom propagation loss at 100 m receiver. c. Upsloping propagation loss contours. d. Upsloping propagation loss at 100 m receiver.

Figure 3.38) Range-independent oceanography, flat bottom vs. upsloping Sargasso water propagation. $z_s = 10$ m, $f = 100$ Hz. a. Flat bottom propagation loss contours. b. Flat bottom propagation loss at 1000 m receiver. c. Upsloping propagation loss contours. d. Upsloping propagation loss at 1000 m receiver.

Figure 3.39) Range-independent oceanography, Sargasso water bottom slope test. $z_s = 10$ m, $f = 100$ Hz. a. Bottom slope -.002, propagation loss contours. b. Bottom slope -.002, propagation loss at 100 m receiver. c. Bottom slope -.003, propagation loss contours. b. Bottom slope -.003, propagation loss at 100 m receiver.

Figure 3.40) Range-independent oceanography, Slope water bottom slope test. $z_s = 10$ m, $f = 50$ Hz. a. Bottom slope -.003, propagation loss contours. b. Bottom slope -.003, propagation loss at 100 m receiver. c. Bottom slope -.004, propagation loss contours. b. Bottom slope -.004, propagation loss at 100 m receiver.

Figure 3.41) Schematic of downsloping topographic effects. a. Primary sound path refracts within flat-bottom waveguide. b. Primary sound path interacts with flat bottom. c. Bottom-glancing propagation paths important.

Figure 3.42) Schematic of upsloping topographic effects. a. Primary sound paths refract within flat-bottom waveguide. b. Bottom-glancing paths important.

Figure 3.43) Range dependent vs. range independent oceanography, Slope to Sargasso water propagation. Bottom depth 3170 m. $z_s = 100$ m, $f = 100$ Hz. a. Sound speed contours, range dependent case. b. Sound speed contours, range independent case. c. Propagation loss contours, range dependent case. d. Propagation loss contours, range independent case.

Figure 3.44) Range dependent vs. range independent oceanography, Slope to Sargasso water propagation. Bottom depth 3170 m. $z_s = 100$ m, $f = 100$ Hz. a. Sound speed contours, range dependent case. b. Sound speed contours, range independent case. c. Propagation loss at 1000 m receiver, range dependent case. d. Propagation loss at 1000 m receiver, range independent case.

Figure 3.45) Range-dependent oceanography, Slope to Sargasso water propagation. Bottom depth 3170 m. $z_s = 100$ m. Realistic bottom. a. Sound speed contours. b. Propagation loss contours, 25 Hz. c. Propagation loss contours, 50 Hz. d. Propagation loss contours, 100 Hz.

Figure 3.46) Range-dependent oceanography, Slope to Sargasso water propagation. Bottom depth 3170 m. $z_s = 100$ m. Realistic bottom. a. Sound speed contours. b. Propagation loss, 100 m receiver, 25 Hz. c. Propagation loss, 100 m receiver, 50 Hz. d. Propagation loss, 100 m receiver, 100 Hz.

Figure 3.47) Range-dependent oceanography, Slope to Sargasso water propagation. Bottom depth 3170 m. $z_s = 100$ m. $f = 50$ Hz. Realistic bottom. a. Propagation loss at 100 m receiver, all three cases overlaid to align the geography. b. Propagation loss contours, starting position 37.3N 72.4W (far from stream). c. Propagation loss contours, starting position 37.1N 72.1W (middle). d. Propagation loss contours, starting position 36.8N 71.8W (close to stream).

Figure 3.48) Range-dependent vs. range-independent oceanography, Sargasso to Slope water propagation. z_s = 750 m, f = 50 Hz. Bottom depth 4440 m, realistic bottom. a. Sound speed contours, Sargasso to Slope water. b. Sound speed contours, Sargasso water range-independent profile. c. Propagation loss contours, Sargasso to Slope water. d. Propagation loss contours, Sargasso water profile.

Figure 3.49) Range-dependent vs. range-independent oceanography, Sargasso to Slope water propagation. z_s = 750 m, f = 50 Hz. Bottom depth 4440 m, realistic bottom. a. Sound speed contours, Sargasso to Slope water. b. Sound speed contours, Sargasso water range-independent profile. c. Propagation loss at 100 m, Sargasso to Slope water. d. Propagation loss at 100 m, Sargasso water profile.

Figure 3.50) Range-dependent oceanography, Sargasso to Slope water propagation. Bottom depth 4440 m. z_s = 100 m. Realistic bottom. a. Sound speed contours. b. Propagation loss contours, f = 25 Hz. c. Propagation loss contours, f = 50 Hz. d. Propagation loss contours, f = 100 Hz.

Figure 3.51) Range-dependent oceanography, Sargasso to Slope water propagation. Bottom depth 4440 m. z_s = 100 m. Realistic bottom. a. Sound speed contours. b. Propagation loss at 100 m, f = 25 Hz. c. Propagation loss at 100 m, f = 50 Hz. d. Propagation loss at 100 m, f = 100 Hz.

Figure 3.52) Range-dependent oceanography, Sargasso to Slope water propagation. Bottom depth 4440 m. z_s = 10 m. Realistic bottom. a. Sound speed contours. b. Propagation loss contours, f = 25 Hz. c. Propagation loss contours, f = 50 Hz. d. Propagation loss contours, f = 100 Hz.

Figure 3.53) Range-dependent oceanography, Sargasso to Slope water propagation. Bottom depth 4440 m. z_s = 10 m. Realistic bottom. a. Sound speed contours. b. Propagation loss at 100 m, f = 25 Hz. c. Propagation loss at 100 m, f = 50 Hz. d. Propagation loss at 100 m, f = 100 Hz.

Figure 3.54) Schematic of Frontal Interaction Effects, flat topography. a. Slope to Sargasso propagation. b. Sargasso to Slope propagation, primary sound paths refract with depth. c. Sargasso to Slope propagation, bottom glancing paths important.

Figure 3.55) Sound speed contours. a. Slope water sound speed profile, 3170 m bottom. b. Slope to Sargasso water, 3170 m bottom. c. Slope water sound speed profile, realistic topography. d. Slope to Sargasso water, realistic topography.

Figure 3.56) Propagation loss contours, z_s = 100 m, f = 100 Hz. a. Slope water sound speed profile, 3170 m bottom. b. Slope to Sargasso water, 3170 m bottom. c. Slope water sound speed profile, realistic topography. d. Slope to Sargasso water, realistic topography.

Figure 3.57) Propagation loss at 100 m receiver, z_s = 100 m, f = 100 Hz. a. Slope water sound speed profile, 3170 m bottom. b. Slope to Sargasso water, 3170 m bottom. c. Slope water sound speed profile, realistic topography. d. Slope to Sargasso water, realistic topography.

Figure 3.58) Realistic topography, Slope to Sargasso water propagation, $z_s = 100$ m. a. Sound speed contours. b. Propagation loss contours, $f = 25$ Hz. c. Propagation loss contours, $f = 50$ Hz. d. Propagation loss contours, $f = 100$ Hz.

Figure 3.59) Realistic topography, Slope to Sargasso water propagation, $z_s = 100$ m. a. Sound speed contours. b. Propagation loss at 100 m, $f = 25$ Hz. c. Propagation loss at 100 m, $f = 50$ Hz. d. Propagation loss at 100 m, $f = 100$ Hz.

Figure 3.60) Sound speed contours. a. Sargasso water sound speed profile, 4440 m bottom. b. Sargasso to Slope water, 4440 m bottom. c. Sargasso water sound speed profile, realistic topography. d. Sargasso to Slope water, realistic topography.

Figure 3.61) Propagation loss contours, $z_s = 750$ m, $f = 100$ Hz. a. Sargasso water sound speed profile, 4440 m bottom. b. Sargasso to Slope water, 4440 m bottom. Realistic topography overlaid. c. Sargasso water sound speed profile, realistic topography. d. Sargasso to Slope water, realistic topography.

Figure 3.62) Propagation loss at 100 m receiver, $z_s = 750$ m, $f = 100$ Hz. a. Sargasso water sound speed profile, 4440 m bottom. b. Sargasso to Slope water, 4440 m bottom. c. Sargasso water sound speed profile, realistic topography. d. Sargasso to Slope water, realistic topography.

Figure 3.63) Realistic topography, Sargasso to Slope water propagation, $z_s = 750$ m. a. Sound speed contours. b. Propagation loss contours, $f = 25$ Hz. c. Propagation loss contours, $f = 50$ Hz. d. Propagation loss contours, $f = 100$ Hz.

Figure 3.64) Realistic topography, Sargasso to Slope water propagation, $z_s = 750$ m. a. Sound speed contours. b. Propagation loss at 100 m, $f = 25$ Hz. c. Propagation loss at 100 m, $f = 50$ Hz. d. Propagation loss at 100 m, $f = 100$ Hz.

Figure 3.65) Contours of propagation loss. $z_s = 100$ m, $f = 25$ Hz. a. Sargasso water sound speed profile, 4440 m bottom. b. Sargasso to Slope water, 4440 m bottom. Realistic topography overlaid. c. Sargasso water sound speed profile, realistic topography. d. Sargasso to Slope water, realistic topography.

Figure 3.66) Contours of propagation loss. $z_s = 100$ m, $f = 50$ Hz. a. Sargasso water sound speed profile, 4440 m bottom. b. Sargasso to Slope water, 4440 m bottom. Realistic topography overlaid. c. Sargasso water sound speed profile, realistic topography. d. Sargasso to Slope water, realistic topography.

Figure 3.67) Contours of propagation loss. $z_s = 100$ m, $f = 100$ Hz. a. Sargasso water sound speed profile, 4440 m bottom. b. Sargasso to Slope water, 4440 m bottom. Realistic topography overlaid. c. Sargasso water sound speed profile, realistic topography. d. Sargasso to Slope water, realistic topography.

Figure 3.68) Contours of propagation loss. $z_s = 10$ m, $f = 25$ Hz. a. Sargasso water sound speed profile, 4440 m bottom. b. Sargasso to Slope water, 4440 m bottom. Realistic topography overlaid. c. Sargasso water sound speed profile,

realistic topography. d. Sargasso to Slope water, realistic topography.

Figure 3.69) Contours of propagation loss. $z_s = 10$ m, $f = 50$ Hz. a. Sargasso water sound speed profile, 4440 m bottom. b. Sargasso to Slope water, 4440 m bottom. Realistic topography overlaid. c. Sargasso water sound speed profile, realistic topography. d. Sargasso to Slope water, realistic topography.

Figure 3.70) Contours of propagation loss. $z_s = 10$ m, $f = 100$ Hz. a. Sargasso water sound speed profile, 4440 m bottom. b. Sargasso to Slope water, 4440 m bottom. Realistic topography overlaid. c. Sargasso water sound speed profile, realistic topography. d. Sargasso to Slope water, realistic topography.

Figure 3.71) Contours of propagation loss. $z_s = 100$ m, $f = 25$ Hz. Sediment parameters: $\rho = 1.352$ gm/cm^3, $\beta = .9$ dB/λ, $c_w/c_b = 1.0$, $\partial c/\partial z = 1.227$ sec^{-1}, $z_{sed} = 100$ m. a. Sargasso water sound speed profile, 4440 m bottom. b. Sargasso to Slope water, 4440 m bottom. Realistic topography overlaid. c. Sargasso water sound speed profile, realistic topography. d. Sargasso to Slope water, realistic topography.

Figure 3.72) Contours of propagation loss. $z_s = 100$ m, $f = 100$ Hz. Sediment parameters: $\rho = 1.352$ gm/cm^3, $\beta = .9$ dB/λ, $c_w/c_b = 1.0$, $\partial c/\partial z = 1.227$ sec^{-1}, $z_{sed} = 100$ m. a. Sargasso water sound speed profile, 4440 m bottom. b. Sargasso to Slope water, 4440 m bottom. Realistic topography overlaid. c. Sargasso water sound speed profile, realistic topography. d. Sargasso to Slope water, realistic topography.

Figure 3.73) Schematic of Oceanographic/Topographic Interactions. a. Slope to Sargasso water. b. Sargasso to Slope water, primary sound paths refract with depth. c. Sargasso to Slope water, bottom glancing paths important; significant trapped mode excitation. d. Sargasso to Slope water, bottom glancing paths important; weak trapped mode excitation.

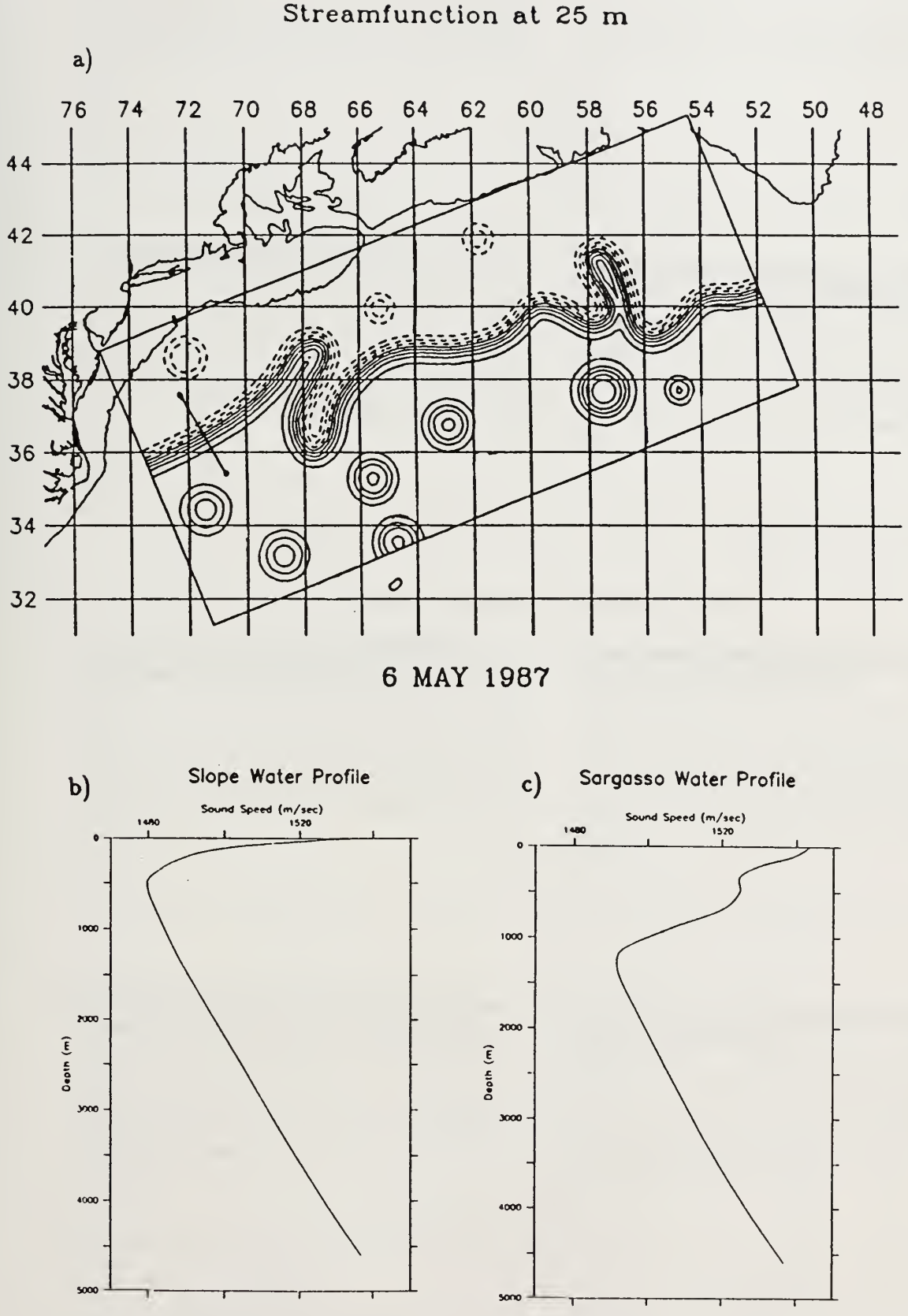

Figure 3.1) a. Gulf Stream region streamfunction fields, time = 0. b. Slope water sound speed profile. c. Sargasso water sound speed profile.

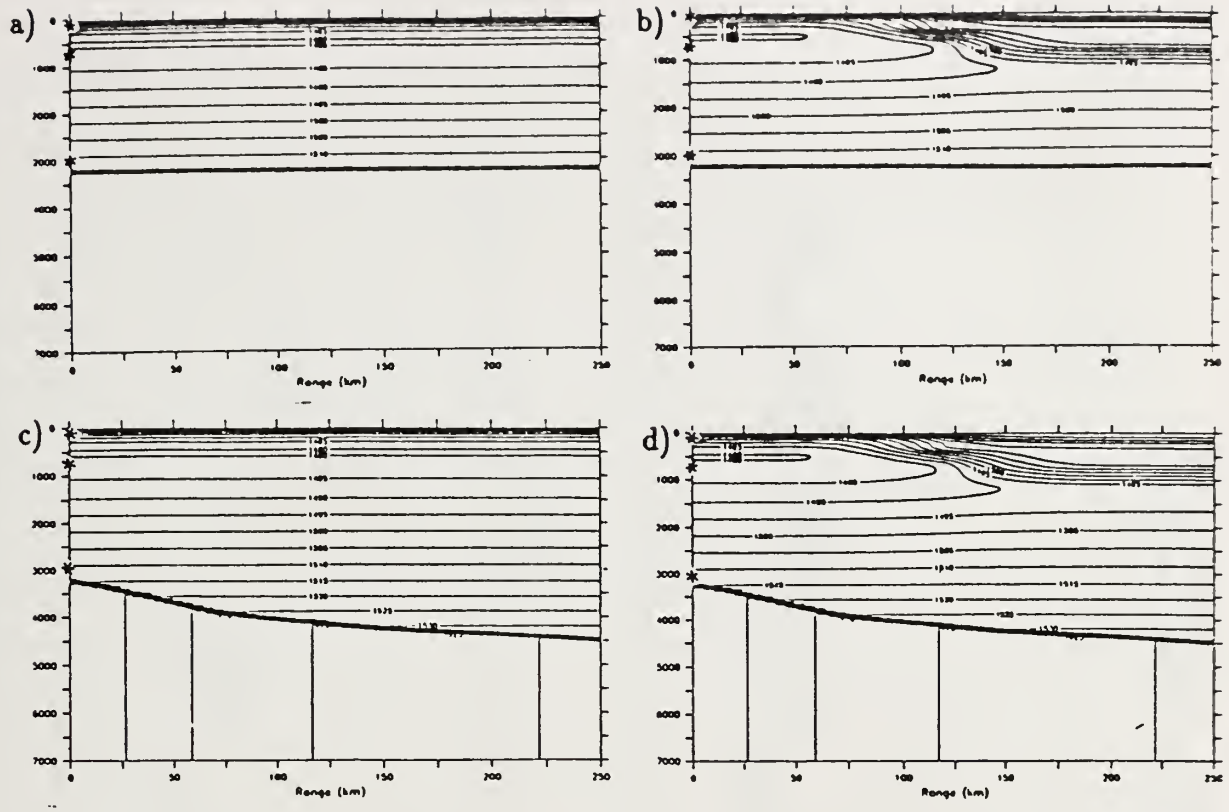

Southeast Point 35.7 N 70.4 W, 315° T

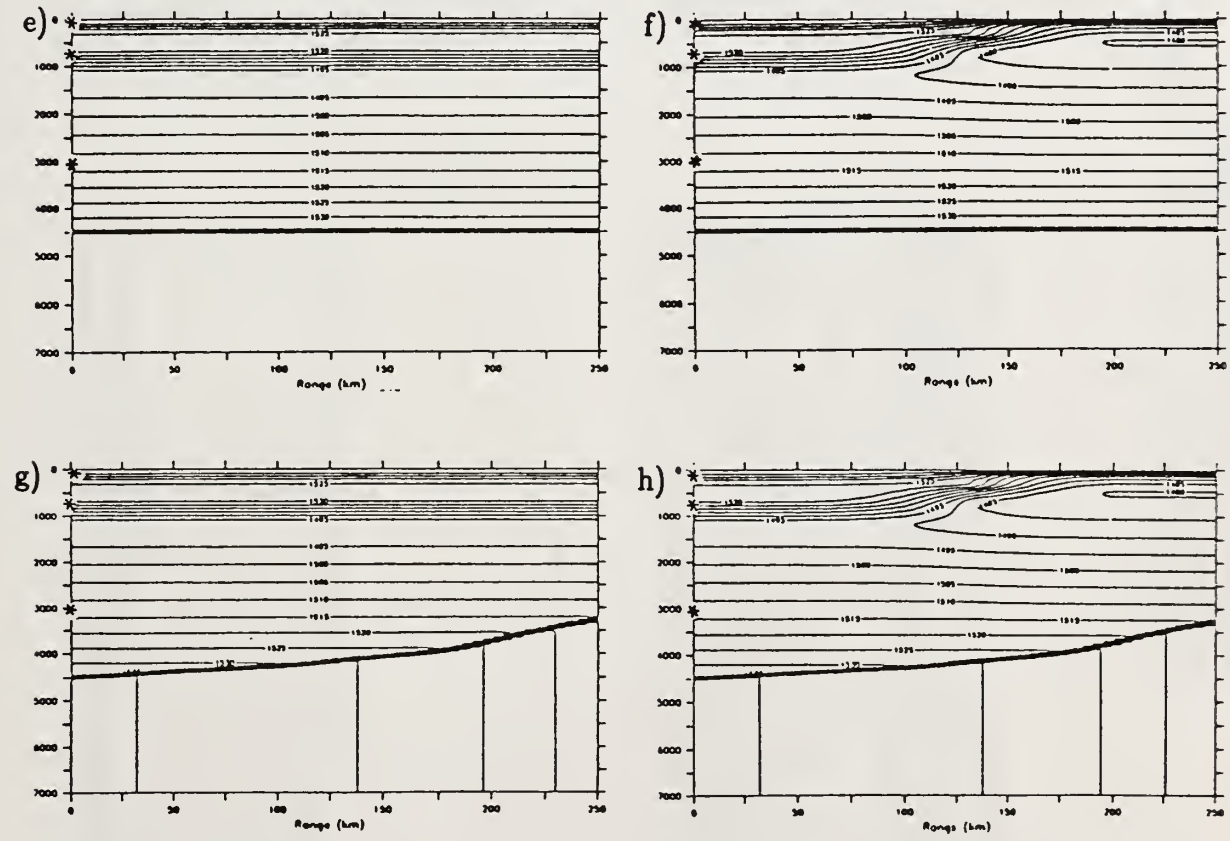

Figure 3.2) a. Range independent Slope water sound speed fields, z_{bot} = 3170 m. b. Range dependent Slope to Sargasso water sound speed fields, z_{bot} = 3170 m. c. Range independent Slope water sound speed fields, downsloping topography. d. Range dependent Slope to Sargasso water sound speed fields, downsloping topography. e. Range independent Sargasso water sound speed fields, z_{bot} = 4440 m. f. Range dependent Sargasso to Slope water sound speed fields, upsloping topography. g. Range independent Sargasso water sound speed fields, z_{bot} = 4440 m. h. Range dependent Sargasso to Slope water sound speed fields, upsloping topography.

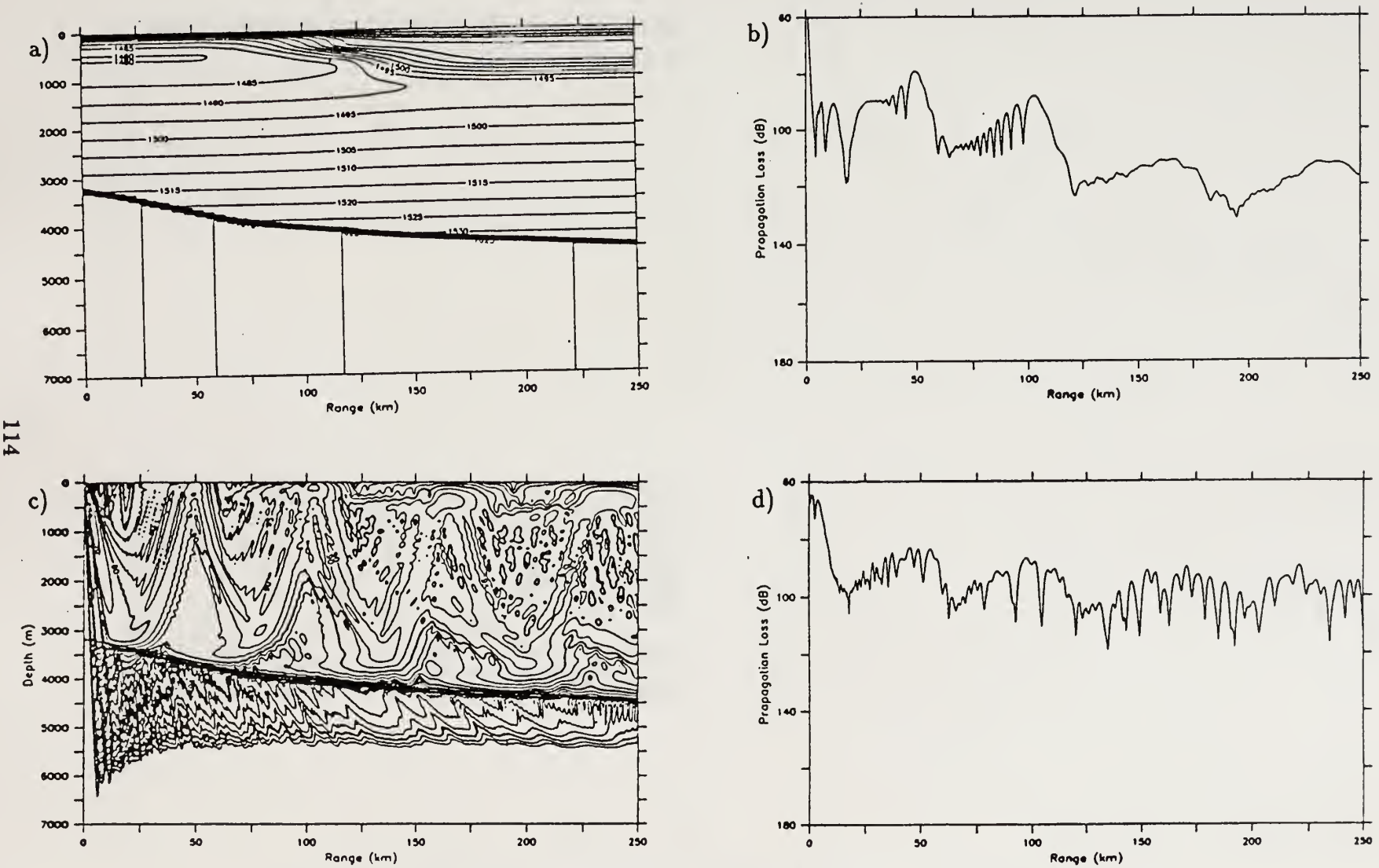

Figure 3.3) Propagation from Slope to Sargasso water, $z_s = 10$ m, $f = 25$ Hz. a. Sound speed contours. b. Propagation loss at 100 m. c. Propagation loss contours. d. Propagation loss at 1000 m.

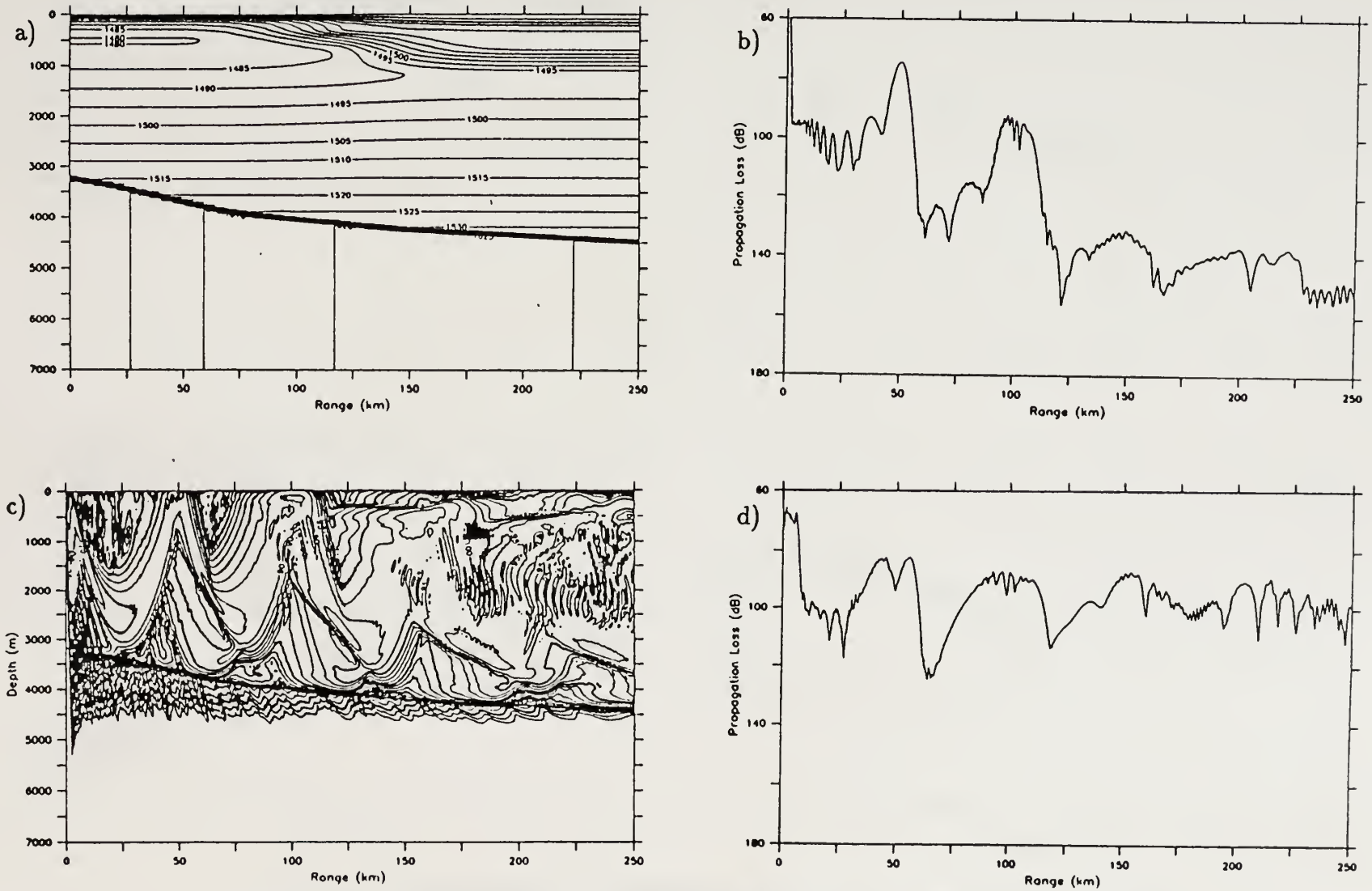

Figure 3.4) Propagation from Slope to Sargasso water, $z_s = 10$ m, $f = 100$ Hz. a. Sound speed contours. b. Propagation loss at 100 m. c. Propagation loss contours. d. Propagation loss at 1000 m.

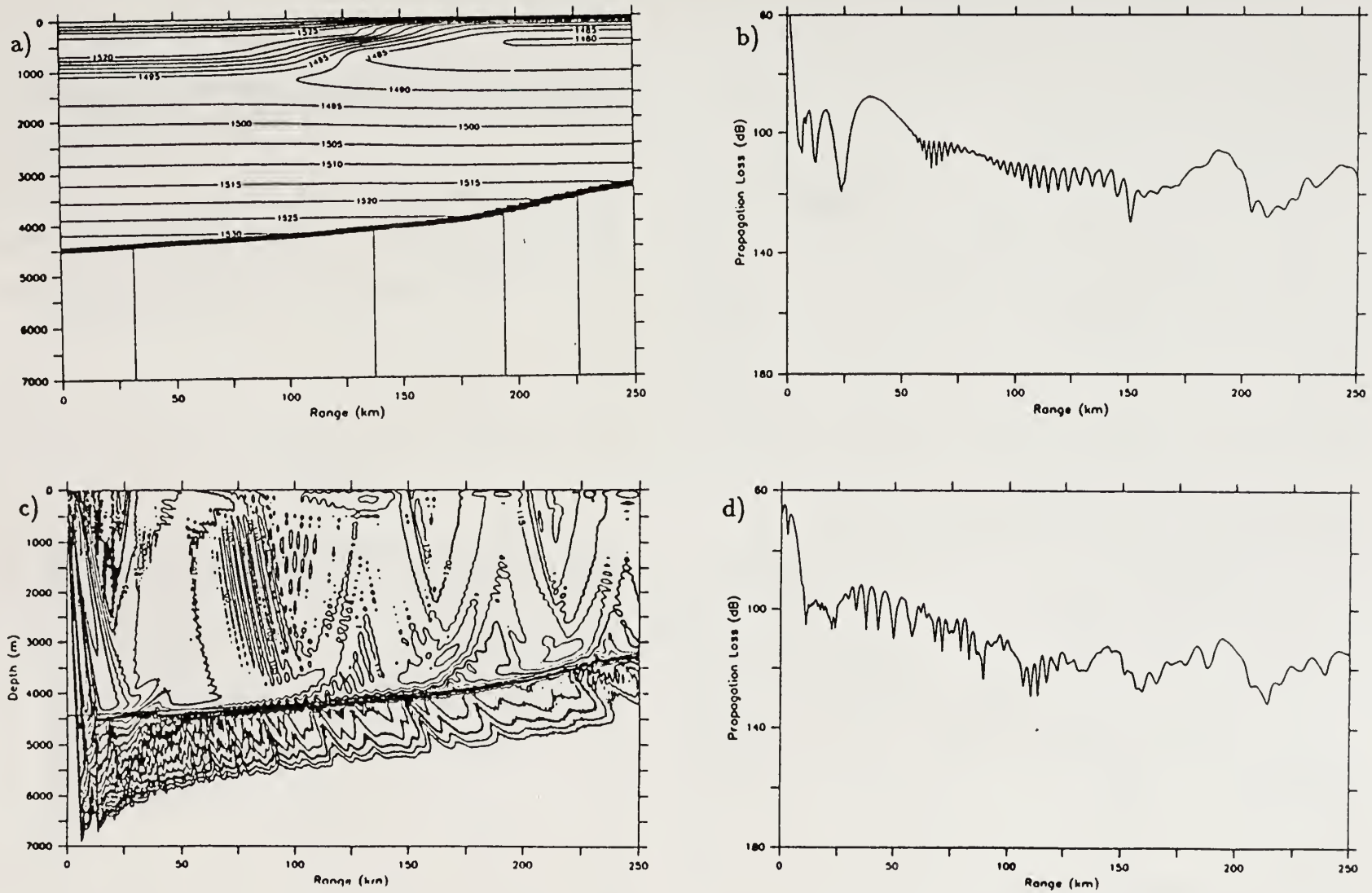

Figure 3.5) Propagation from Sargasso to Slope water, $z_s = 100$ m, $f = 25$ Hz. a. Sound speed contours. b. Propagation loss at 100 m. c. Propagation loss contours. d. Propagation loss at 1000 m.

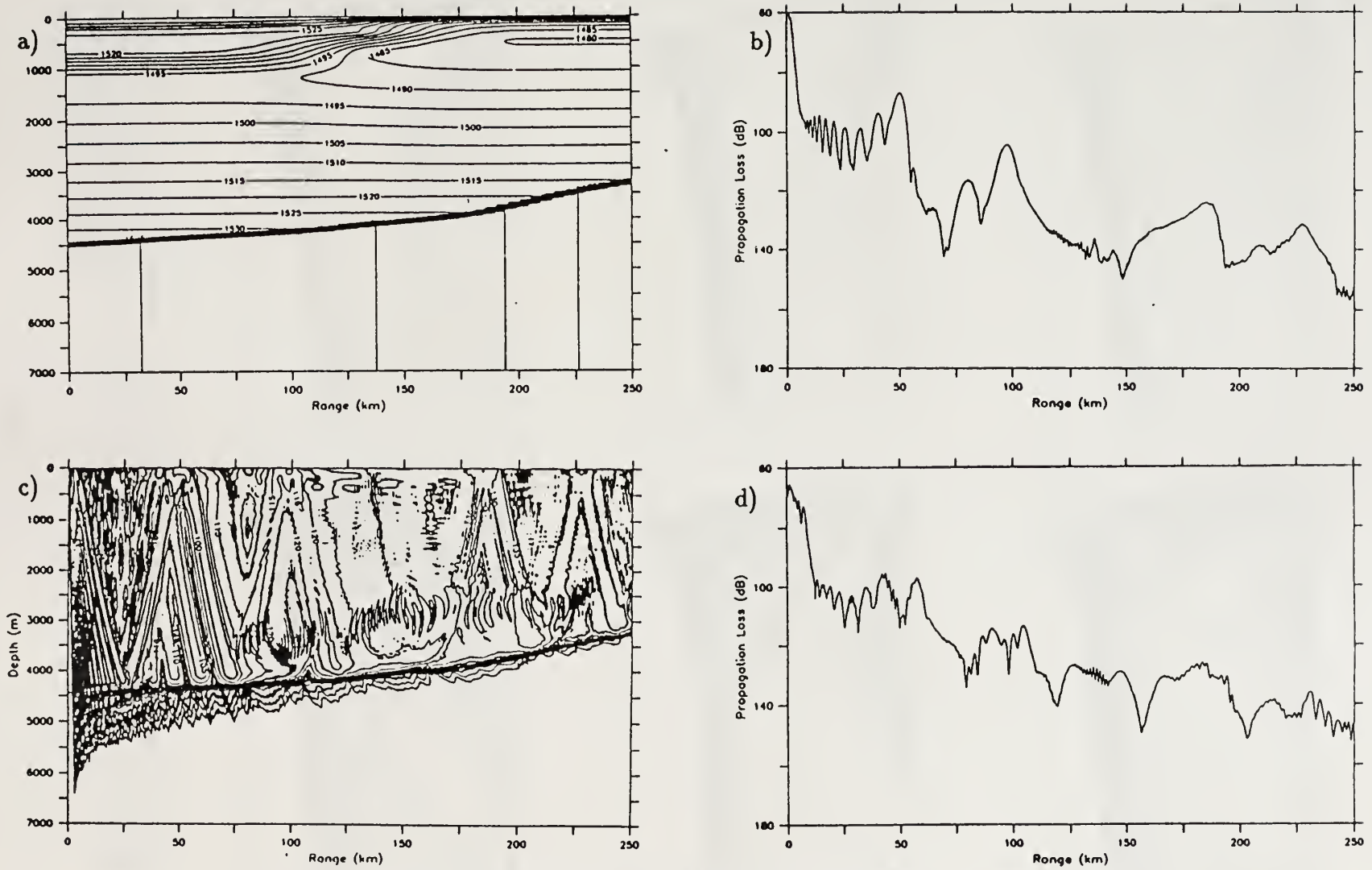

Figure 3.6) Propagation from Sargasso to Slope water, z_s = 100 m, f = 100 Hz. a. Sound speed contours. b. Propagation loss at 100 m. c. Propagation loss contours. d. Propagation loss at 1000 m.

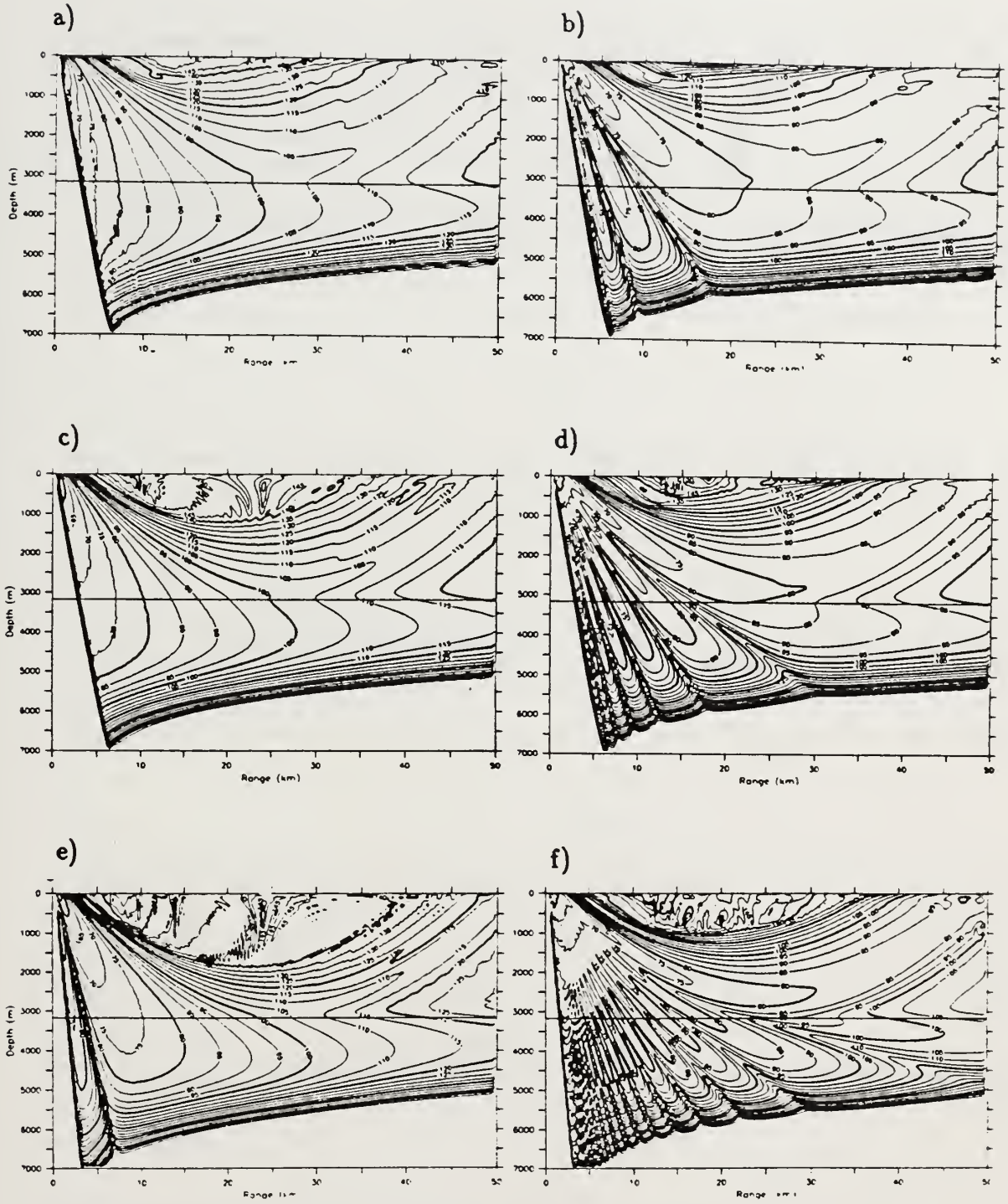

Figure 3.7) Range-independent oceanography, flat bottom Slope water acoustic propagation, first 50 km. a. $z_s = 10$ m, $f = 25$ Hz. b. $z_s = 100$ m, $f = 25$ Hz. c. $z_s = 10$ m, $f = 50$ Hz. d. $z_s = 100$ m, $f = 50$ Hz. e. $z_s = 10$ m, $f = 100$ Hz. f. $z_s = 100$ m, $f = 100$ Hz.

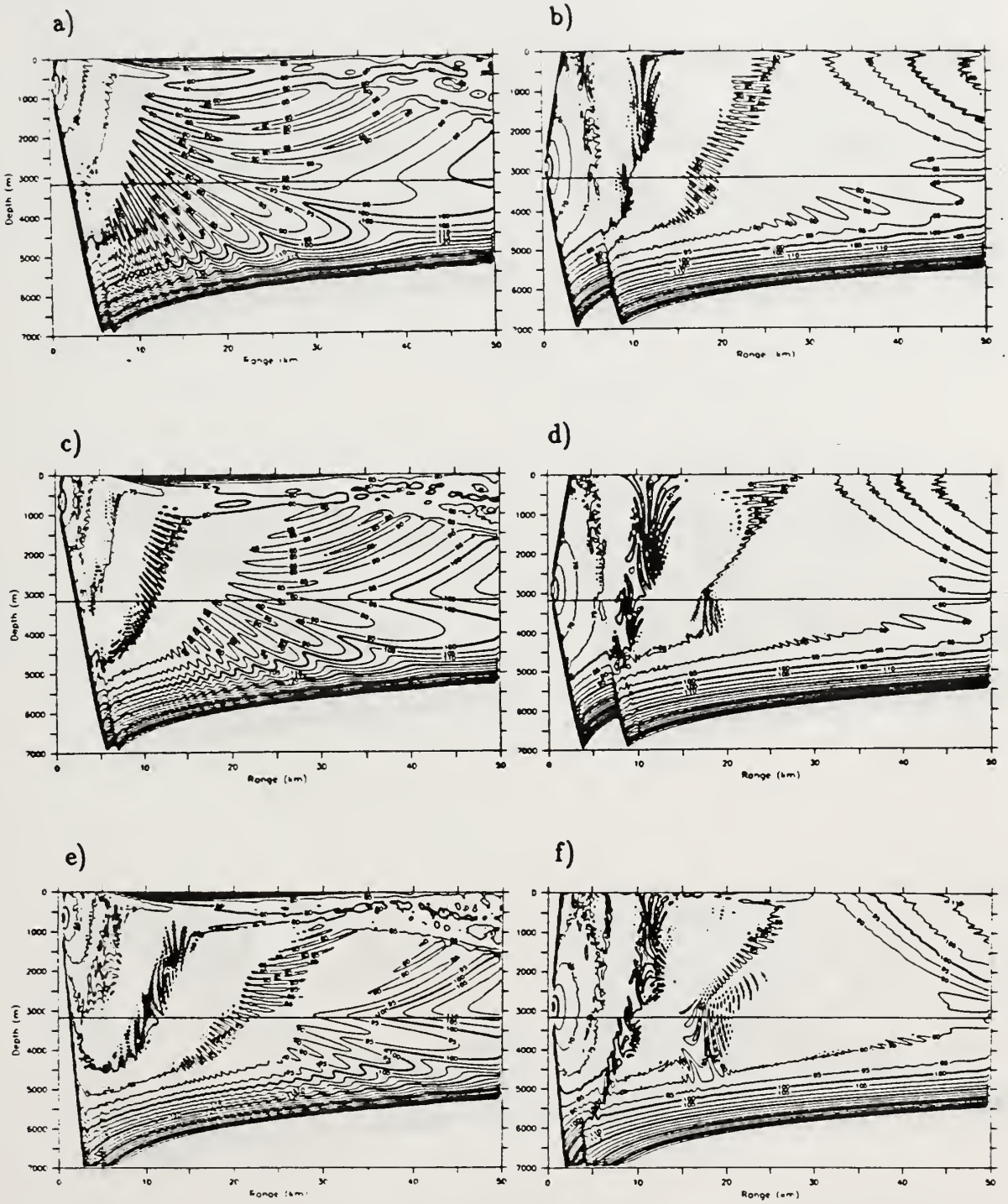

Figure 3.8) Range-independent oceanography, flat bottom Slope water acoustic propagation, first 50 km. a. $z_s = 750$ m, $f = 25$ Hz. b. $z_s = 3000$ m, $f = 25$ Hz. c. $z_s = 750$ m, $f = 50$ Hz. d. $z_s = 3000$ m, $f = 50$ Hz. e. $z_s = 750$ m, $f = 100$ Hz. f. $z_s = 3000$ m, $f = 100$ Hz.

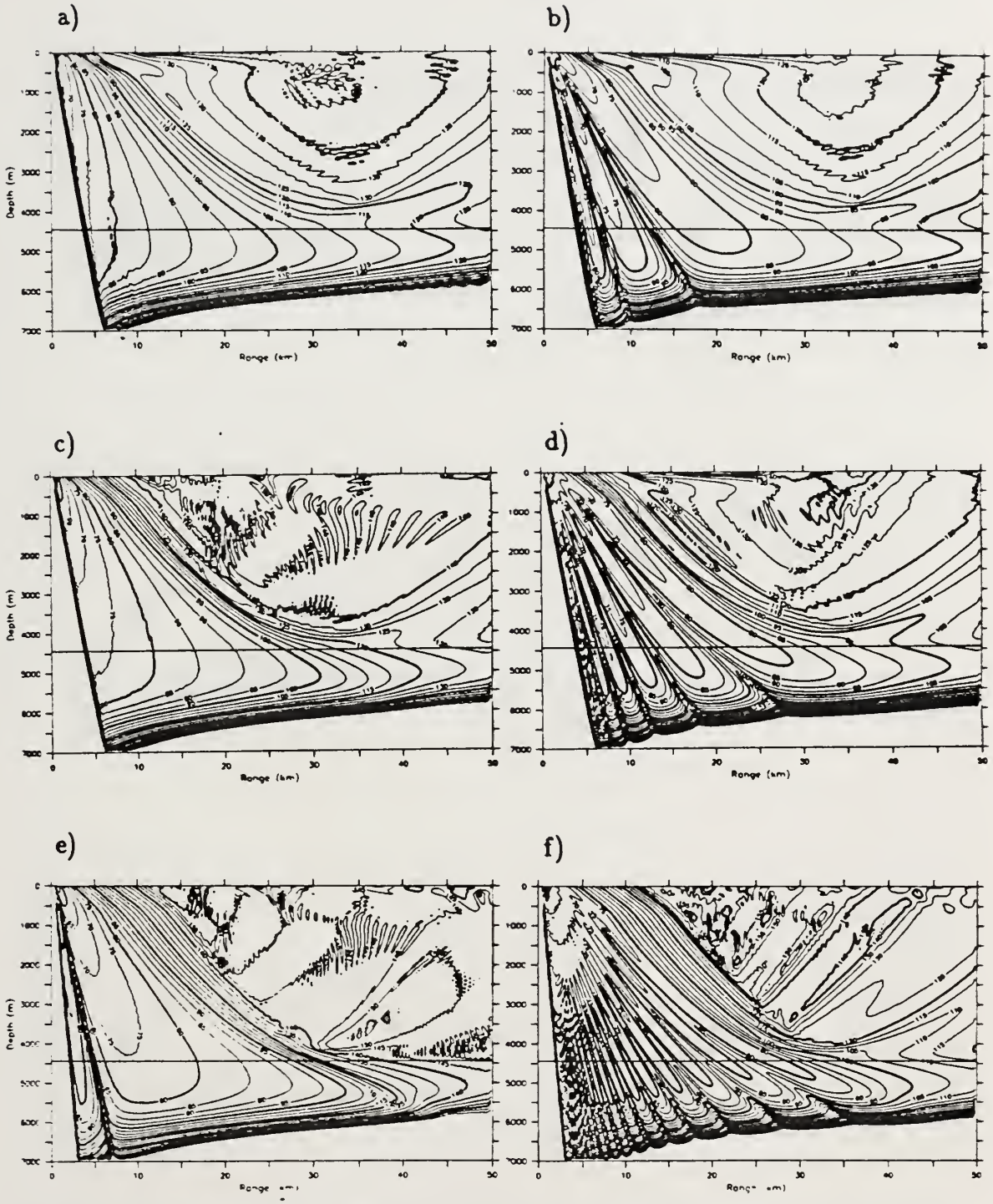

Figure 3.9) Range-independent oceanography, flat bottom Sargasso water acoustic propagation, first 50 km. a. $z_s = 10$ m, $f = 25$ Hz. b. $z_s = 100$ m, $f = 25$ Hz. c. $z_s = 10$ m, $f = 50$ Hz. d. $z_s = 100$ m, $f = 50$ Hz. e. $z_s = 10$ m, $f = 100$ Hz. f. $z_s = 100$ m, $f = 100$ Hz. Note the weak sound trapping near 400 m depth from the secondary sound speed duct.

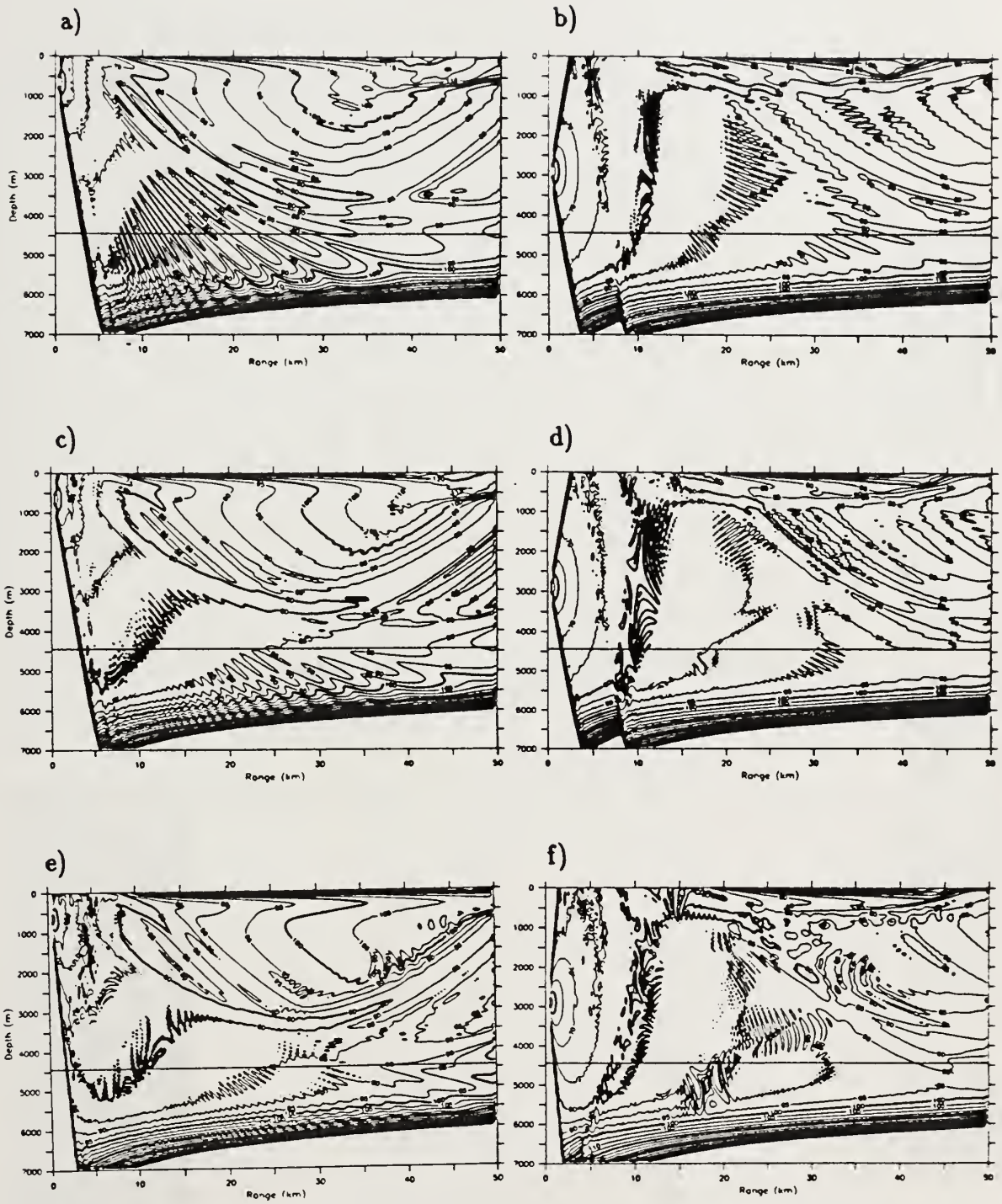

Figure 3.10)Range-independent oceanography, flat bottom Sargasso water acoustic propagation, first 50 km. a. $z_s = 750$ m, $f = 25$ Hz. b. $z_s = 3000$ m, $f = 25$ Hz. c. $z_s = 750$ m, $f = 50$ Hz. d. $z_s = 3000$ m, $f = 50$ Hz. e. $z_s = 750$ m, $f = 100$ Hz. f. $z_s = 3000$ m, $f = 100$ Hz.

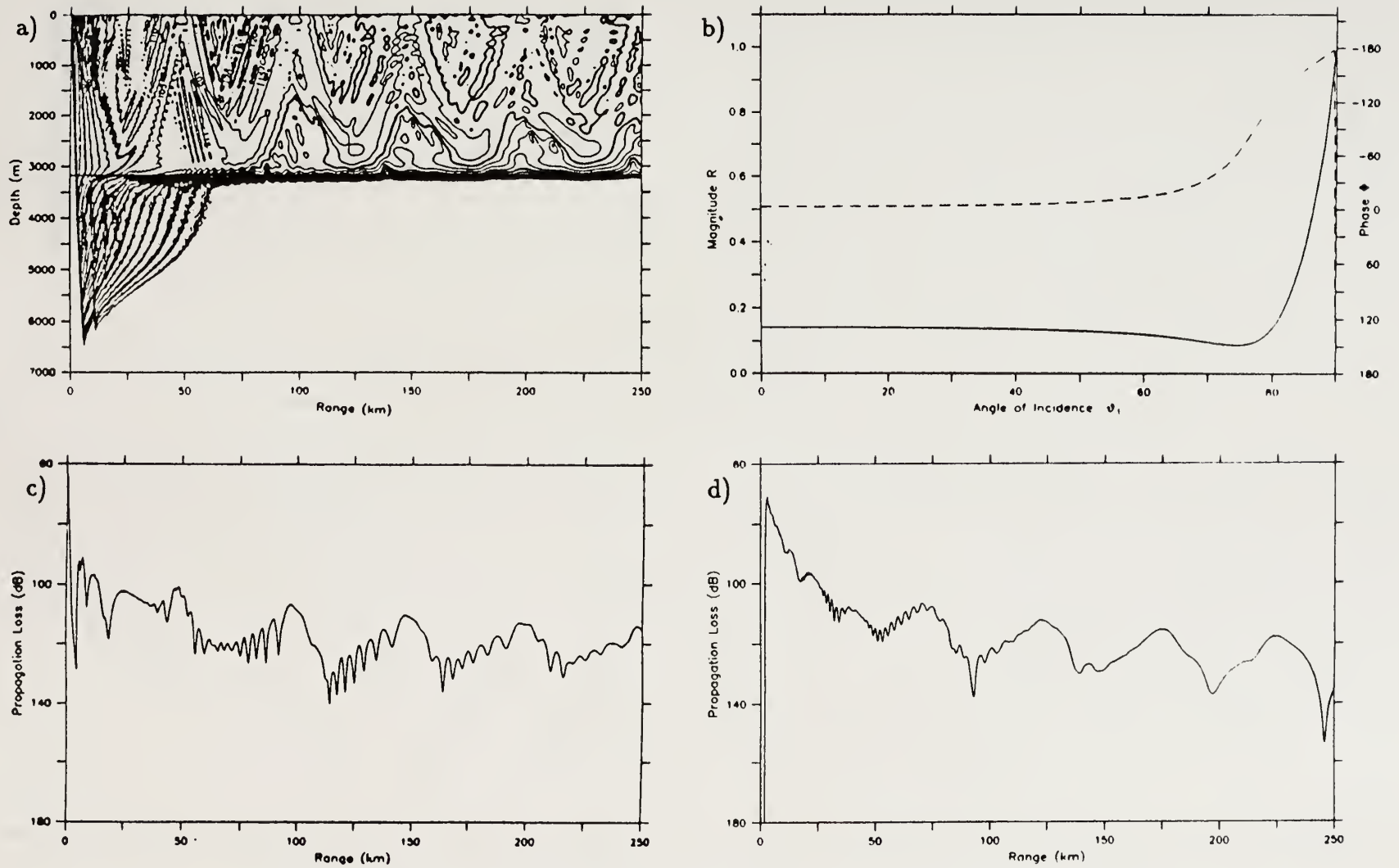

Figure 3.11) Range-independent oceanography, flat bottom Slope water propagation. $z_s = 10$ m, $f = 25$ Hz. "Realistic bottom:" $\rho = 1.352$ gm/cm^3, $\beta = .9$ dB/λ, $c_w/c_b = 1.017$, $\partial c/\partial z = 1.227$ sec^{-1}, $z_{sed} = 100$ m. a. Propagation loss contours. b. R_{12}. c. Propagation loss at 100 m receiver. d. Propagation loss at 3000 m receiver.

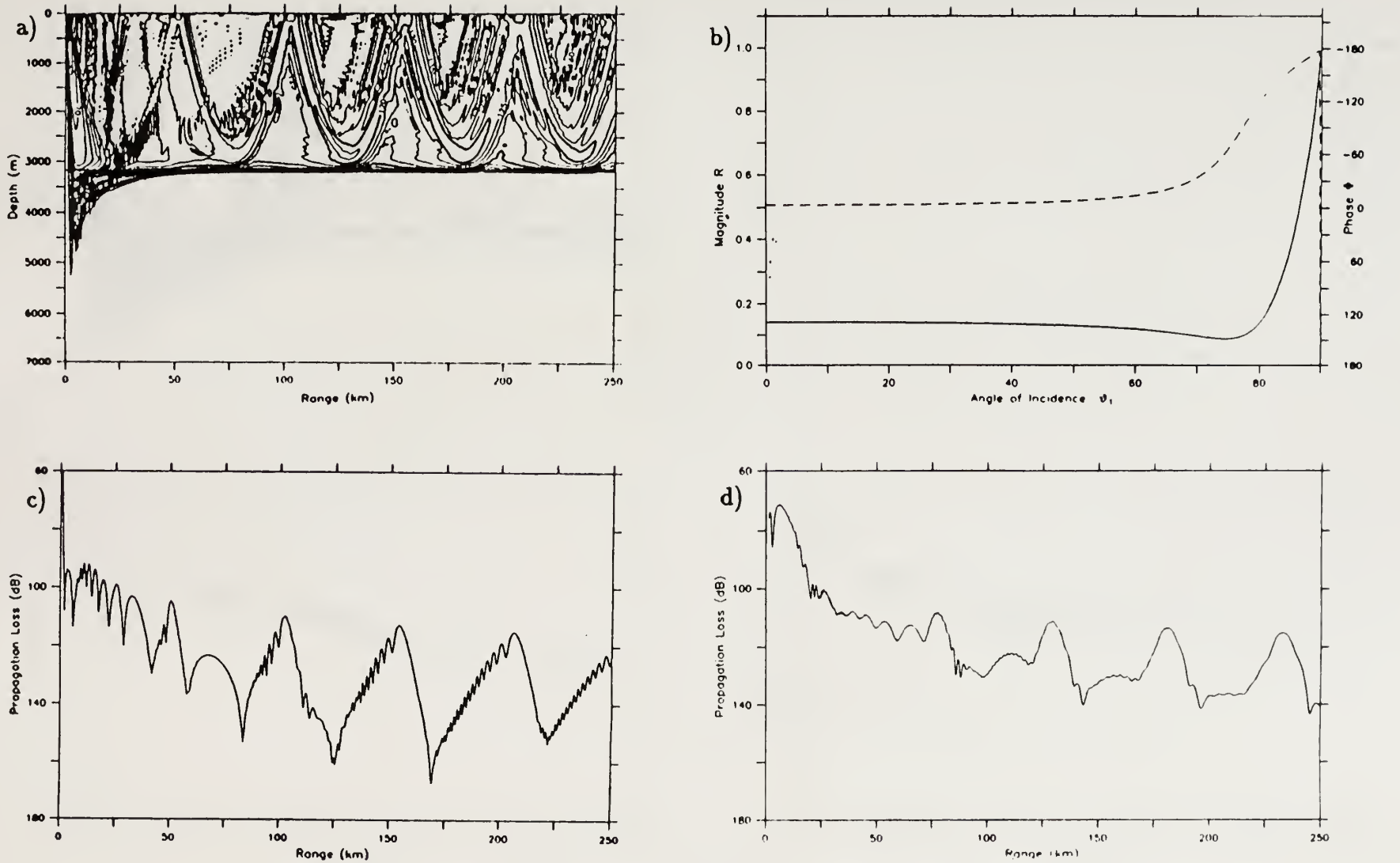

Figure 3.12) Range-independent oceanography, flat bottom Slope water propagation. $z_s = 10$ m, $f = 100$ Hz. Realistic bottom. a. Propagation loss contours. b. R_{12}. c. Propagation loss at 100 m receiver. d. Propagation loss at 3000 m receiver.

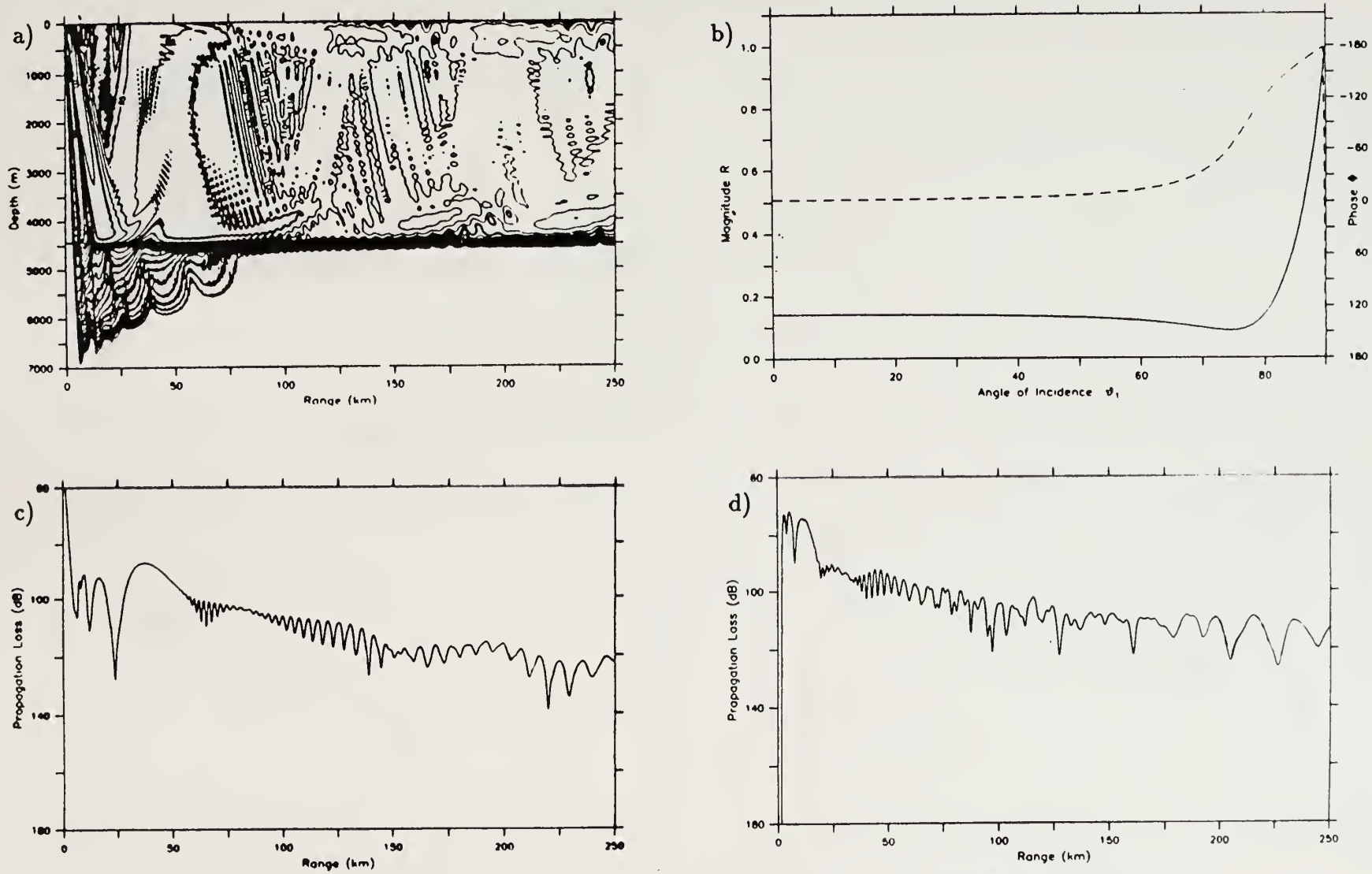

Figure 3.13) Range-independent oceanography, flat bottom Sargasso water propagation. $z_s = 100$ m, $f = 25$ Hz. Realistic bottom. a. Propagation loss contours. b. R_{12}. c. Propagation loss at 100 m receiver. d. Propagation loss at 3000 m receiver.

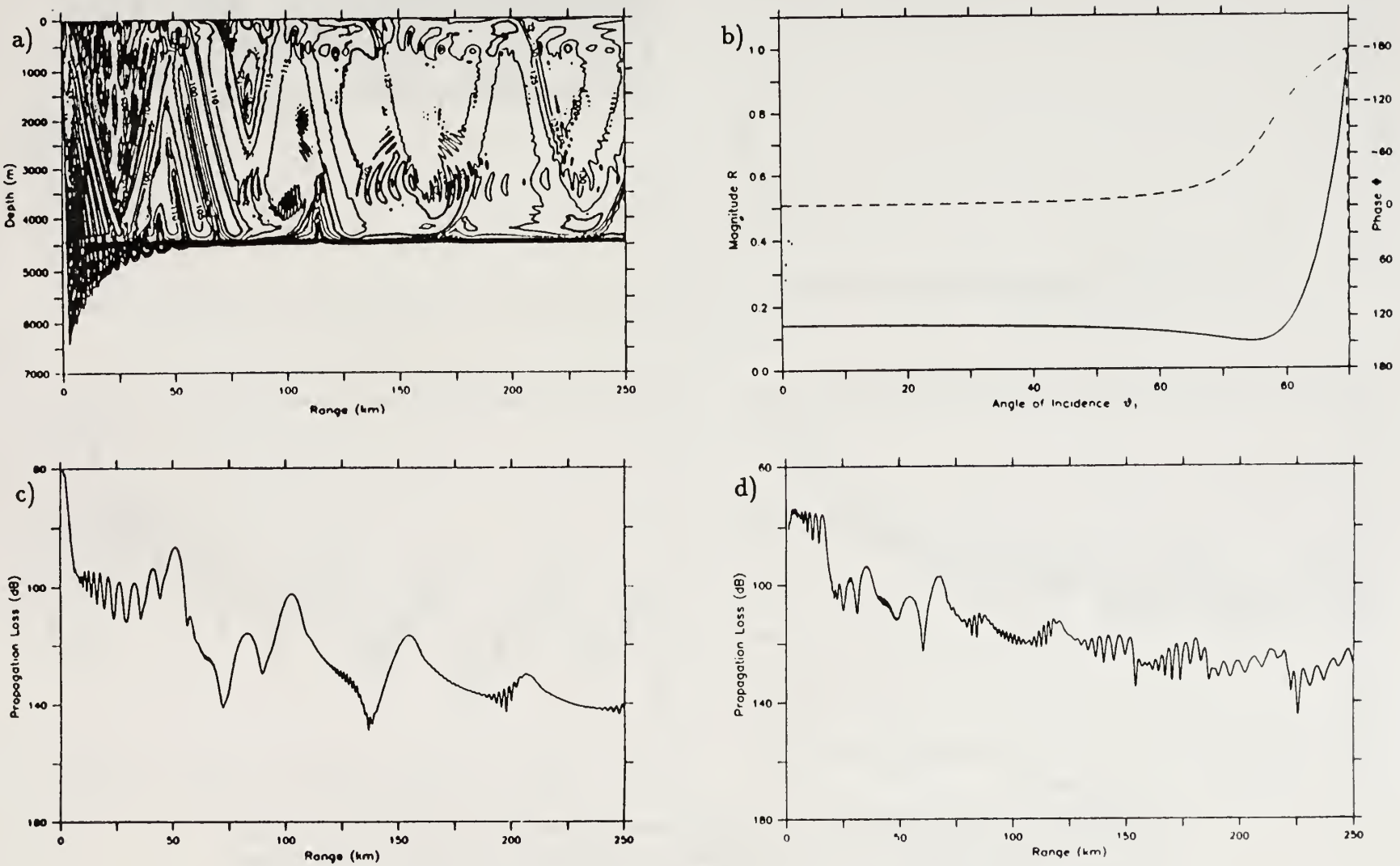

Figure 3.14) Range-independent oceanography, flat bottom Sargasso water propagation. z_s = 100 m, f = 100 Hz. Realistic bottom. a. Propagation loss contours. b. R_{12}. c. Propagation loss at 100 m receiver. d. Propagation loss at 3000 m receiver.

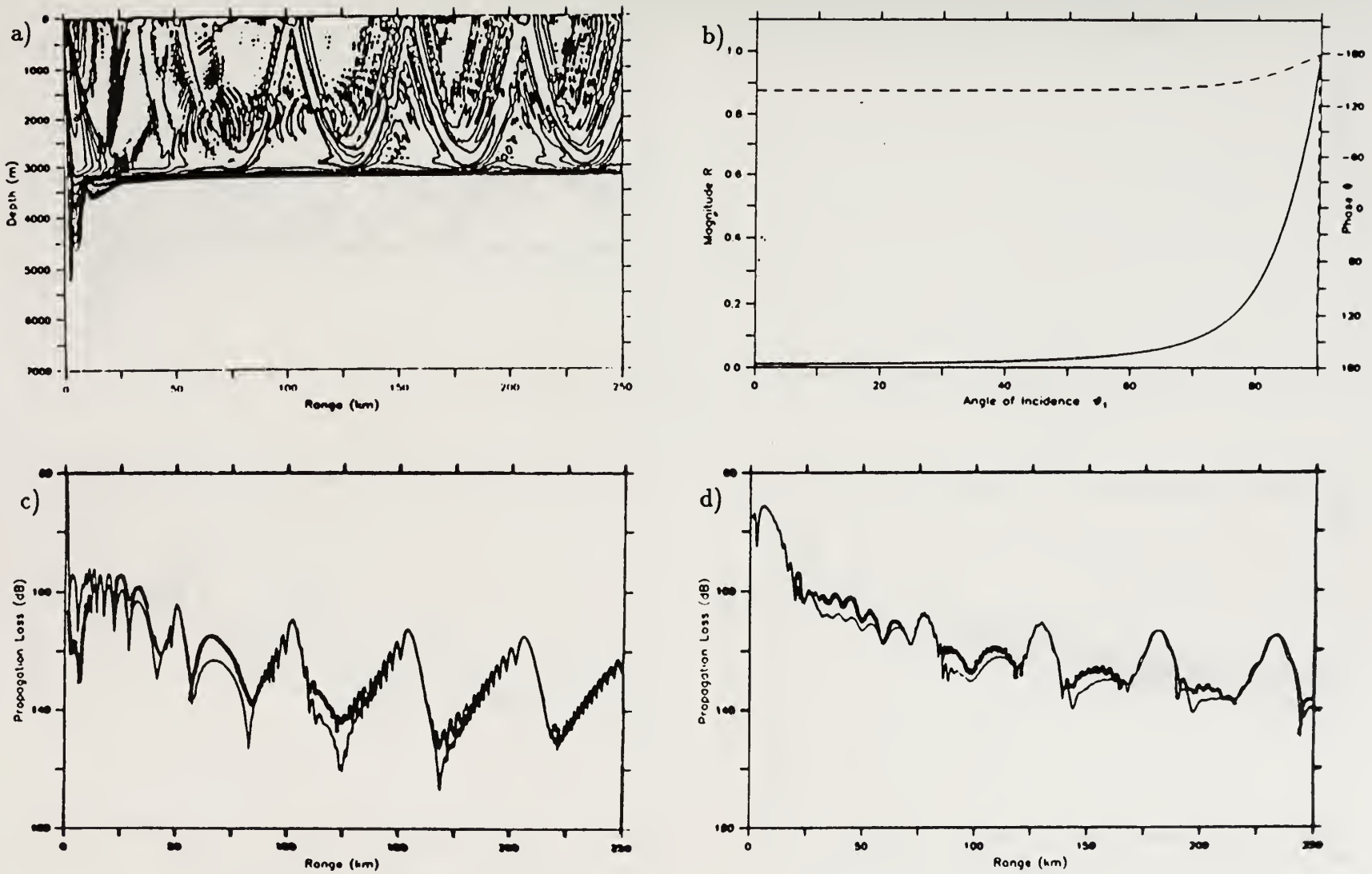

Figure 3.15) Range-independent oceanography, flat bottom Slope water propagation. $z_s = 10$ m, $f = 100$ Hz. $\rho = 1.0$ gm/cm^3, $\beta = .9$ dB/λ, $c_w/c_b = 1.017$, $\partial c/\partial z = 1.227$ sec^{-1}, $z_{sed} = 100$ m. Receiver plots overlaid with corresponding receivers from figure 3.11, present case bold. a. Propagation loss contours. b. R_{12}. c. Propagation loss at 100 m receivers. d. Propagation loss at 3000 m receivers.

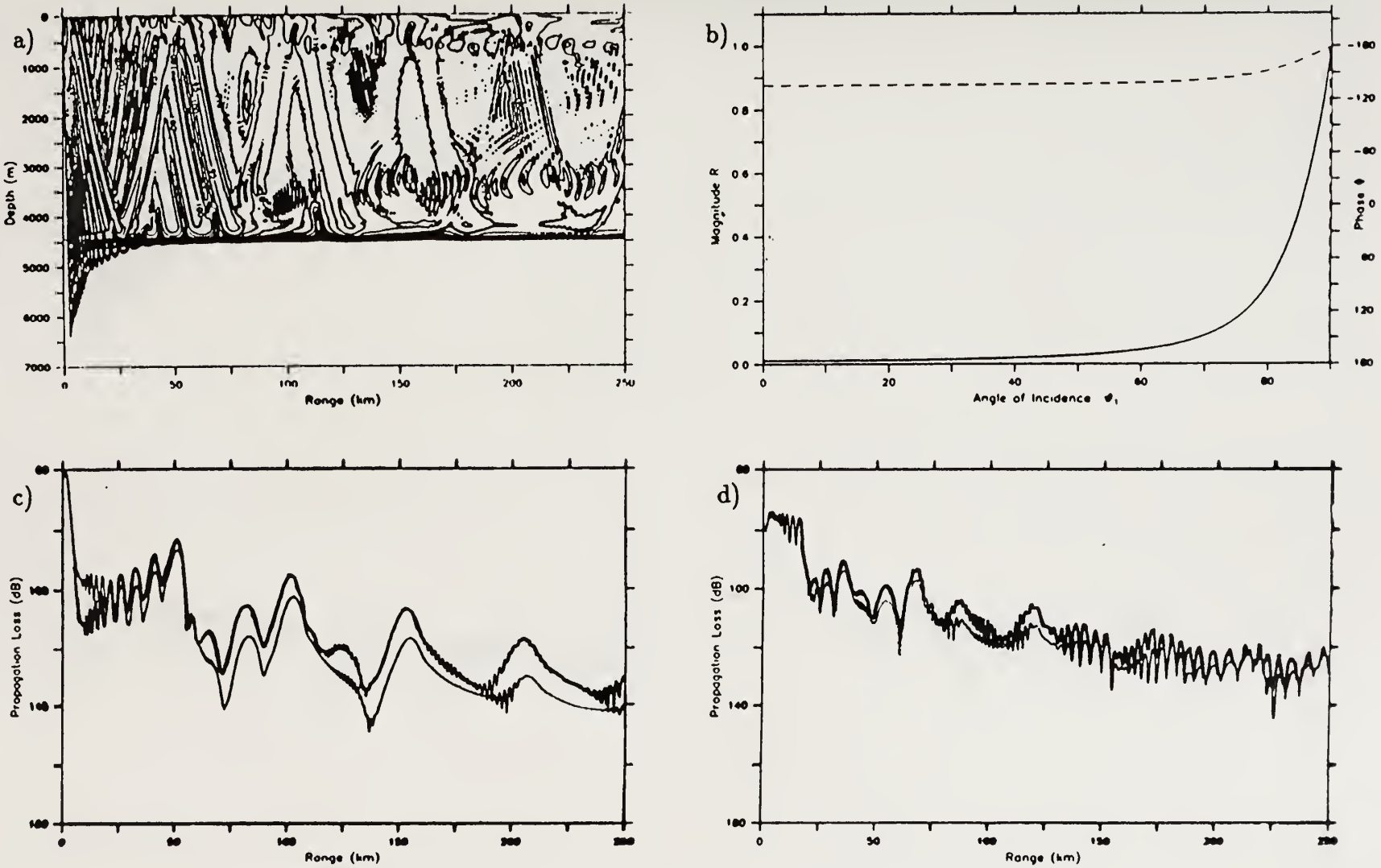

Figure 3.16) Range-independent oceanography, flat bottom Sargasso water propagation. $z_s = 100$ m, $f = 100$ Hz. $\rho = 1.0$ gm/cm^3, $\beta = .9$ dB/λ, $c_w/c_b = 1.017$, $\partial c/\partial z = 1.227$ sec^{-1}, $z_{sed} = 100$ m. Receiver plots overlaid with corresponding receivers from figure 3.13, present case bold. a. Propagation loss contours. b. R_{12}. c. Propagation loss at 100 m receivers. d. Propagation loss at 3000 m receivers.

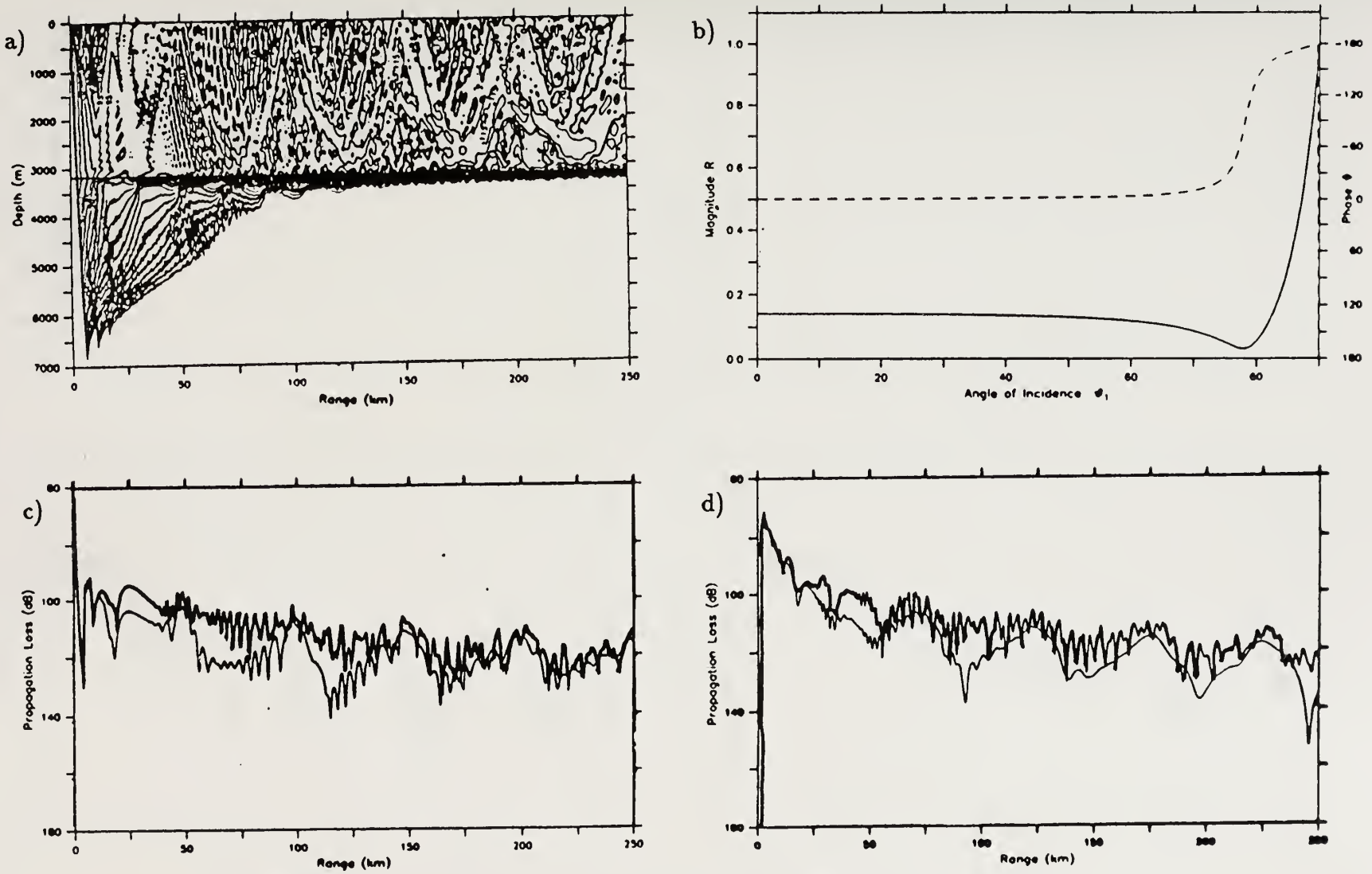

Figure 3.17) Range-independent oceanography, flat bottom Slope water propagation. $z_s = 10$ m, $f = 25$ Hz. $\rho = 1.352$ gm/cm^3, $\beta = .25$ dB/λ, $c_w/c_b = 1.017$, $\partial c/\partial z = 1.227$ sec^{-1}, $z_{sed} = 100$ m. Receiver plots overlaid with corresponding receivers from figure 3.10, present case bold. a. Propagation loss contours. b. R_{12}. c. Propagation loss at 100 m receivers. d. Propagation loss at 3000 m receivers.

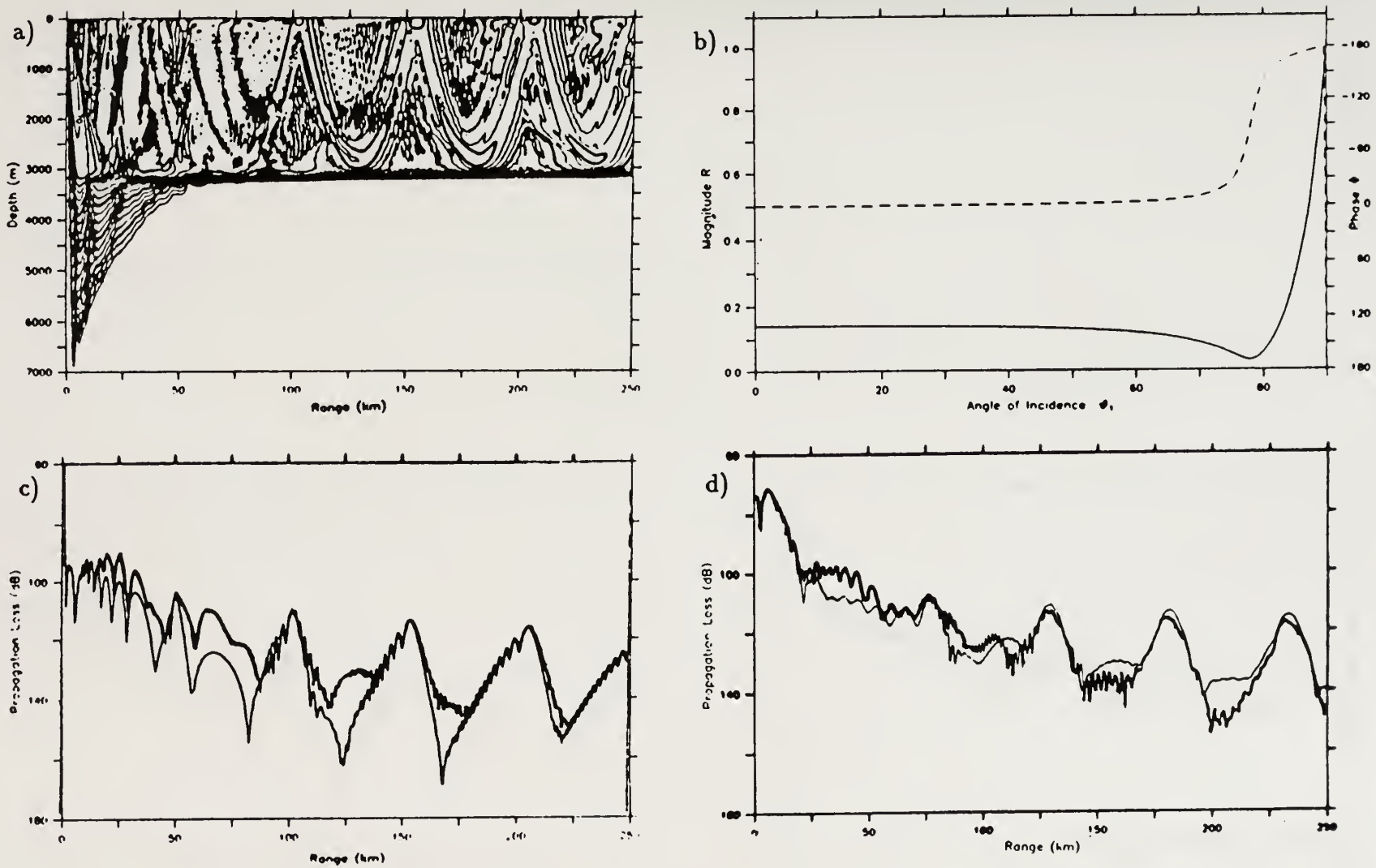

Figure 3.18) Range-independent oceanography, flat bottom Slope water propagation. $z_s = 10$ m, $f = 100$ Hz. $\rho = 1.352$ gm/cm^3, $\beta = .25$ dB/λ, $c_w/c_b = 1.017$, $\partial c/\partial z = 1.227$ sec^{-1}, $z_{sed} = 100$ m. Receiver plots overlaid with corresponding receivers from figure 3.11, present case bold. a. Propagation loss contours. b. R_{12}. c. Propagation loss at 100 m receivers. d. Propagation loss at 3000 m receivers.

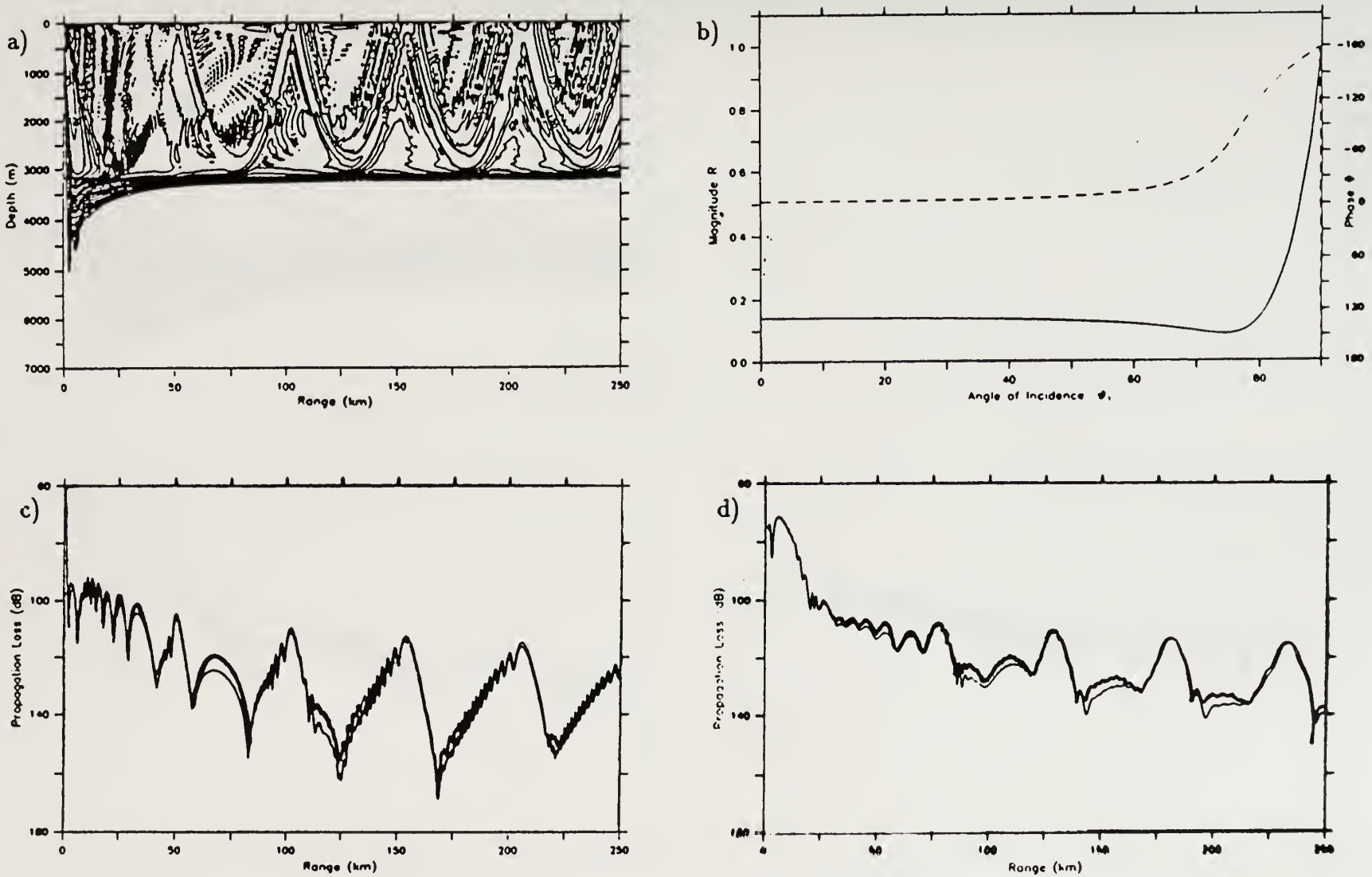

Figure 3.19) Range-independent oceanography, flat bottom Slope water propagation. $z_s = 10$ m, $f = 100$ Hz. $\rho = 1.352$ gm/cm^3, $\beta = .9$ dB/λ, $c_w/c_b = 1.017$, $\partial c/\partial z = 0.0$ sec^{-1}, $z_{sed} = 100$ m. Receiver plots overlaid with corresponding receivers from figure 3.11, present case bold. a. Propagation loss contours. b. R_{12}. c. Propagation loss at 100 m receivers. d. Propagation loss at 3000 m receivers.

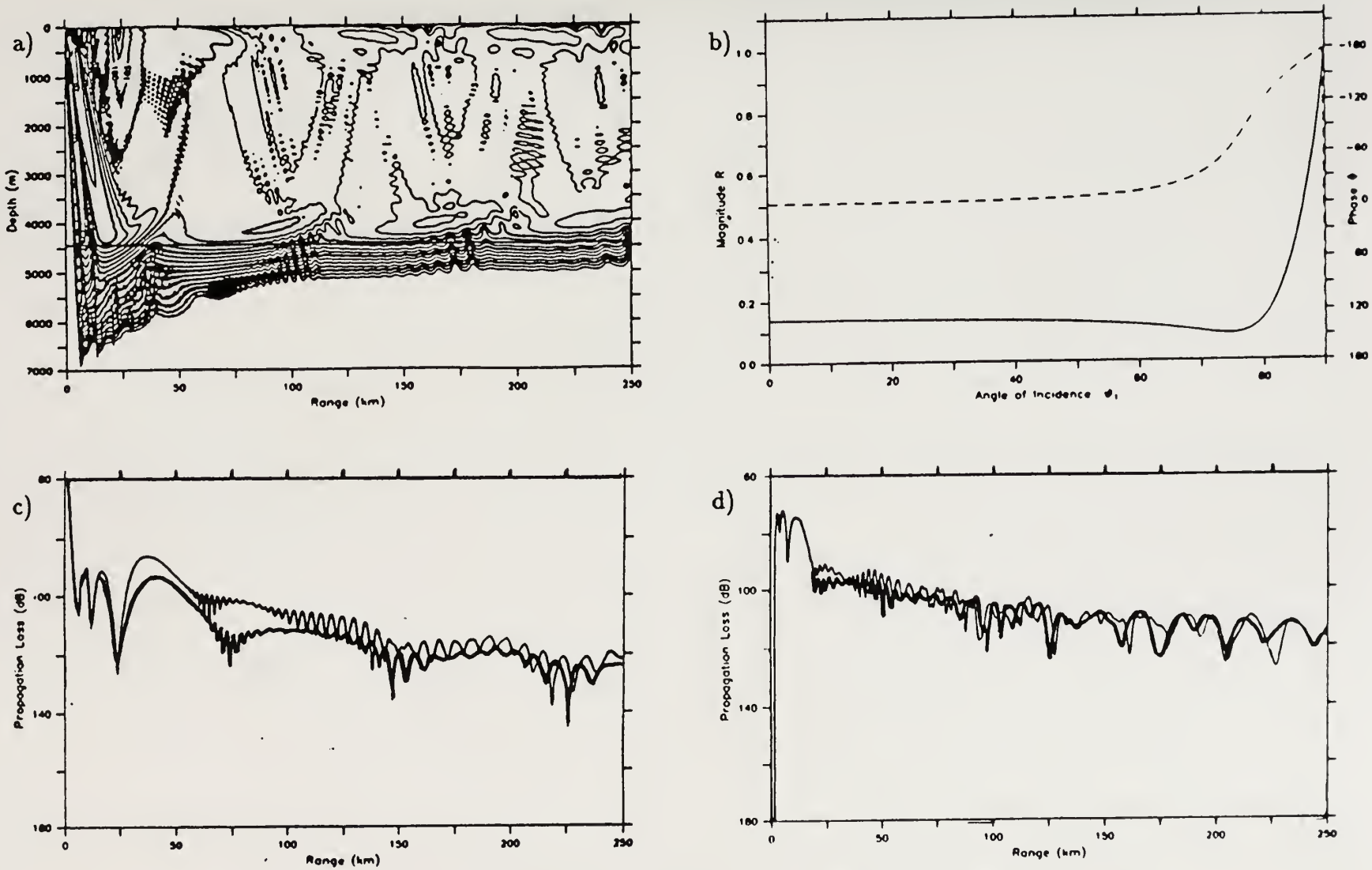

Figure 3.20) Range-independent oceanography, flat bottom Sargasso water propagation. $z_s = 100$ m, $f = 25$ Hz. $\rho = 1.352$ gm/cm^3, $\beta = .9$ dB/λ, $c_w/c_b = 1.017$, $\partial c/\partial z = 0.0$ sec^{-1}, $z_{sed} = 100$ m. Receiver plots overlaid with corresponding receivers from figure 3.12, present case bold. a. Propagation loss contours. b. R_{12}. c. Propagation loss at 100 m receivers. d. Propagation loss at 3000 m receivers.

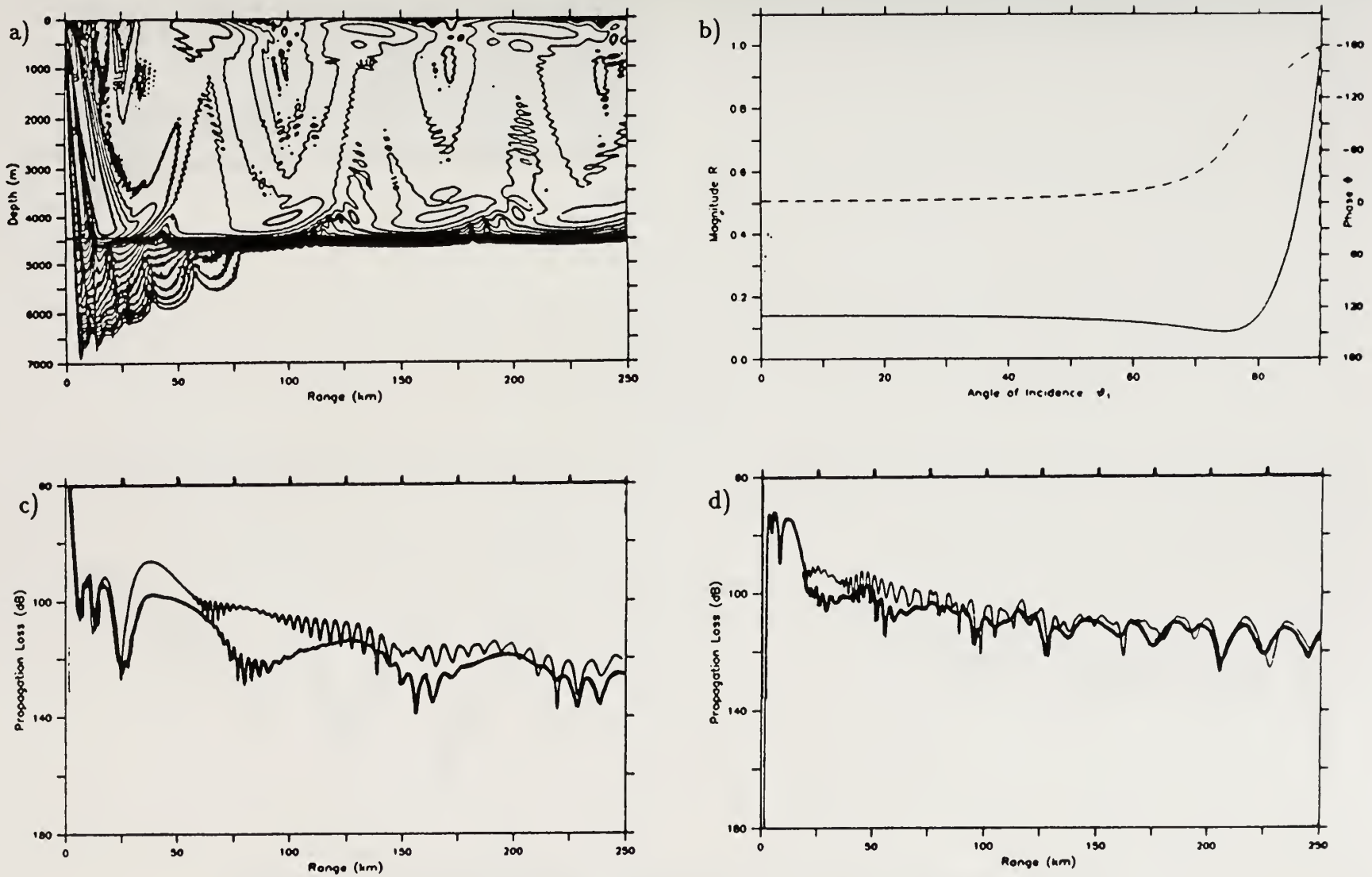

Figure 3.21) Range-independent oceanography, flat bottom Sargasso water propagation. $z_s = 100$ m, $f = 25$ Hz. $\rho = 1.352$ gm/cm^3, $\beta = .9$ dB/λ, $c_w/c_b = 1.017$, $\partial c/\partial z = 0.75$ sec^{-1}, $z_{sed} = 100$ m. Receiver plots overlaid with corresponding receivers from figure 3.12, present case bold. a. Propagation loss contours. b. R_{12}. c. Propagation loss at 100 m receivers. d. Propagation loss at 3000 m

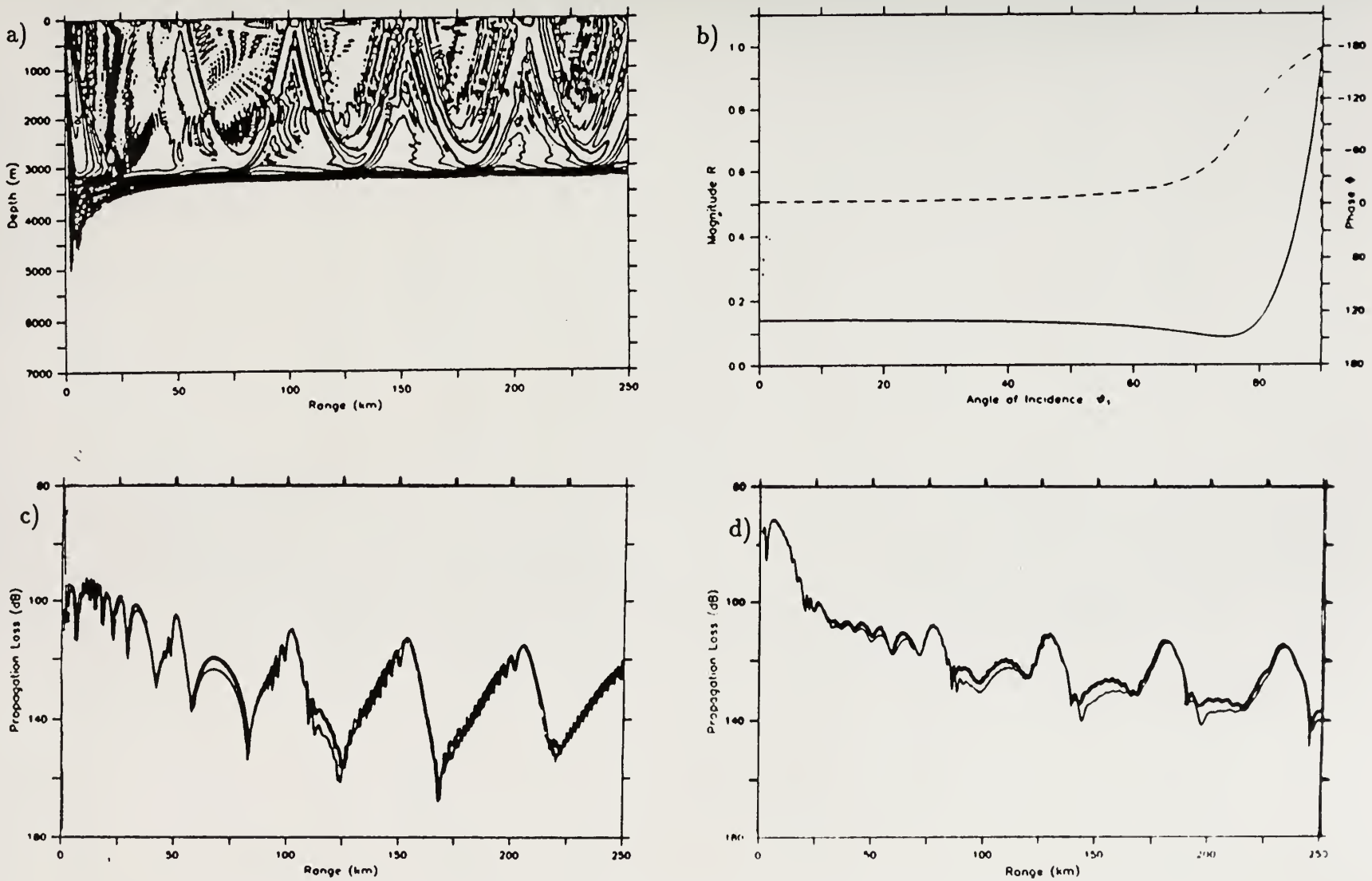

Figure 3.22) Range-independent oceanography, flat bottom Slope water propagation. $z_s = 10$ m, $f = 100$ Hz. $\rho = 1.352$ gm/cm^3, $\beta = .9$ dB/λ, $c_w/c_b = 1.017$, $\partial c/\partial z = 1.227$ sec^{-1}, $z_{sed} = 0$ m. Receiver plots overlaid with corresponding receivers from figure 3.11, present case bold. a. Propagation loss contours. b. R_{12}. c. Propagation loss at 100 m receivers. d. Propagation loss at 3000 m receivers.

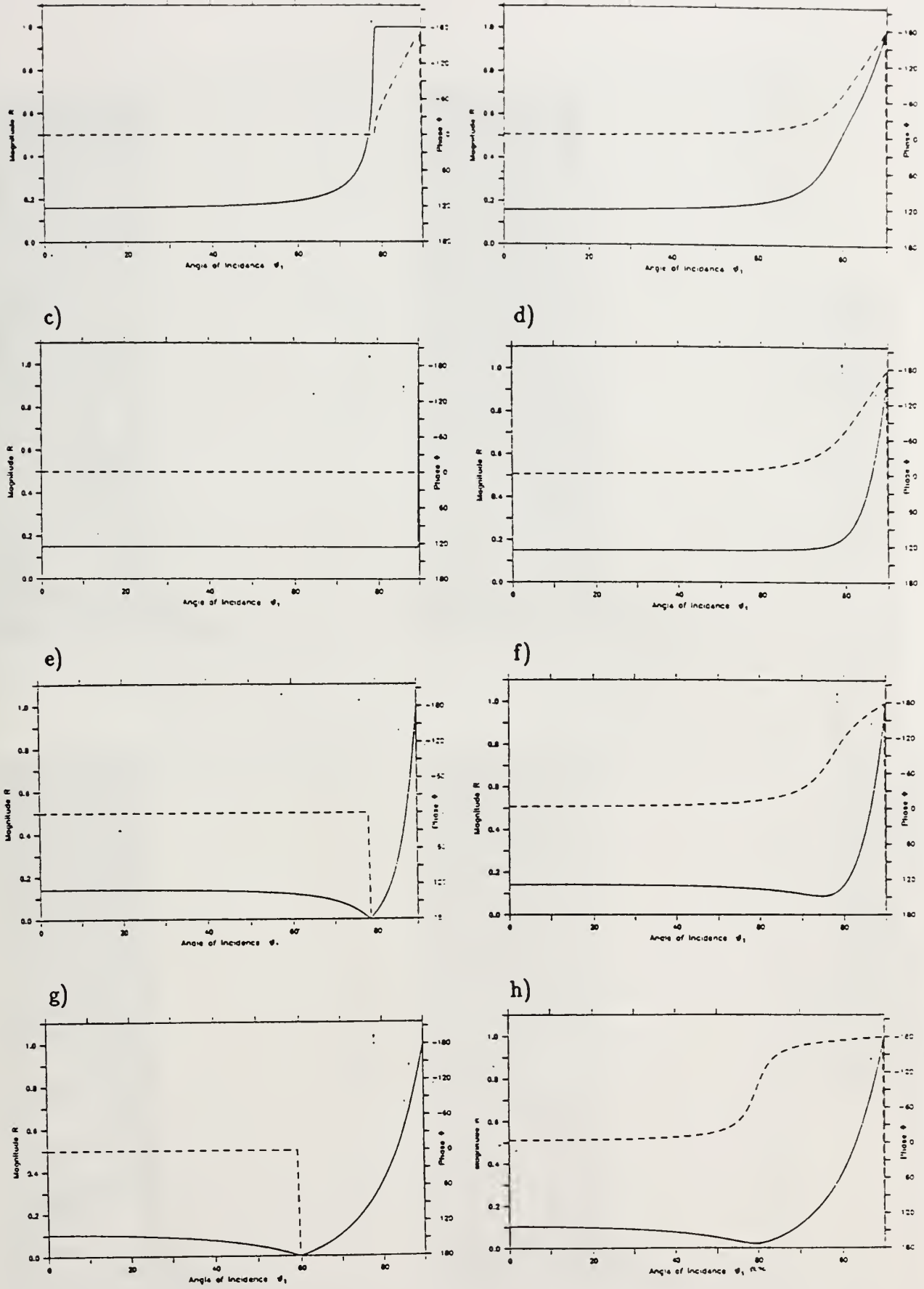

Figure 3.23) Rayleigh reflection coefficient R_{12}. a. $\rho = 1.352$ gm/cm^3, $\beta = 0$ dB/λ, $c_w/c_b = .98$. b. $\rho = 1.352$ gm/cm^3, $\beta = 0.9$ dB/λ, $c_w/c_b = .98$. c. $\rho = 1.352$ gm/cm^3, $\beta = 0$ dB/λ, $c_w/c_b = 1.000$. d. $\rho = 1.352$ gm/cm^3, $\beta = 0.9$ dB/λ, $c_w/c_b = 1.000$. e. $\rho = 1.352$ gm/cm^3, $\beta = 0$ dB/λ, $c_w/c_b = 1.017$. f. $\rho = 1.352$ gm/cm^3, $\beta = 0.9$ dB/λ, $c_w/c_b = 1.017$. g. $\rho = 1.352$ gm/cm^3, $\beta = 0$ dB/λ, $c_w/c_b = 1.1$. h. $\rho = 1.352$ gm/cm^3, $\beta = 0.9$ dB/λ, $c_w/c_b = 1.1$.

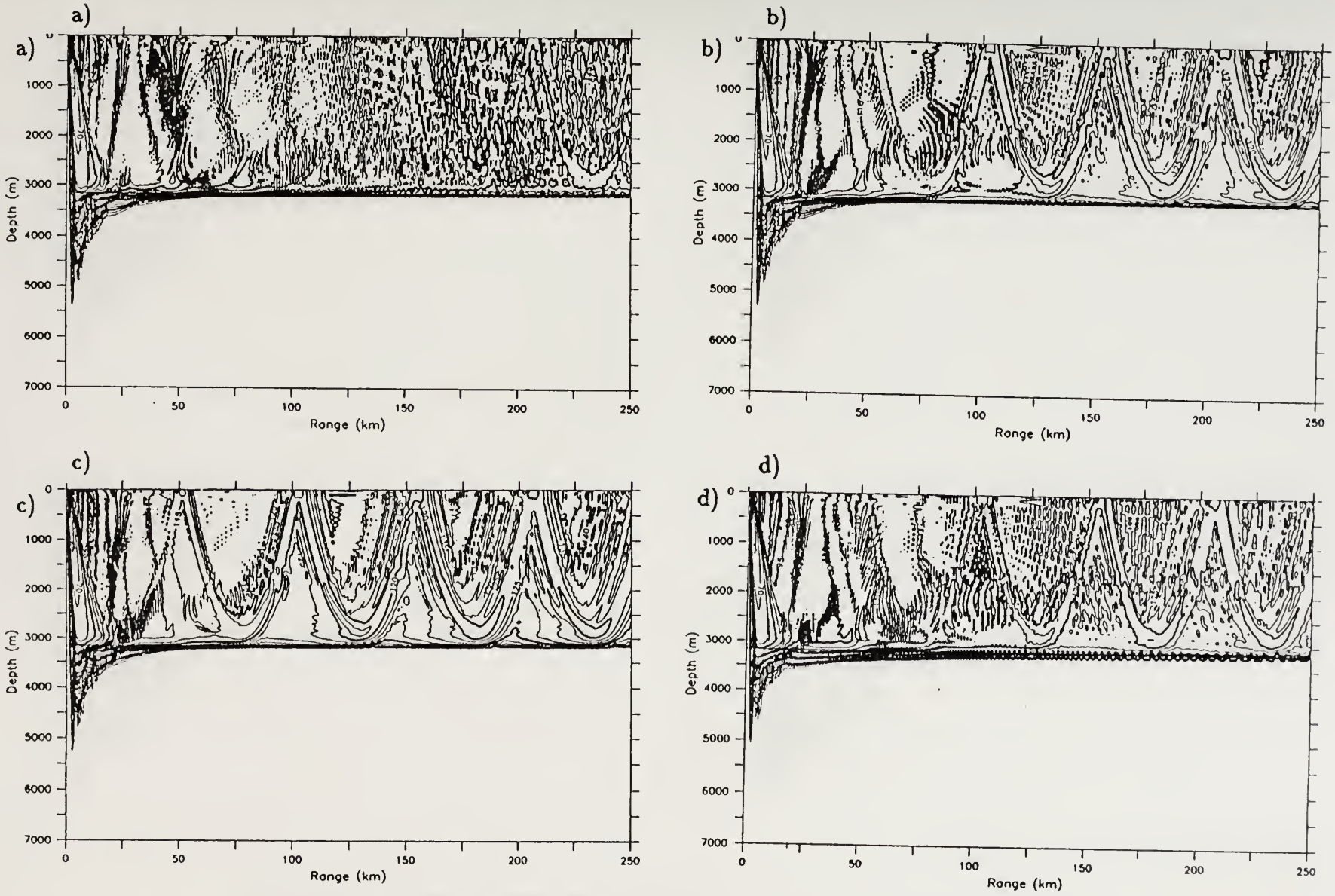

Figure 3.24) Range-independent oceanography, flat bottom Slope water propagation. Propagation loss contours. $z_s = 10$ m, $f = 100$ Hz. $\rho = 1.352$ gm/cm^3, $\beta = .9$ dB/λ, $\partial c/\partial z = 1.227$ sec^{-1}, $z_{sed} = 100$ m. a. $c_w/c_b = .98$. b. $c_w/c_b = 1.0$. c. $c_w/c_b = 1.017$. d. $c_w/c_b = 1.1$.

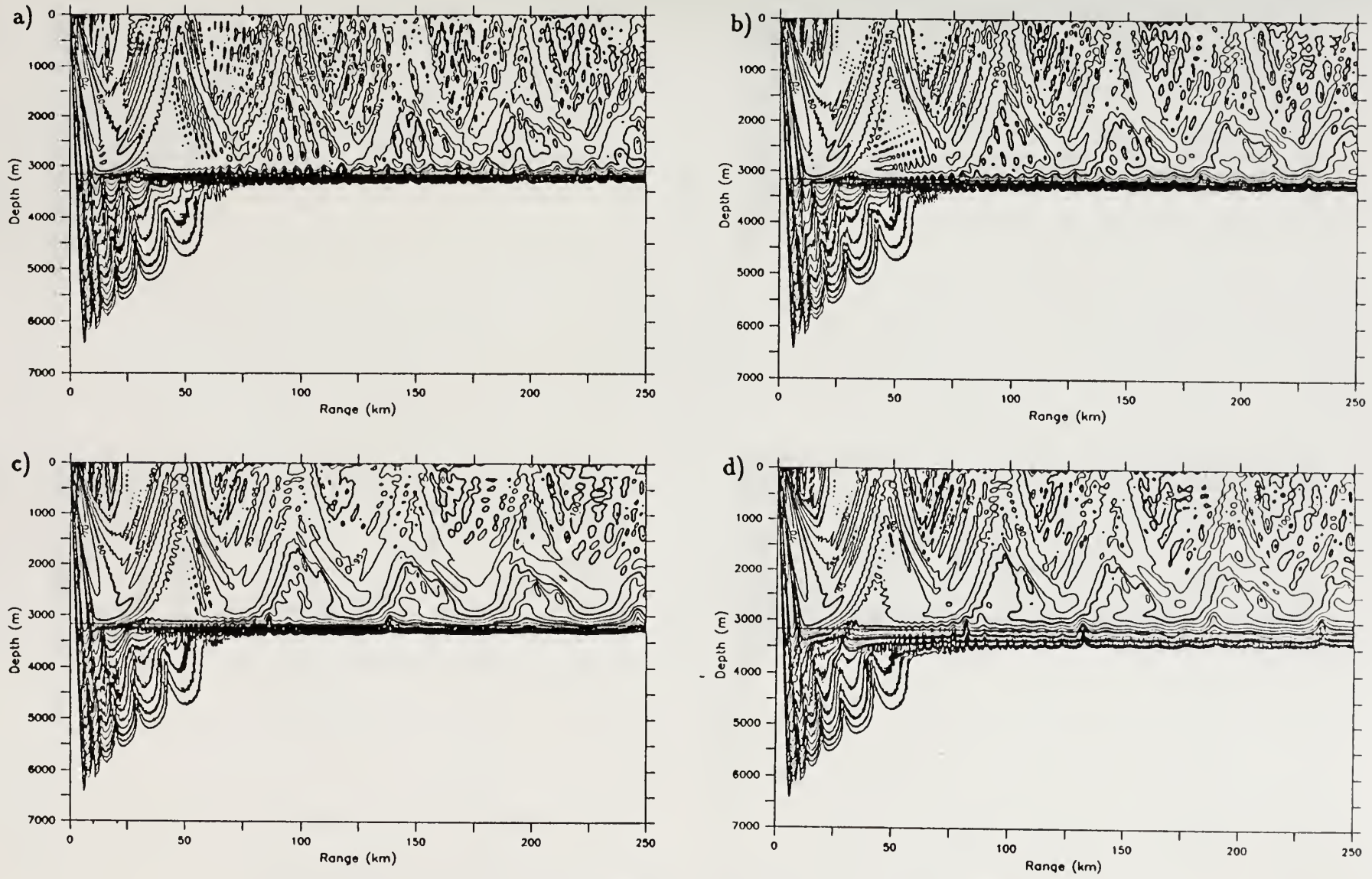

Figure 3.25) Range-independent oceanography, flat bottom Slope water propagation. Propagation loss contours. $z_s = 100$ m, $f = 25$ Hz. $\rho = 1.352$ gm/cm^3, $\beta = .9$ dB/λ, $\partial c/\partial z = 1.227$ sec^{-1}, $z_{sed} = 100$ m. a. $c_w/c_b = .98$. b. $c_w/c_b = 1.0$. c. $c_w/c_b = 1.017$. d. $c_w/c_b = 1.1$.

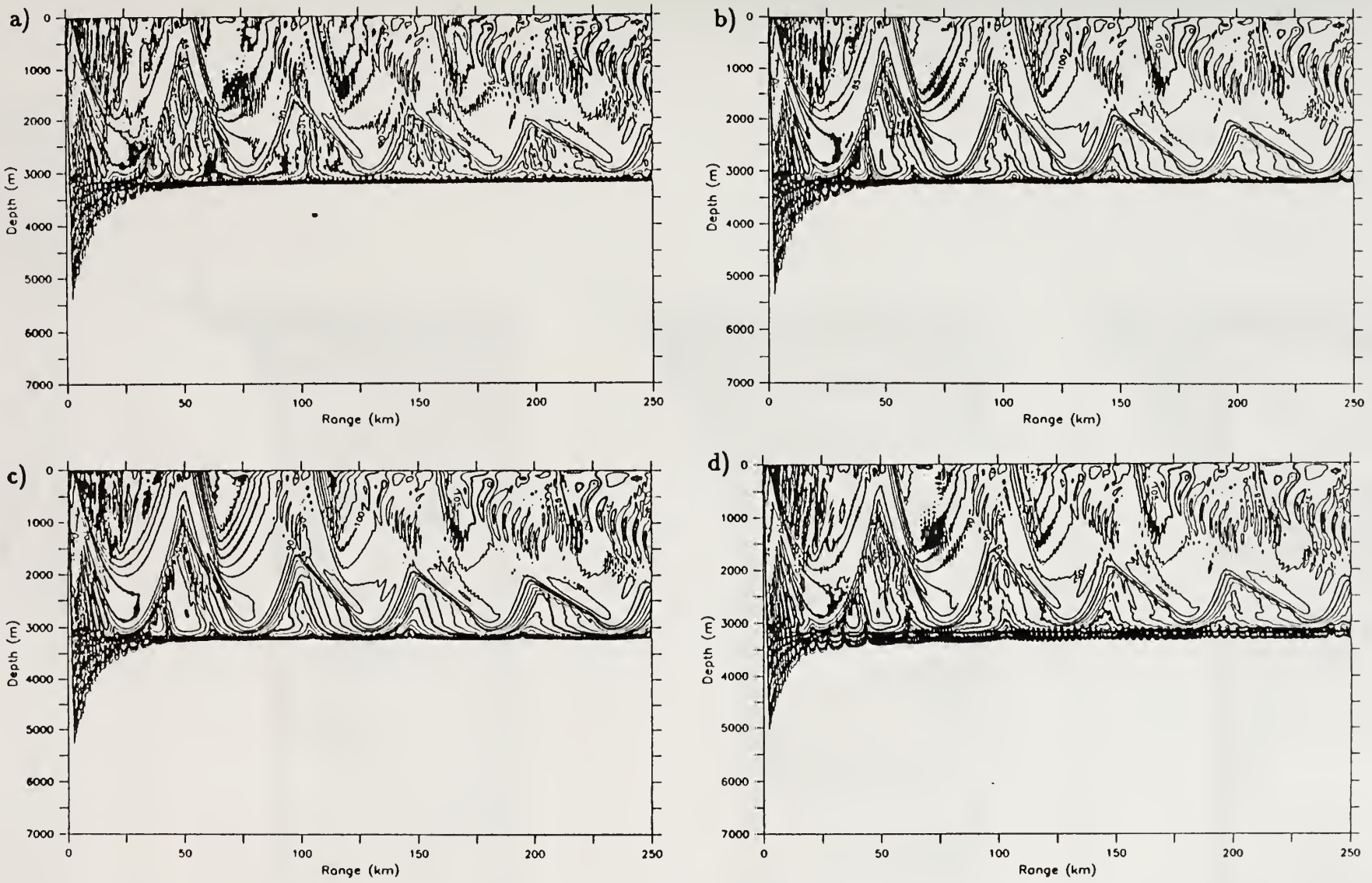

Figure 3.26) Range-independent oceanography, flat bottom Slope water propagation. Propagation loss contours. $z_s = 100$ m, $f = 100$ Hz. $\rho = 1.352$ gm/cm^3, $\beta = .9$ dB/λ, $\partial c/\partial z = 1.227$ sec^{-1}, $z_{sed} = 100$ m. a. $c_w/c_b = .98$. b. $c_w/c_b = 1.0$. c. $c_w/c_b = 1.017$. d. $c_w/c_b = 1.1$.

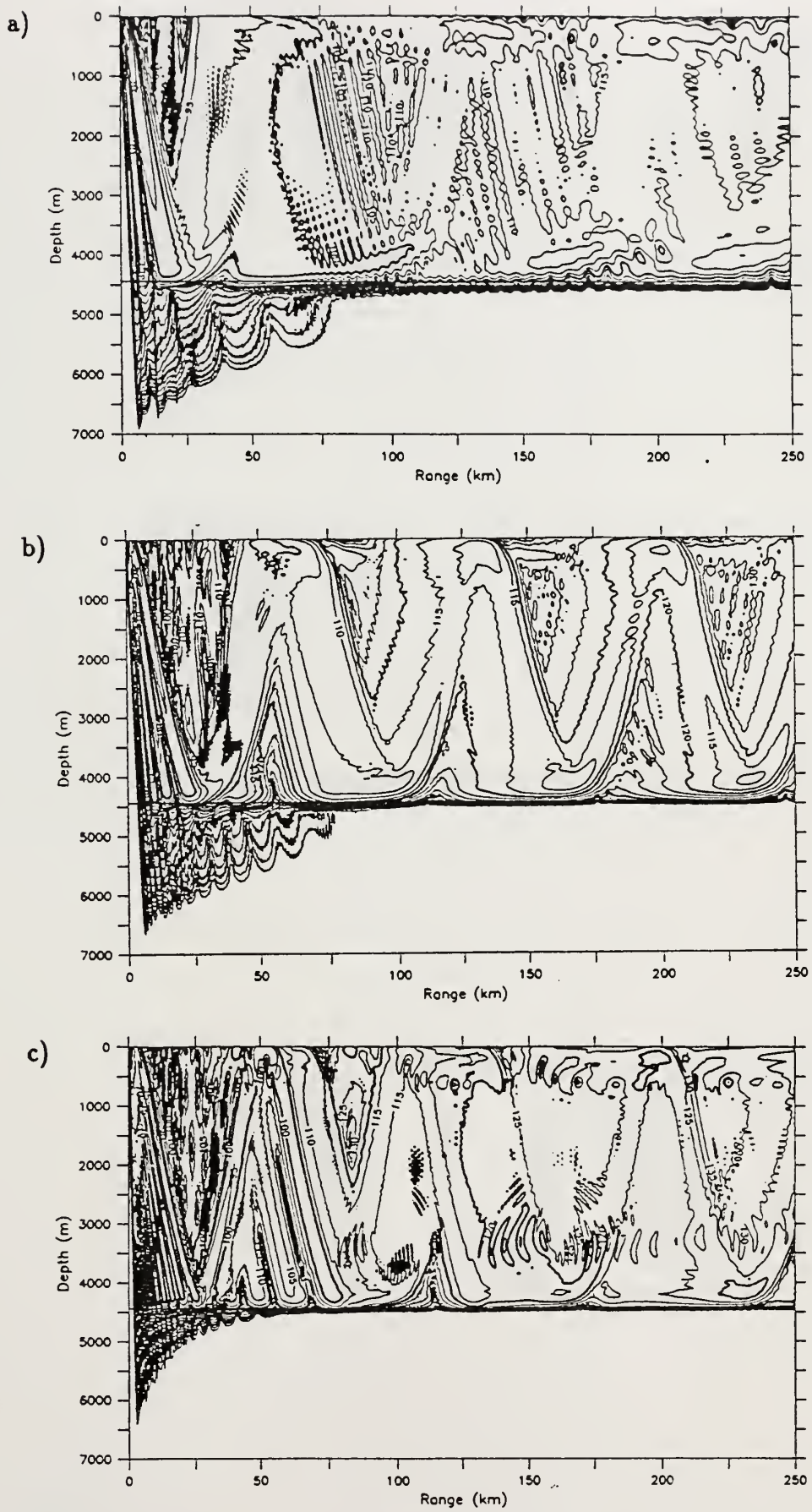

Figure 3.27) Range-independent oceanography, flat bottom Sargasso water propagation. Propagation loss contours. $z_s = 100$ m, $\rho = 1.352$ gm/cm^3, $\beta = .9$ dB/λ, $c_w/c_b = 1.017$, $\partial c/\partial z = 1.227$ sec^{-1}, $z_{sed} = 100$ m. a. $f = 25$ Hz. b. $f = 50$ Hz. c. $f = 100$ Hz.

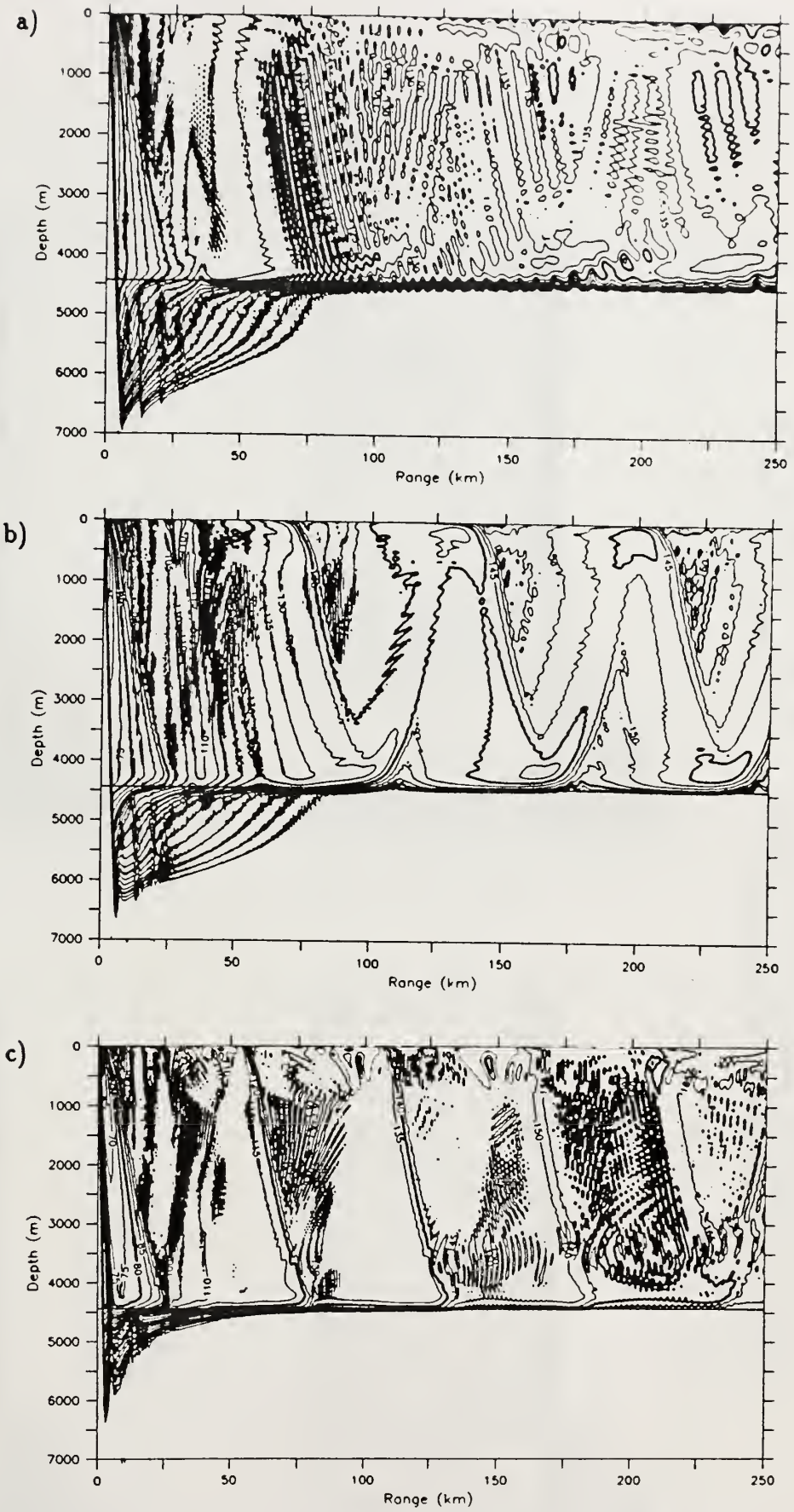

Figure 3.28) Range-independent oceanography, flat bottom Sargasso water propagation. Propagation loss contours. $z_s = 10$ m, $\rho = 1.352$ gm/cm^3, $\beta = .9$ dB/λ, $c_w/c_b = 1.017$, $\partial c/\partial z = 1.227$ sec^{-1}, $z_{sed} = 100$ m. a. $f = 25$ Hz. b. $f = 50$ Hz. c. $f = 100$ Hz.

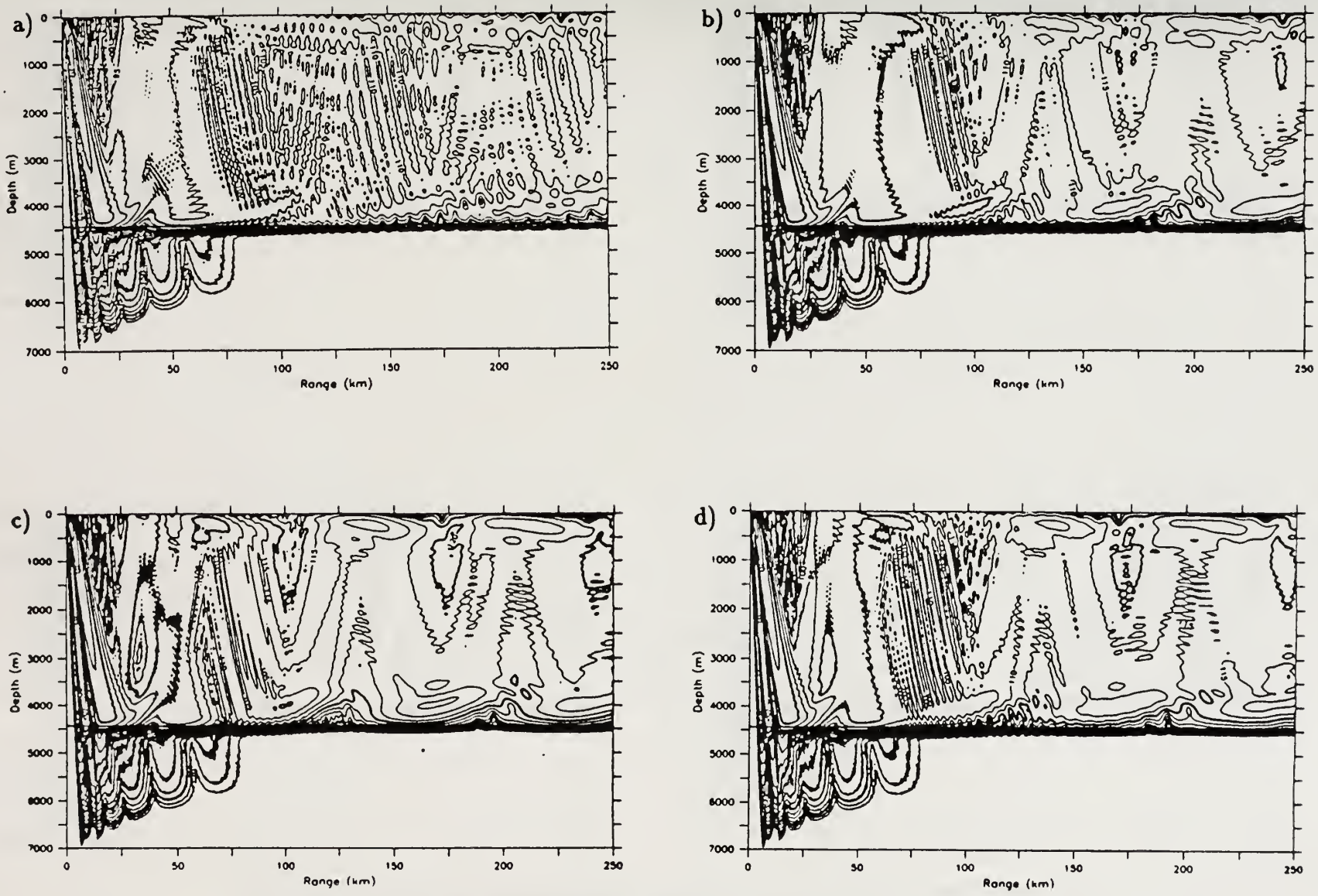

Figure 3.29) Range-independent oceanography, flat bottom Sargasso water propagation. Propagation loss contours. $z_s = 100$ m, $f = 25$ Hz, $\rho = 1.352$ gm/cm^3, $\beta = .9$ dB/λ, $\partial c/\partial z = 1.227$ sec^{-1}, $z_{sed} = 100$ m. a. $c_w/c_b = 1.01$. b. $c_w/c_b = 1.02$. c. $c_w/c_b = 1.03$. d. $c_w/c_b = 1.04$.

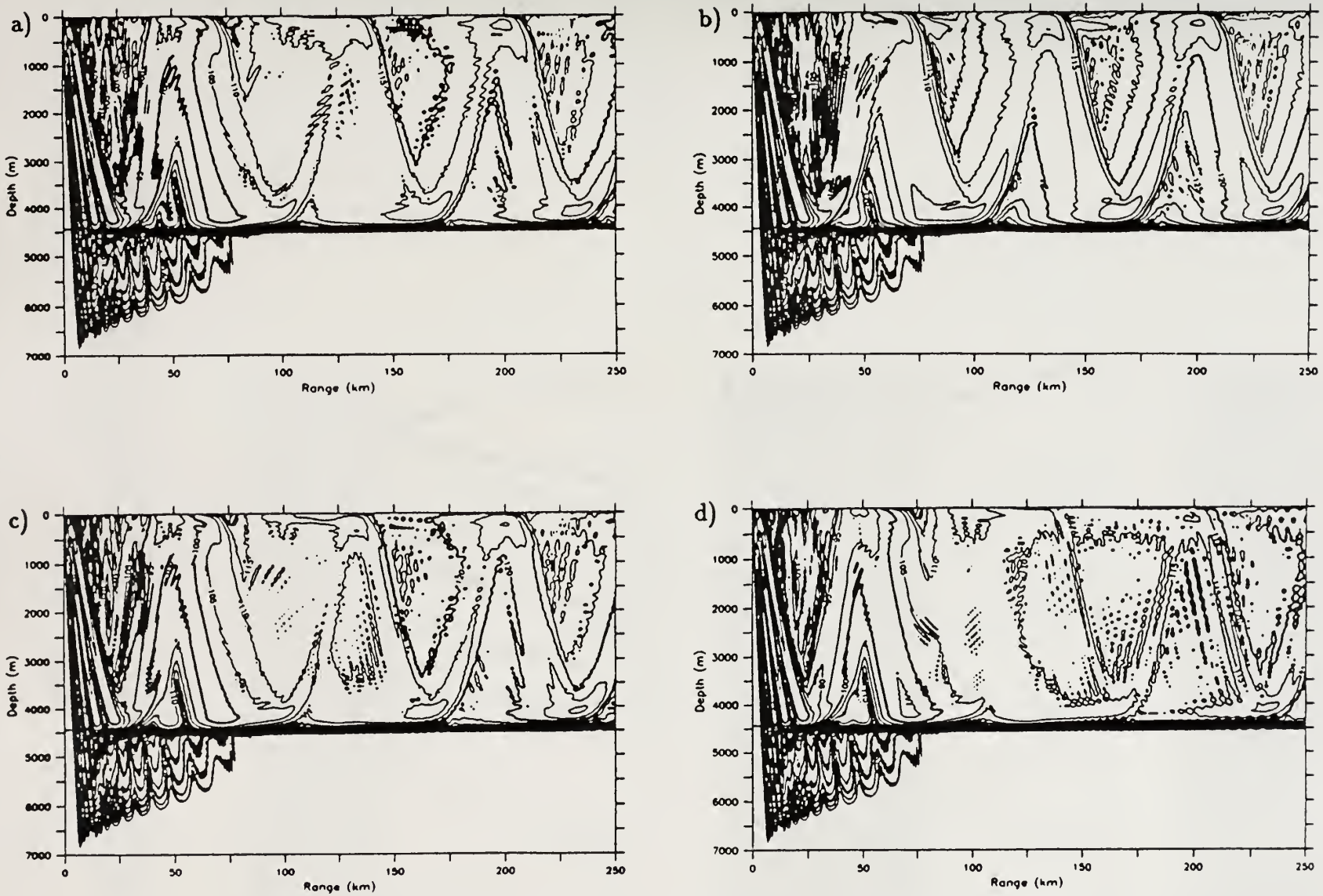

Figure 3.30) Range-independent oceanography, flat bottom Sargasso water propagation. Propagation loss contours. $z_s = 100$ m, $f = 50$ Hz, $\rho = 1.352$ gm/cm^3, $\beta = .9$ dB/λ, $\partial c/\partial z = 1.227$ sec^{-1}, $z_{sed} = 100$ m. a. $c_w/c_b = 1.01$. b. $c_w/c_b = 1.02$. c. $c_w/c_b = 1.03$. d. $c_w/c_b = 1.04$.

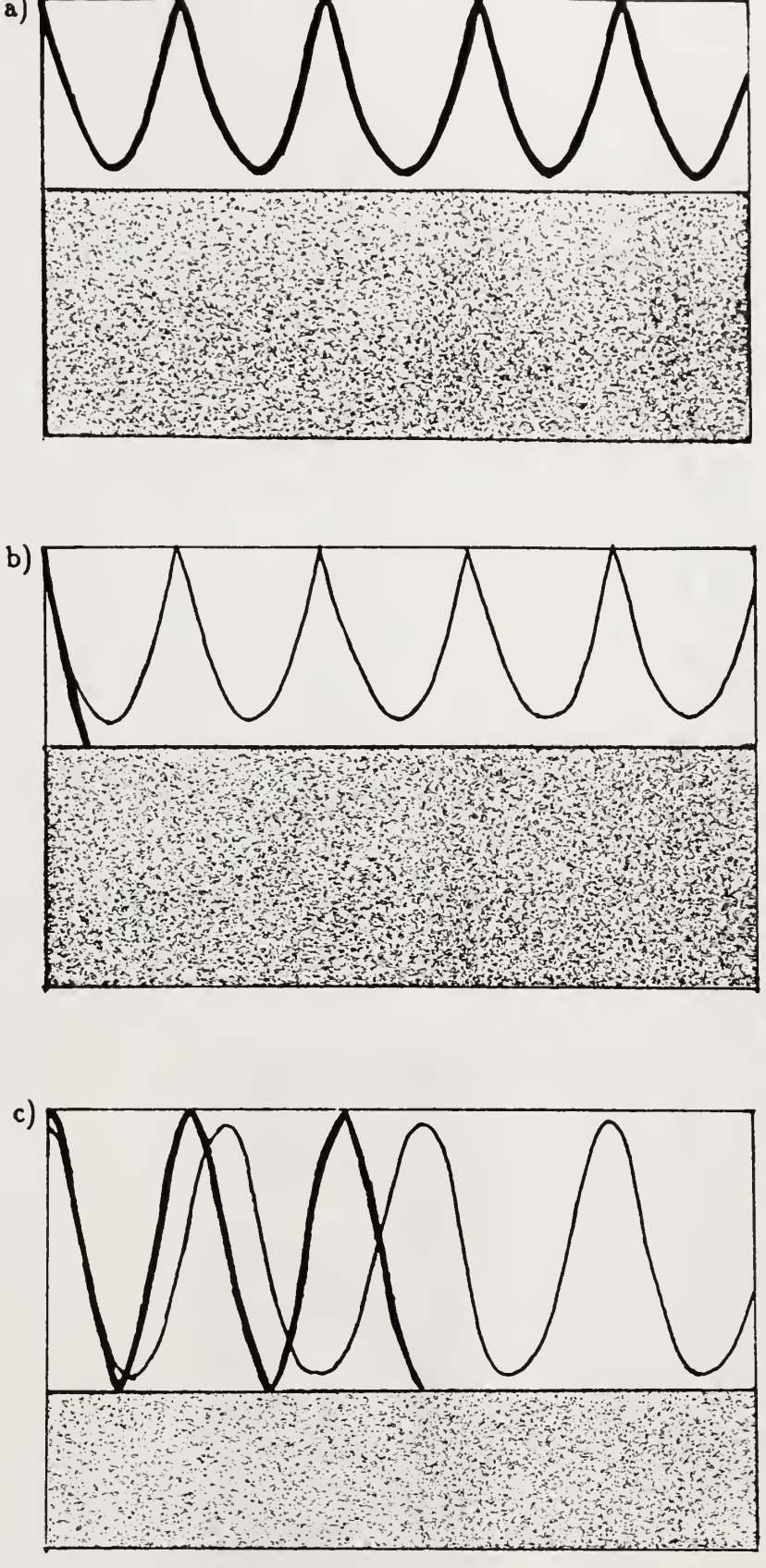

Figure 3.31) Schematic of Sediment Interaction Effects. a. Principal sound path refracts with depth. b. Principal sound path interacts with sediment. c. Bottom glancing paths important.

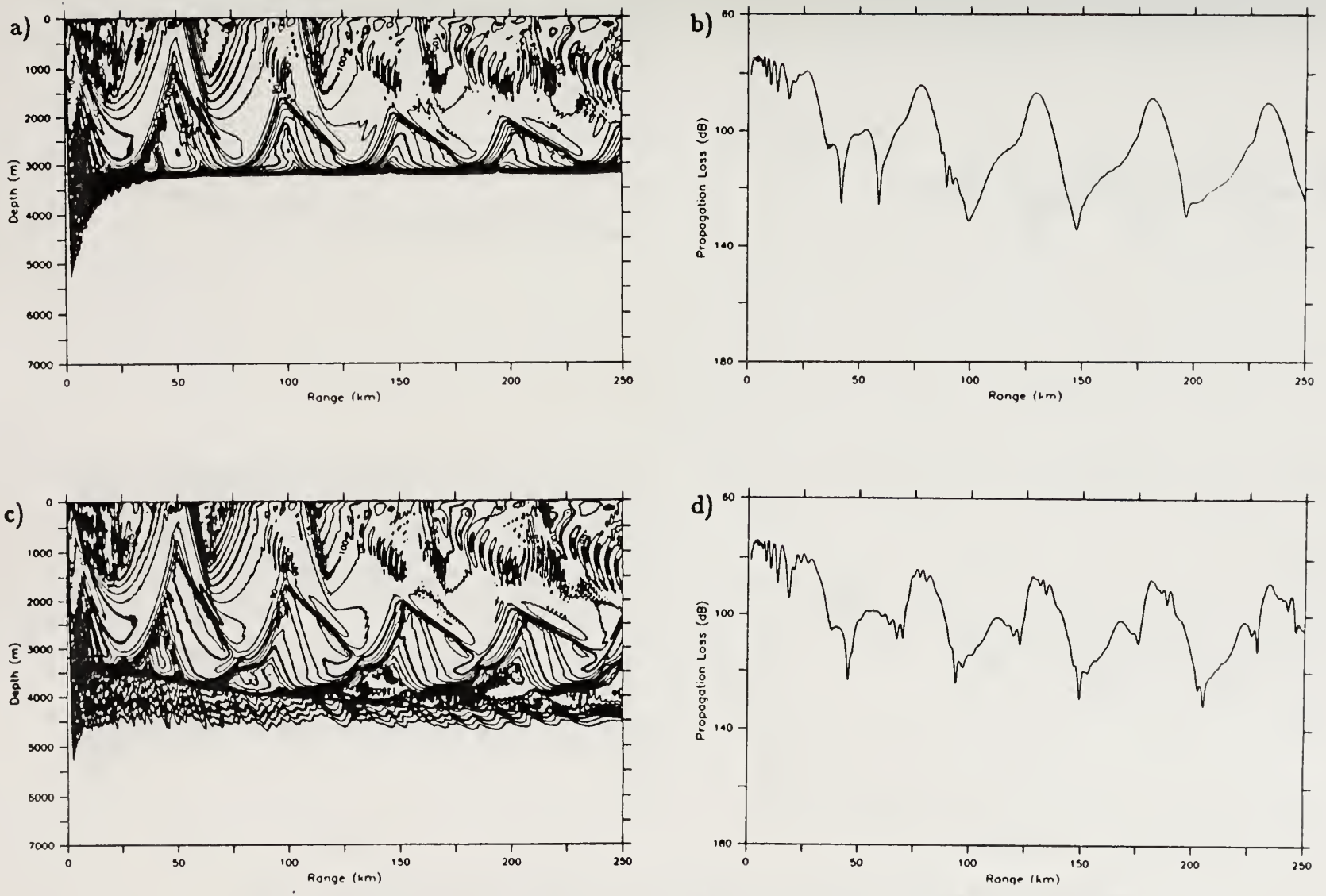

Figure 3.32) Range-independent oceanography, flat bottom vs. downsloping Slope water propagation. z_s = 100 m, f = 100 Hz. a. Flat bottom propagation loss contours. b. Flat bottom propagation loss at 3000 m receiver. c. Downsloping propagation loss contours. d. Downsloping propagation loss at 3000 m receiver.

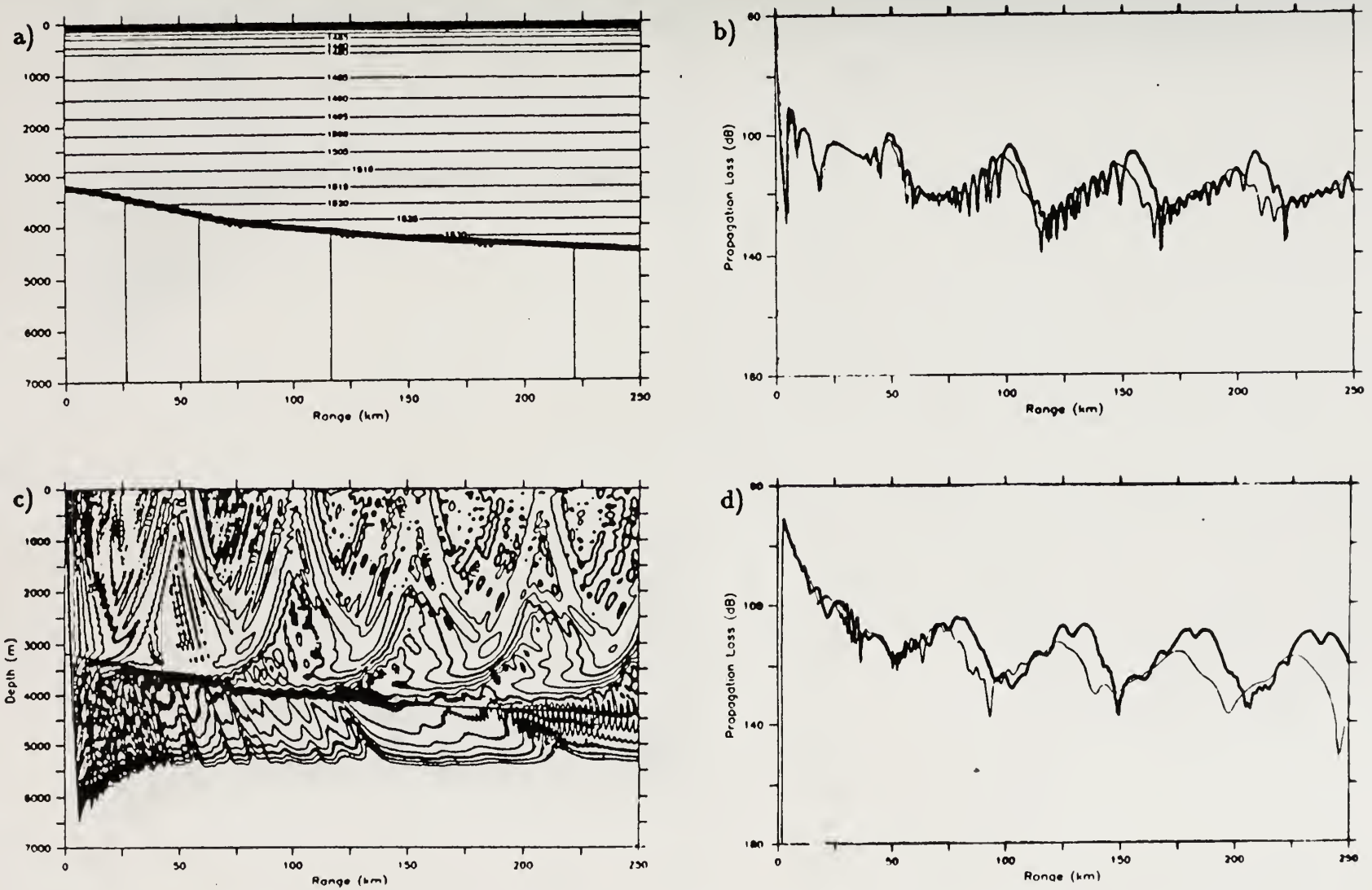

Figure 3.33) Range-independent oceanography, downsloping Slope water propagation. $z_s = 10$ m, $f = 25$ Hz. Receivers overlaid with corresponding receivers from figure 3.10. a. Sound speed contours. b. Propagation loss at 100 m receivers. c. Propagation loss contours. d. Propagation loss at 3000 m receivers.

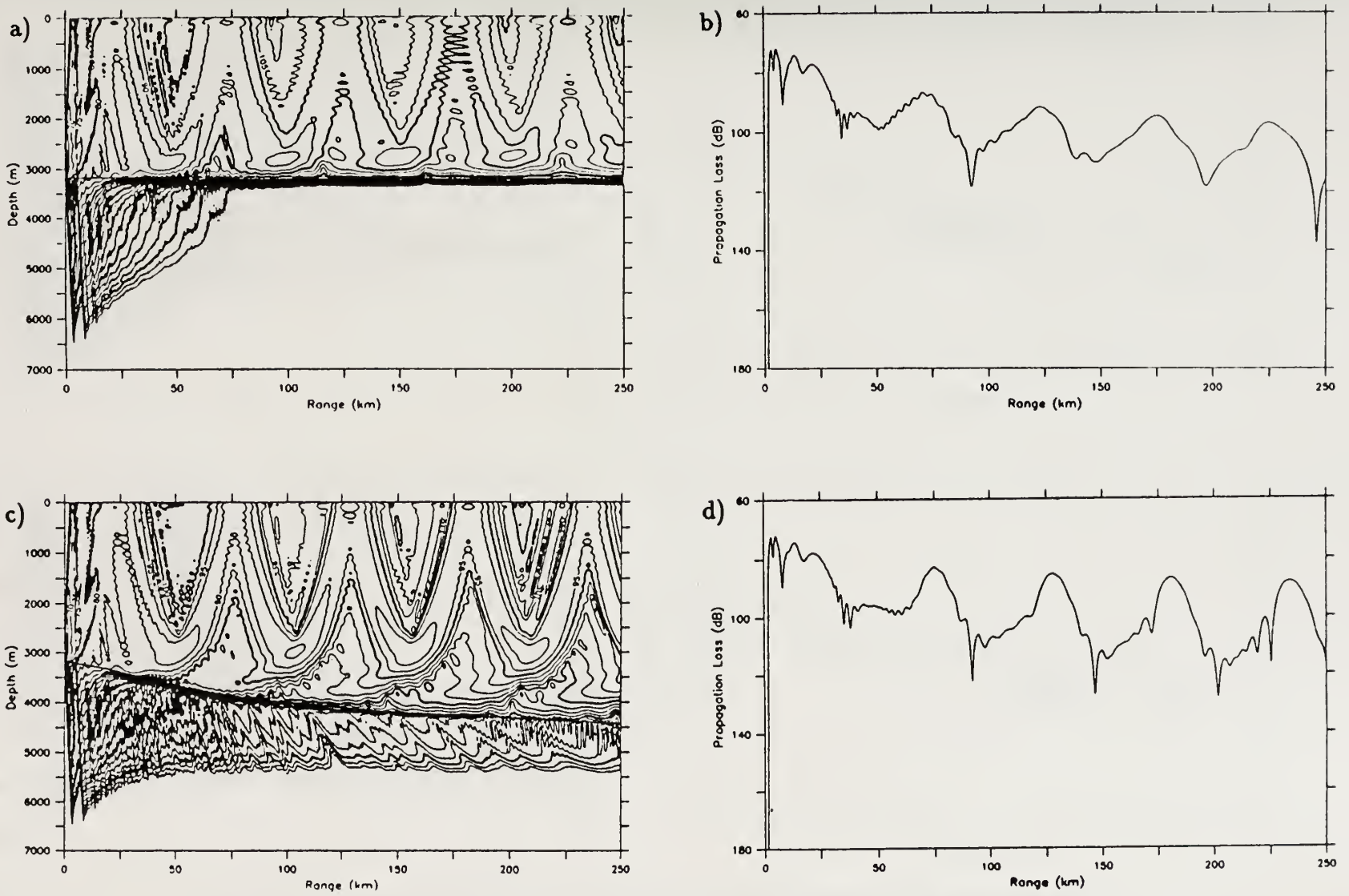

Figure 3.34) Range-independent oceanography, flat bottom vs. downsloping Slope water propagation. z_s = 3000 m, f = 25 Hz. a. Flat bottom propagation loss contours. b. Flat bottom propagation loss at 100 m receiver. c. Downsloping propagation loss contours. d. Downsloping propagation loss at 100 m receiver.

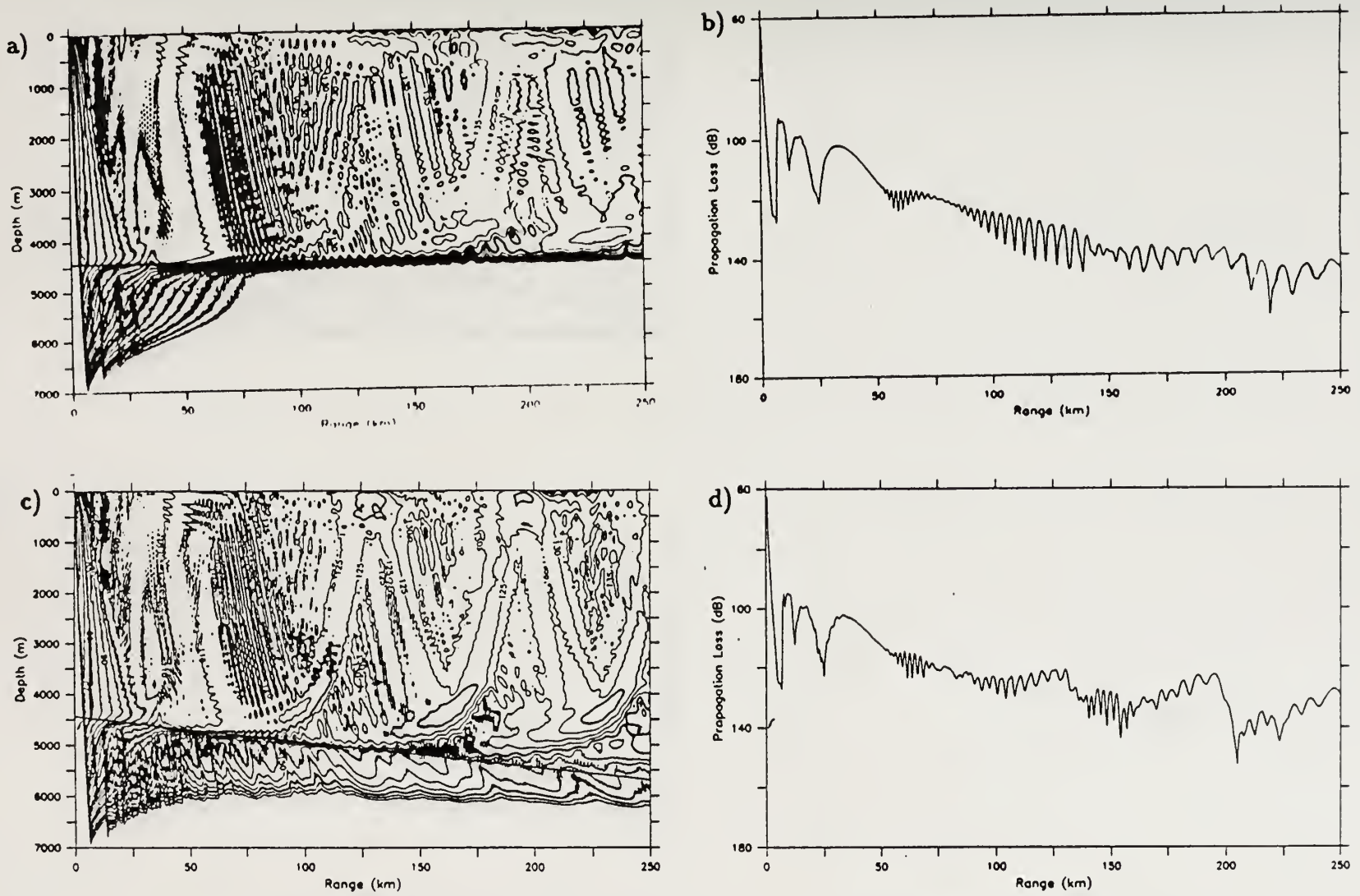

Figure 3.35) Range-independent oceanography, flat bottom vs. downsloping Sargasso water propagation, bottom slope $\Delta z/\Delta r = .005$. $z_s = 10$ m, $f = 25$ Hz. a. Flat bottom propagation loss contours. b. Flat bottom propagation loss at 100 m receiver. c. Downsloping propagation loss contours. d. Downsloping propagation loss at 100 m receiver.

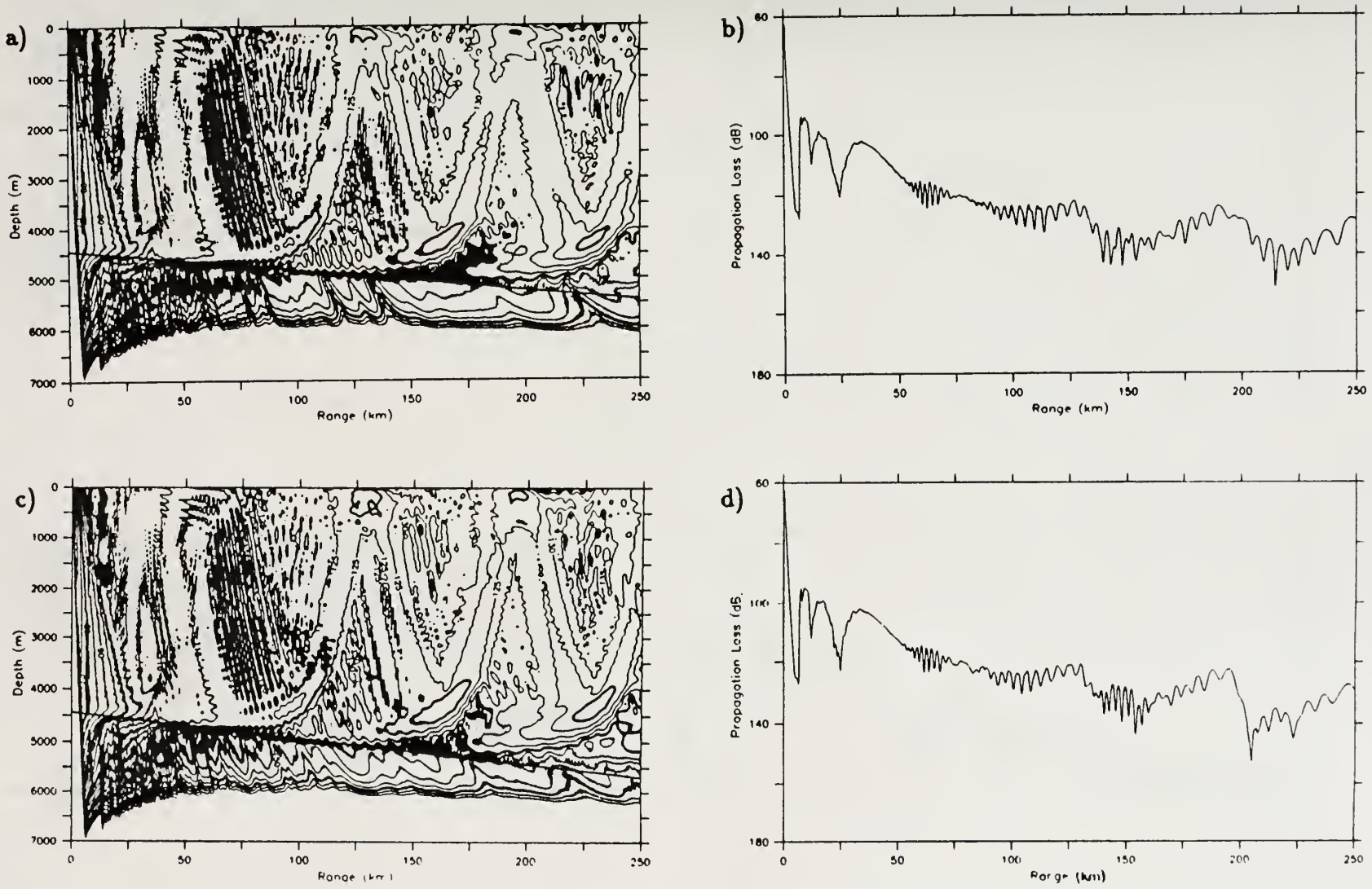

Figure 3.36) Range-independent oceanography, Sargasso water profile, bottom slope $\Delta z/\Delta r = .004$ vs. $\Delta z/\Delta r = .005$. $z_s = 10$ m, $f = 25$ Hz. a. Flat bottom propagation loss contours. b. Flat bottom propagation loss at 100 m receiver. c. Downsloping propagation loss contours. d. Downsloping propagation loss at 100 m receiver.

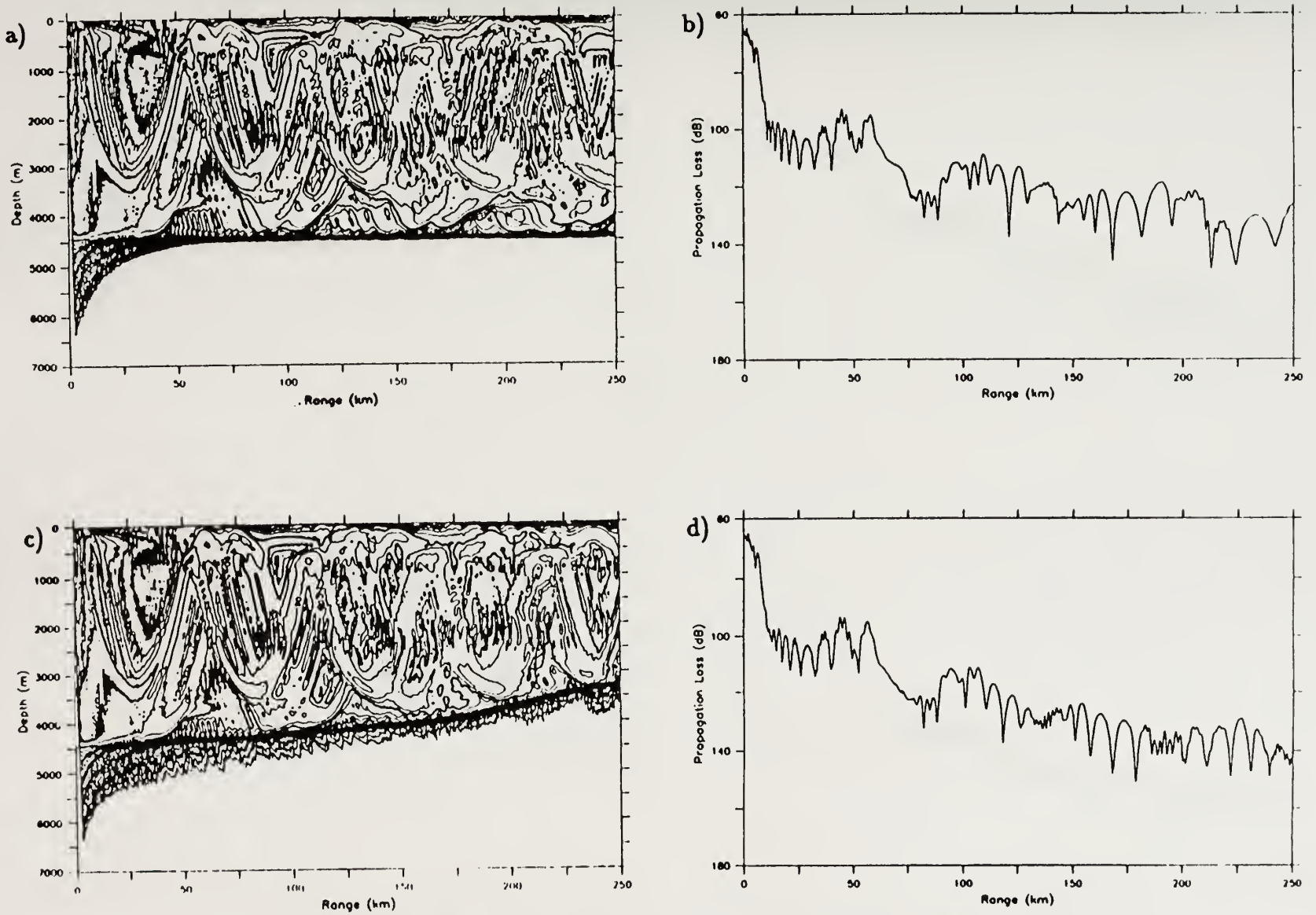

Figure 3.37) Range-independent oceanography, flat bottom vs. upsloping Sargasso water propagation. $z_s = 750$ m, $f = 100$ Hz. a. Flat bottom propagation loss contours. b. Flat bottom propagation loss at 100 m receiver. c. Upsloping propagation loss contours. d. Upsloping propagation loss at 100 m receiver.

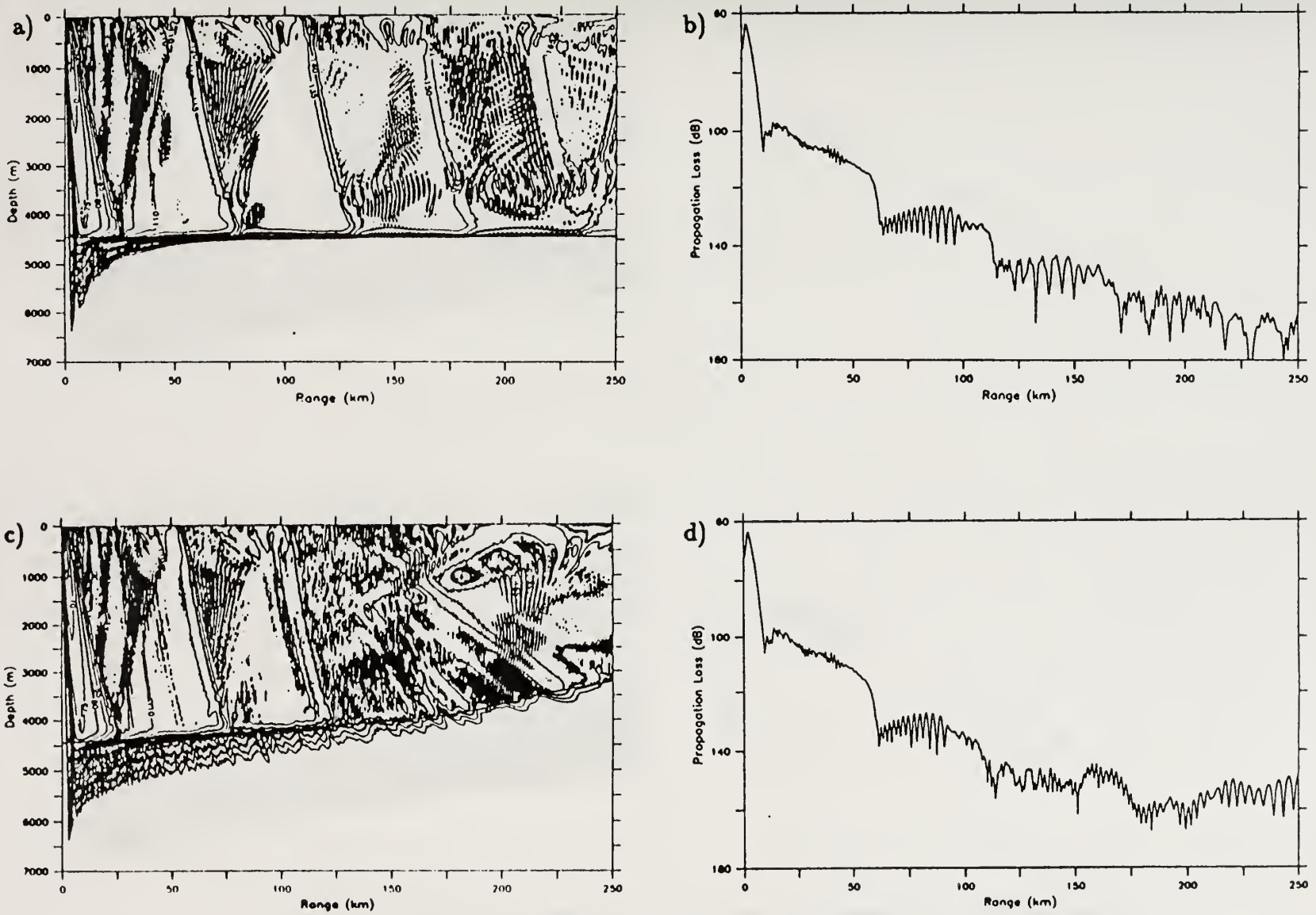

Figure 3.38) Range-independent oceanography, flat bottom vs. upsloping Sargasso water propagation. $z_s = 10$ m, $f = 100$ Hz. a. Flat bottom propagation loss contours. b. Flat bottom propagation loss at 1000 m receiver. c. Upsloping propagation loss contours. d. Upsloping propagation loss at 1000 m receiver.

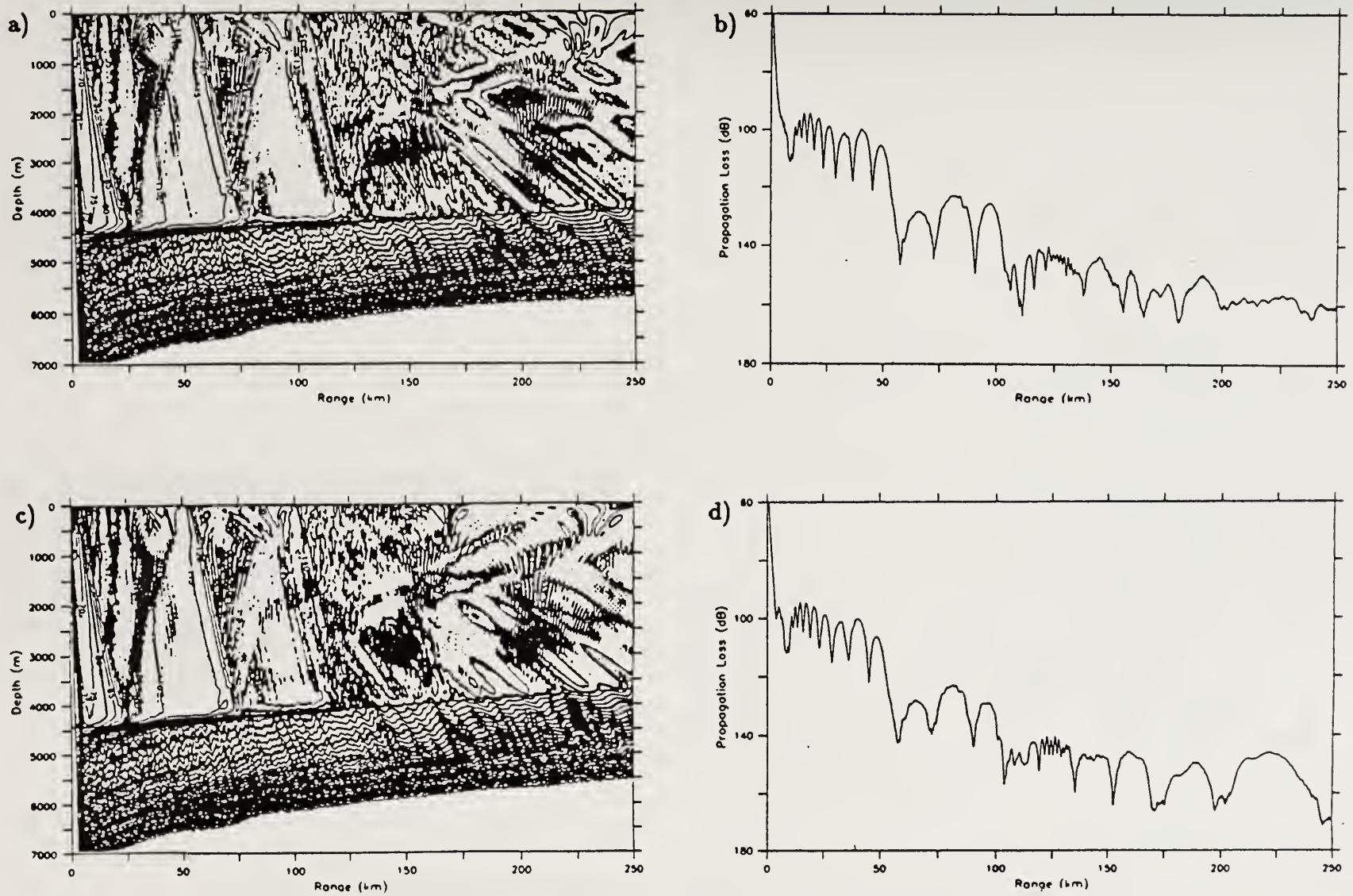

Figure 3.39) Range-independent oceanography, Sargasso water bottom slope test. z_s = 10 m, f = 100 Hz. a. Bottom slope -.002, propagation loss contours. b. Bottom slope -.002, propagation loss at 100 m receiver. c. Bottom slope -.003, propagation loss contours. b. Bottom slope -.003, propagation loss at 100 m receiver.

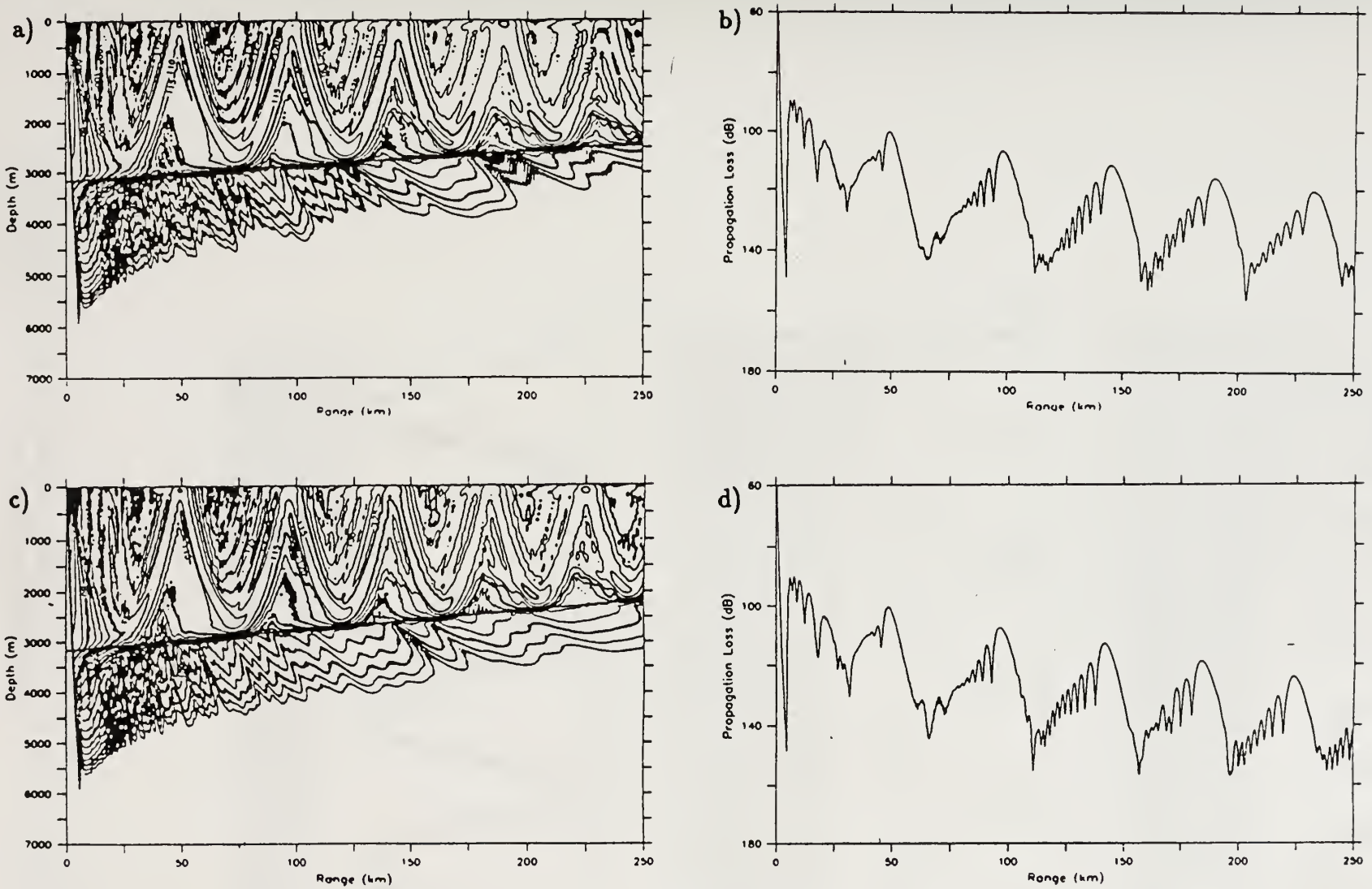

Figure 3.40) Range-independent oceanography, Slope water bottom slope test. z_s = 10 m, f = 50 Hz. a. Bottom slope -.003, propagation loss contours. b. Bottom slope -.003, propagation loss at 100 m receiver. c. Bottom slope -.004, propagation loss contours. b. Bottom slope -.004, propagation loss at 100 m receiver.

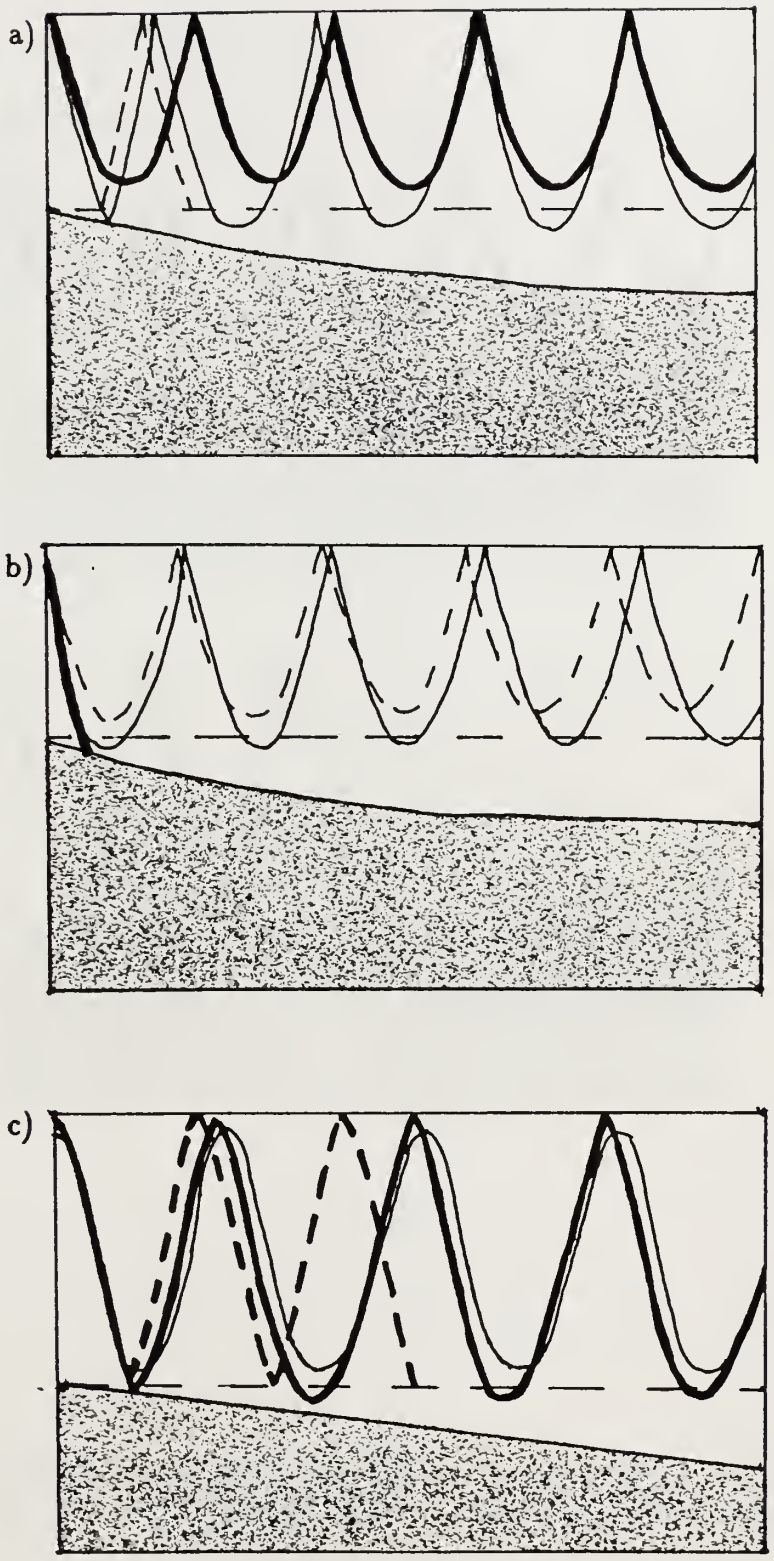

Figure 3.41) Schematic of downsloping topographic effects. a. Primary sound path refracts within flat-bottom waveguide. b. Primary sound path interacts with flat bottom. c. Bottom-glancing propagation paths important.

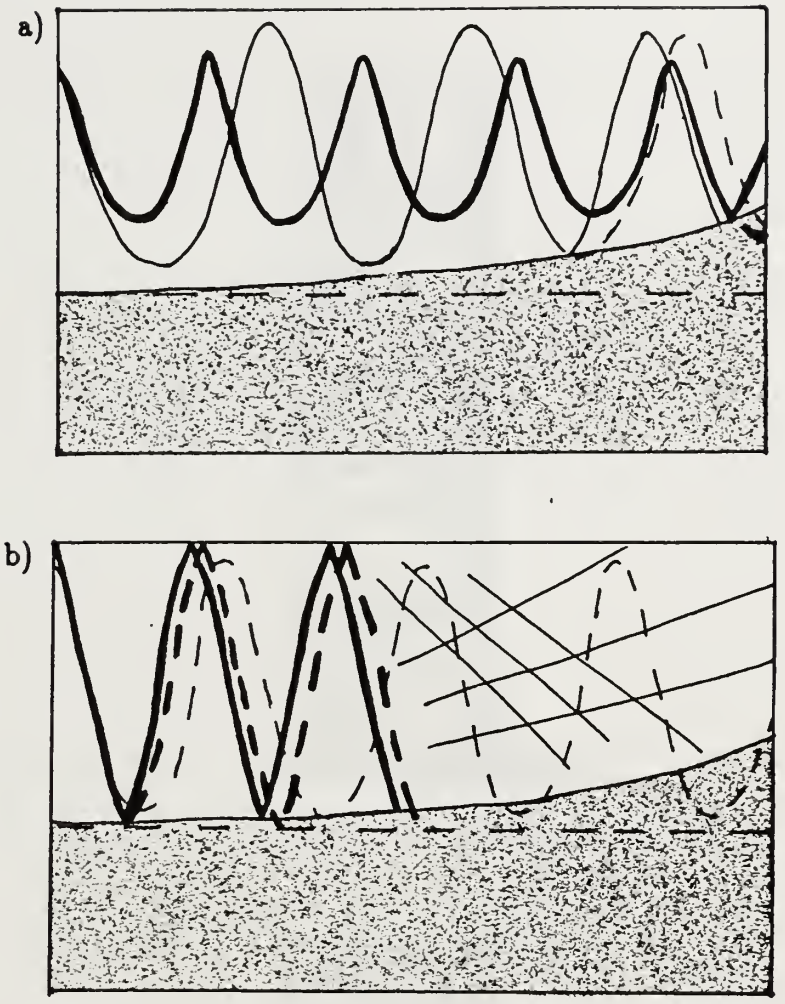

Figure 3.42) Schematic of upsloping topographic effects. a. Primary sound paths refract within flat-bottom waveguide. b. Bottom-glancing paths important.

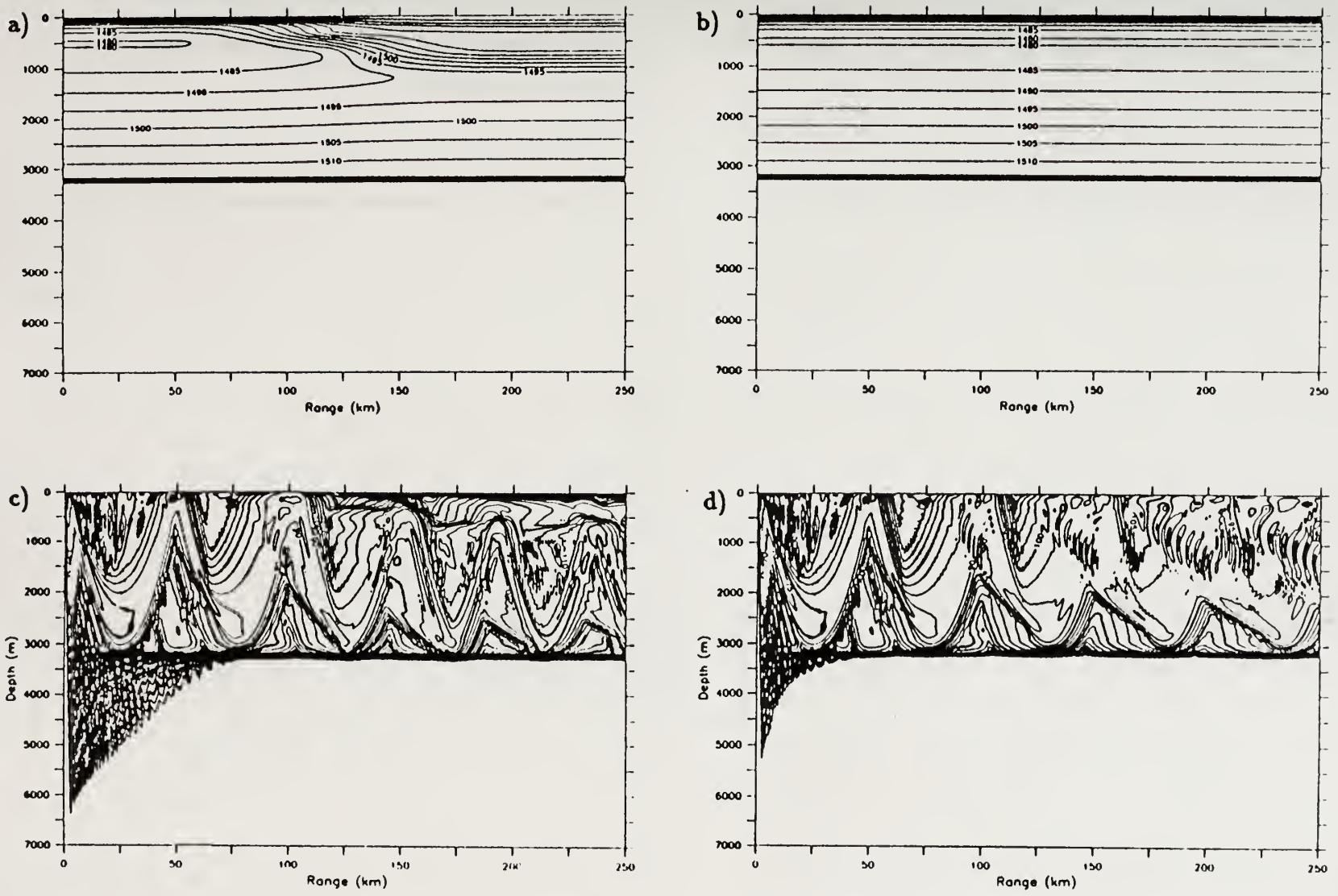

Figure 3.43) Range dependent vs. range independent oceanography, Slope to Sargasso water propagation. Bottom depth 3170 m. z_s = 100 m, f = 100 Hz. a. Sound speed contours, range dependent case. b. Sound speed contours, range independent case. c. Propagation loss contours, range dependent case. d. Propagation loss contours, range independent case.

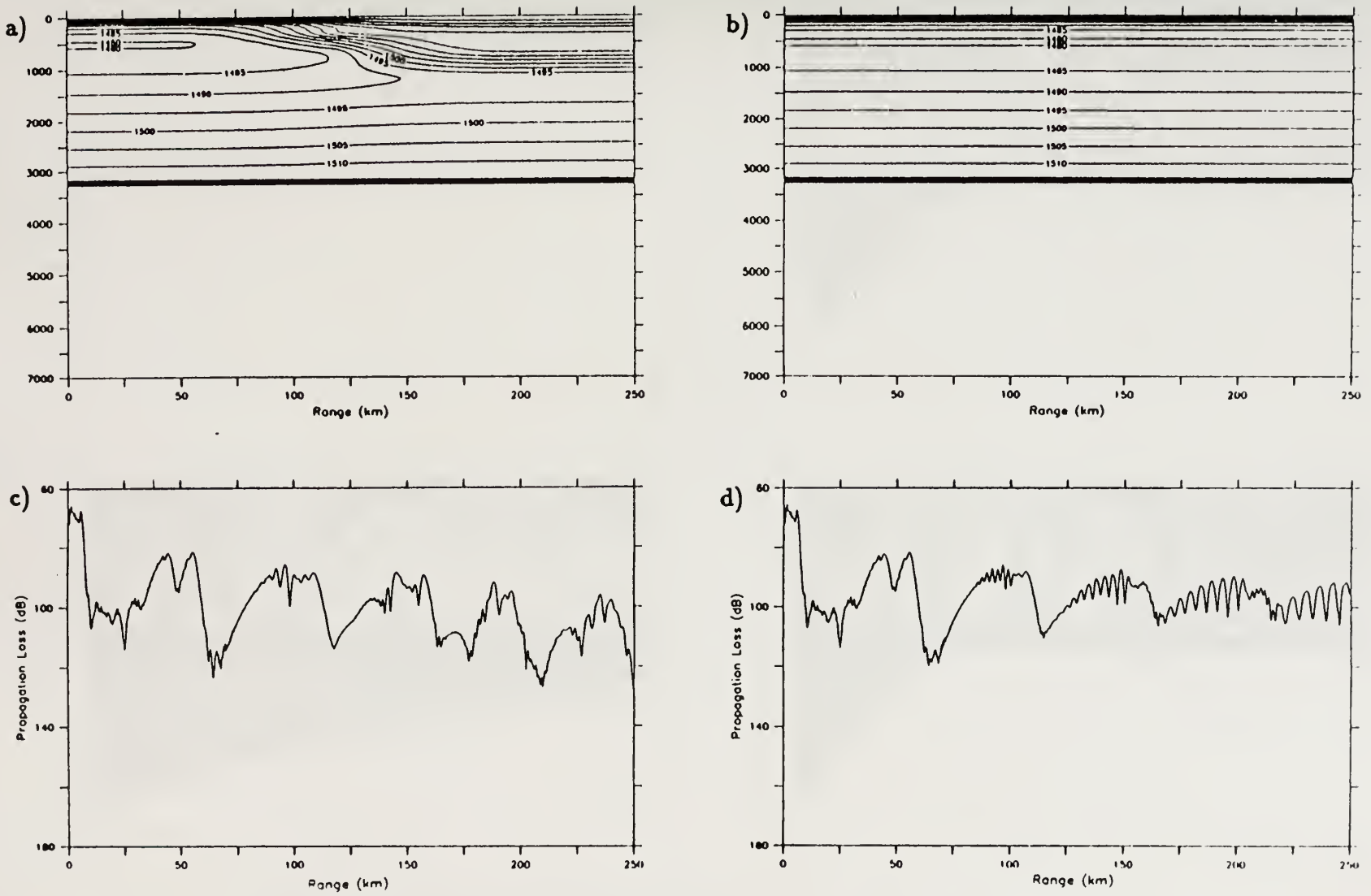

Figure 3.44) Range dependent vs. range independent oceanography, Slope to Sargasso water propagation. Bottom depth 3170 m. z_s = 100 m, f = 100 Hz. a. Sound speed contours, range dependent case. b. Sound speed contours, range independent case. c. Propagation loss at 1000 m receiver, range dependent case. d. Propagation loss at 1000 m receiver, range independent case.

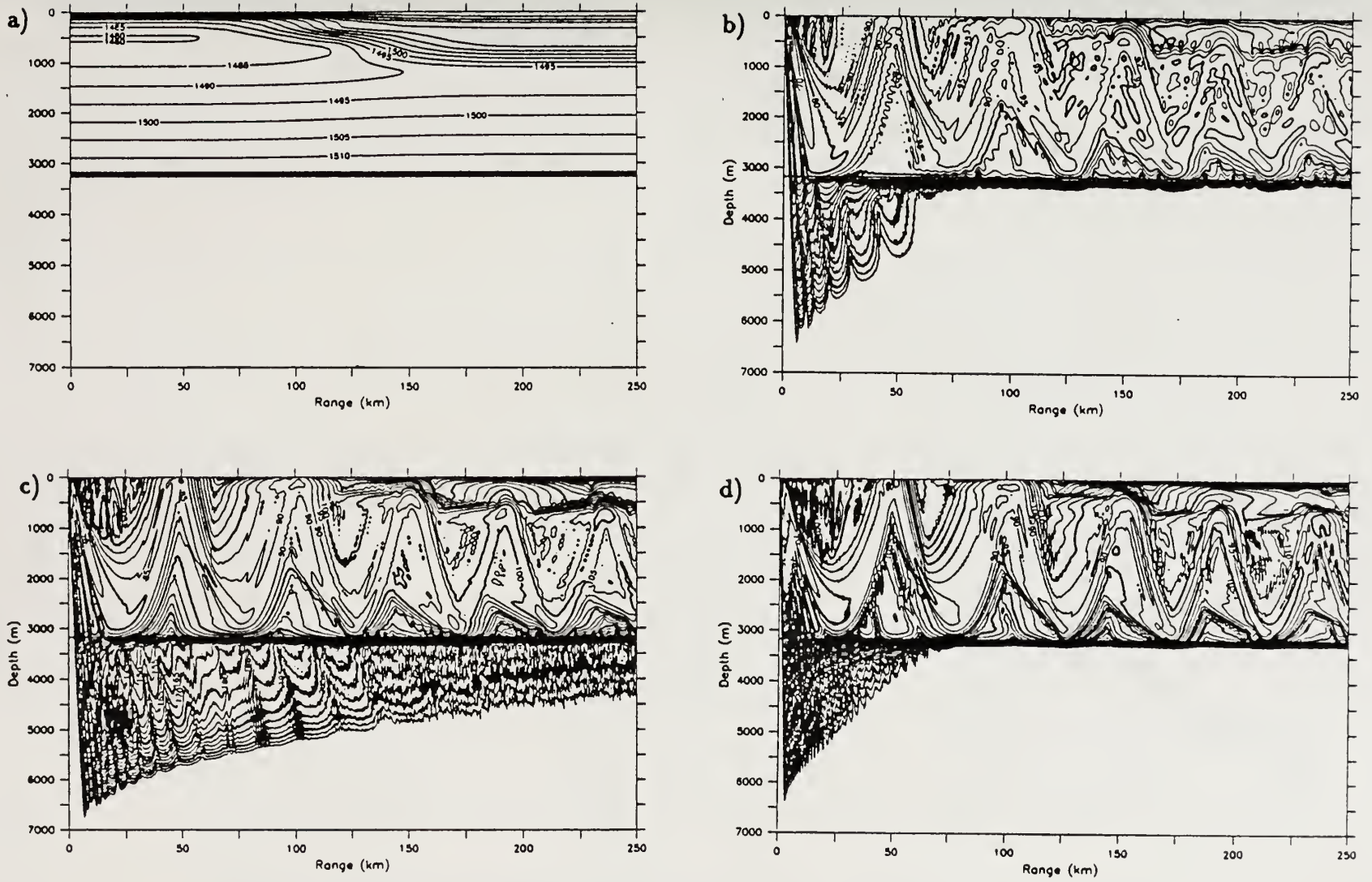

Figure 3.45) Range-dependent oceanography, Slope to Sargasso water propagation. Bottom depth 3170 m. z_s = 100 m. Realistic bottom. a. Sound speed contours. b. Propagation loss contours, 25 Hz. c. Propagation loss contours, 50 Hz. d. Propagation loss contours, 100 Hz.

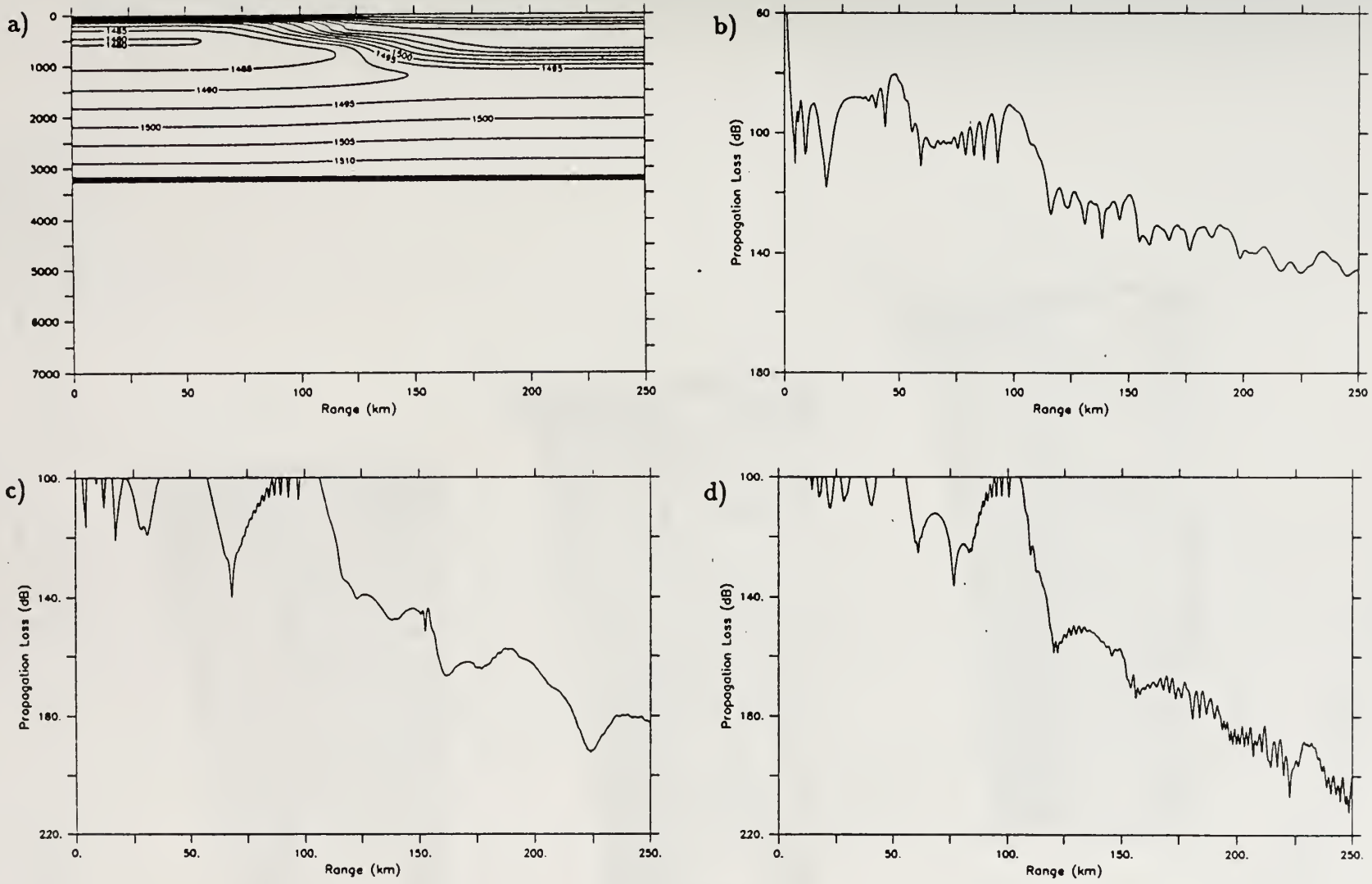

Figure 3.46) Range-dependent oceanography, Slope to Sargasso water propagation. Bottom depth 3170 m. z_s = 100 m. Realistic bottom. a. Sound speed contours. b. Propagation loss, 100 m receiver, 25 Hz. c. Propagation loss, 100 m receiver, 50 Hz. d. Propagation loss, 100 m receiver, 100 Hz.

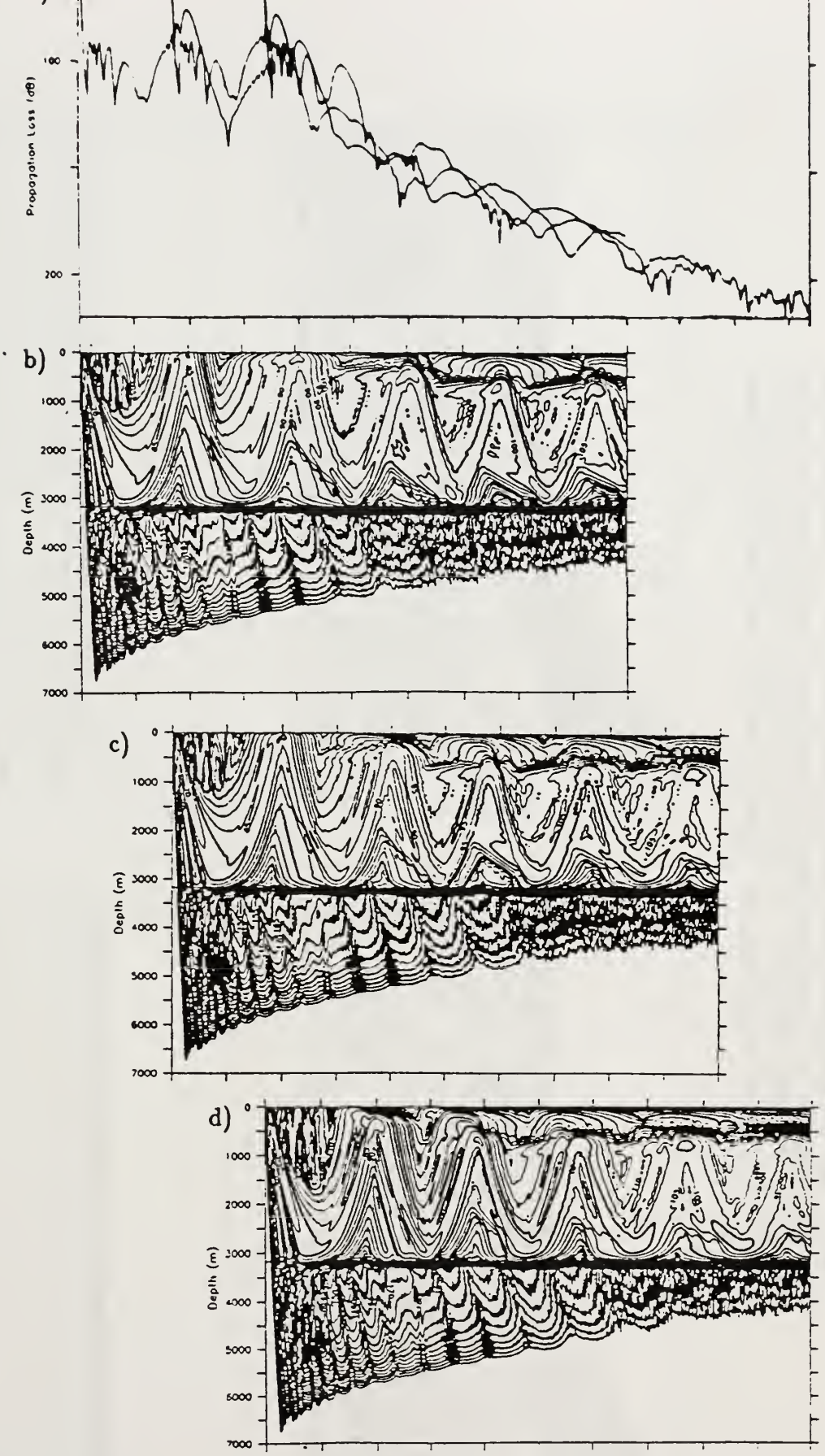

Figure 3.47) Range-dependent oceanography, Slope to Sargasso water propagation. Bottom depth 3170 m. z_s = 100 m. f = 50 Hz. Realistic bottom. a. Propagation loss at 100 m receiver, all three cases overlaid to align the geography. b. Propagation loss contours, starting position 37.3N 72.4W (far from stream). c. Propagation loss contours, starting position 37.1N 72.1W (middle). d. Propagation loss contours, starting position 36.8N 71.8W (close to stream).

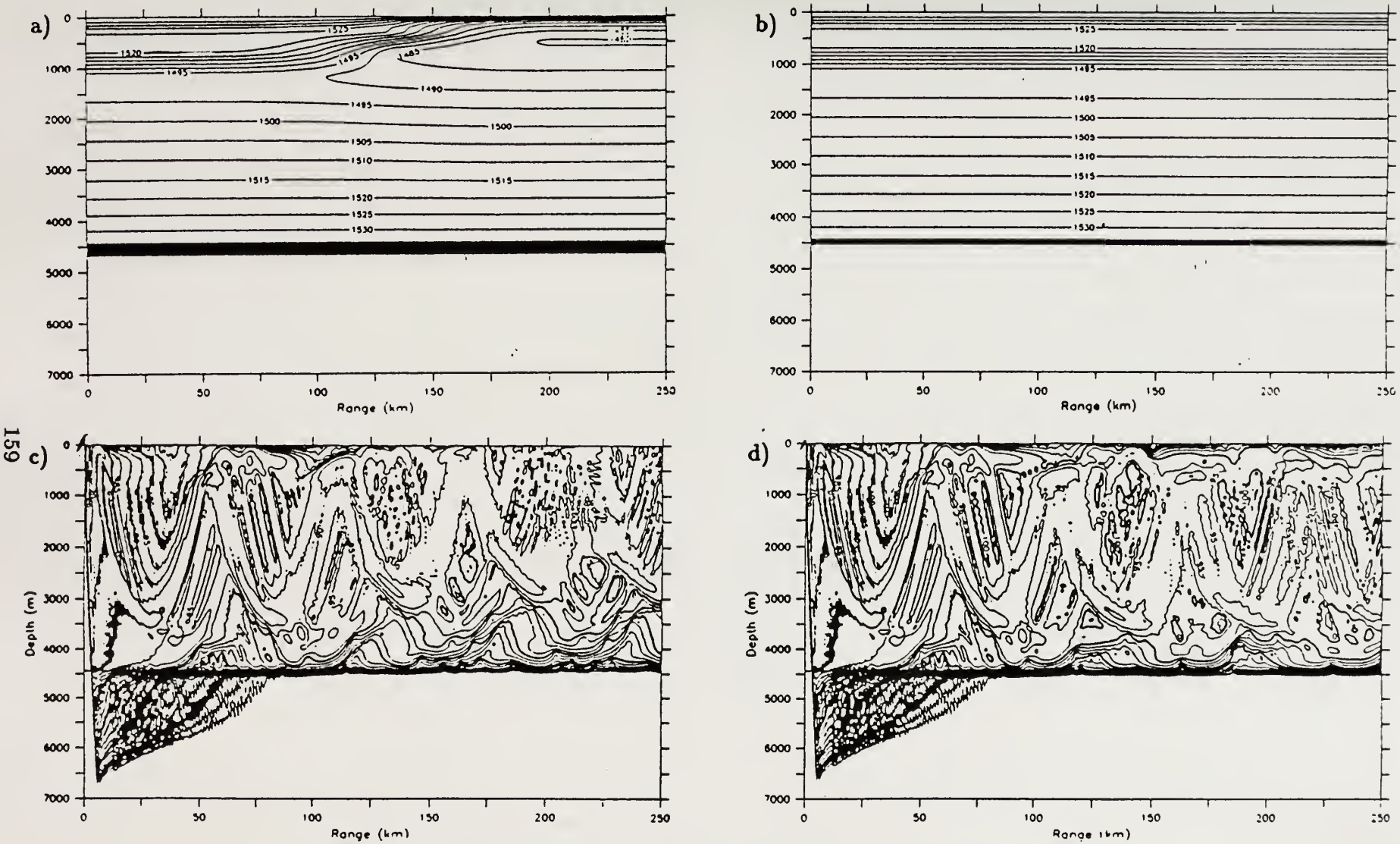

Figure 3.48) Range-dependent vs. range-independent oceanography, Sargasso to Slope water propagation. z_s = 750 m, f = 50 Hz. Bottom depth 4440 m, realistic bottom. a. Sound speed contours, Sargasso to Slope water. b. Sound speed contours, Sargasso water range-independent profile. c. Propagation loss contours, Sargasso to Slope water. d. Propagation loss contours, Sargasso water profile.

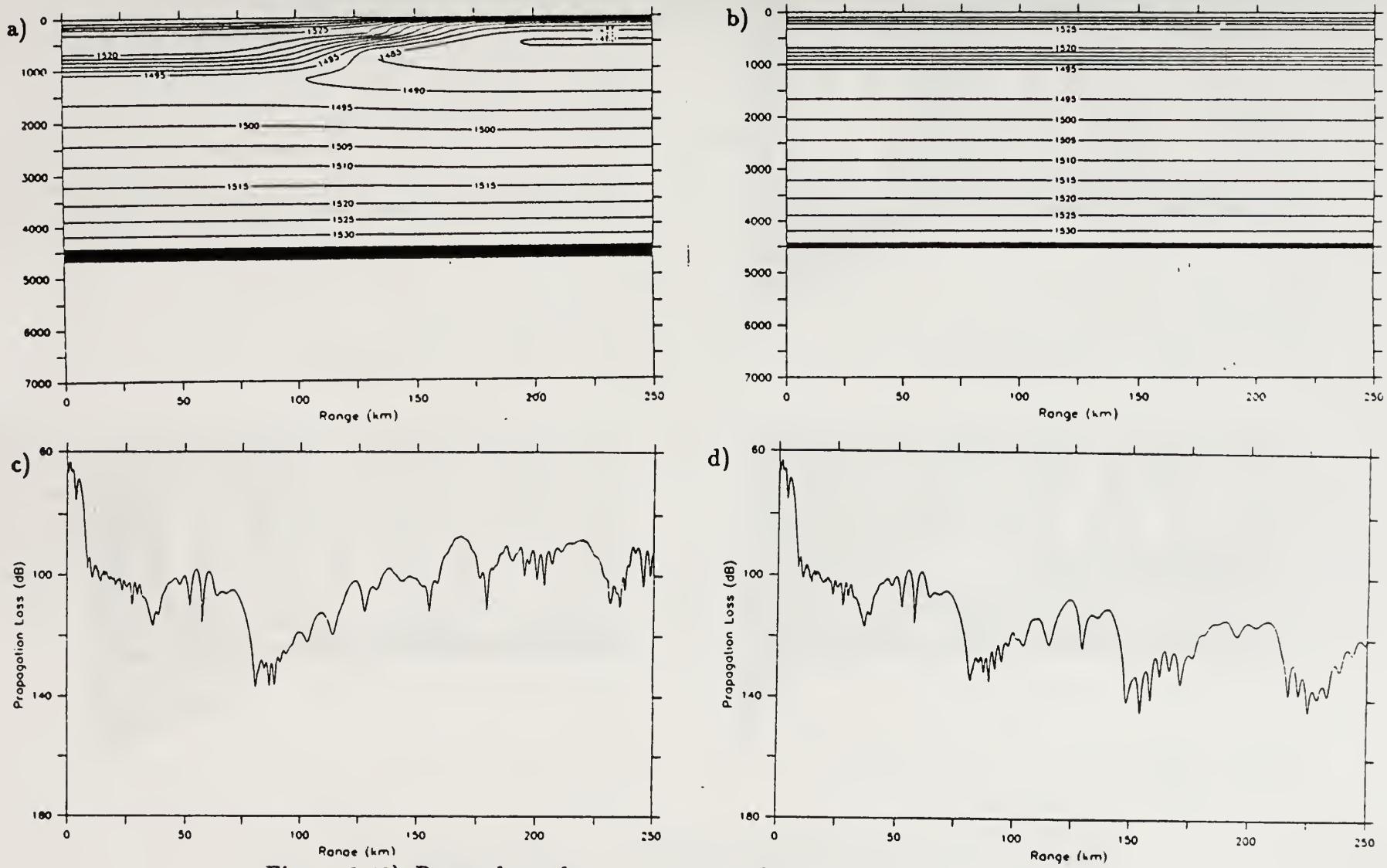

Figure 3.49) Range-dependent vs. range-independent oceanography, Sargasso to Slope water propagation. z_s = 750 m, f = 50 Hz. Bottom depth 4440 m, realistic bottom. a. Sound speed contours, Sargasso to Slope water. b. Sound speed contours, Sargasso water range-independent profile. c. Propagation loss at 100 m, Sargasso to Slope water. d. Propagation loss at 100 m, Sargasso water profile.

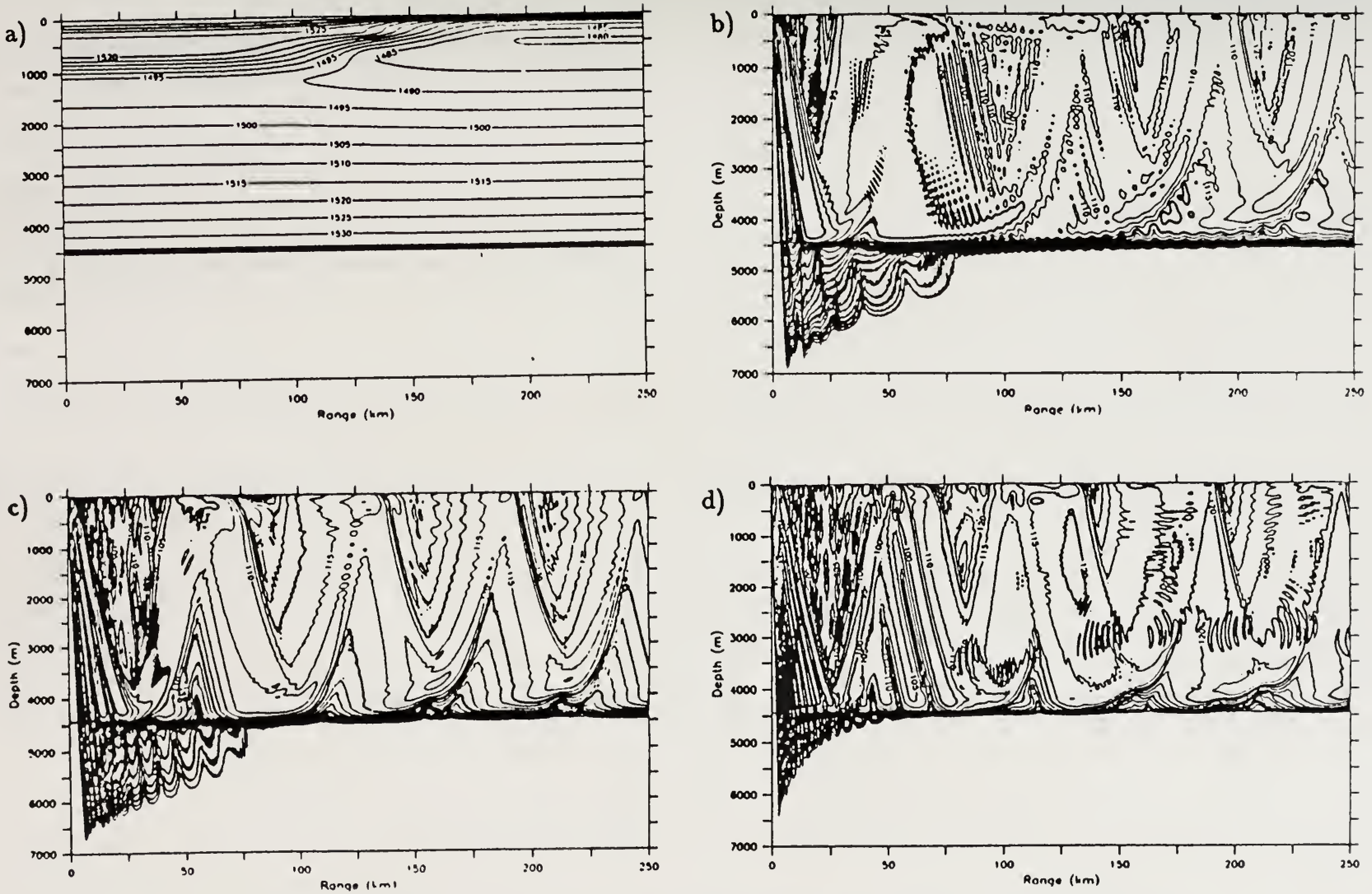

Figure 3.50) Range-dependent oceanography, Sargasso to Slope water propagation. Bottom depth 4440 m. $z_s = 100$ m. Realistic bottom. a. Sound speed contours. b. Propagation loss contours, $f = 25$ Hz. c. Propagation loss contours, $f = 50$ Hz. d. Propagation loss contours, $f = 100$ Hz.

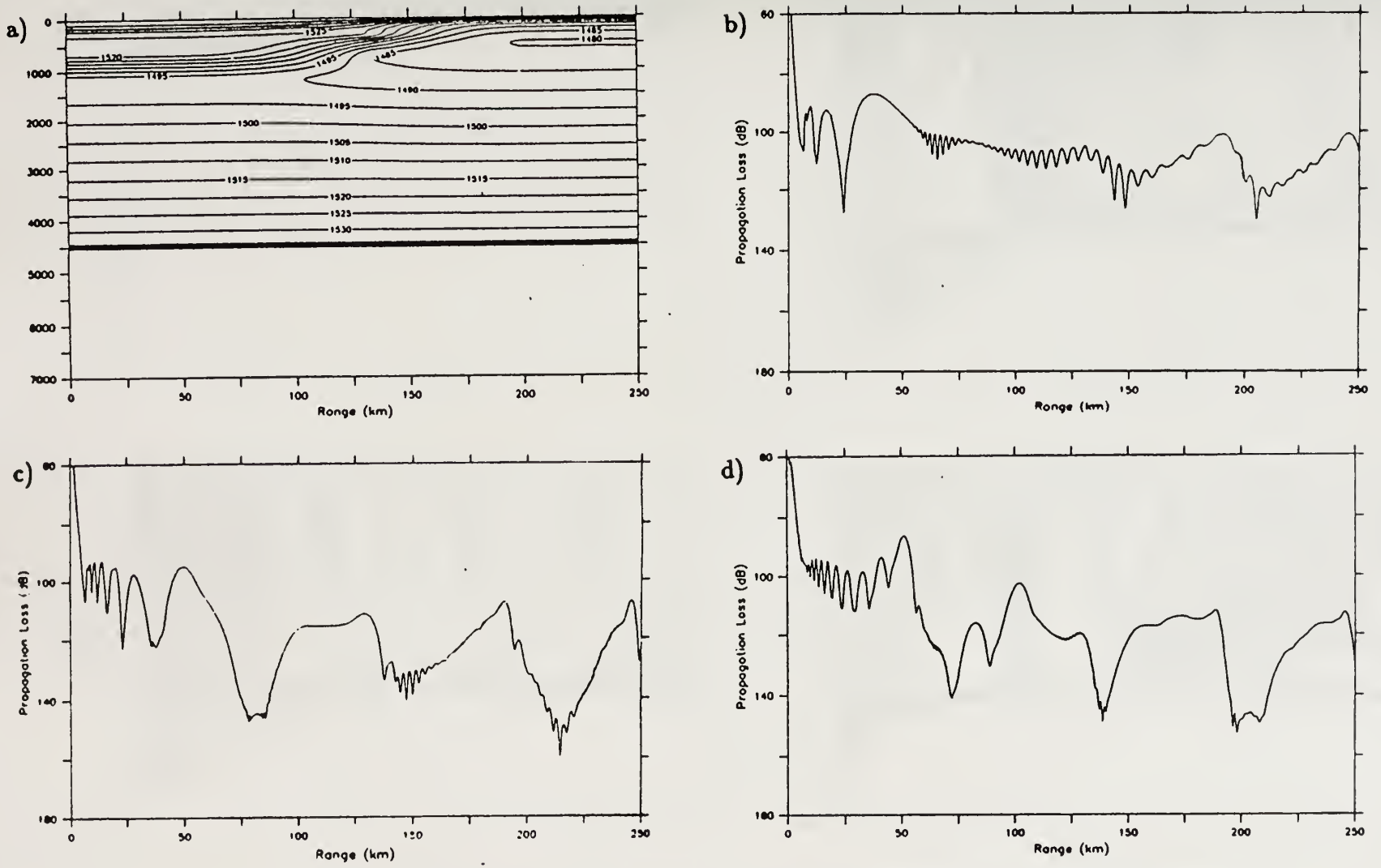

Figure 3.51) Range-dependent oceanography, Sargasso to Slope water propagation. Bottom depth 4440 m. $z_s = 100$ m. Realistic bottom. a. Sound speed contours. b. Propagation loss at 100 m, $f = 25$ Hz. c. Propagation loss at 100 m, $f = 50$ Hz. d. Propagation loss at 100 m, $f = 100$ Hz.

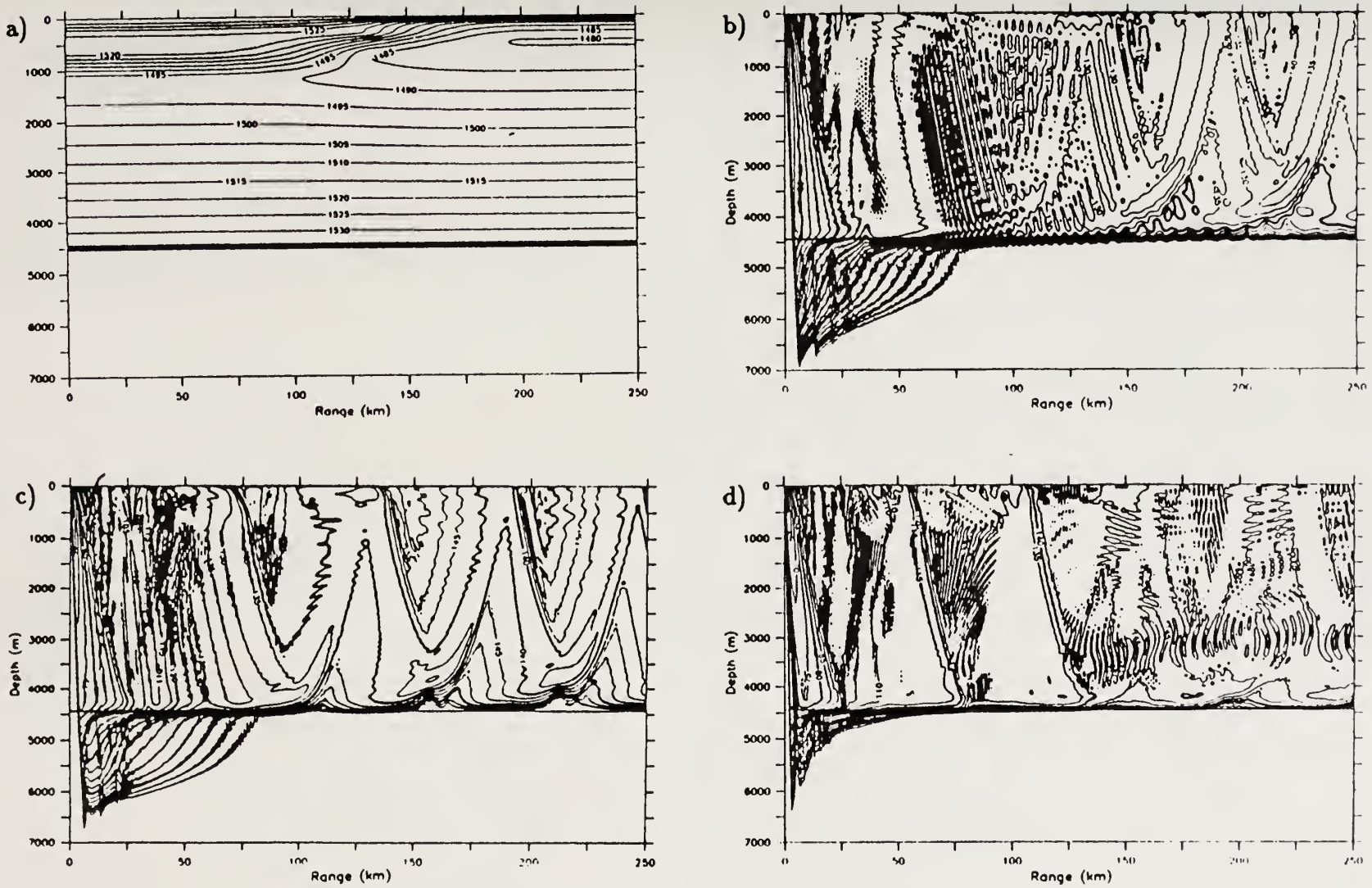

Figure 3.52) Range-dependent oceanography, Sargasso to Slope water propagation. Bottom depth 4440 m. z_s = 10 m. Realistic bottom. a. Sound speed contours. b. Propagation loss contours, f = 25 Hz. c. Propagation loss contours, f = 50 Hz. d. Propagation loss contours, f = 100 Hz.

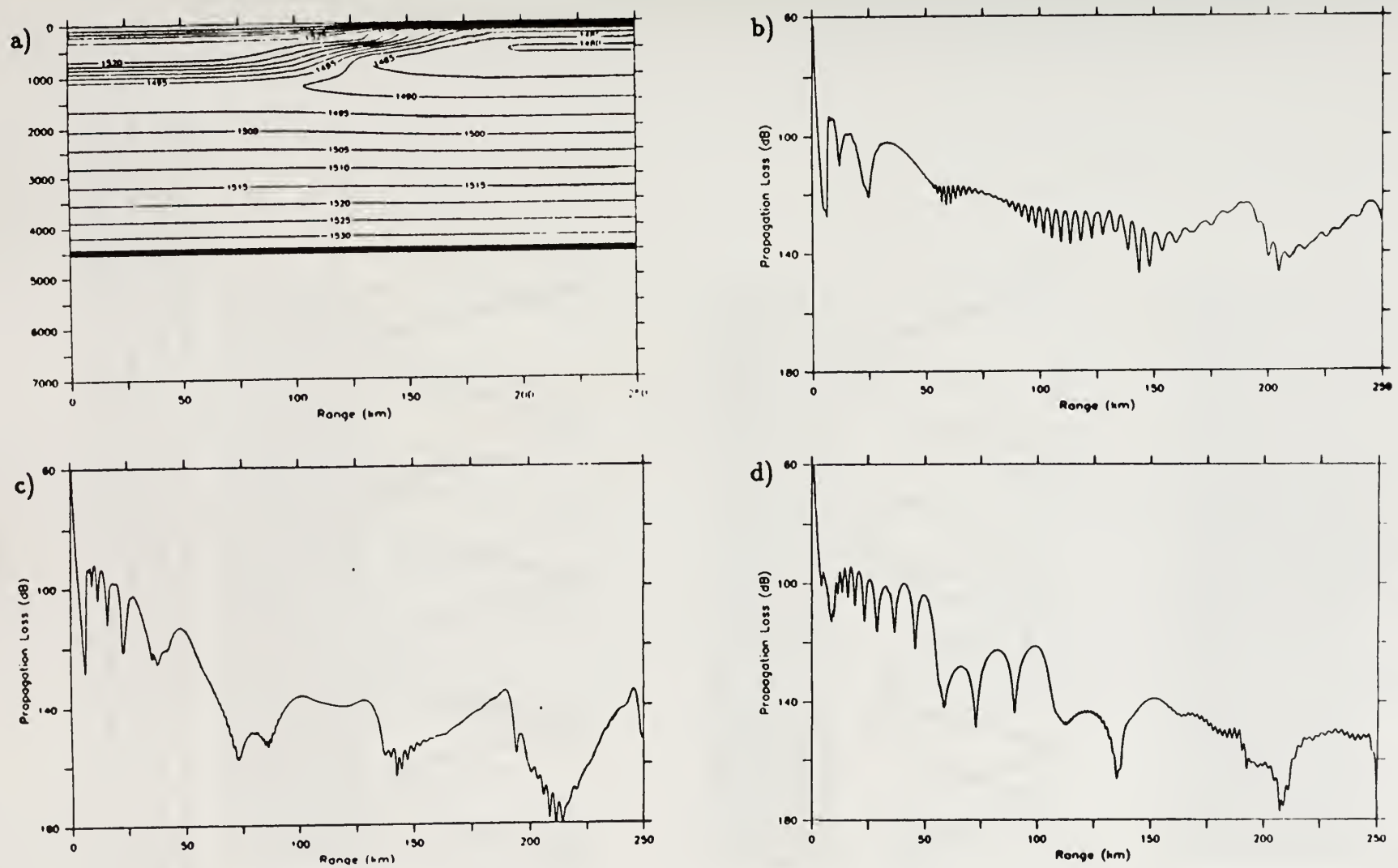

Figure 3.53) Range-dependent oceanography, Sargasso to Slope water propagation. Bottom depth 4440 m. $z_s = 10$ m. Realistic bottom. a. Sound speed contours. b. Propagation loss at 100 m, $f = 25$ Hz. c. Propagation loss at 100 m, $f = 50$ Hz. d. Propagation loss at 100 m, $f = 100$ Hz.

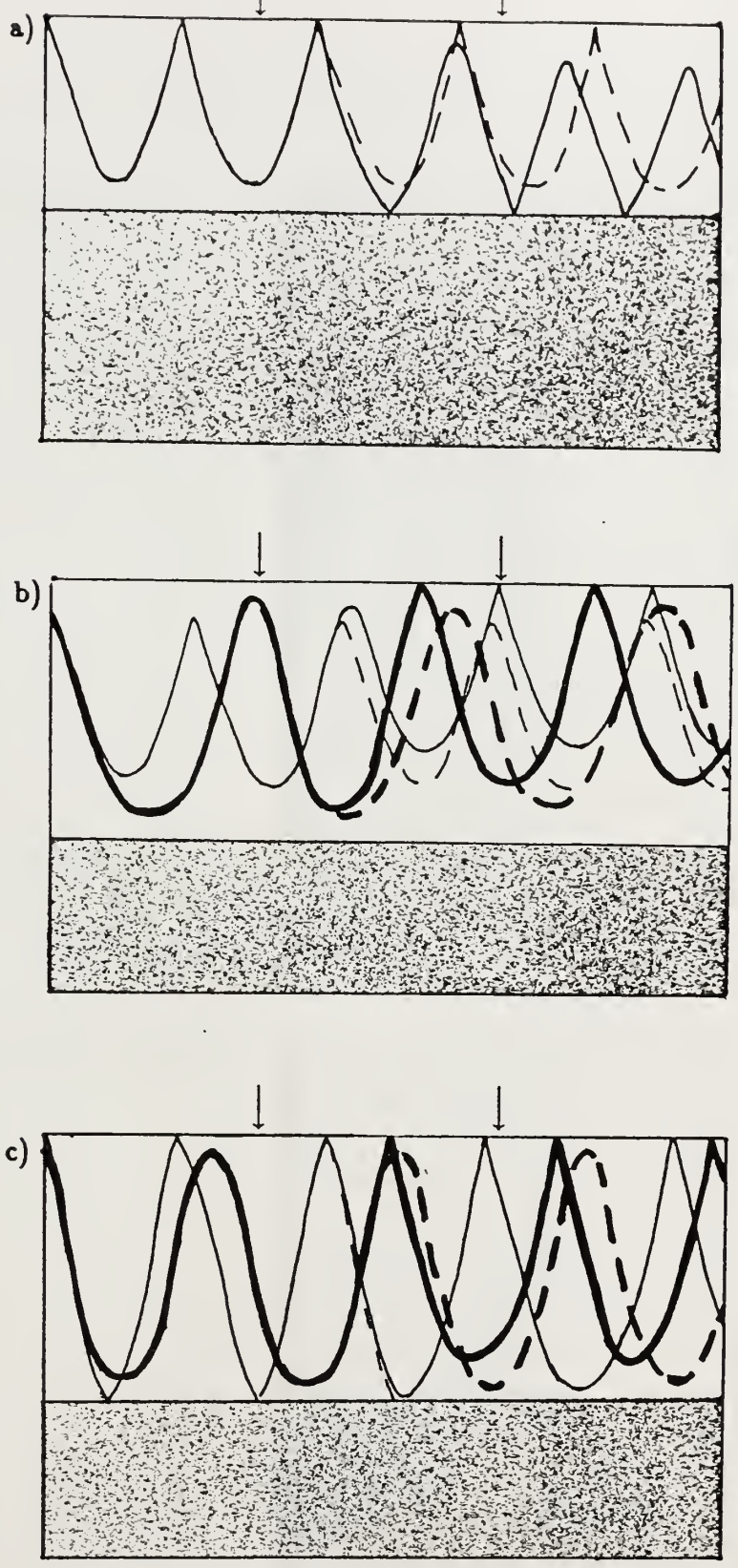

Figure 3.54) Schematic of Frontal Interaction Effects, flat topography. Arrows represent approximate beginning and ending of Gulf Stream. a. Slope to Sargasso propagation. b. Sargasso to Slope propagation, primary sound paths refract with depth. c. Sargasso to Slope propagation, bottom glancing paths important.

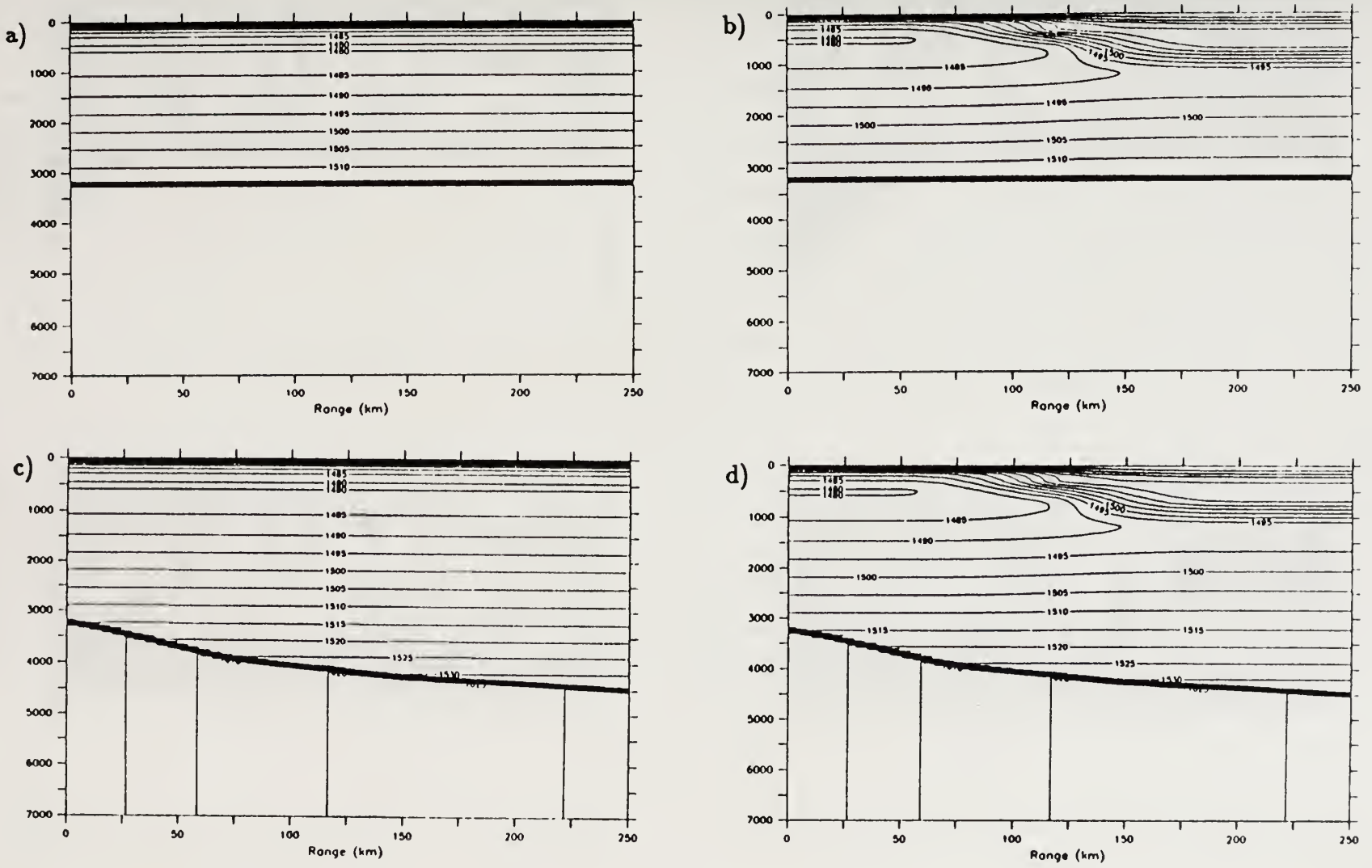

Figure 3.55) Sound speed contours. a. Slope water sound speed profile, 3170 m bottom. b. Slope to Sargasso water, 3170 m bottom. c. Slope water sound speed profile, realistic topography. d. Slope to Sargasso water, realistic topography.

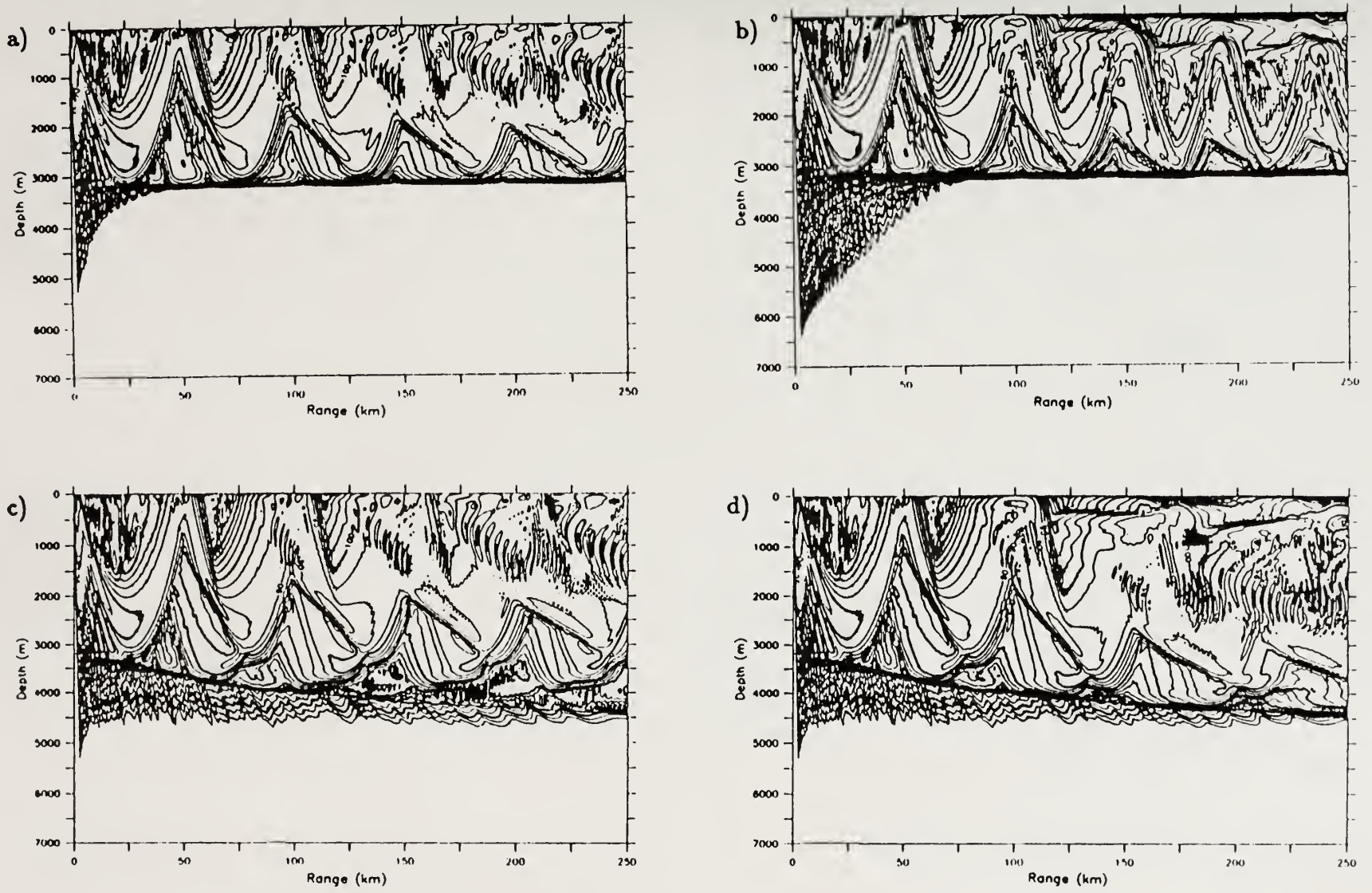

Figure 3.56) Propagation loss contours, $z_s = 100$ m, $f = 100$ Hz. a. Slope water sound speed profile, 3170 m bottom. b. Slope to Sargasso water, 3170 m bottom. c. Slope water sound speed profile, realistic topography. d. Slope to Sargasso water, realistic topography.

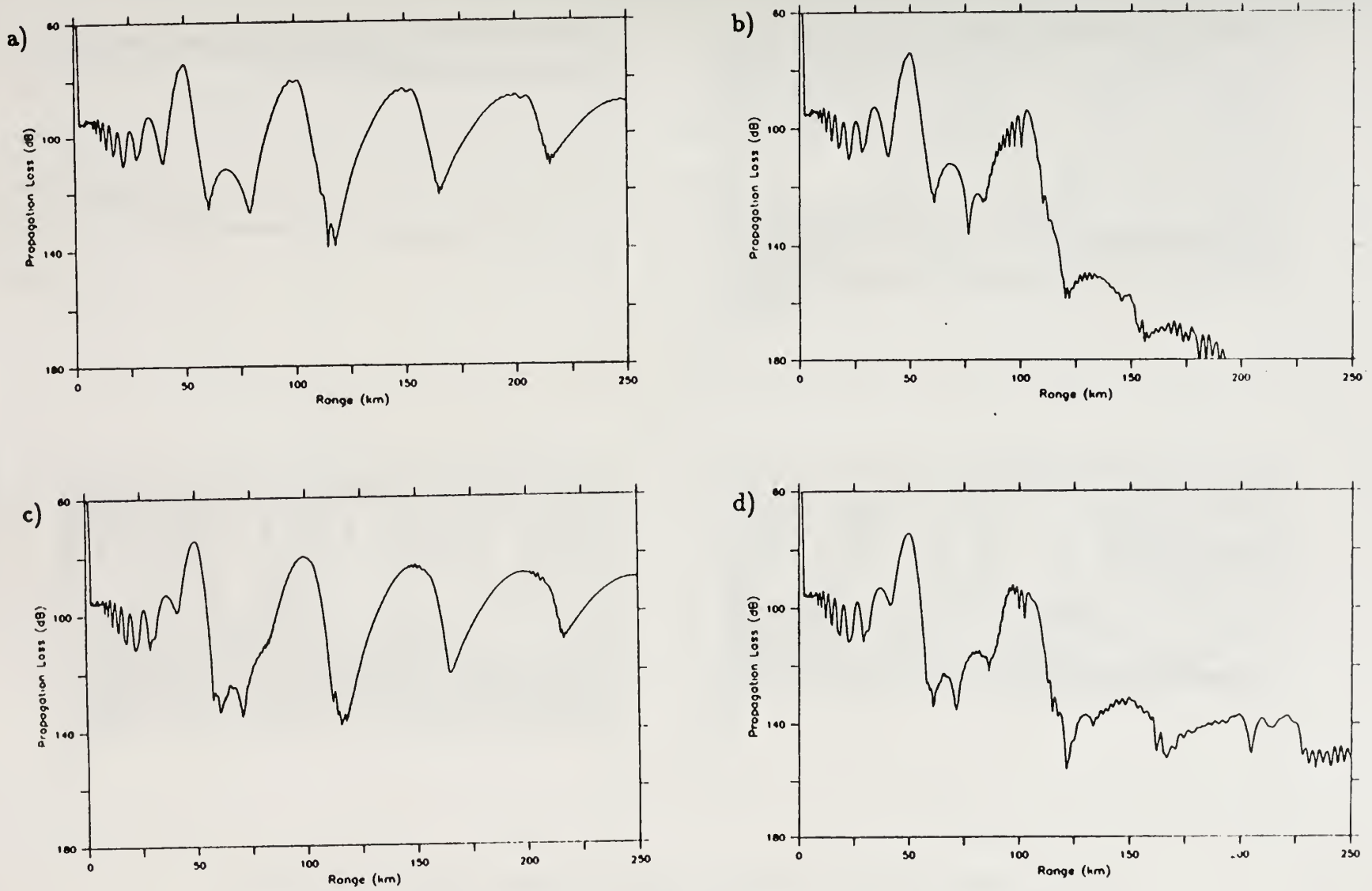

Figure 3.57) Propagation loss at 100 m receiver, $z_s = 100$ m, $f = 100$ Hz. a. Slope water sound speed profile, 3170 m bottom. b. Slope to Sargasso water, 3170 m bottom. c. Slope water sound speed profile, realistic topography. d. Slope to Sargasso water, realistic topography.

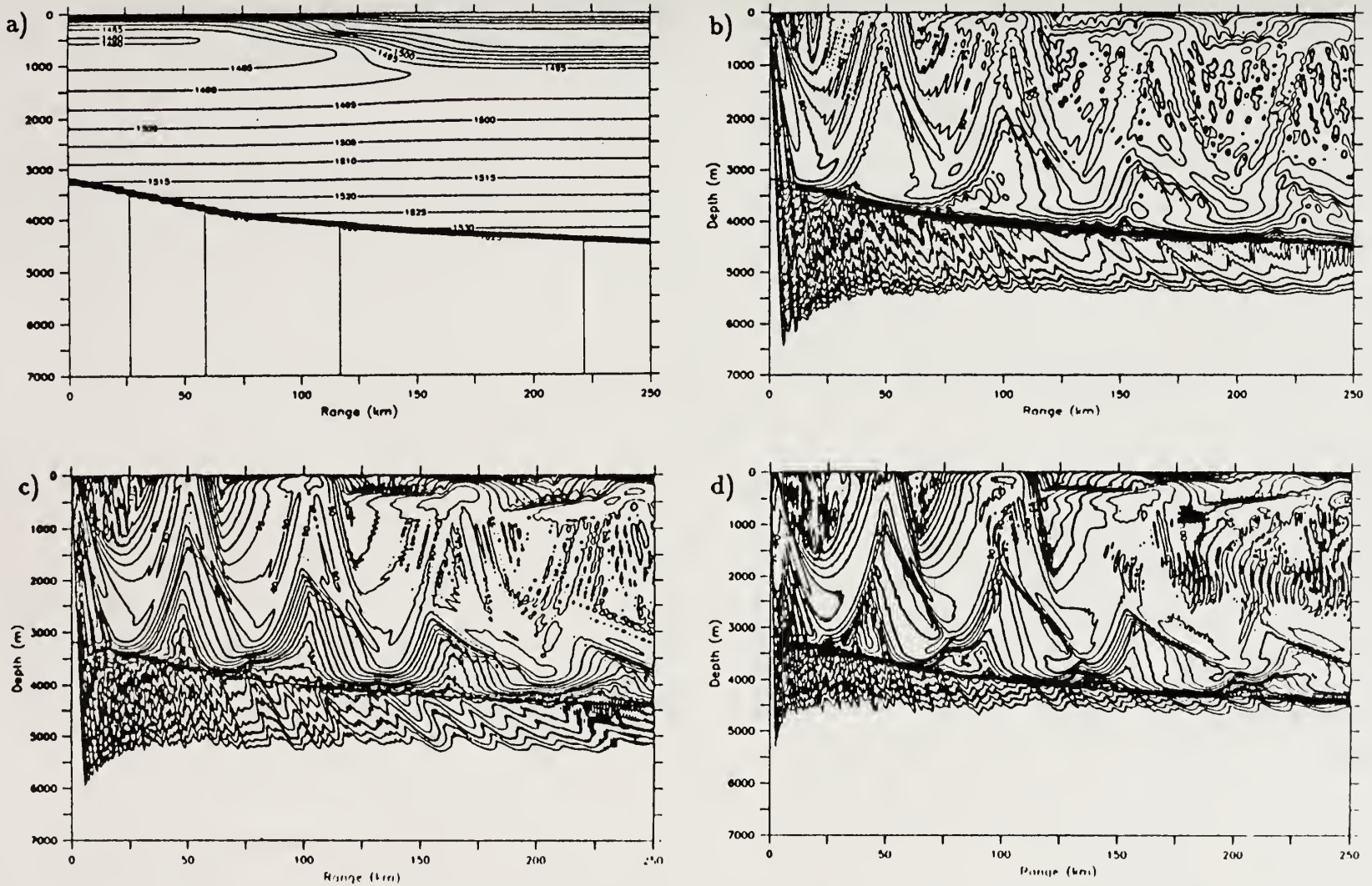

Figure 3.58) Realistic topography, Slope to Sargasso water propagation, $z_s = 100$ m. a. Sound speed contours. b. Propagation loss contours, $f = 25$ Hz. c. Propagation loss contours, $f = 50$ Hz. d. Propagation loss contours, $f = 100$ Hz.

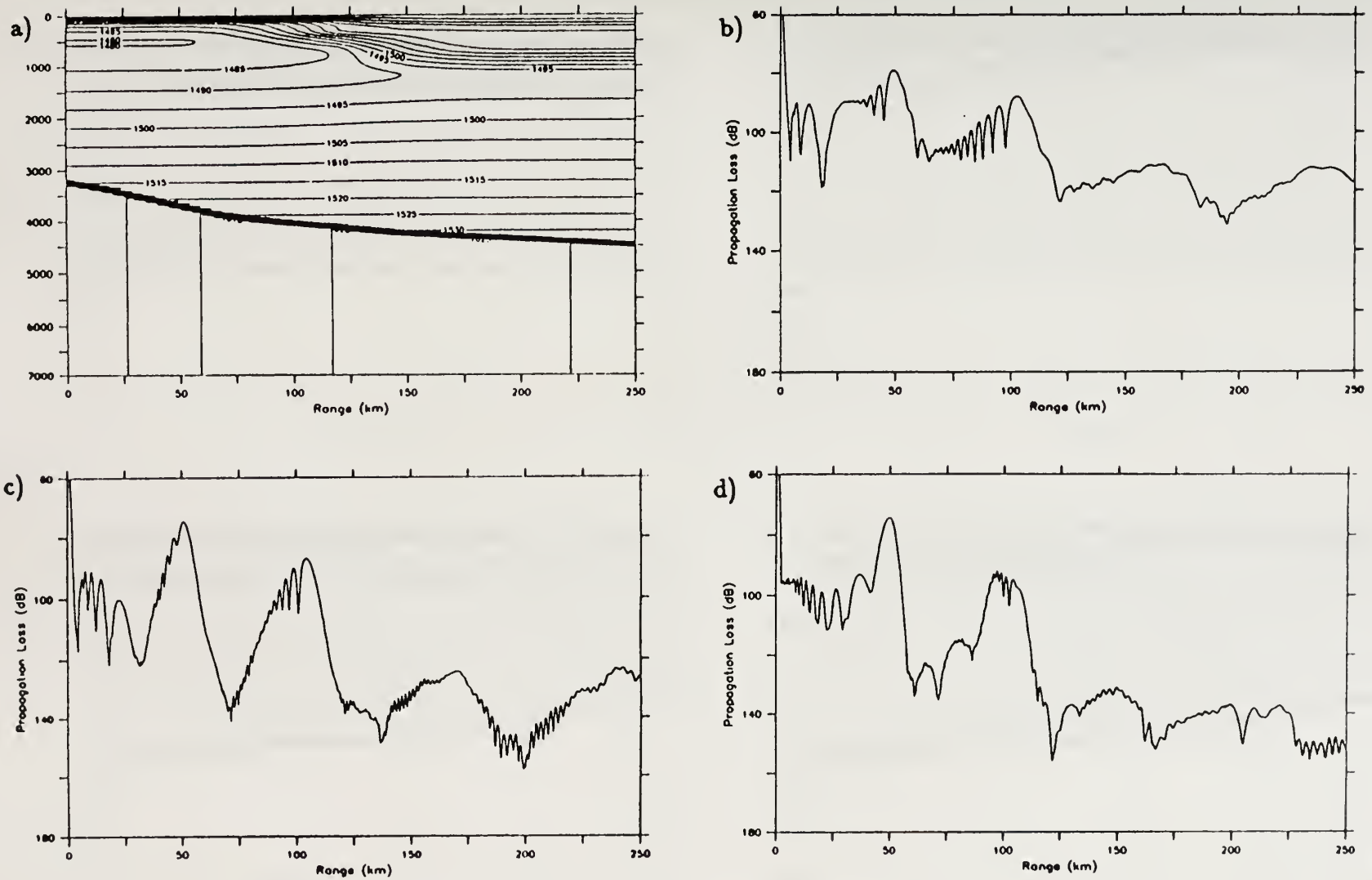

Figure 3.59) Realistic topography, Slope to Sargasso water propagation, $z_s = 100$ m. a. Sound speed contours. b. Propagation loss at 100 m, $f = 25$ Hz. c. Propagation loss at 100 m, $f = 50$ Hz. d. Propagation loss at 100 m, $f = 100$ Hz.

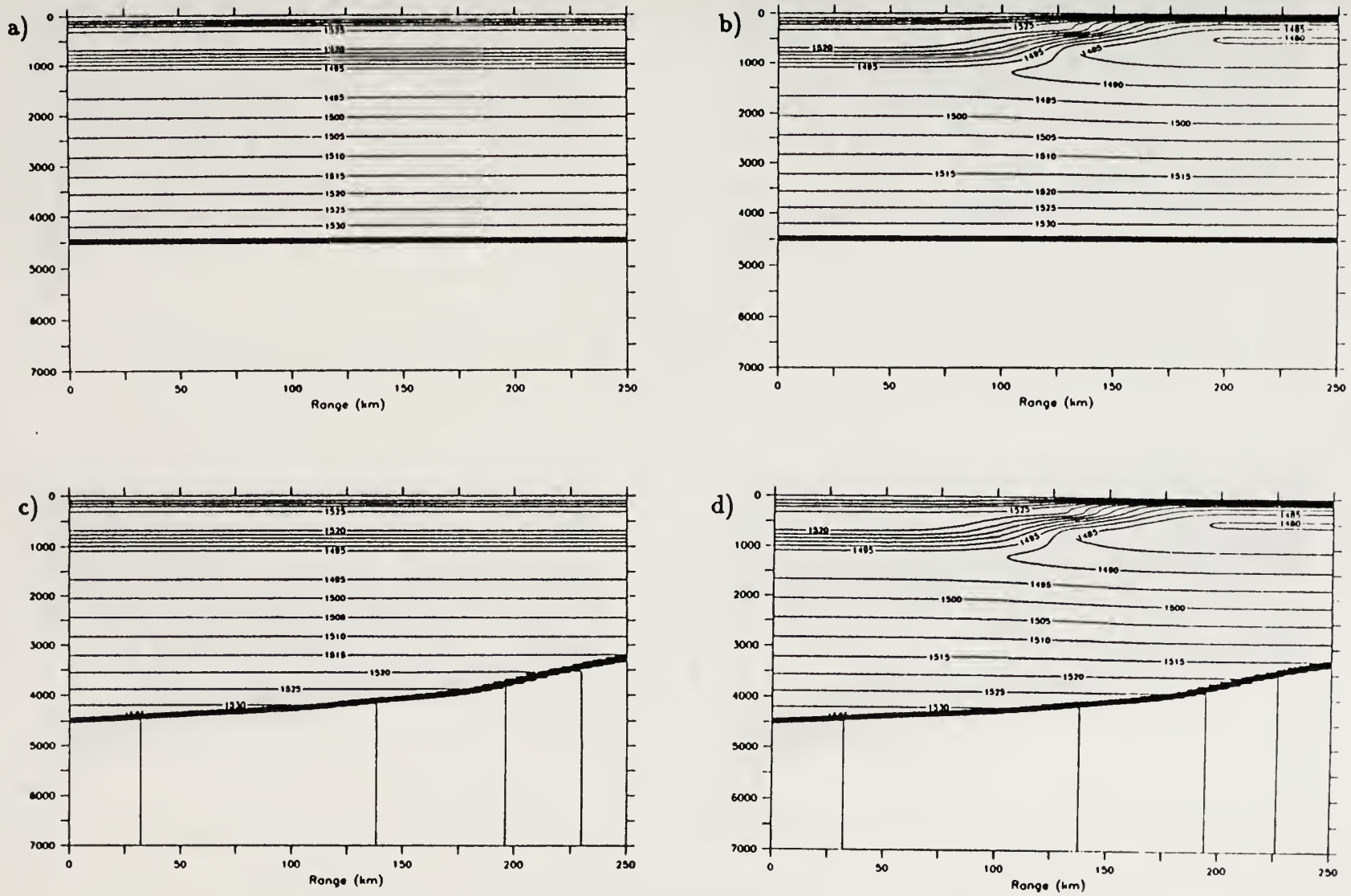

Figure 3.60) Sound speed contours. a. Sargasso water sound speed profile, 4440 m bottom. b. Sargasso to Slope water, 4440 m bottom. c. Sargasso water sound speed profile, realistic topography. d. Sargasso to Slope water, realistic topography.

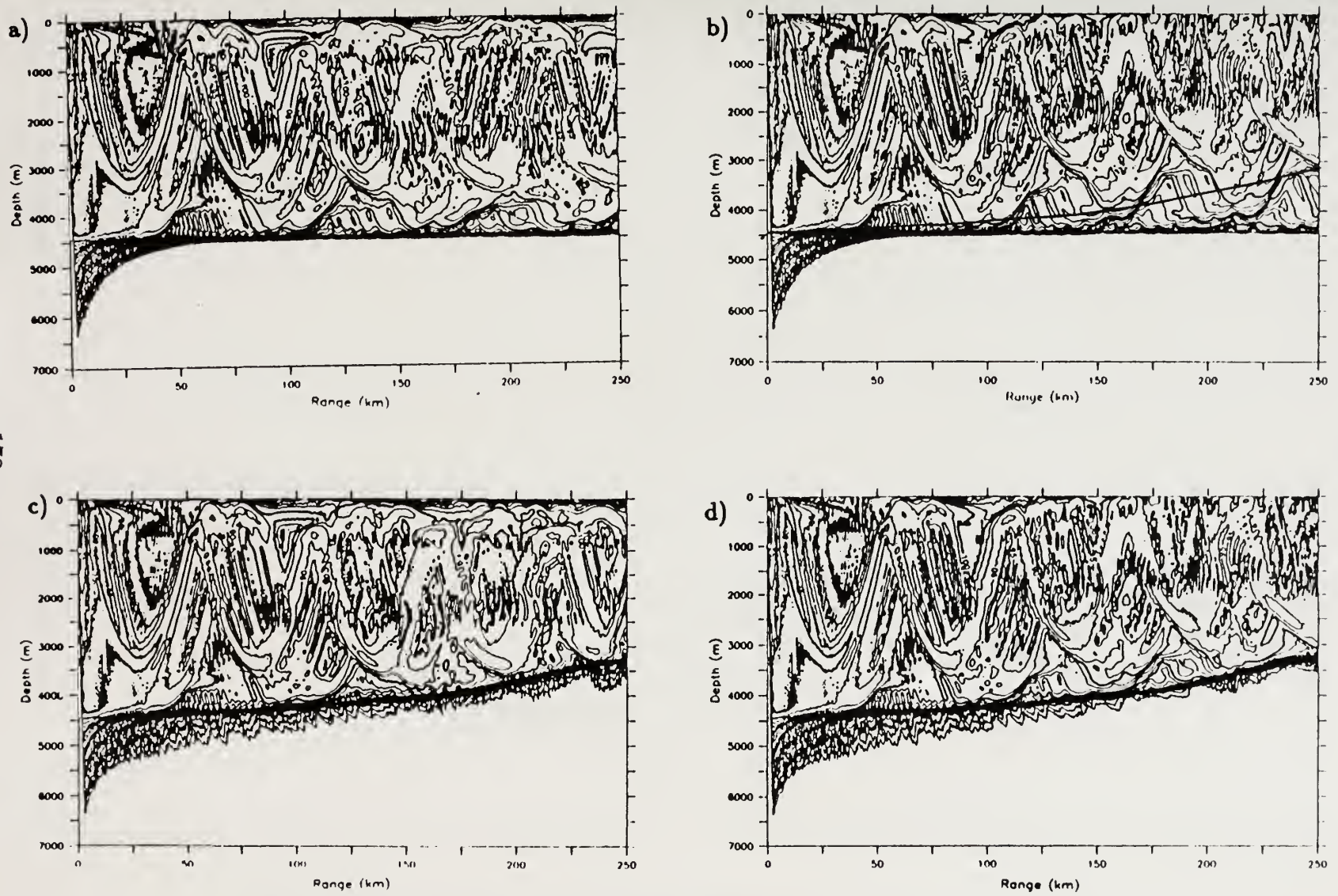

Figure 3.61) Propagation loss contours, $z_s = 750$ m, $f = 100$ Hz. a. Sargasso water sound speed profile, 4440 m bottom. b. Sargasso to Slope water, 4440 m bottom. Realistic topography overlaid. c. Sargasso water sound speed profile, realistic topography. d. Sargasso to Slope water, realistic topography.

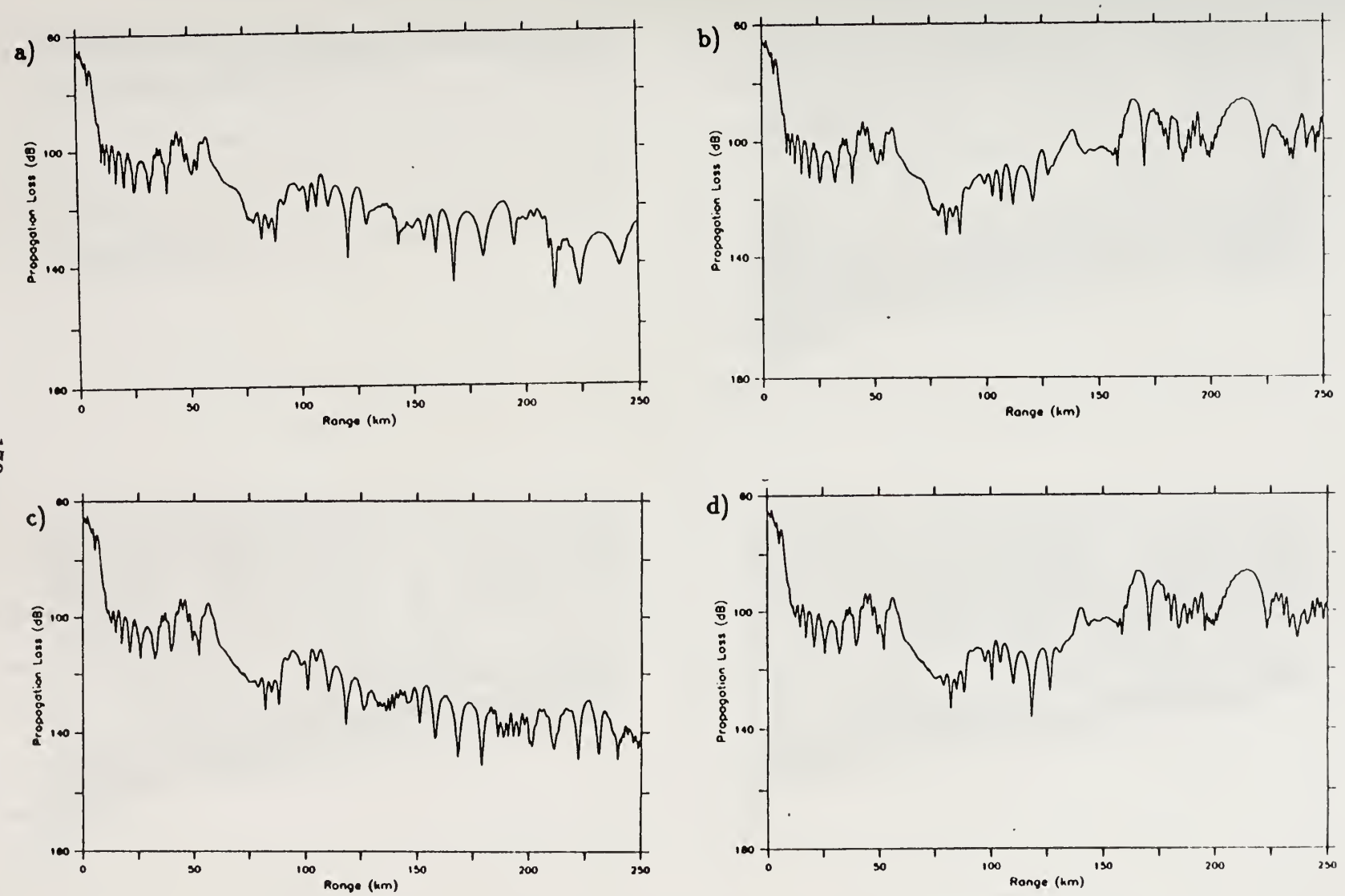

Figure 3.62) Propagation loss at 100 m receiver, $z_s = 750$ m, $f = 100$ Hz. a. Sargasso water sound speed profile, 4440 m bottom. b. Sargasso to Slope water, 4440 m bottom. c. Sargasso water sound speed profile, realistic topography. d. Sargasso to Slope water, realistic topography.

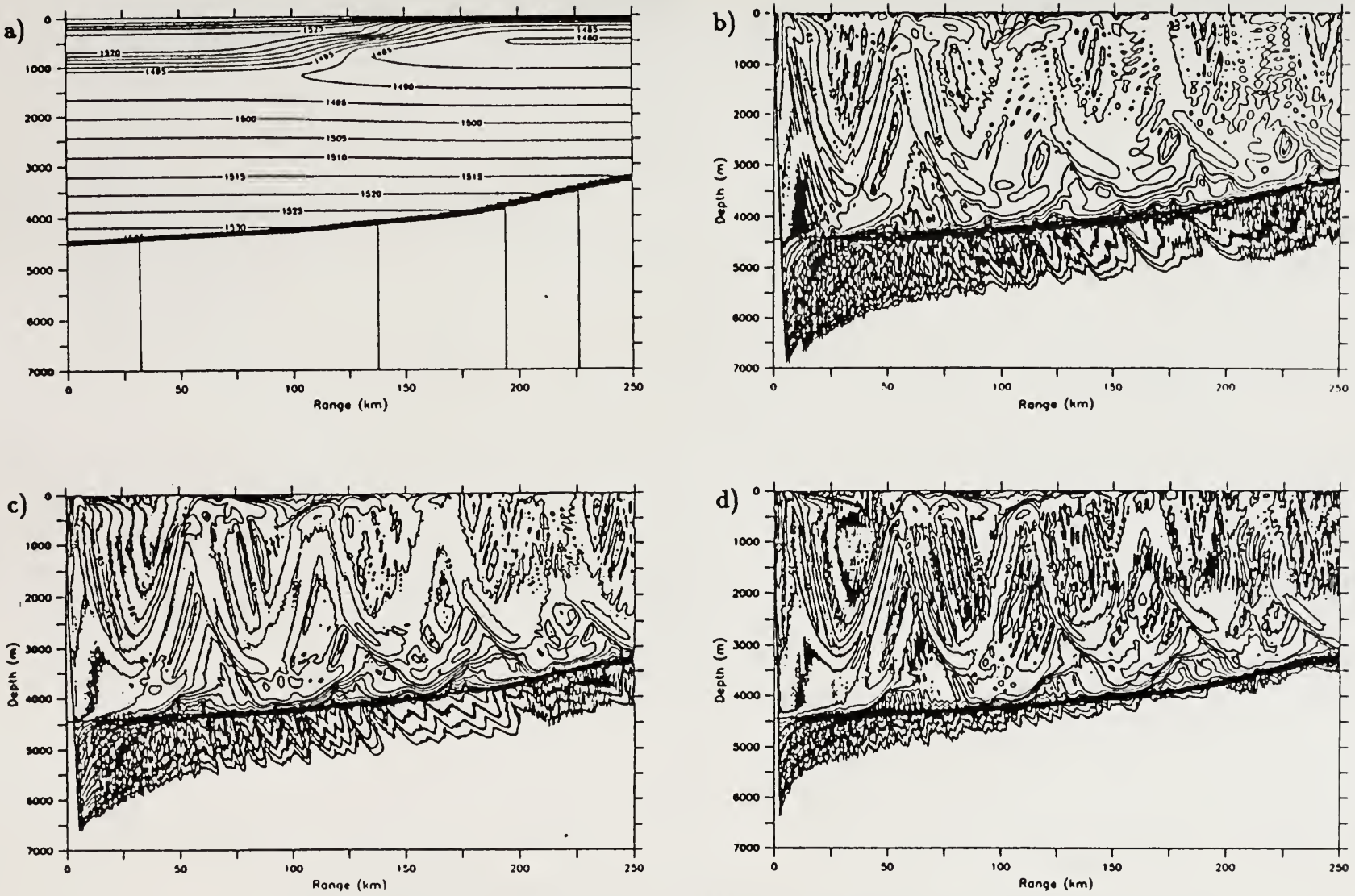

Figure 3.63) Realistic topography, Sargasso to Slope water propagation, $z_s = 750$ m. a. Sound speed contours. b. Propagation loss contours, $f = 25$ Hz. c. Propagation loss contours, $f = 50$ Hz. d. Propagation loss contours, $f = 100$ Hz.

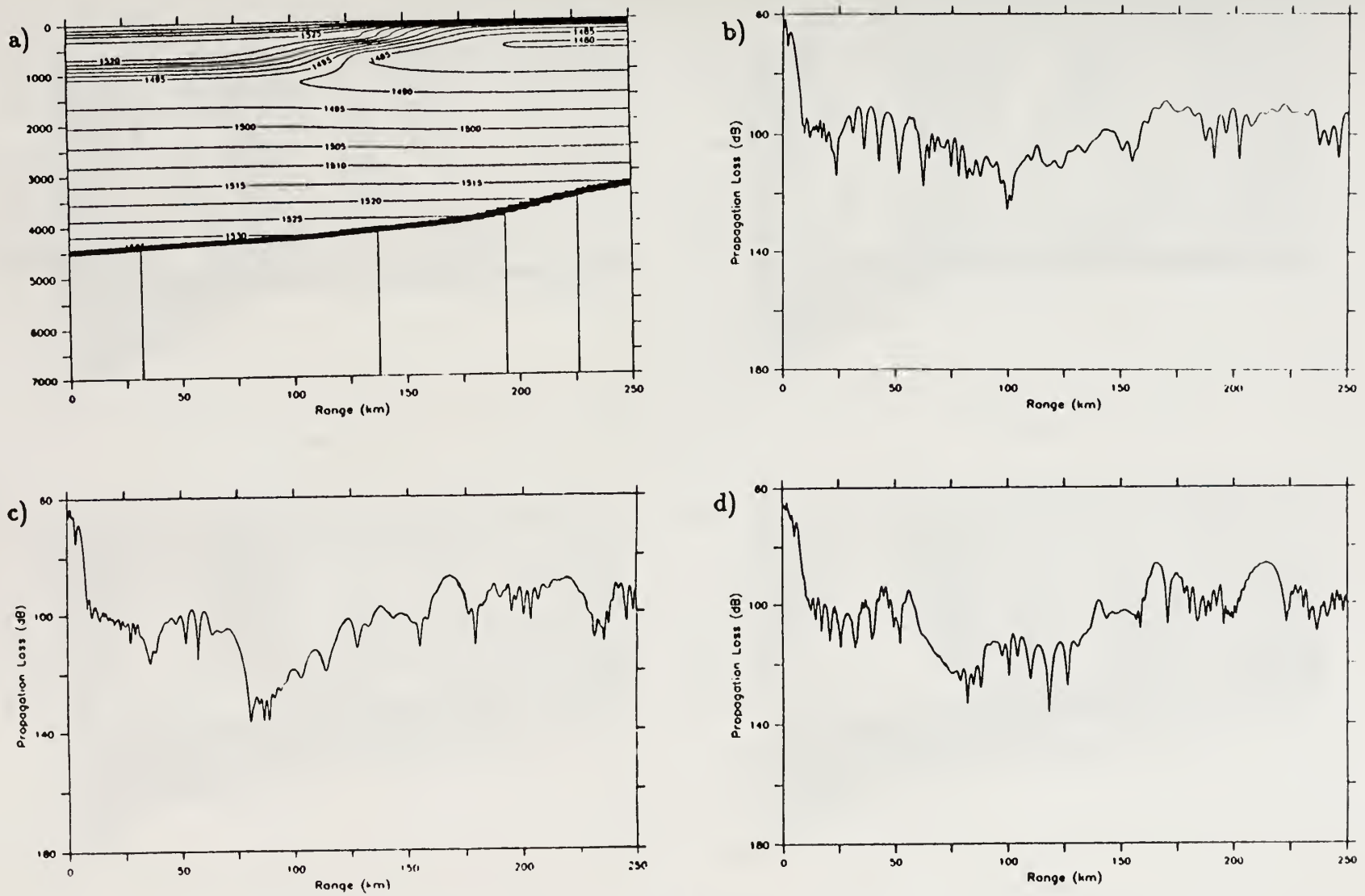

Figure 3.64) Realistic topography, Sargasso to Slope water propagation, $z_s = 750$ m. a. Sound speed contours. b. Propagation loss at 100 m, $f = 25$ Hz. c. Propagation loss at 100 m, $f = 50$ Hz. d. Propagation loss at 100 m, $f = 100$ Hz.

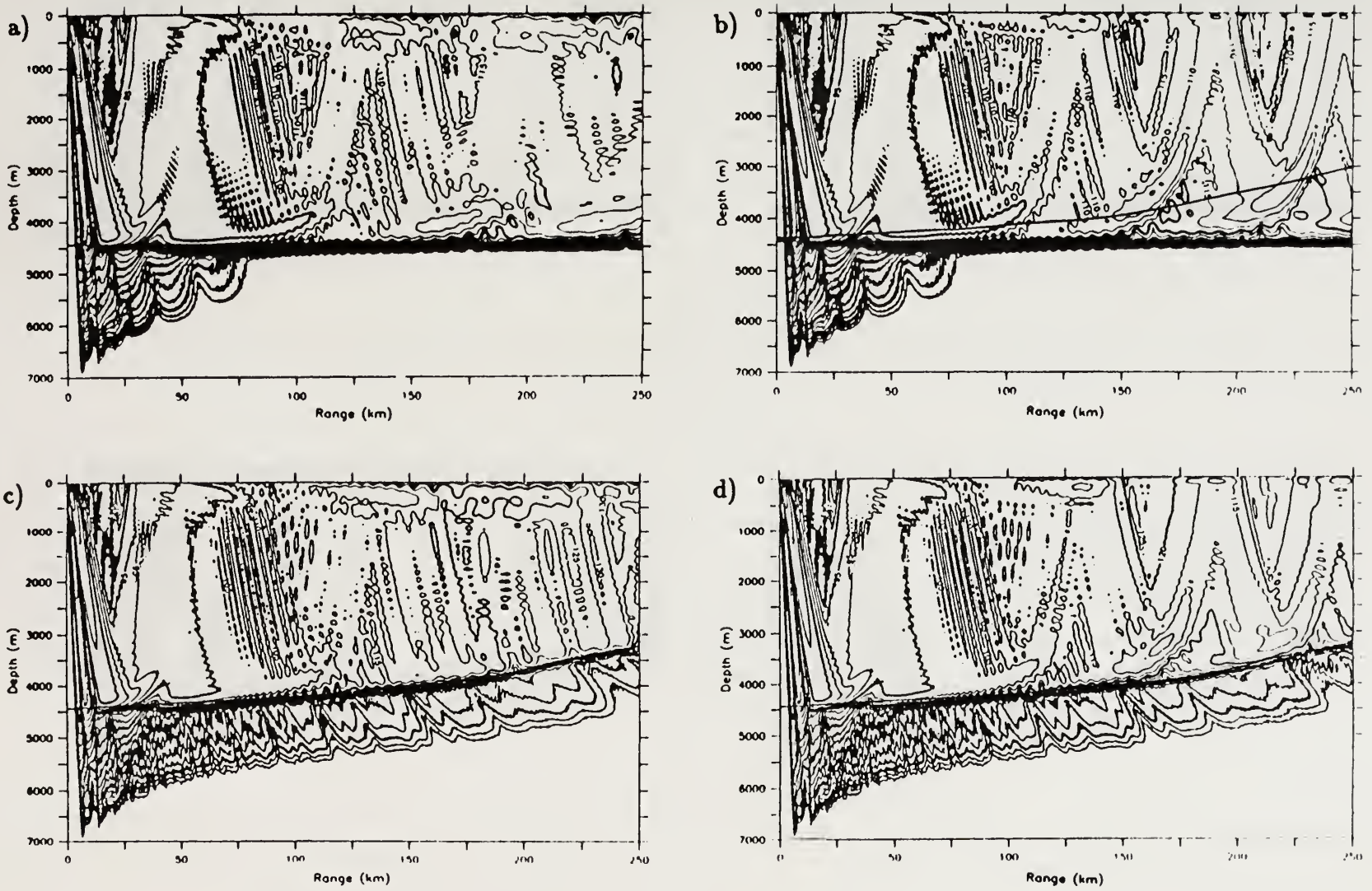

Figure 3.65) Contours of propagation loss. $z_s = 100$ m, $f = 25$ Hz. a. Sargasso water sound speed profile, 4440 m bottom. b. Sargasso to Slope water, 4440 m bottom. Realistic topography overlaid. c. Sargasso water sound speed profile, realistic topography. d. Sargasso to Slope water, realistic topography.

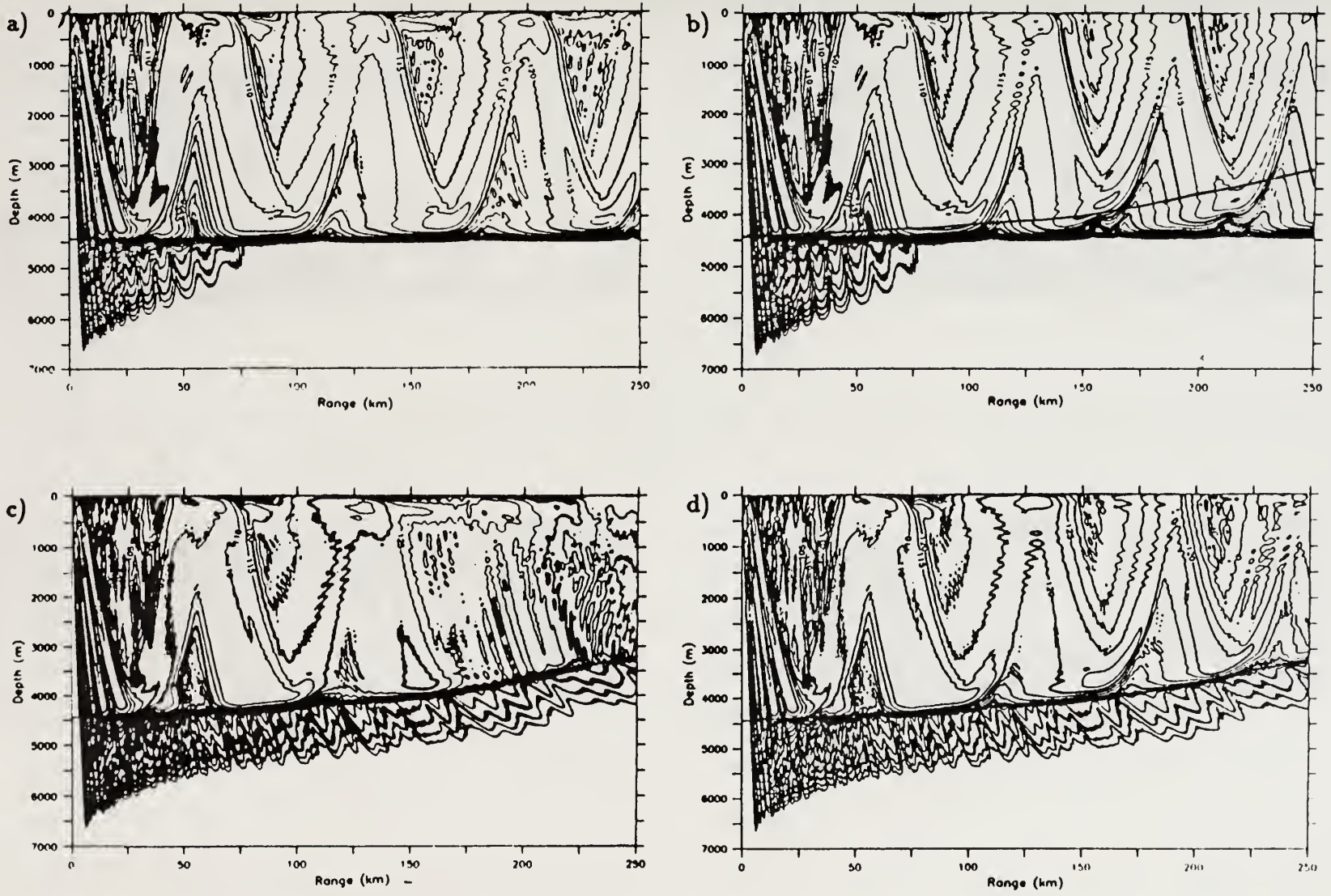

Figure 3.66) Contours of propagation loss. $z_s = 100$ m, $f = 50$ Hz. a. Sargasso water sound speed profile, 4440 m bottom. b. Sargasso to Slope water, 4440 m bottom. Realistic topography overlaid. c. Sargasso water sound speed profile, realistic topography. d. Sargasso to Slope water, realistic topography.

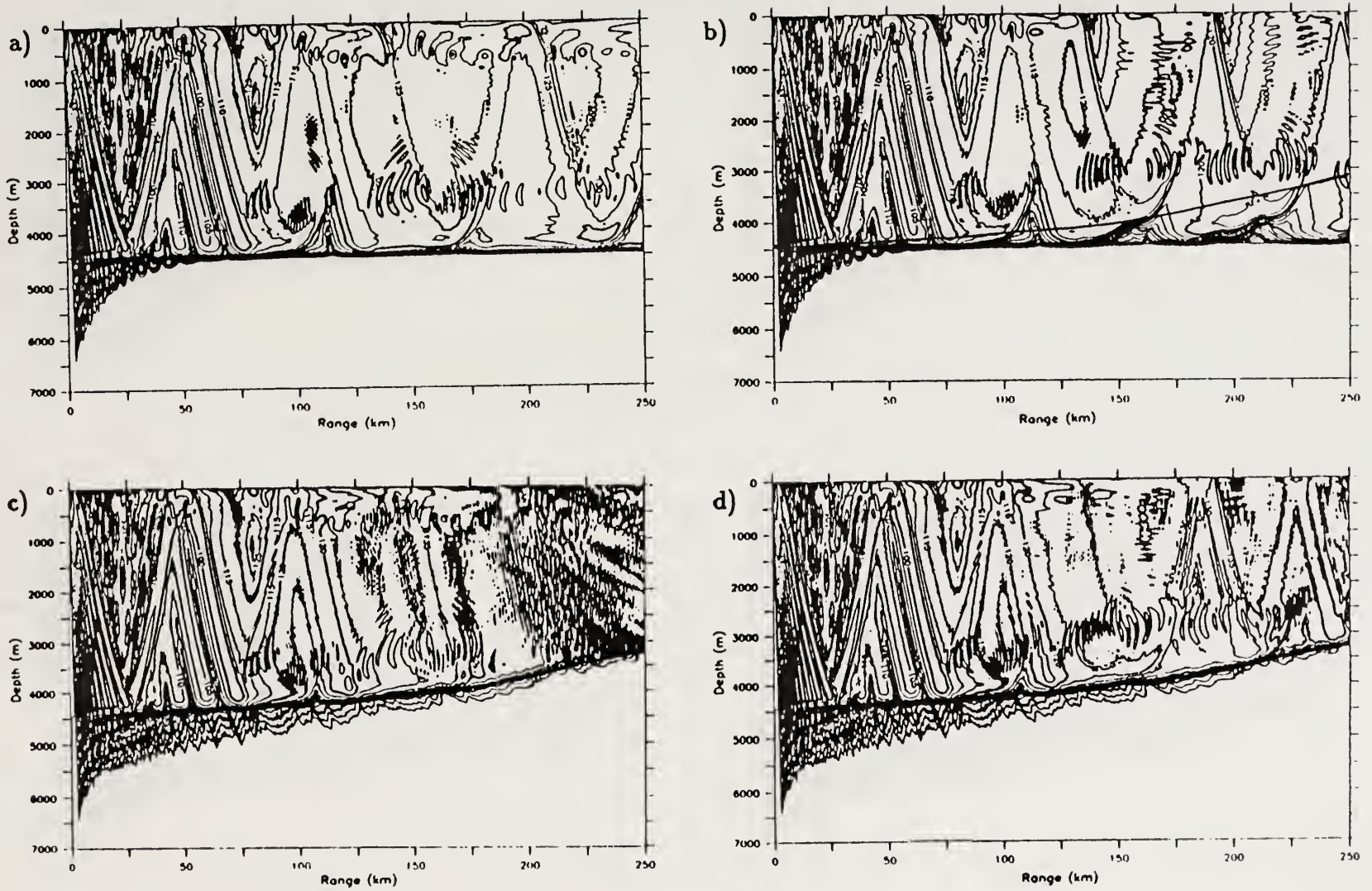

Figure 3.67) Contours of propagation loss. $z_s = 100$ m, $f = 100$ Hz. a. Sargasso water sound speed profile, 4440 m bottom. b. Sargasso to Slope water, 4440 m bottom. Realistic topography overlaid. c. Sargasso water sound speed profile, realistic topography. d. Sargasso to Slope water, realistic topography.

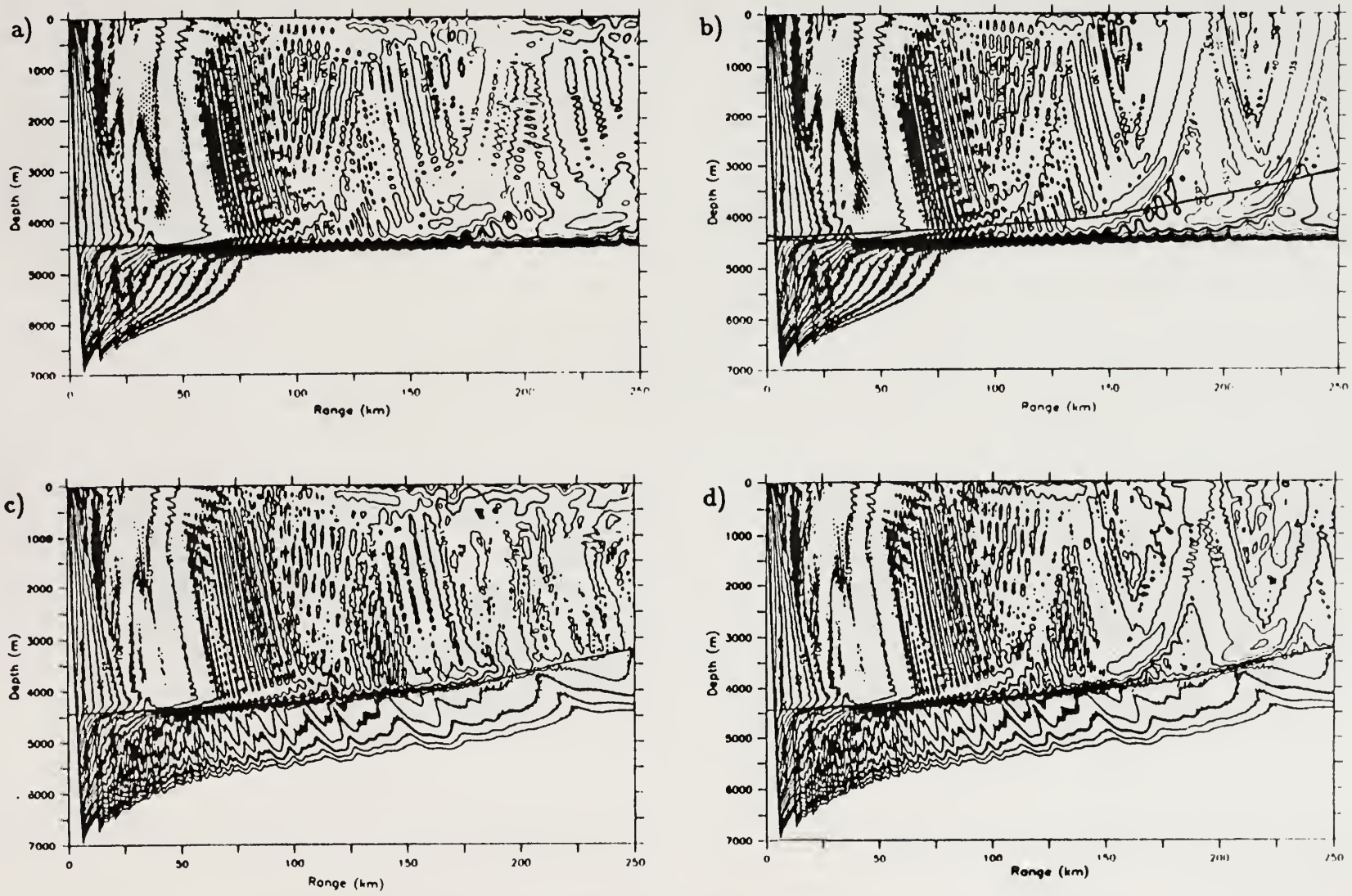

Figure 3.68) Contours of propagation loss. $z_s = 10$ m, $f = 25$ Hz. a. Sargasso water sound speed profile, 4440 m bottom. b. Sargasso to Slope water, 4440 m bottom. Realistic topography overlaid. c. Sargasso water sound speed profile, realistic topography. d. Sargasso to Slope water, realistic topography.

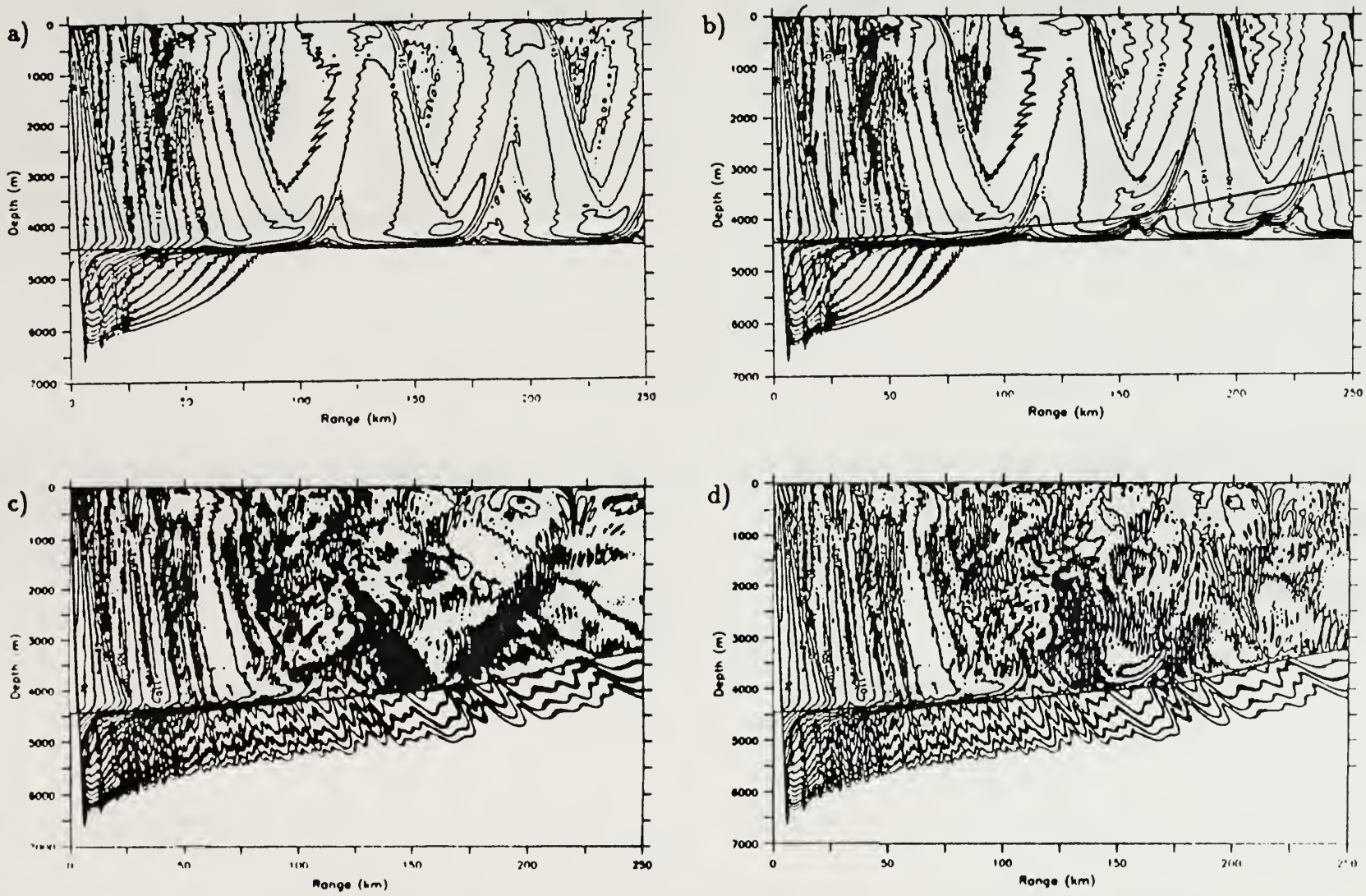

Figure 3.69) Contours of propagation loss. $z_s = 10$ m, $f = 50$ Hz. a. Sargasso water sound speed profile, 4440 m bottom. b. Sargasso to Slope water, 4440 m bottom. Realistic topography overlaid. c. Sargasso water sound speed profile, realistic topography. d. Sargasso to Slope water, realistic topography.

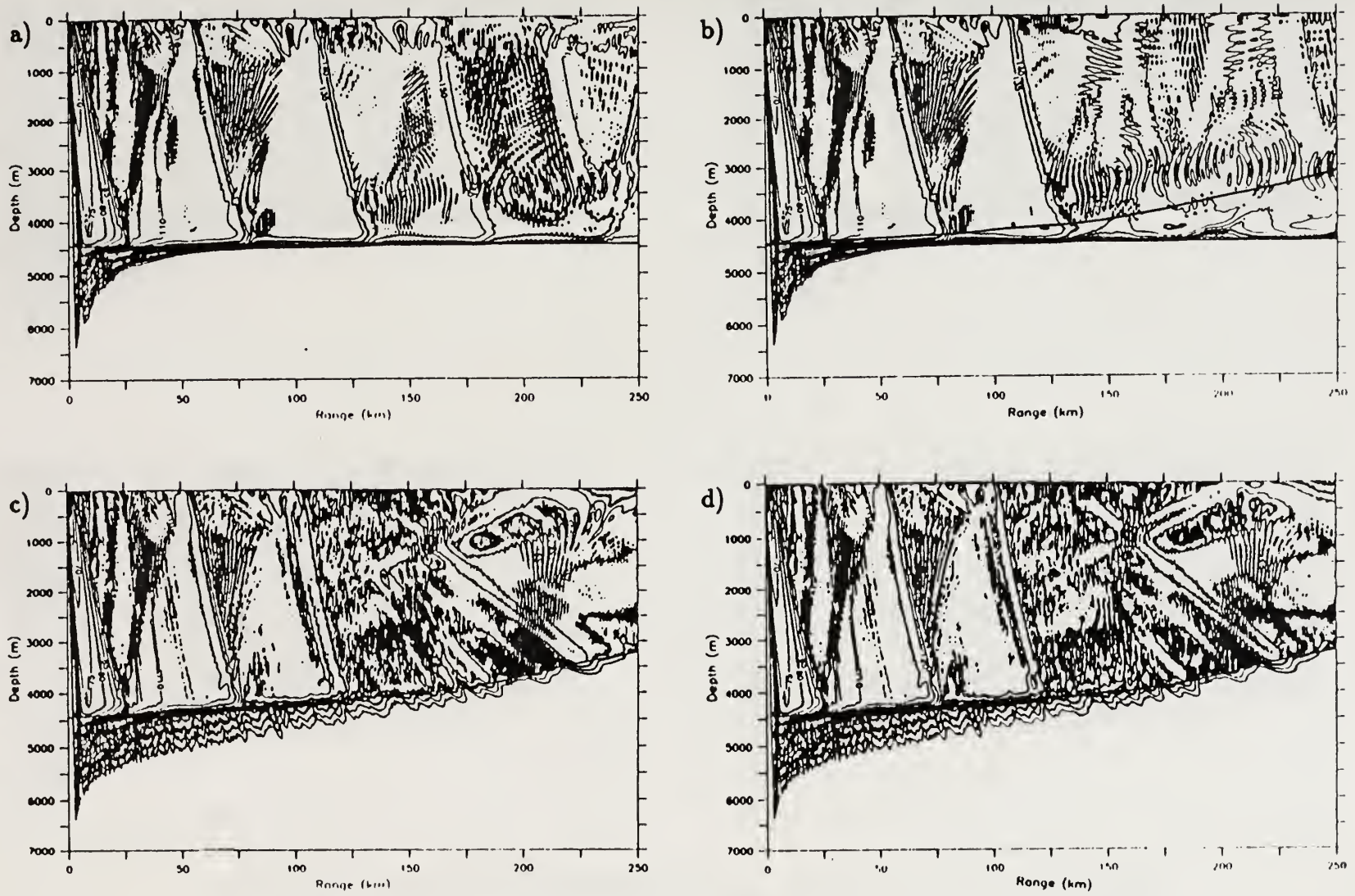

Figure 3.70) Contours of propagation loss. $z_s = 10$ m, $f = 100$ Hz. a. Sargasso water sound speed profile, 4440 m bottom. b. Sargasso to Slope water, 4440 m bottom. Realistic topography overlaid. c. Sargasso water sound speed profile, realistic topography. d. Sargasso to Slope water, realistic topography.

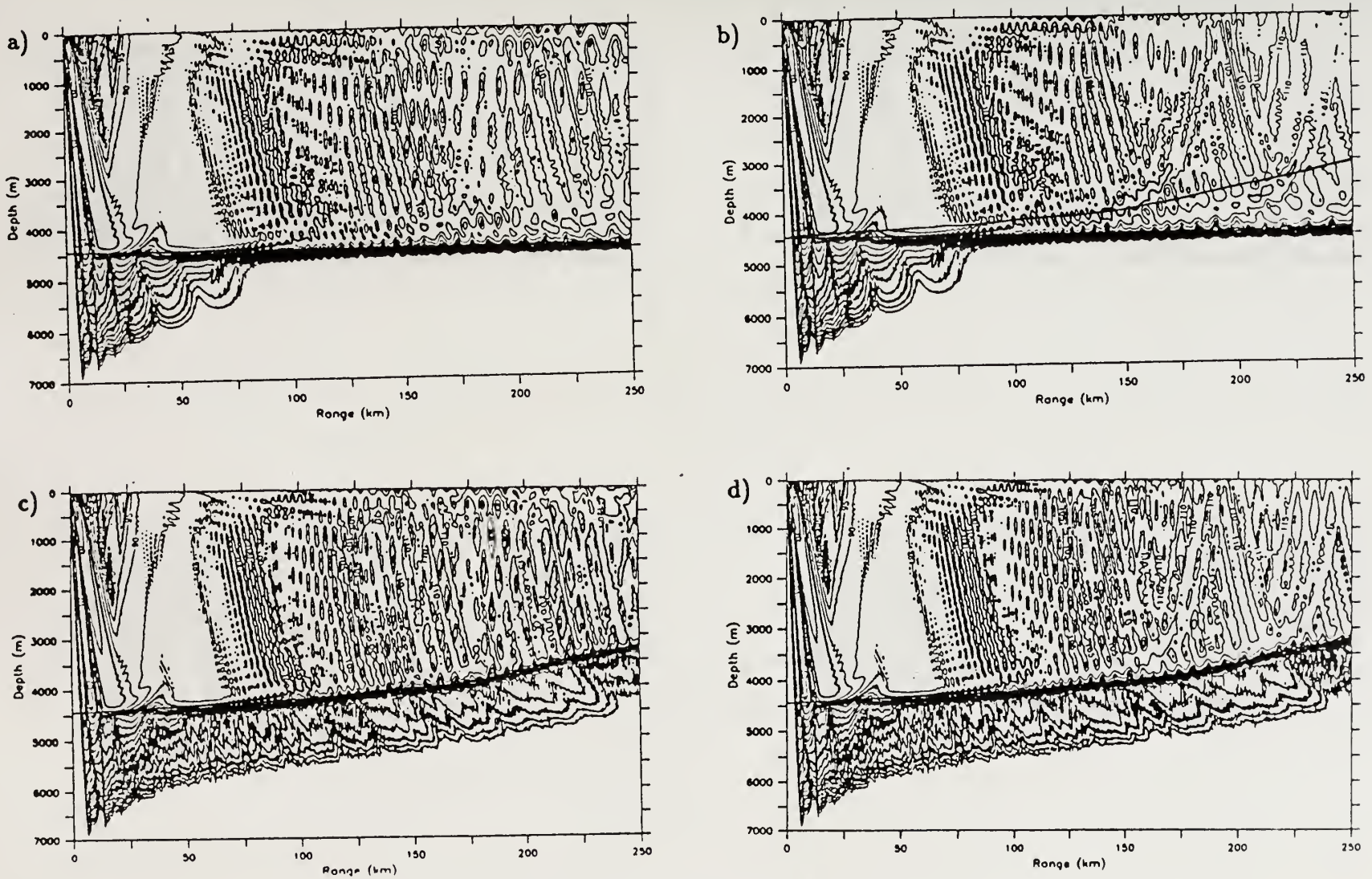

Figure 3.71) Contours of propagation loss. $z_s = 100$ m, $f = 25$ Hz. Sediment parameters: $\rho = 1.352$ gm/cm^3, $\beta = .9$ dB/λ, $c_w/c_b = 1.0$, $\partial c/\partial z = 1.227$ sec^{-1}, $z_{sed} = 100$ m. a. Sargasso water sound speed profile, 4440 m bottom. b. Sargasso to Slope water, 4440 m bottom. Realistic topography overlaid. c. Sargasso water sound speed profile, realistic topography. d. Sargasso to Slope water, realistic topography.

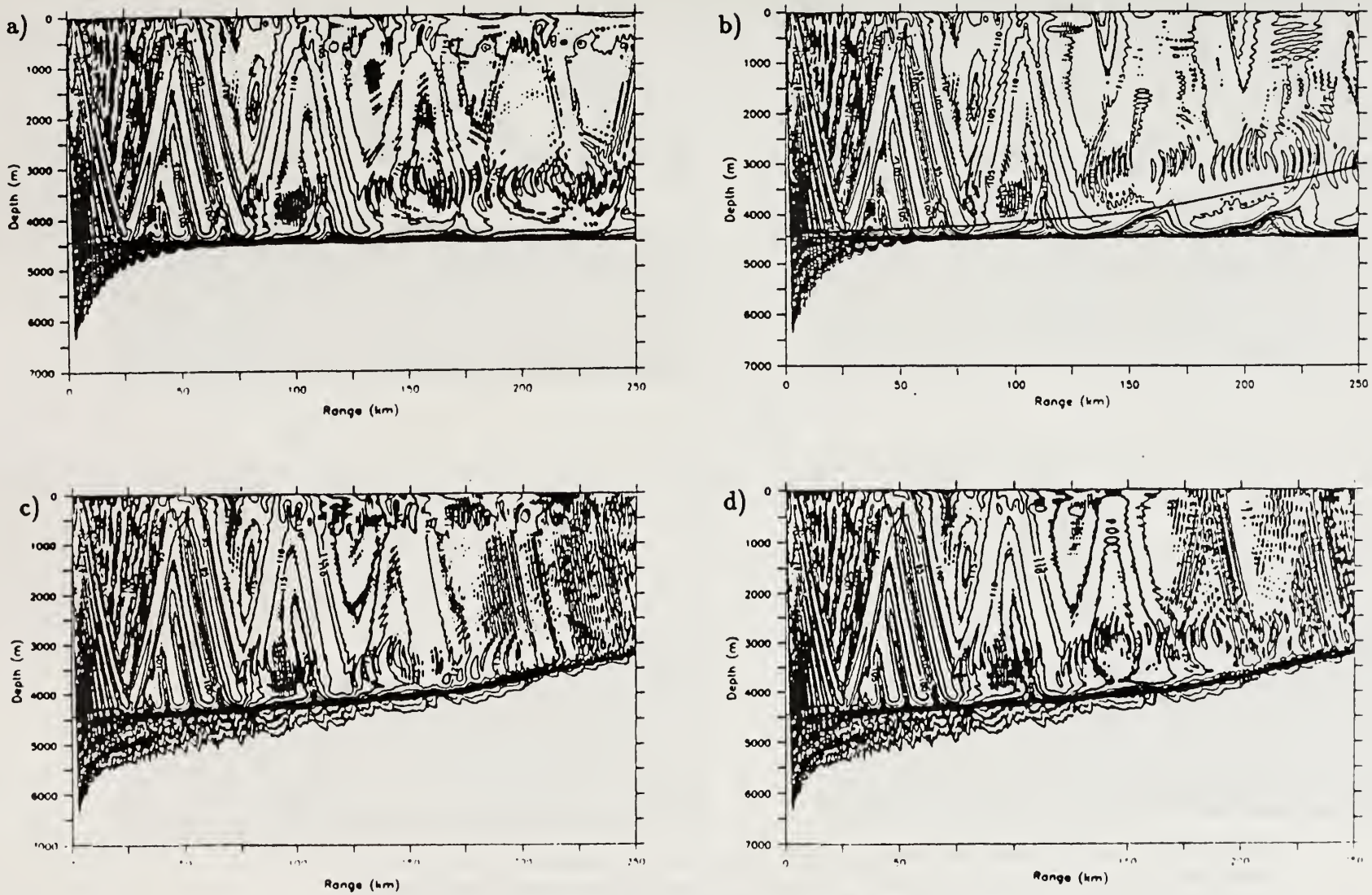

Figure 3.72) Contours of propagation loss. $z_s = 100$ m, $f = 100$ Hz. Sediment parameters: $\rho = 1.352$ gm/cm^3, $\beta = .9$ dB/λ, $c_w/c_b = 1.0$, $\partial c/\partial z = 1.227$ sec^{-1}, $z_{sed} = 100$ m. a. Sargasso water sound speed profile, 4440 m bottom. b. Sargasso to Slope water, 4440 m bottom. Realistic topography overlaid. c. Sargasso water sound speed profile, realistic topography. d. Sargasso to Slope water, realistic topography.

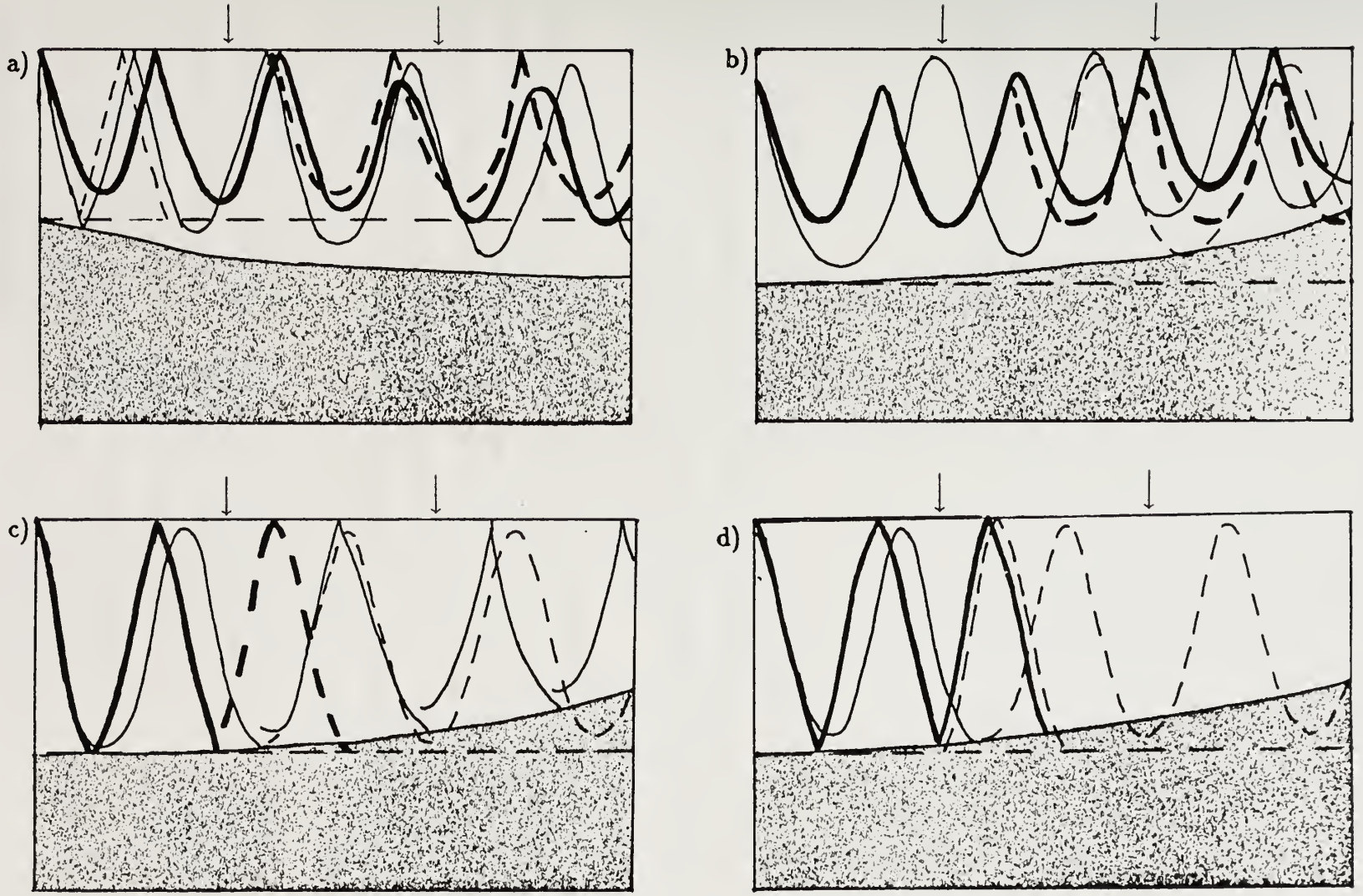

Figure 3.73) Schematic of Oceanographic/Topographic Interactions. Arrows represent approximate beginning and ending of Gulf Stream. a. Slope to Sargasso water. b. Sargasso to Slope water, primary sound paths refract with depth. c. Sargasso to Slope water, bottom glancing paths important; significant trapped mode excitation. d. Sargasso to Slope water, bottom glancing paths important; weak trapped mode excitation.

Chapter 4

Regional Acoustics

The analyses of oceanographic and topographic interactions presented in chapter 3 were specific to the form of the acoustic fields and the topographic configurations found in that region. The underlying physical principles delineated, however, can be applied in any region of the ocean.

In this chapter, we will look at acoustic propagation patterns in two widely differing oceanographic regions of the North Atlantic, the North Atlantic Drift current and the Iceland-Faeroes front. The North Atlantic Drift current is a meandering extension of the Gulf Stream, with a profusion of mesoscale eddies. The oceanographic variations are not as strong as in the Gulf Stream, but they do nevertheless affect the acoustic propagation. Topography in the particular region used was quite flat and does not strongly affect acoustic propagation.

The Iceland-Faeroes front, on the other hand, lies at the interface between the North Atlantic Drift and the colder Norwegian Sea water. An extension of the continental shelf runs between Iceland and Great Britain which drops off sharply to the ocean basin on either side, so the region is one of sharp topography. The Iceland-Faeroes front is a permanent water mass boundary that is trapped to the topographic shelf; the frontal position and shape varies, and mesoscale eddies form. The conjunction of the two physical features profoundly affects acoustic propagation in the region.

4.1 AthenA Region

An oceanographic experiment was carried out in the North Atlantic during July and August of 1988 near 52.5 N 25.5 W by the French Navy, on board their oceanographic research vessel *B.O. D'Entrecasteaux*, with three Harvard scientific personnel on board. The experimental region was known as AthenA (Acquisition de données de Topographie de surface et d'Hydrologie dans l'Est Nord Atlantique); the location was selected in view of the presence of mesoscale eddies of the North Atlantic Drift current, the relatively flat bathymetry, and excellent satellite altimetric coverage (le Squere, 1989). The data collected consisted of two separate realizations of the hydrographic fields from CTD and XBT stations, three moorings with current meters, and a meteorological buoy for acquisition of air-sea interaction data. Two Maresonde GT drifting buoys provided confirmation of the hydrographic fields. Satellite altimetric data received onboard the *B.O. D'Entrecasteaux* gave further information on frontal strength and location. The Harvard Open Ocean Model was run in the resulting oceanographic fields; additionally, the excellent data resolution and availability of meteorological information made this region an excellent choice to test the effects of inclusion of the oceanographic surface boundary layer effects on acoustic propagation. The six-level QG model outputs provided values of sound speed at depths of 125, 325, 675, 1375, 2175, and 2975 m. The surface boundary layer model that was coupled to the QG model provided values of sound speed at depths of 6, 19, 33, 49, 66, 85, 107, and 130 m. Sound speed fields were prepared from simple QG model outputs as well as the QG-SBL model outputs; where the SBL level was deeper than the QG level, the SBL output was accepted in preference to the QG value. The IFD model linearly extrapolates from the resulting profile to find a surface and bottom sound speed, then uses the Akima spline routine to smoothly interpolate between these points. Acoustic calculations were performed in day 3 of the model runs, to capture the evolution of the surface boundary layer.

At the top of figure 4.1 we have the streamfunction fields at 125 m depth, with the transect chosen for propagation drawn in. Propagation was across the southward-flowing jet between the warm anticyclonic feature to the west and the colder cyclonic eddy to the east. Temperatures were approximately 3.5°C higher in the warmer eddy than the cooler; the southward current between them flowed at speeds up to 50–60 cm/sec. Figures 4.1b and 4.1c show the sound speed

profiles at the westernmost and easternmost extent along the transect; in figure 4.1b, we have a broad, deep channel with axis near 1200 m depth and a weak increase in sound speed toward the surface. In figure 4.1c, the sound channel is sharper and the axis is shallower, near 500 m depth; the sound speed increases more rapidly toward the surface.

Figures 4.1d and 4.1e show temperature and streamfunction fields from the parallel QG-SBL calculation done in the dataset, with figures 4.1f and 4.1g again showing the sound speed profiles at the western and eastern extremes of the transect. In figure 4.1f we see that the primary effect of the surface boundary layer on the west side of the transect was to increase the sound speed in the upper 49 m by approximately 5 m/sec, and to modify the shape of the upper portion of the sound channel. On the east side of the transect, figure 4.1g shows that the surface boundary layer model did not increase the value of sound speed at the surface over that obtained from QG model outputs alone (an extrapolated value), but it did more closely define the shape of the upper portion of the sound channel. Note that this added definition in the upper part changed the spline fit near the channel axis slightly; the sound channel minimum is some 2 m/sec faster and 140 m deeper than with QG model outputs alone.

Sediment parameters used for the IFD model in this region were density $\rho = 1.604$ gm/cm^3, attenuation $\beta = 1.35$ dB/λ, interface sound speed ratio $c_w/c_b = 0.996$, sediment sound speed gradient $\partial c/\partial z = 1.71$ sec^{-1}, and sediment depth $z_{sed} = 300$ m. These parameters were obtained by using a geological atlas (Choubert and Faure-Muret, 1976) to determine sediment type and depth; numerical values were then obtained from Hamilton (1980). Based on the analysis of chapter 3, in view of the value of c_w/c_b we might expect the propagation patterns to be highly affected by bottom reflections; however, in figure 4.1 we saw that the sound speed profiles have $c_{bot} > c_{src}$ by a significant amount; according to the analysis of chapter 3, sound in waterborne paths will dominate propagation patterns and these cases will be relatively insensitive to the exact choice of sediment parameters.

Acoustic propagation calculations have been performed in four parallel sets of acoustic fields: range-dependent QG output fields from west to east along the transect in figure 4.1a, range-independent QG output fields using the profile in figure 4.1b, range-dependent QG-SBL output fields along the same transect,

and range-independent QG-SBL output fields using the profile in figure 4.1f. The range-dependent oceanographic calculations used realistic topography; the range-independent oceanographic calculations used flat topography with a depth of 3300 m. In view of the relative flatness of the realistic topography, the combinations of range-dependent oceanography with flat topography and vice versa were not calculated. Source depths were chosen at 10 m to be near the surface, 150 m to be below the duct, 500 m to be in the deep sound channel and 750 m to be between the two channel axes; frequencies used were 25, 50, and 100 Hz. In the upcoming calculations, occasional acoustic phenomena occurred that were not observed in the Gulf Stream parameter study, due to the specific choices of source depth, bottom depth, etc. used in that region. These phenomena will be pointed out as they appear.

4.1.1 Surface Boundary Layer Effects

It has been shown in the past that sound at mid to low frequencies will not become trapped in a surface duct; while the transition from ducting to non-ducting behavior can be somewhat nebulous, the formula $f = 1500/(0.008h^{3/2})$ gives a reasonable extimate of the lowest frequency for which sound energy will be trapped in a duct of height h in meters (Porter et al., 1990; Urick, 1983). With this formula we see that the lowest frequency that will be trapped in a 49-meter surface duct could be estimated at 547 Hz, well above the range of frequencies considered in this study; therefore the greatest benefit we can expect from the surface-boundary layer model at these frequencies is to see the effects of more detailed information about the upper structure of the deep sound channel.

This is indeed the case; and for the source near the surface, the increased resolution of the upper part of the profile again had little to no effect on propagation patterns, just changing interference patterns. However, with the source below the surface boundary layer, the increased resolution of the upper profile caused significant changes in ensonification of a receiver in that changed upper region of the sound speed profile and lesser changes to a receiver in the surface layer. We will look closely at the cases with $z_s = 150$ and 500 m.

Figure 4.2 compares acoustic propagation through the range-independent QG and QG-SBL output fields for the 500 m source at 50 Hz. The figures show

contours of propagation loss with the QG profile (upper left), propagation loss at the 10 m receiver (upper right, QG-SBL case bold), contours of propagation loss with the QG-SBL profile (lower left) and propagation loss at the 200 m receivers (lower right, QG-SBL case bold). In the 200 m receiver the QG-SBL example shows an increase in ensonification of 15–20 dB at 65 and 125 km range over the QG case; the increased definition of the upper portion of the QG-SBL sound speed profile causes a lower sound speed in the 50 to 250 m depth range, which permits sound from the deep sound channel to penetrate to shallower depths before refracting around. At the same time, the flatter sound speed gradient between 150 and 400 m depth increases the convergence zone radius of sound in this path. We see these particular refracting returns in the contour plot (lower left) around 250 m depth, 75 and 130 km range. Note in the QG case (upper left) these returns appear near 400 m depth, 80 and 130 km range; in the QG case they are nearly merged with other returns whereas in the QG-SBL case sound in this path is more easily differentiated from sound in other paths. Low frequency effects allow this sound to penetrate into the surface regions; in the QG-SBL 10 m receiver (upper right, bold) we see an increase in the ensonification of 5–8 dB at both 75 and 130 km ranges over the QG case. At 50 Hz this 10 m receiver is under two wavelengths away from the steep increase in the sound speed profile, near 50 m depth.

With the source at 150 m depth, these same effects appear. Figure 4.3 compares propagation with $z_s = 150$ m at 50 Hz through range-independent QG and QG-SBL fields (QG field propagation, top left; QG-SBL, bottom left). Receivers shown are at 10 and 350 m depth this time. In the QG-SBL propagation loss contours (lower left) we can see the effects of the modified sound speed profile increasing the convergence zone radius for shallow-angle sound in the center of the sound channel; the specific returns appear around 500 m depth at 70 and 125 km range. In the 350 m receiver (lower right, QG-SBL bold) this increase in convergence zone radius causes an increase of 20–25 dB over the QG case in the convergence zone null at 125 km range. Low frequency effects again allow some of this sound to penetrate into near-surface regions; the receiver at 10 m (upper right, QG-SBL case bold) shows an increase of 10–15 dB over the QG case at the same range.

These propagation comparisons between the QG and QG-SBL fields are

the first examples of a phenomenon that appears in subsequent such comparisons: due to the increase in sound speed in the surface boundary layer, the QG-SBL profile is slightly more downward-refracting than the QG profile. In the original Lloyd's Mirror pattern from the source and image, the interference beams that strike the sediment do so at shorter ranges and with steeper angles in the QG-SBL case than the QG case. Thus bottom reflection returns seen near 25–40 and 75 km range in the 10 m receivers are slightly closer to the source in the QG-SBL case than the QG case. Additionally, the interference beams that refract with depth do so at slightly greater depth in the QG-SBL profile, causing a slightly greater convergence zone radius than in the QG case. In this example the effect can be discerned in the 10 m receiver by the third convergence zone near 150 km range; in subsequent examples these phenomena will be even more obvious.

Additionally, this case with the source at 150 m provides an excellent demonstration of low-frequency interference phenomena when two of the original Lloyd's Mirror pattern energy lobes refract with depth, which was not seen in chapter 3 due to the specific source/frequency/bottom depth configurations. For example, in figure 4.3 we see a beam of energy refracting near 25 km range and 1750 m depth, and another near 3000 m depth; there is a null in between them that would not be seen in the infinite-frequency ray approximation. All the sound energy in the water column is effectively segregated into two groups—that which refracts at depth less than 2000 m, and that which refracts between 2300 and 3000 m. The calculation distance was not great enough to determine long-range effects of this segregation.

At 100 Hz, an interesting effect of the surface boundary layer appears, that can be best shown in the range independent calculations. Figure 4.4 compares acoustic propagation through range independent QG and QG-SBL fields for the 500 m source at 100 Hz. The figures show contours of propagation loss with the QG profile (upper left), propagation loss at 10 m receivers (upper right, QG-SBL case bold), contours of propagation loss with the QG-SBL profile (lower left), and propagation loss at 200 m receivers (lower right, QG-SBL case bold). In the propagation loss contour plots we see the same effect noted above of the increased resolution of the upper portion of the sound profile permitting sound in some paths to penetrate further upward in the channel and changing the convergence zone radii of sound in the center of the channel. The specific

modified returns appear near 250 m depth at 70 and 125 km ranges in the QG-SBL propagation loss contours. In the QG contour plot we see these same returns near 400 m depth at the same ranges.

These returns cause corresponding increases of 15–20 dB in the magnitude at the 200 m QG-SBL receiver over the magnitude at the 200 m receiver in the QG example. Note again that in the 10 m receivers the QG-SBL case does not show the increase; at 100 Hz the QG-SBL 10 m receiver shows a 7–10 dB decrease in ensonification over the QG 10 m receiver at these ranges. The increase in frequency has been sufficient to effectively prevent this sound from penetrating into the surface regions; at 100 Hz this 10 m receiver is closer to 3 wavelengths away from the steep increase in the sound speed profile, near 50 m depth. Although the surface boundary layer is too thin to form a duct for 100 Hz sound, it nevertheless effectively bars some of the deeper sound from reaching the surface at this frequency.

We can also see this effect with the 150 m source at 100 Hz; figure 4.5 compares range independent 100 Hz propagation through QG fields (top left) with propagation through QG-SBL fields (bottom left), receivers are at 10 and 200 m with the QG-SBL case bold. In the QG propagation loss contours (upper left) we see a sound maximum of 80–85 dB reach the surface near 110 km range. In the QG-SBL case (lower left), sound in this path refracts around at the base of the surface boundary layer, causing a broadening of this propagation path with magnitudes 85–90 dB and decreasing at this range. The QG-SBL 200 m receiver (bold) shows a corresponding 15–20 dB increase in magnitude near 125 km over the QG 200 m receiver, due to the alteration in propagation path. Note that at 100 Hz this secondary sound maximum is effectively prevented from penetrating into the surface region by the higher sound speeds within the surface boundary layer. In the 10 m receiver, we see a decrease of 10 dB magnitude at 110 km; indeed, the whole secondary maximum that appears at that range in the QG case is not present in the SBL case. Thus at 50 Hz (figure 4.3) we saw an increase in ensonification of the surface layer of approximately 10 dB due to diffraction from the altered sound path in the improved resolution of the upper profile; at 100 Hz we see a decrease in near-surface ensonification due to higher-frequency blocking from the surface mixed layer.

Due to the particular source location and frequency, this example demon-

strates particularly dramatically the shifting of bottom reflection returns and convergence zone returns due to the increase in downward refraction in the QG-SBL profile over that in the QG profile. In the 10 m receivers, the bottom bounce returns near 25–35 km and 75 km have shorter ranges in the QG-SBL case than the QG profile; additionally, the convergence zones near 50, 100, and 150 km have increased radii in the QG-SBL case. These same differences appear in the 200 m receivers. This case shows these phenomena strongly because of the particular spacing of interference lobes seen for this source depth and frequency.

4.1.2 Range Dependent Effects

Adding range-dependence to the propagation comparisons, we see in figure 4.6 for the QG-output case with source at 150 m, that the effect of the range-dependent oceanography is to both decrease the value of sound speed at the sound channel axis and to make that axis shallower, although surface sound speeds do not decrease. Inclusion of realistic topography adds the small underwater hill seen at left in figure 4.6a. The plots of receivers at 10 m depth (upper right) and 200 m depth (lower right) are overlaid with corresponding receivers from the range-independent QG case, with range dependent receivers bold.

We see that the primary effect of the oceanography has been to shorten the convergence zone radius. In the range-independent case we see surface convergence zones near 50, 100, and 150 km range; with the range dependent oceanography these convergence zones occur at 50, 95, and 135 km range. Comparing the contours of propagation loss in the range dependent case to the QG range independent case (figure 4.3a) we see that the shortening of convergence zone radius modifies the shallow-angle part of the sound field more than the deep-angle part, throwing the two major propagation paths out of phase. This differential effect may decrease convergence zone coherence or lead to "split" convergence zones at greater ranges than calculated here.

The primary effect of the topographic hill has been to change the locations of the reflected returns from lesser, steep-angle Lloyd's Mirror maxima, by changing the depths at which they reflect. Since the IFD model treats the bottom as locally flat, the angle of topography will not affect the angle of reflection; however, since these beams have finite width, the change in depth over

the beam's width will cause interference phenomena. The third Lloyd's Mirror lobe strikes the bottom near 18 km range at the edge of the hill, and thus at almost the same depth as in the flat bottom example. This return appears near 30 km range in the 10 m receiver; interference effects cause the beam to split into three separate maxima. The QG-SBL range dependent output fields (figure 4.7) show the same effects of shortening the convergence zone radii and topographic reflection effects.

4.1.3 Summary of AthenA Region Propagation Effects

Thus we have seen two separate types of propagation phenomena in this region, one due to inclusion of a surface boundary layer and the other due to inclusion of range dependent oceanographic fields. The inclusion of the surface boundary layer alters the shape of the upper profile, both through an increase in sound speed in the layer, and through the better definition of the region just below the layer. The increased resolution below the surface boundary layer caused a decrease of sound speed in the 50–250 m deep region, compared with the sound speed fields from the QG model alone. For a source deep in the sound channel, this condition alters the propagation paths of some of the sound, permitting propagation closer to the surface. Figure 4.8a schematizes this case, where the bold line represents propagation through QG-SBL outputs and the light line represents propagation through QG outputs. The altered QG-SBL profile permits greater shallow excursion of the sound, which can alter sound magnitudes by 20 dB or more at the location of the path; at low frequencies this sound can penetrate into the surface region and increase sound magnitudes by 10–20 dB.

Under other propagation conditions, inclusion of the surface boundary layer can alter sound paths away from the surface. Figure 4.8b schematizes this situation, with the shallow angle paths drawn to long ranges. SBL case is bold, QG case is light. The higher sound speeds in the surface mixed layer have prevented the particular propagation path from reaching the surface, which alters local ensonification by 20–30 dB or more. At 25 and 50 Hz, low-frequency diffraction permitted some sound in this deeper path to reach the surface (although magnitudes were less, only 10 dB, at 50 Hz), while at 100 Hz the sound was excluded from surface regions. Thus at frequencies too low for trapping within a

surface duct, there will be a range of low frequencies for which the low-frequency diffraction will permit ensonification of the surface regions, and a range of middle frequencies at which sound will be excluded from the surface regions. We can expect the division between these two regimes to be somewhat diffuse, and the frequencies and strength of this effect to depend on both surface layer depth and magnitude of sound speed increase in the layer.

Additionally, inclusion of the surface boundary layer renders the profile more downwardly refracting, as schematized in the deep paths drawn in figure 4.8b, with the SBL case bold and QG case light. The higher sound speeds near the surface influence the Lloyd's Mirror interference patterns, causing the energy maxima to propagate more steeply than in the QG-output case. The steeper propagation of the deepest refracting maximum increases convergence zone radius by as much as 1–2 km, while the steeper propagation of the bottom-reflecting maxima decreases their repeat distance by as much as 2–3 km. The magnitude of this effect will vary, depending on frequency, profile shape, and source depth via the original interference patterns.

Inclusion of range dependence in the oceanographic fields involved both a decrease in channel axis sound speed and a shallowing of the channel axis. The decrease in sound speed at the channel axis increases the curvature of propagation paths and decreases the convergence zone radius, as schematized in figure 4.8c, with range dependent propagation bold and range independent light. The shallowing of the channel axis causes sound to reflect off the surface, where in the range independent case the corresponding path refracted close to the surface. The range dependent propagation paths return to the surface at shorter distances as they encounter the altered fields. The decrease can cause local differences of 30–40 dB in sound magnitude.

Also shown in figure 4.8c is the effect of the realistic topography, with its small hill at left. Interference maxima which strike the sediment at shallower depth return to the surface at shorter range than those which encountered the deeper flat bottom. These cases showed a change of approximately 5 km range in the near-surface return. The magnitude of topographic effect will depend on location, although the AthenA region was chosen in part for its flat bathymetry.

4.2 Iceland-UK Gap Region

The Iceland-Faeroes front forms the boundary between the North Atlantic Drift current and the colder Norwegian Sea water. The front is permanently tied to the topographic ridge between Iceland and Britain, and tilts vertically toward the Norwegian Sea; perturbations to the flow cause meanders and eddies to form. The flow is generally from west to east, with magnitudes which peak between 25–50 cm/sec (Robinson et al., 1989).

Data used to initialize the Harvard Model generally consists of AXBTs, supplemented by a climatological temperature-salinity correlation; GEOSAT altimetric data provides additional information on both location and strength of the front. The quasigeostrophic model was used alone in this region. The sparse mapping of AXBT data generally limits the resolution of the front in the initialization; the Harvard Model has been shown to strengthen dynamically local gradients and improve this resolution (Denbo et al., 1988). Acoustic calculations were performed in day 10 of the model run, to demonstrate phenomena in the more realistic frontal fields.

As mentioned in chapter 2, acoustic propagation was calculated in the Gap region under several conditions. Calculations were performed along two transects, both of which start in shallow water on the ridge and march into the deeper water of the Norwegian basin, over the steep topography. One transect contained a developing eddy midway along its extent, and the other crossed the main Iceland-Faeroes front. Figure 4.9a shows contours of quasigeostrophic streamfunction at 50 m depth, with the two propagation transects drawn in. In addition, propagation results were calculated using these range-dependent oceanographic fields and flat topography, both shallow and deep, with the results confirming those of Jensen et al. (in press) that the topography plays a dominant role in determining the acoustic propagation patterns, with lesser but significant modifications by the oceanography. Due to the extensive length of propagation over shallow topography along these transects, we can expect propagation patterns to be substantially different from those seen in deep ocean regimes, where the increase in sound speed with pressure (depth) causes the sound to refract back toward the surface. With a shallow flat bottom, the effect of the oceanography is primarily to change the horizontal distance between bottom interactions and thus to ad-

just the amount of bottom loss; with a deep flat bottom the propagation patterns are those of convergence zones. Both these propagation regimes are different in character than that observed with the realistic topography, and few meaningful comparisons can be made between flat-bottom and realistic topography regimes. The main effort was therefore given to studying the effects of the oceanography in the presence of the realistic topography. Calculations were performed at frequencies of 25 and 50 Hz, with source depths of 10, 300, and 600 m. These depths were chosen to be near the top, center, and bottom of the starting profiles.

In an effort to separate what aspects of the propagation were due to oceanography and what due to topography, the range-dependent oceanographic calculations were compared with range-independent oceanographic calculations. Rather than compare propagation through the range-dependent oceanographic fields against the range-independent case of the starting profile, as was done in the previous studies in this work, a pair of sound speed profiles was selected that were typical of the Atlantic water and the Arctic water in this region, and which closely resembled either starting or perturbing profiles for these transects, allowing for profile truncation in shallow topography. These two profiles were used as the comparison profiles for calculations along both the selected transects, in the hopes of isolating particular topographic phenomena; the effort met with limited success due to the complexity of the topographic interactions.

The two sound speed profiles are shown in figures 4.9b and 4.9c. The Atlantic sound speed profile, figure 4.9b, shows a deep surface duct to 250 m depth; according to Porter et al. (1990) this is consistent with mixed layer depths observed by weather ships in the region. Using the formula $f = 1500/(0.008h^{3/2})$ to estimate the lowest frequency for which the duct will trap sound (Porter et al. 1990, Urick, 1983) we calculate 47 Hz as the lower bound for duct trapping, although the transition between trapping and non-trapping behavior will be somewhat nebulous. The Atlantic sound speed profile has a deep sound channel near 780 m depth; additionally we note that for most depths in this region (2500 m or less) the relatively high sound speeds in the surface layers ensure that propagation with this profile will be strongly bottom-interacting. The Arctic sound speed profile shown in figure 4.9c has a much shallower sound channel axis, near 590 m depth, with another much weaker duct near 305 m depth. This secondary duct has a magnitude of .07 m/sec and does not trap sound, although

it does affect refraction patterns.

The sediment parameters selected for this region were density $\rho = 1.6$ gm/cm^3, attenuation $\beta = 4.8$ dB/λ, interface sound speed discontinuity $c_w/c_b = 1.031$, sediment sound speed gradient $\partial c/\partial z = .5$ sec^{-1}, and sediment depth $z_{sed} = 5$ m. Values were obtained from Frisk, Doutt and Hays (1986) from their shallow site, in order to characterize the more strongly bottom-interacting sediment regions more accurately. Figure 4.9d shows the magnitude and phase of the water-sediment reflection coefficient for this parametrization; note that these conditions are strongly reflecting for sound at all angles of incidence, while sound near grazing incidence will again approach 100% reflection. This value of β is extremely high and is used to model compressional wave conversions to shear waves at the shallow sediment-substrate layer, and subsequent shear wave attenuation, as discussed in section 2.6. We note that in a realistic sediment this shallow, we could expect compressional wave reflections off the sediment-basement interface; these reflections were not included in the IFD model of the sediment since we maintain a constant density and sound speed across the perfectly transmitting interface between fluid sediment layer and artificial absorbing bottom. To more realistically handle the situation, a discontinuity in density or sound speed could be used across the interface, or another layer added.

For propagation across the developing warm eddy, the most meaningful comparison was to propagation in the range independent Arctic profile; the eddy can be thought of as a pertubation to the Arctic water mass. For propagation across the frontal transect, comparisons to propagation through both the Arctic and Atlantic profiles proved informative.

Propagation patterns in the Gap region in any case appear to be a balance between whichever is the strongest of several factors. First, the higher the sound speed at the source is relative to that at the sediment, the more important will be the bottom interactions to the entire water column propagation patterns. Conversely, the closer the source is to the sound channel axis, the more strongly excited will be the modes that make up shallow-angle sound paths near the channel axis. Additionally, the Atlantic water surface duct will overwhelm other surface phenomena at $f = 50$ Hz but will only serve to increase the surface sound speeds at $f = 25$ Hz. Propagation in each case seems to be governed by the relative strengths of each of these effects, for each source location and

frequency. An exact determination of the interplay would require closer study with a simplified topography.

4.2.1 Propagation through Warm Eddy

4.2.1.1 Shallow, Flat Bottom Propagation

To demonstrate the effects of the oceanography on shallow, flat-bottom propagation and provide an aid to interpretation of upcoming results, figure 4.10 compares propagation through the range-dependent oceanographic sound speed fields along transect A with propagation through the Arctic sound speed profile, for a source at 10 m and frequency 25 Hz, with a bottom depth of 607 m. This depth was chosen to match the real starting depth along this transect. We can see from the contours of sound speed that the Arctic water profile is very similar to the sound speed profile on either side of the eddy; the eddy represents a perturbation which greatly increases the surface sound speeds near 50 km range in figure 4.10a and increases the strength of the downward-refracting gradient below it. In the range-independent contour plots of propagation loss, we see a large number of vertical propagation paths between the sediment and the surface up to 25 km range; the dominant propagation paths thereupon become more shallow as the sediment interactions selectively remove the steeper propagation paths. Comparing with the range-dependent oceanographic case, the contours of propagation loss (figure 4.10b) retain their vertical structure until after interaction with the eddy perturbation; the downward refraction of the eddy causes the sound in shallower paths to bend downward and interact more frequently with the sediment. The effect of the eddy will be an increased number of bottom interactions and thus increased loss. In the plots of propagation loss at the 10 m receivers, we see that the sound levels in the range-dependent case are approximately 60 dB lower by 100 km range than they are in the range-independent case. Thus with a downward-refracting profile and a shallow lossy bottom, changes to the sound speed profile serve to modify the horizontal frequency of bottom interactions and thus to adjust the amount of loss.

4.2.1.2 Realistic Topography, Shallow Source

When realistic topography is used for calculations with different oceanographic conditions, the result is an amazing array of propagation patterns about which generalization is difficult. Several points must first be noted; first, over the shallow regions, the sound will undergo an extremely large number of bottom interactions. In view of the different angles of these interactions the sound will not be in coherent uni-directional beams when the topography slopes away, as we have seen in deeper oceanic regimes. Rather, at each location magnitudes will be due to sound travelling along various different paths.

Additionally, the angular dependence of the Rayleigh reflection coefficient means that sound in shallower propagation paths will persist to longer ranges than will sound in steeper paths; while over the shallow topography such sound undergoes both fewer bottom interactions and less loss with each interaction. We note that with the steep topography changes have slope of approximately $\Delta z/\Delta r = .03$, still relatively small.

In many cases a pattern of magnitudes appeared in the shallow receiver ($z_{rcvr} = 10$ m) that was almost invariant to oceanography but which depended on topography. Figure 4.11 shows an example of this invariance by comparing propagation through the eddy at $f = 50$ Hz, source $z_s = 10$ m with propagation from the same source with the same frequency through the Arctic profile. Receiver depths in these figures are 10 and 600 m; the eddy receivers are bold. Note in the 10 m receivers the pattern of minima near 40 and 65 km range with a broad maximum in between, followed by that broad maximum extending between 75 and 125 km. This occurs geographically coincident with the warm eddy, and might be considered an effect of the oceanography, except that the range-independent Arctic case does not contain the eddy perturbation. Other sources show a similar pattern in the shallow receiver; there may be slight modifications but it is nearly always present, especially the minima near 40 and 65 km range. Because of its relative invariance to oceanography and dependence on topography, it seems to be due to a broad reflection of the incoherent sound off the sloping shelf and the particular reinforcing patterns of the superimposed sound. A different form of topographic pattern occured in the range-dependent and range-independent oceanographic calculations along transect B; the topog-

raphy proved too irregular to attach specific meaning to these patterns. These patterns will be pointed out in the upcoming examples. An experiment testing various different artificial, controlled topographic conditions would assist in determining the cause. At 25 Hz for this case, a similar pattern of topographic interactions dominated the entire water column propagation.

Propagation along this transect with the Atlantic water profile (figure 4.12) and 10 m source at 50 Hz shows an example of the primary instance in which the oceanographic effects overwhelmed this topographic effect. Recall that for a surface duct of 250 m depth, we can expect surface trapping for sound at 47 Hz and above; in figure 4.12c we see sound propagating to long distances in the upper region of the water column. Note in the 10 m receiver the greatly enhanced sound levels over the other two cases, figure 4.11c of the 10 m receivers in the eddy and Arctic profiles. This surface trapping is sufficient to overwhelm any topographic effects seen in the shallow receiver, whenever it occurs.

4.2.1.3 Realistic Topography, Middle Source

With the source near the center of the shallow water column the interaction of oceanography and topography takes a slightly different form. Figure 4.13 compares propagation loss along the path through the eddy for $z_s = 300$ m and $f = 50$ Hz with the corresponding case in the range-independent Arctic profile. The receivers shown are at 10 and 750 m depth; the first 42 km of magnitudes in the 750 m receivers have been blanked out as they are below the bottom. In the 10 m receiver we can see the topographic effect; in this case the minimum near 65 km is broader but it is followed by the same wide maximum at greater ranges. To see the effects of the oceanographic interaction with the topography, we must look at propagation loss patterns in the deeper water. In the contours of propagation loss for the eddy case we see that the stronger sound speed gradient below the eddy has refracted sound away from the surface between 35 and 65 km range; as in the shallow, flat-bottom case, this causes an increase in the amount of bottom interactions and thus an increase in loss. As the topography deepens after 75 km, the sound propagates to long distances in the deep sound channel with a very coherent convergence zone pattern. Magnitudes within the sound channel vary between 115 and 120 dB by 150 km range, and the 750 m receiver shows the regular pattern of maxima. Without the eddy present, there is

both less loss due to bottom interactions and a less coherent propagation pattern within the deep sound channel. In the range independent contours of propagation loss we see this broad, diffuse ensonification within the center of the sound channel which appears as a nearly constant pattern of sound intensity in the 750 m receiver, with magnitude of 90–95 dB, 20–25 dB greater than with the eddy present. What periodicity can be found within the sound channel is roughly the same as that observed in the eddy case, although locations of maxima may differ. Thus in this case, interaction between the eddy and topography caused an increase in loss and a more clearly defined convergence zone pattern than in the Arctic profile case. At 25 Hz, propagation across the eddy again increased loss and sound confinement to the sound channel axis, as well as shifting the phase of convergence zone propagation when compared with propagation in the Arctic profile.

This example presents an interesting comparison with acoustic propagation through the outputs of the primitive equation oceanographic model run in the Gap region. By day 10, the PE model had evolved this eddy slightly differently than the QG model had, moving it more to the northeast. Thus propagation along the same transect in the PE model outputs encountered the eddy at a greater range, over slightly deeper water. Figure 4.14 compares propagation across the eddy in the PE model outputs with the range independent Arctic water case. The contours of PE sound speed show the eddy near 75 km range, right where the topography begins to deepen significantly. In the receiver at 10 m we see the minimum near 65 km range associated with the topography; note the decrease in magnitude after 100 km which may be due to destructive interference from the water column sound. The range dependent contours of propagation loss show the downward-refracting effect of the eddy between 50 and 100 km range. With the eddy interaction delayed until almost past the deepening topography, we see fewer bottom interactions over the shallow topography than in the QG model case (figure 4.13) but more interactions and thus more loss than with the range-independent Arctic profile. Note that the ensonification in the deep sound channel shown in figure 4.14d shows levels of 100–105 dB, between the levels in either the QG or range independent case; propagation loss magnitudes at the 750 m receiver only shows a decrease of 10–15 dB relative to the range independent case, rather than the 20–25 dB decrease observed in the QG case with the eddy over the shallower topography. Additionally, convergence zone propagation

patterns are more amorphous than than in the QG case, with its early eddy interaction, and more defined than in the range-independent Arctic profile case. Within the deeper sound channel, horizontal wavelength of the convergence zone oscillations depends on the sharpness of the sound speed gradients on either side of the sound channel axis; in the QG case the gradients are quite strong and the convergence zone distances are approximately 20 km. In the PE case the convergence zones are less well defined than in the QG case, due perhaps to the location of the eddy—sediment interaction, but the convergence zone radii are approximately 40 km. To determine the exact effect of the eddy location with respect to the topography on the phase and coherence of propagation within the deep sound channel, it would be necessary to perform a set of experiments with identical eddies in various locations with respect to the topography.

4.2.1.4 Realistic Topography, Near Bottom Source

Propagation through the eddy with the source near the bottom of the shallow water profile ($z_s = 600$ m) at $f = 25$ Hz showed an interesting effect of the interaction of oceanography with topography. Figure 4.15 compares this case with the corresponding case of propagation through the Arctic profile. Receivers shown are at 10 and 400 m depth. In the 10 m receivers we see the form of topographic interaction typical of this bottom configuration and frequency; note the minima near 65 km range preceded by a weak maximum near 55 km, followed by broad maxima. At 25 Hz we do not see a magnitude decrease near 150 km range. In the contours of propagation loss for propagation through the eddy we can see the effects of the downward refraction of the eddy between 35 and 60 km range as the sound refracts away from the surface. As we saw in the shallow, flat-bottom case, this will cause an increase in bottom interactions and thus an increase in loss, even of sound that used to be propagating at shallow angles. Indeed, when the bottom topography deepens near 75 km the propagation pattern found in the sound channel appears to be dominated by a single mode propagating down the center of the channel, with magnitude between 120–125 dB by 150 km range; recall that deeper sources will excite the modes propagating near the center of the sound channel more strongly than will shallow sources. Traces of higher modes remain in the modulations to the channel axis pattern. Note also the refracted sound propagation down the topographic slope; this effect

was also documented by Jensen and Kuperman (1980a).

The receiver at 400 m shows the small-scale pattern of maxima associated with this single mode, as well as the modulations by other modes. Comparing to the Arctic profile case, we see no such downward refraction near 35 km; instead the topography simply removes the more steeply-propagating sound leaving the sound in more shallow paths. Thus after the topography deepens near 75 km range, more sound remains in the sound channel at a wider variety of propagation angles, forming broad convergence zones with magnitudes between 110 and 115 dB by 150 km range. The receiver at 400 m shows the broader pattern of maxima associated with the convergence pattern, as well as the increased ensonification associated with the lesser loss. At 50 Hz, propagation with the 600 m source past the eddy showed a similar increase in the degree of trapping in the sound channel over the Arctic profile case, although a greater number of shallow angle modes remained near the sound channel at the higher frequency.

4.2.2 Propagation Across the Front

4.2.2.1 Realistic Topography, Shallow Source

Propagation through the front along transect B also proved to be a complex interaction of source depth, frequency, and topography about which few generalizations could be made, except to say again that deeper sources more strongly excite shallow-angle sound in the channel axis. With the source at the top of the starting profile, bottom interactions set up at the beginning of propagation dominate the entire range of calculation. Figure 4.16 shows propagation across the front for a source at 10 m depth at 25 Hz; receivers are at 10 and 250 m depth. The receiver plots contain overlays of the same receivers from propagation across this topography in both the Atlantic sound speed profile and the Arctic profile; the frontal case is bold, Atlantic case medium, and Arctic case light. From the sound speed contours we see the typical frontal slant toward the Arctic water; at depth, the frontal contrast is within the first 25 km of calculation, while at the surface it is at approximately 150 km range. Note that propagation along this transect is in primarily Arctic type water; we see no deep surface duct past 15 km range and only the location of strong sound speed gradient toward the surface changes. In the 10 m receiver we see the form of the topography interaction

along this transect with its slightly different bottom configuration; propagation loss with all three oceanographic conditions is nearly identical at this receiver. The minima near 30 and 80 km range, together with the maximum near 50 km, occur in a great number of the cases. Additionally, the receiver at 250 m depth shows great similarity in the propagation patterns between the Atlantic profile and the frontal transect; thus conditions at the beginning of the profile have a very strong effect on propagation. Note the qualitative difference in the Arctic receiver; the destination water mass has relatively little effect on propagation patterns.

Comparing this range-dependent oceanographic case with the propagation contours in either the Atlantic water or the Arctic water (figure 4.17) with the same source depth and frequency again reveals this dependency: propagation through the Atlantic water profile shows the same pattern of bottom interactions and the same qualitative propagation patterns throughout the water column as does the propagation across the front. Alternatively, propagation through the Arctic water profile shows a diffuse convergence zone propagation pattern which appears to overwhelm the bottom interactions seen in the other two cases. Note in the Arctic water 250 m receiver that sound levels in the convergence zones are approximately 120–125 dB by 175 km range; sound levels in the 250 m receivers for the frontal oceanography and the Atlantic profile are about 133 dB at the same range. In the Arctic profile, a water-propagating pattern seems to overwhelm the topographic effects seen in both the frontal and Atlantic cases.

We note that for the Atlantic profile, which is most similar to the starting profile of the frontal crossing, the main sound channel axis is near 780 m depth; for the Arctic profile, the main sound channel axis is near 590 m depth and the sound speeds are considerably lower in the upper water column than in the Atlantic profile. The starting bottom depth along this transect is 734 m; thus for the Arctic sound speed profile there is some very small amount of upward refraction before the bottom is encountered, which the downward topography will increase, permitting water-refracting sound to propagate within close ranges of the source. In the Atlantic sound speed profile with its deeper sound channel axis, this topography configuration does not permit any water-refracting sound until after 25 km range. In the realistic frontal oceanography, the shallowing of the sound speed channel in conjunction with the deepening topography permits

water-refracting sound after approximately 10 km. Apparently this is not soon enough in the propagation pattern to overwhelm the bottom-interacting sound that makes up those topographic acoustic patterns seen in the shallow receivers, and the resulting propagation patterns into the Norwegian Sea are dominated by the presence of Atlantic water at the source location. At 50 Hz for this source depth, the bottom interactions set up at the beginning of the propagation again dominated the entire calculation. Propagation patterns appeared very sensitive to the conditions in short ranges.

4.2.2.2 Realistic Topography, Middle Source

With the source in the center of the starting water column, a different propagation effect obtains; propagation across the front shows effects of Arctic water, modified by bottom interactions generated near the source. Figure 4.18 shows propagation across the frontal transect for the source at 300 m depth at 25 Hz with receivers at 10 and 750 m. Overlaid on the receiver plots again are the corresponding receivers from propagation through Atlantic and Arctic sound speed profile, with frontal case bold, Atlantic case medium, and Arctic case light. In the 10 m receiver we again see the pattern of bottom interactions in both the frontal and Atlantic cases, while the 750 m receivers easily distinguish between the three cases. The contour plot of propagation loss shows a convergence zone propagation pattern within the sound channel, however, as does the receiver at 750 m depth. Comparing this range-dependent case against the matching propagation contours through the Atlantic profile (figure 4.19, left) we see in that case a broad interference pattern that appears to be the bottom interactions that obtain for this topographic configuration and source depth. With matching conditions in the Arctic profile (figure 4.19, right), however, once the topography deepens enough to permit sound channel propagation, significant amounts of sound propagate to long ranges within the channel. The regular pattern formed in the channel axis is reminiscent of the propagation patterns observed by Jensen and Kuperman (1980b) and Collins et al. (1988) for their examples of parabolic approximation propagation in shallow water with only the three lowest modes excited; thus the particular choice of source depth in this sound speed profile with this amount of bottom losses seems to filter out all but a very small number of modes, probably two, in the center of this profile. Traces of other modes

exist and can be seen as modifications to the propagation patterns, such as the modulations of magnitude and the small oscillations near 1400 m depth in the contours of propagation loss. It would be interesting to directly calculate the vertical modes for these sound speed profiles.

We can see a similarity in the locations and forms of these maxima in the Arctic-profile case to the maxima in the convergence zone pattern seen in the realistic oceanographic case, figure 4.18c. In that case the locations are slightly shifted, and the small-scale oscillations similar to the bottom interacting interference pattern overlay the channel axis propagation. The 750 m receivers clearly differentiate between the Arctic profile pattern of oscillations, the Atlantic profile interference pattern, and the realistic propagation pattern which shows traces of both. Thus for this source depth, the sound in water-propagating paths was strong enough to overwhelm the interference effects caused by the early profile; propagation patterns this time are dominated by characteristics of the destination Arctic water mass, with modifications due to the presence of Atlantic water at the starting location. At 50 Hz with the same source depth, propagation conditions across the front again showed oceanographic effects with an overlay of bottom interaction interference.

4.2.2.3 Realistic Topography, Near Bottom Source

When the source is at 600 m depth, it is very close to the Arctic profile 590 m sound channel axis and fairly close to the Atlantic profile 780 m sound channel axis; we can expect strong excitation of shallow-angle sound in that axis. This is indeed the case, as we see in figure 4.20 for the 600 m source at 50 Hz with realistic oceanography; receivers shown are at 10 and 300 m depth. Again, receivers are overlaid with corresponding cases from both Atlantic and Arctic profiles; the frontal case is bold, Atlantic case medium, and Arctic case light. The contours of propagation loss show the sound to be tightly constrained within the sound channel axis around 600 m depth, with a very small amount of vertical extent. Comparing this case with similar propagation through the Atlantic profile (figure 4.21, left), we see that in the Atlantic profile the strong sound speed gradient between 300 and 600 m depth, in conjunction with the large amount of loss to steeply propagating sound in shallow regions, has removed propagation paths with large vertical angle and strongly confined the sound to

the center of the Atlantic sound channel axis near 750 m depth. Propagation in the range-independent Atlantic sound speed profile shows sound trapping in the surface duct, which did not appear in the range-dependent case due to the lack of duct beyond 15 km range. Additionally, the Atlantic profile with its steep gradient between 300 and 700 m depth strongly confines sound to the channel axis, while interactions with the early shallow bottom remove steep-angle sound. Range-independent propagation in the Arctic profile (figure 4.21, right), with its shallower sound channel axis and more gradual increase in sound speed toward the surface, permits a greater range of vertical propagation around the center of the sound speed duct with less bottom loss and thus greater ensonification at a wider range of depths.

As might be believed, the amount of ensonification within the duct in the range-dependent case is intermediate between the duct sound magnitudes seen in either range-independent case; with the range dependent oceanography, sound levels in the duct range between 90 and 95 dB by 200 km range. With the Atlantic sound speed profile (figure 4.21c) sound levels in the duct are lower, and range between 95 and 100 dB at the same range; the increased bottom losses associated with the stronger surface sound speed gradient have removed more sound from the propagation pattern. With the Arctic sound speed profile (figure 4.21d) sound levels in the channel axis are higher, and range between 85 and 90 dB by 200 km range, as the weaker sound speed gradient in the upper profile has decreased the amount of bottom interaction.

The 10 m receivers display these effects; in the frontal case, there is little ensonification of shallow regions. The 10 m receiver from the Atlantic profile shows increased magnitudes due to surface ducting, and the Arctic case shows variable increased magnitudes due to the greater range of vertical propagation permitted with that profile. Note in the 300 m receivers that the frontal case shows the same decreased magnitudes due to the strong downward-refracting gradients in the early profile; as the vertical tilt of the Iceland-Faeroes front causes these gradients to shallow, ensonification increases at the 300 m receiver although the greatest sound magnitude remains trapped at the center of the channel. Thus with the source near the bottom of the starting water column, the strong excitation of shallow angle modes at the center of the channel and rapid extinction of steeper-angle sound due to bottom losses causes propagation to be

mostly limited to sound in the channel axis. The location of that channel axis is determined by the destination Arctic water mass; the strong losses are caused by the interaction of the early Atlantic water mass with the shallow topography. Similar results appeared for the 25 Hz case.

4.2.3 Summary of Iceland-UK Gap Propagation Effects

Propagation within the Iceland-UK Gap region has been shown to be extremely varied and is difficult to generalize, but is governed by the interactions of several effects. First, due to the large horizontal range of propagation in a downward-refracting profile over shallow topography, the sound undergoes an extremely large number of bottom interactions with different repeat distances and incident angles; when the topography deepens, the sound field will not consist of coherent uni-directional beams. Rather, at each location the magnitude will consist of sound travelling along various different paths. These bottom interactions will also preferentially filter out sound with steep propagation paths due to the smaller magnitude of the reflection coefficient for steep angle sound. Changes in the oceanographic sound speed profile over this shallow topography alter the horizontal frequency of the bottom interactions, and thus adjust the amounts of loss.

Additionally, in many of the calculations shown, a complex propagation pattern appeared that was almost invariant to oceanography and thus was attributed to the topography. The appearance of this pattern was stronger for shallower sources, which were more strongly bottom-interacting due to their weaker excitation of shallow-angle modes in the center of the sound channel. The form of this topographically induced pattern is not understood due to the complexity of the topographic variations.

Deeper sources closer to the sound channel axis (which was close to the shallow bottom) will excite the shallow-angle modes in the center of the sound channel more greatly; thus their propagation patterns were more strongly affected by the oceanography and its variations with range. Topographic losses still occur over the early propagation range, but their magnitude is less due to the larger amount of shallow-angle sound.

Propagation along the transect containing the developing eddy primarily showed the effects of the increased bottom losses due to the strongly downward-refracting gradient at its base. These increased losses more effectively removed the steep-angle sound than did the oceanographic fields without the eddy. Figure 4.22a schematizes these eddy-induced losses, while figure 4.22b shows range-independent fields for comparison. The increased losses due to the eddy effectively remove all but the shallowest-angle sound in the center of the sound channel, reducing sound magnitudes by 10–15 dB in the channel and 20–25 dB elsewhere. Different source depths will excite different amounts of shallow-angle modes so the propagation pattern will depend strongly on source depth, but the effect of the eddy will always be to remove preferentially the steeper-angle sound.

Propagation along the transect across the Iceland-Faeroes front resulted in sound patterns revealing the effects of both water masses, that at the source and that at greater distance. Figure 4.22c schematizes propagation across the frontal transect, showing strong downward refraction due to the deep steep sound speed gradient in the early Atlantic water mass, followed by propagation closely limited to the center of the sound channel. In figure 4.22c, the wide-angle long range path is drawn dashed to indicate that sound did propagate in wider angle paths, but with greatly reduced intensity compared with the shallower angle sound (20–25 dB less).

For comparison, figure 4.22d schematizes propagation through Atlantic water sound speed fields, with the surface duct trapping some sound near the surface and the deep strong gradient which, in conjunction with the shallow topography, strongly confines sound to the channel axis. Figure 4.22e shows propagation patterns in the Arctic water sound speed fields, with the shallow-angle sound bold and the wide-angle sound light, to indicate relative intensities. Comparing propagation across the front with the two range independent cases, we see that the early Atlantic-type sound speed profile strongly confined sound to the channel axis, but that channel axis slowly became shallower on the Arctic side of the front. The transition to Arctic-type water with its shallower surface gradient permitted some wider angle sound to propagate, but with reduced intensity due to the early Atlantic profile bottom interactions (10–15 dB less). These principles were seen in many cases, but the types of propagation patterns they produced depended strongly on source depth via the relative amounts of sound in different

modes. In some cases, primarily with shallower sources, the propagation patterns depended almost entirely on the sound speed profile at the source. In other cases, usually with deeper sources, the propagation patterns were more determined by the destination water type.

4.3 Summary and Comparison of Regional Propagation Effects

The above two sections demonstrated dramatically different regional propagation effects, because of the different physical conditions within the two regions. Both regions do, however, demonstrate that inclusion of a surface duct can have important effects on the propagation patterns even at frequencies too low for duct trapping to take place. Proper description of the surface mixed layer and the strong sound speed gradient just below it can alter propagation patterns in the deeper water as well as prevent sound from penetrating into the surface regions; the effect is important for sources within the deep sound channel. The frequency range over which the latter effect will be significant will depend on the duct depth; very low frequencies will penetrate into the duct due to strong non-ray effects, while relatively high frequencies will be trapped within the duct. In between is a middle range of frequencies effectively barred from the near-surface regions due to the increase in sound speed.

In the AthenA region we saw significant low-frequency ensonification in the surface region at 25 and 50 Hz, while sound at 100 Hz was barred from the duct. In the Iceland-Faeroes Gap region, the deeper duct trapped 50 Hz sound, while the 25 Hz calculations with realistic topography showed too many topographic interaction effects to determine if sound was barred from the surface layer. Calculations with the deep flat bottom, while not relevant for comparisons with the realistic topography, do have academic interest and it may be noted that propagation in the Atlantic profile with the bottom at 3000 m and source at 600 m at 25 Hz showed a significant decrease in surface ensonification over propagation in the Arctic profile under the same conditions. These calculations are shown in appendix C.

Topography within the AthenA region was so flat as to have little to no effect on sound propagation; the only exception might be the directly bottom-reflecting sound. In the Gap region, however, topographic effects are so strong

and complicated that they dominate the propagation patterns, with lesser but quite important modifications by the oceanography within the limits imposed by the topography. In some cases propagation patterns invariant to oceanography were seen; little can be said about the form of these topographically-dominated patterns at this stage of work. To determine the reasons for the bottom interaction patterns and the conditions under which they occur, it would be necessary to test propagation over various carefully controlled artificial topographic configurations, and the dependency of these patterns on source depth and frequency.

Additionally, these topographic interference patterns would undoubtedly be modified by inclusion of range dependence in the sediment model; sedimentation conditions can be expected to differ dramatically between the shallow and deep regions and would affect propagation patterns. In a region of strongly three-dimensionally varying topography such as this one, we could also expect azimuthal topography variations to greatly alter both topographic interference patterns and their interactions with oceanographic variations. The steep topography might additionally cause significant backscatter on certain propagation paths.

With thin sediment layers such as we have on the topographic heights, we might also realistically expect to see reflections off the substrate; addition of a change in density on sound speed below the sediment would improve the sediment model in shallow regions. With these thin sediment layers we might also expect significant shear wave excitation at the sediment-substrate interface. We have parametrized shear wave losses through a large value of attenuation which may reasonably provide the desired loss; however, sediment attenuation also modifies the water-sediment reflection coefficient. A more realistic modeling of shear wave excitation might produce the desired loss mechanism without altering the water-sediment reflection coefficient. Such modifications to the model would greatly increase the accuracy of these acoustic predictions, but documentation of the effects of these changes to the sediment model would require considerable further study.

Figure Captions, Chapter 4

Figure 4.1) a. AthenA region streamfunction fields, 125 m depth; transect for acoustic propagation drawn in. b. Sound speed profile at 53.3N 26.2W, QG fields only. c. Sound speed profile at 53.3N 24.2W, QG fields only. d. AthenA region temperature fields for coupled QG-SBL model, 6 m depth; transect for acoustic propagation drawn in. e. Corresponding streamfunction fields at 125 m depth. f. QG-SBL sound speed profile at 53.3N 26.2W. g. QG-SBL sound speed profile at 53.3N 24.2W.

Figure 4.2) Range independent propagation, QG vs. QG-SBL sound speed fields. $f = 50$ Hz, $z_s = 500$ m. a. Contours of propagation loss, QG sound speed profile. b. Propagation loss at 10 m receivers, QG-SBL case bold. c. Contours of propagation loss, QG-SBL sound speed profile. d. Propagation loss at 200 m receivers, QG-SBL case bold.

Figure 4.3) Range independent propagation, QG vs. QG-SBL sound speed fields. $f = 50$ Hz, $z_s = 150$ m. a. Contours of propagation loss, QG sound speed profile. b. Propagation loss at 10 m receivers, QG-SBL case bold. c. Contours of propagation loss, QG-SBL sound speed profile. d. Propagation loss at 350 m receivers, QG-SBL case bold.

Figure 4.4) Acoustic propagation through range-independent QG vs. QG-SBL sound speed fields. $f = 100$ Hz, $z_s = 500$ m. a. Contours of propagation loss, QG sound speed profile. b. Propagation loss at 10 m receivers, QG-SBL case bold. c. Contours of propagation loss, QG-SBL sound speed profile. d. Propagation loss at 200 m receivers, QG-SBL case bold.

Figure 4.5) Acoustic propagation through range-independent QG vs. QG-SBL sound speed fields. $f = 100$ Hz, $z_s = 150$ m. a. Contours of propagation loss, QG sound speed profile. b. Propagation loss at 10 m receivers, QG-SBL case bold. c. Contours of propagation loss, QG-SBL sound speed profile. d. Propagation loss at 200 m receivers, QG-SBL case bold.

Figure 4.6) Acoustic propagation through range-dependent QG sound speed fields. $f = 50$ Hz, $z_s = 150$ m. Receiver plots overlaid with corresponding range-independent QG receivers. a. Contours of sound speed. b. Propagation loss at 10 m receivers, range-dependent case bold. c. Contours of propagation loss. d. Propagation loss at 200 m receivers, range-dependent case bold.

Figure 4.7) Acoustic propagation through range-dependent QG-SBL sound speed fields. $f = 50$ Hz, $z_s = 150$ m. Receiver plots overlaid with corresponding range-independent QG-SBL receivers. a. Contours of sound speed. b. Propagation loss at 10 m receivers, range-dependent case bold. c. Contours of propagation loss. d. Propagation loss at 200 m receivers, range-dependent case bold.

Figure 4.8) Schematic of AthenA region propagation effects. a. QG-SBL vs. QG: shallower excursion of sound in QG-SBL (bold) case. b. QG-SBL vs. QG: refraction of sound away from surface in QG-SBL (bold) case, deeper refraction in QG-QBL case. c. Range dependent (bold) vs. range-independent propagation. Arrows represent approximate locations of start and stop of sound speed change.

Figure 4.9) a. Gap region quasigeostrophic streamfunction fields at 50 m depth, day 10. Transect A: propagation across a developing eddy. Transect B: propagation across the front. b. Atlantic water sound speed profile. c. Arctic water sound speed profile. d. Magnitude and phase of Rayleigh reflection coefficient, $\rho = 1.6$, $c_w/c_b = 1.031$, $\beta = 4.8$.

Figure 4.10) Shallow water propagation, range dependent (through eddy) vs. range independent (Arctic) oceanography. $z_s = 10$ m, $f = 25$ Hz. Bottom depth $z_{bot} = 607$ m. a. Range dependent sound speed contours. b. Range dependent propagation loss contours. c. Range dependent propagation loss, $z_{rcvr} = 10$ m. d. Range independent (Arctic) sound speed contours. e. Range independent propagation loss contours. f. Range independent propagation loss, $z_{rcvr} = 10$ m.

Figure 4.11) Comparison of propagation through eddy, with propagation through Arctic sound speed profile; realistic topography. $z_s = 10$ m, $f = 50$ Hz. a. Range dependent sound speed contours. b. Arctic profile sound speed contours. c. Propagation loss at 10 m receivers, eddy case bold. d. Range dependent contours of propagation loss. e. Range independent contours of propagation loss. f. Propagation loss at 600 m receivers, eddy case bold.

Figure 4.12) Propagation through Atlantic profile, realistic topography. $z_s = 10$ m, $f = 50$ Hz. a. Sound speed contours. b. Propagation loss at 10 m receiver. c. Contours of propagation loss. d. Propagation loss at 600 m receiver.

Figure 4.13) Comparison of propagation through eddy, with propagation through Arctic sound speed profile; realistic topography. $z_s = 300$ m, $f = 50$ Hz. a. Range dependent sound speed contours. b. Arctic profile sound speed contours. c. Propagation loss at 10 m receivers, eddy case bold. d. Range dependent contours of propagation loss. e. Range independent contours of propagation loss. f. Propagation loss at 750 m receivers, eddy case bold. Return blanked out prior to 42 km range as it is below the bottom.

Figure 4.14) Comparison of propagation through eddy, PE model outputs, with propagation through Arctic sound speed profile; realistic topography. $z_s = 300$ m, $f = 50$ Hz. a. Range dependent sound speed contours. b. Arctic profile sound speed contours. c. Propagation loss at 10 m receivers, eddy case bold. d. Range dependent contours of propagation loss. e. Range independent contours of propagation loss. f. Propagation loss at 750 m receivers, eddy case bold. Return blanked out prior to 42 km range as it is below the bottom.

Figure 4.15) Comparison of propagation through eddy, QG model outputs, with propagation through Arctic sound speed profile; realistic topography. $z_s = 600$ m, $f = 25$ Hz. a. Range dependent sound speed contours. b. Arctic profile sound speed contours. c. Propagation loss at 10 m receivers, eddy case bold. d. Range dependent contours of propagation loss. e. Range independent contours of propagation loss. f. Propagation loss at 400 m receivers, eddy case bold.

Figure 4.16) Propagation across front, realistic topography. $z_s = 10$ m, $f = 25$ Hz. a. Sound speed contours. b. Propagation loss at 10 m receivers, frontal case bold, Atlantic case medium, Arctic case light. c. Contours of propagation loss. d. Propagation loss at 250 m receivers, frontal case bold, Atlantic case medium, Arctic case light.

Figure 4.17) Propagation through Atlantic and Arctic profiles, realistic topography. $z_s = 10$ m, $f = 25$ Hz. a. Sound speed contours, Atlantic profile. b. Sound speed contours, Arctic profile. c. Contours of propagation loss, Atlantic profile. d. Contours of propagation loss, Arctic profile.

Figure 4.18) Propagation across front, realistic topography. $z_s = 300$ m, $f = 25$ Hz. a. Sound speed contours. b. Propagation loss at 10 m receivers, frontal case bold, Atlantic case medium, Arctic case light. c. Contours of propagation loss. d. Propagation loss at 750 m receivers, frontal case bold, Atlantic case medium, Arctic case light.

Figure 4.19) Propagation through Atlantic and Arctic profiles, realistic topography. $z_s = 300$ m, $f = 25$ Hz. a. Sound speed contours, Atlantic profile. b. Sound speed contours, Arctic profile. c. Contours of propagation loss, Atlantic profile. d. Contours of propagation loss, Arctic profile.

Figure 4.20) Propagation across front, realistic topography. $z_s = 600$ m, $f = 50$ Hz. a. Sound speed contours. b. Propagation loss at 10 m receivers, frontal case bold, Atlantic case medium, Arctic case light. c. Contours of propagation loss. d. Propagation loss at 300 m receivers, frontal case bold, Atlantic case medium, Arctic case light.

Figure 4.21) Propagation through Atlantic and Arctic profiles, realistic topography. $z_s = 600$ m, $f = 50$ Hz. a. Sound speed contours, Atlantic profile. b. Sound speed contours, Arctic profile. c. Contours of propagation loss, Atlantic profile. d. Contours of propagation loss, Arctic profile.

Figure 4.22) Schematic of Iceland-UK Gap propagation. a. Propagation through eddy. Arrows represent start and end of eddy. b. Propagation through Arctic water sound speed fields. c. Propagation across Iceland-Faeroes front. Arrows represent approximate locations of deep and surface front, respectively. d. Propagation through Atlantic water sound speed fields. e. Propagation through Arctic water sound speed fields.

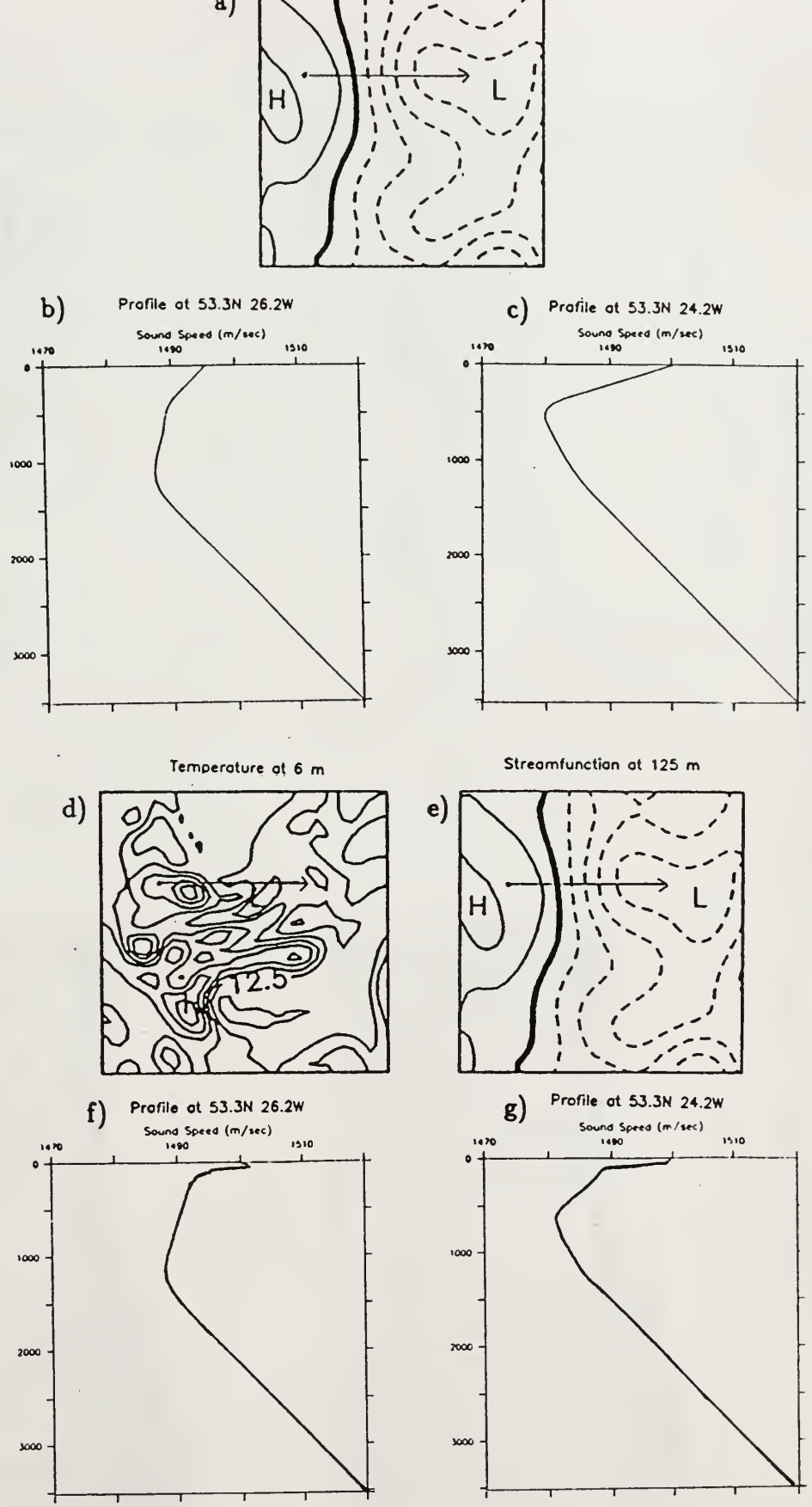

Figure 4.1) a. AthenA region streamfunction fields, 125 m depth; transect for acoustic propagation drawn in. b. Sound speed profile at 53.3N 26.2W, QG fields only. c. Sound speed profile at 53.3N 24.2W, QG fields only. d. AthenA region temperature fields for coupled QG-SBL model, 6 m depth; transect for acoustic propagation drawn in. e. Corresponding streamfunction fields at 125 m depth. f. QG-SBL sound speed profile at 53.3N 26.2W. g. QG-SBL sound speed profile at 53.3N 24.2W.

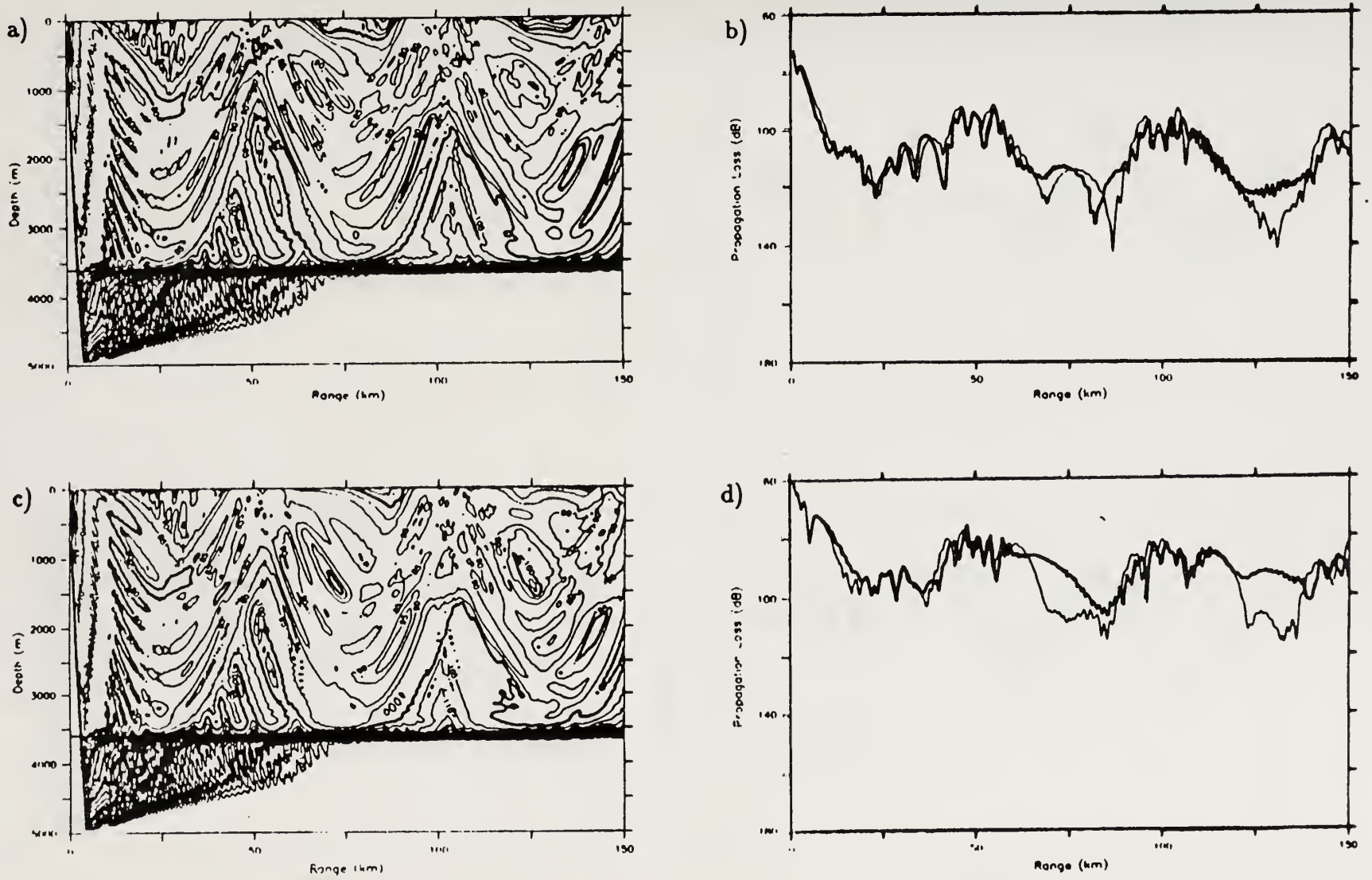

Figure 4.2) Range independent propagation, QG vs. QG-SBL sound speed fields. f = 50 Hz, z_s = 500 m. a. Contours of propagation loss, QG sound speed profile. b. Propagation loss at 10 m receivers, QG-SBL case bold. c. Contours of propagation loss, QG-SBL sound speed profile. d. Propagation loss at 200 m receivers, QG-SBL case bold.

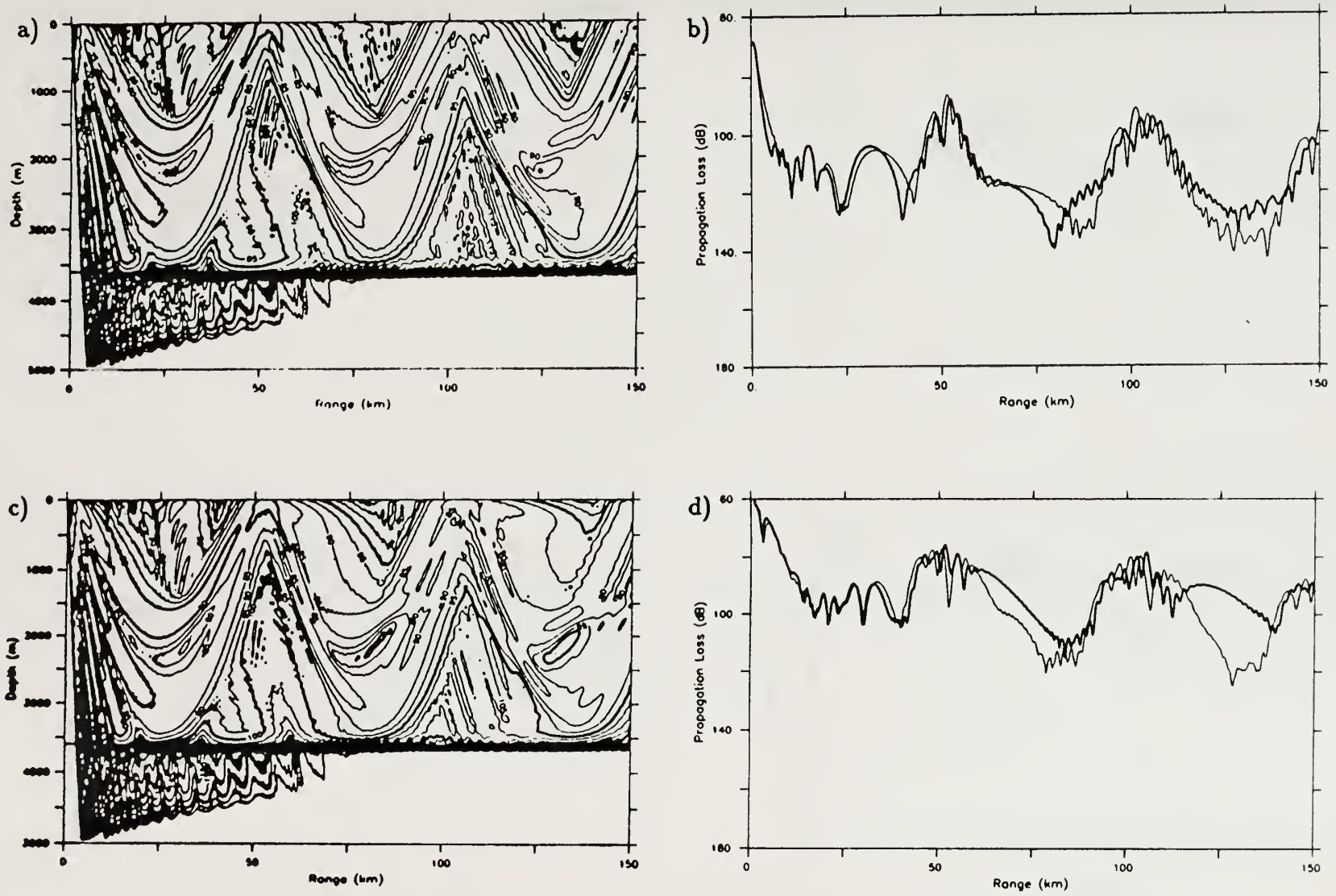

Figure 4.3) Range independent propagation, QG vs. QG-SBL sound speed fields. $f = 50$ Hz, $z_s = 150$ m. a. Contours of propagation loss, QG sound speed profile. b. Propagation loss at 10 m receivers, QG-SBL case bold. c. Contours of propagation loss, QG-SBL sound speed profile. d. Propagation loss at 350 m receivers, QG-SBL case bold.

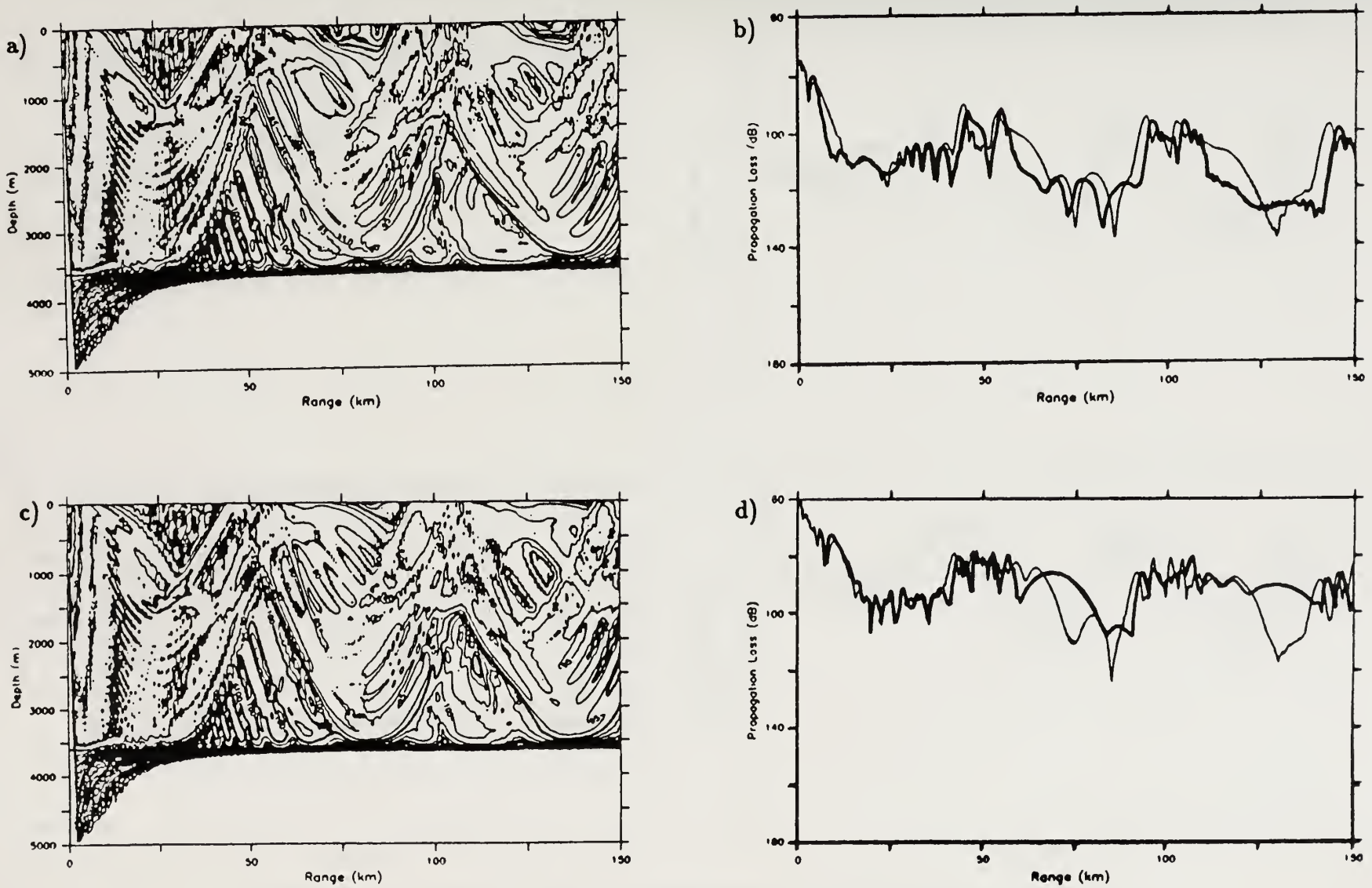

Figure 4.4) Acoustic propagation through range-independent QG vs. QG-SBL sound speed fields. $f = 100$ Hz, $z_s = 500$ m. a. Contours of propagation loss, QG sound speed profile. b. Propagation loss at 10 m receivers, QG-SBL case bold. c. Contours of propagation loss, QG-SBL sound speed profile. d. Propagation loss at 200 m receivers, QG-SBL case bold.

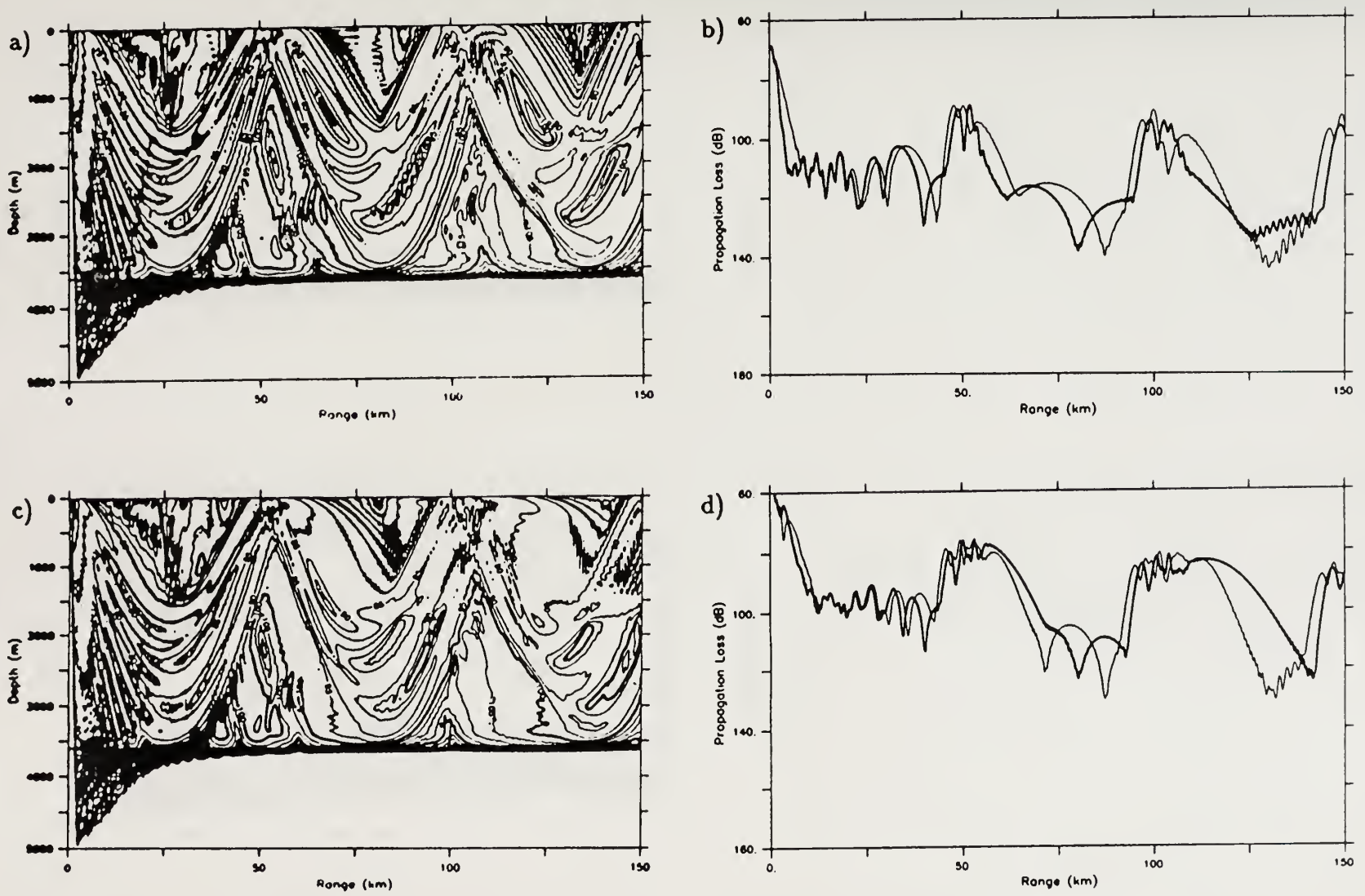

Figure 4.5) Acoustic propagation through range-independent QG vs. QG-SBL sound speed fields. $f = 100$ Hz, $z_s = 150$ m. a. Contours of propagation loss, QG sound speed profile. b. Propagation loss at 10 m receivers, QG-SBL case bold. c. Contours of propagation loss, QG-SBL sound speed profile. d. Propagation loss at 200 m receivers, QG-SBL case bold.

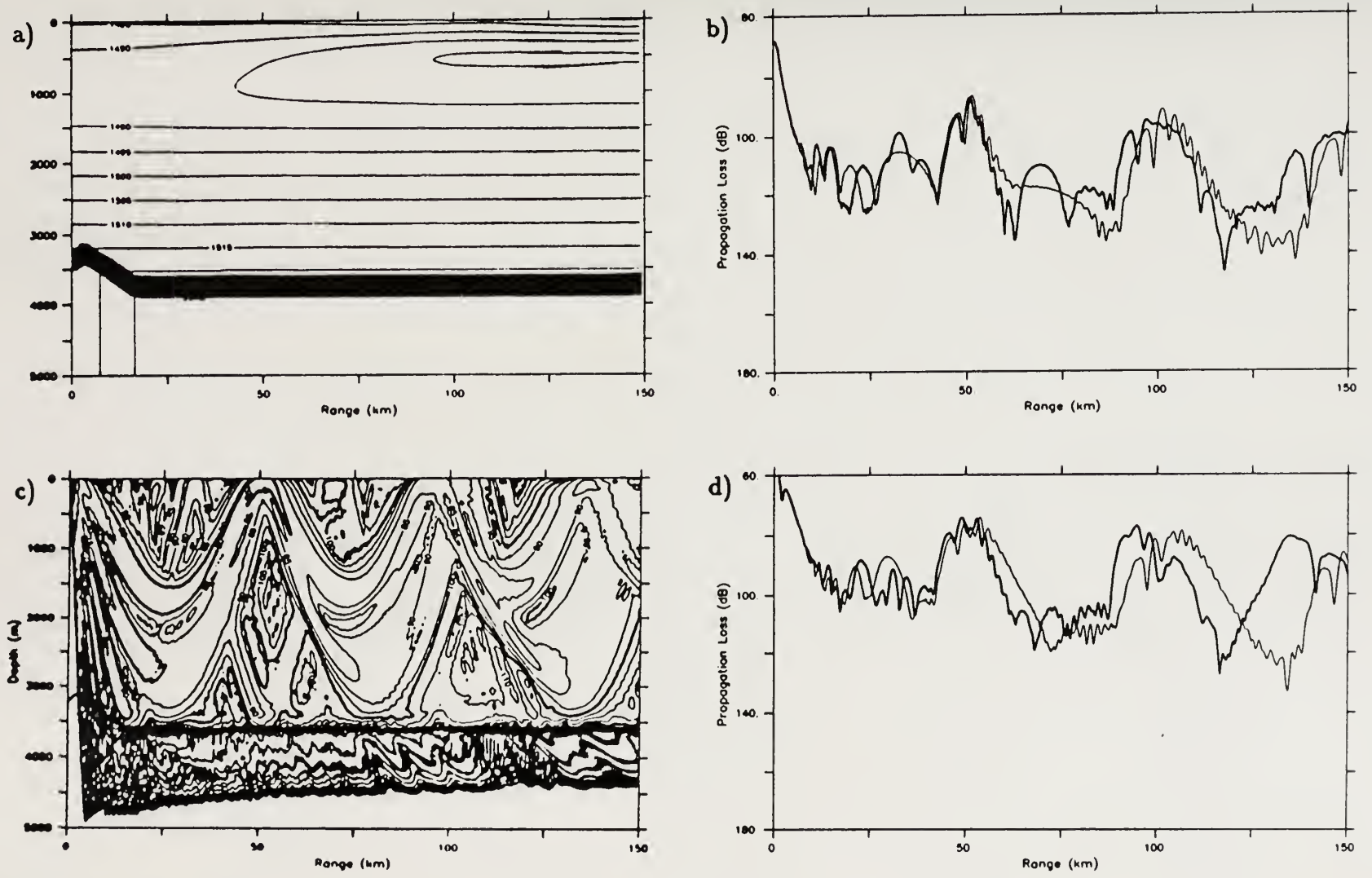

Figure 4.6) Acoustic propagation through range-dependent QG sound speed fields. $f = 50$ Hz, $z_s = 150$ m. Receiver plots overlaid with corresponding range-independent QG receivers. a. Contours of sound speed. b. Propagation loss at 10 m receivers, range-dependent case bold. c. Contours of propagation loss. d. Propagation loss at 200 m receivers, range-dependent case bold.

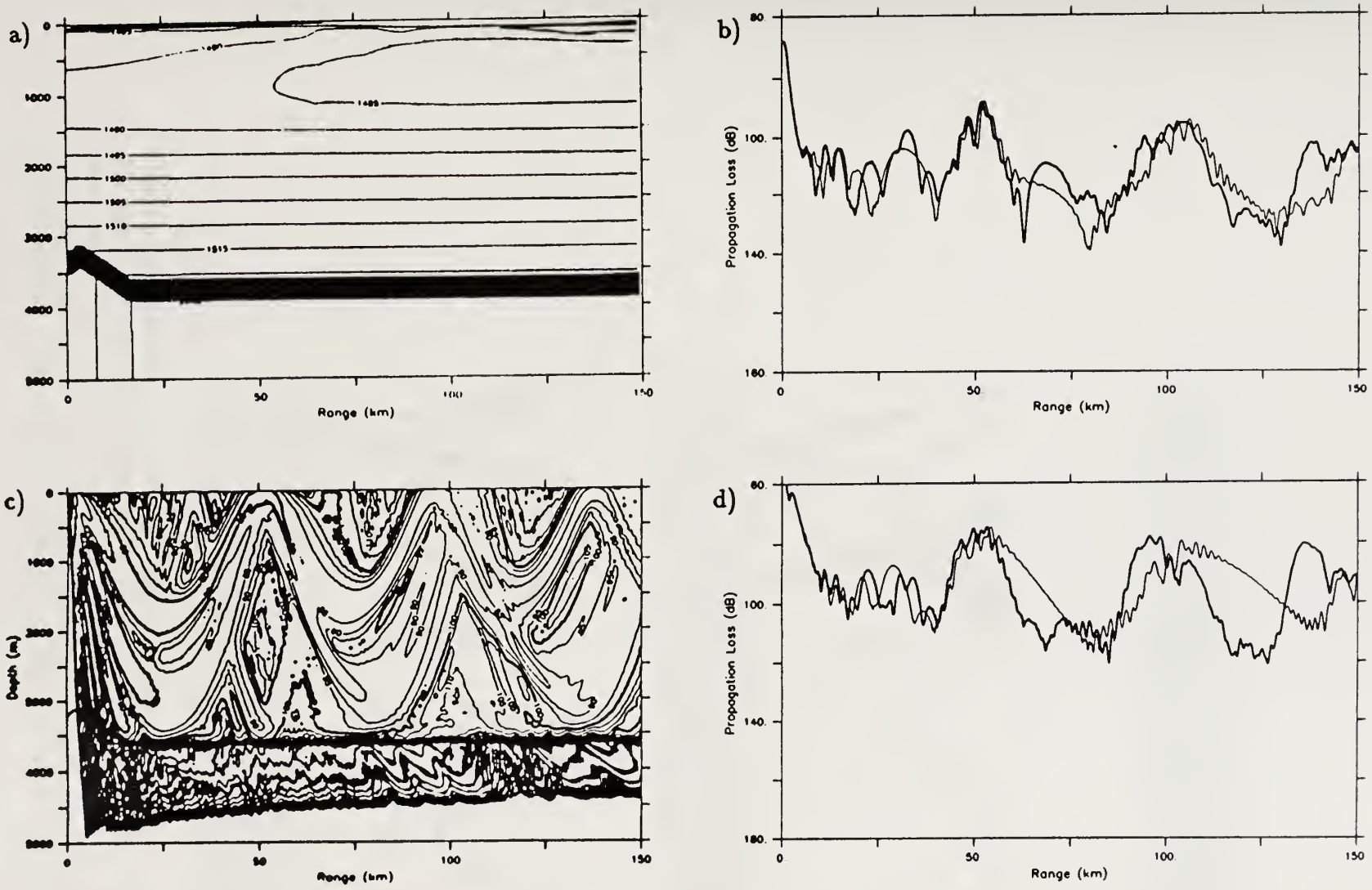

Figure 4.7) Acoustic propagation through range-dependent QG-SBL sound speed fields. $f = 50$ Hz, $z_s = 150$ m. Receiver plots overlaid with corresponding range-independent QG-SBL receivers. a. Contours of sound speed. b. Propagation loss at 10 m receivers, range-dependent case bold. c. Contours of propagation loss. d. Propagation loss at 200 m receivers, range-dependent case bold.

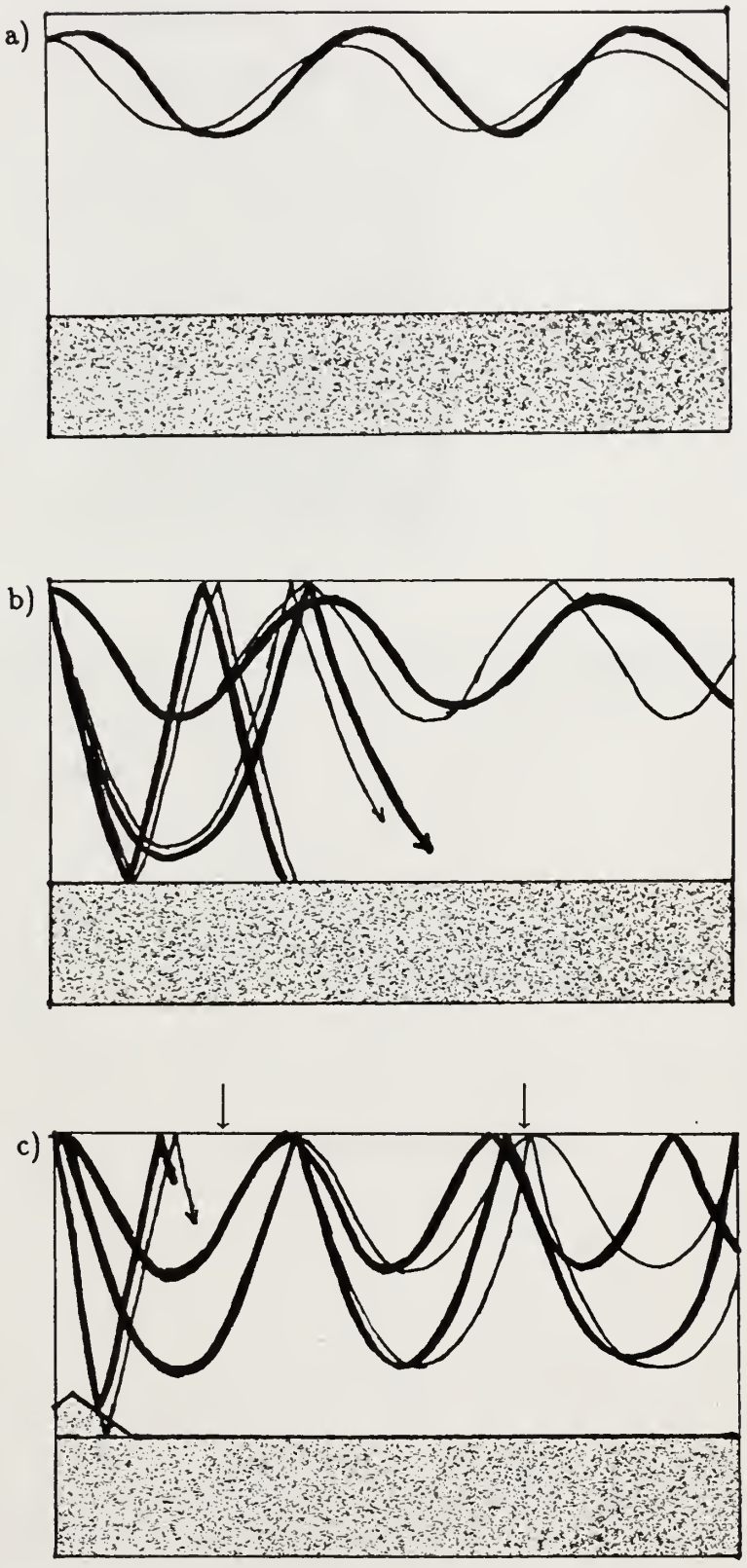

Figure 4.8) Schematic of AthenA region propagation effects. a. QG-SBL vs. QG: shallower excursion of sound in QG-SBL (bold) case. b. QG-SBL vs. QG: refraction of sound away from surface in QG-SBL (bold) case, deeper refraction in QG-QBL case. c. Range dependent (bold) vs. range-independent propagation. Arrows represent approximate locations of start and stop of sound speed change.

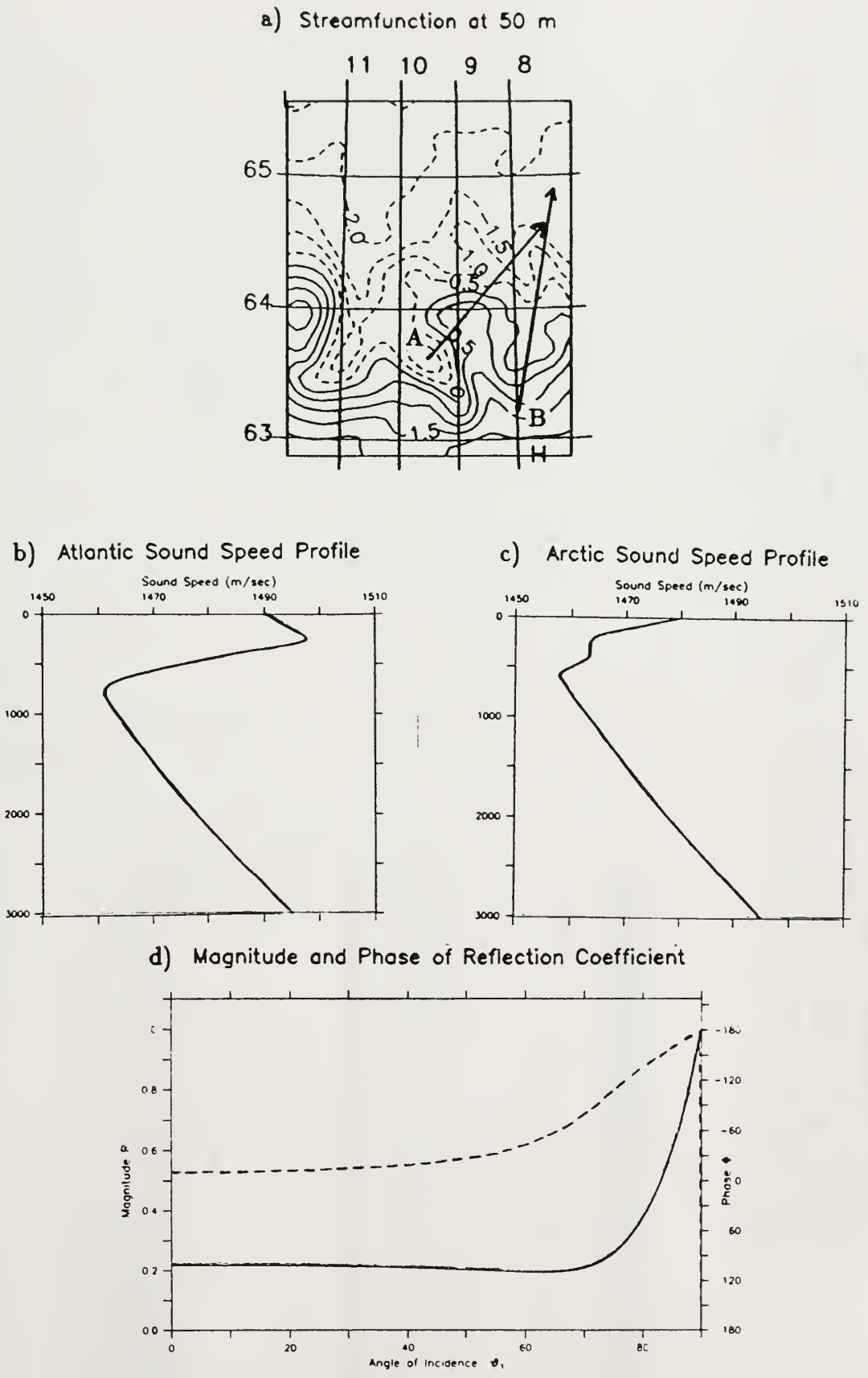

Figure 4.9) a. Gap region quasigeostrophic streamfunction fields at 50 m depth, day 10. Transect A: propagation across a developing eddy. Transect B: propagation across the front. b. Atlantic water sound speed profile. c. Arctic water sound speed profile. d. Magnitude and phase of Rayleigh reflection coefficient, $\rho = 1.6$, $c_w/c_b = 1.031$, $\beta = 4.8$.

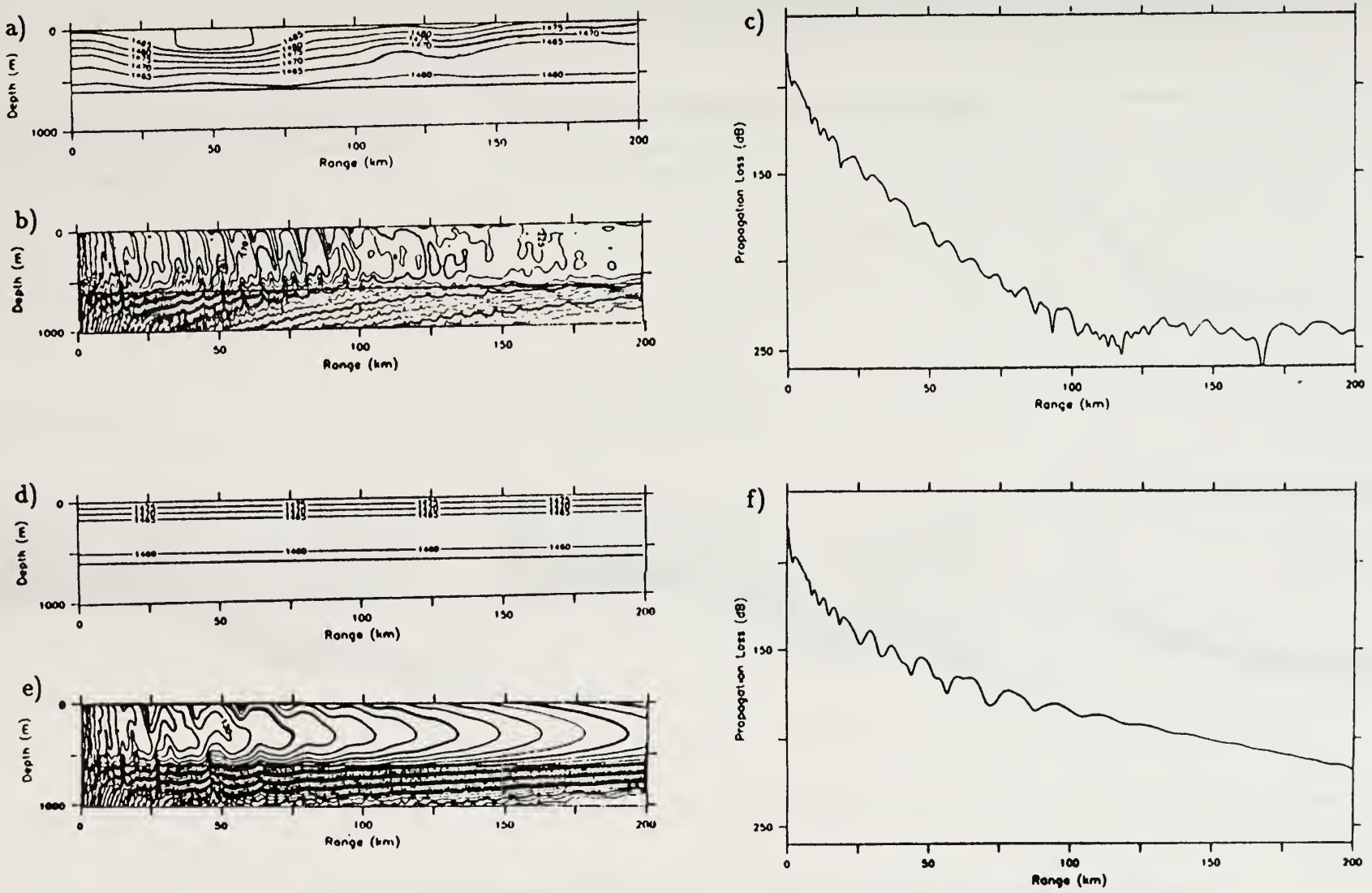

Figure 4.10)Shallow water propagation, range dependent (through eddy) vs. range independent (Arctic) oceanography. $z_s = 10$ m, $f = 25$ Hz. Bottom depth $z_{bot} = 607$ m. a. Range dependent sound speed contours. b. Range dependent propagation loss contours. c. Range dependent propagation loss, $z_{rcvr} = 10$ m. d. Range independent (Arctic) sound speed contours. e. Range independent propagation loss contours. f. Range independent propagation loss, $z_{rcvr} = 10$ m.

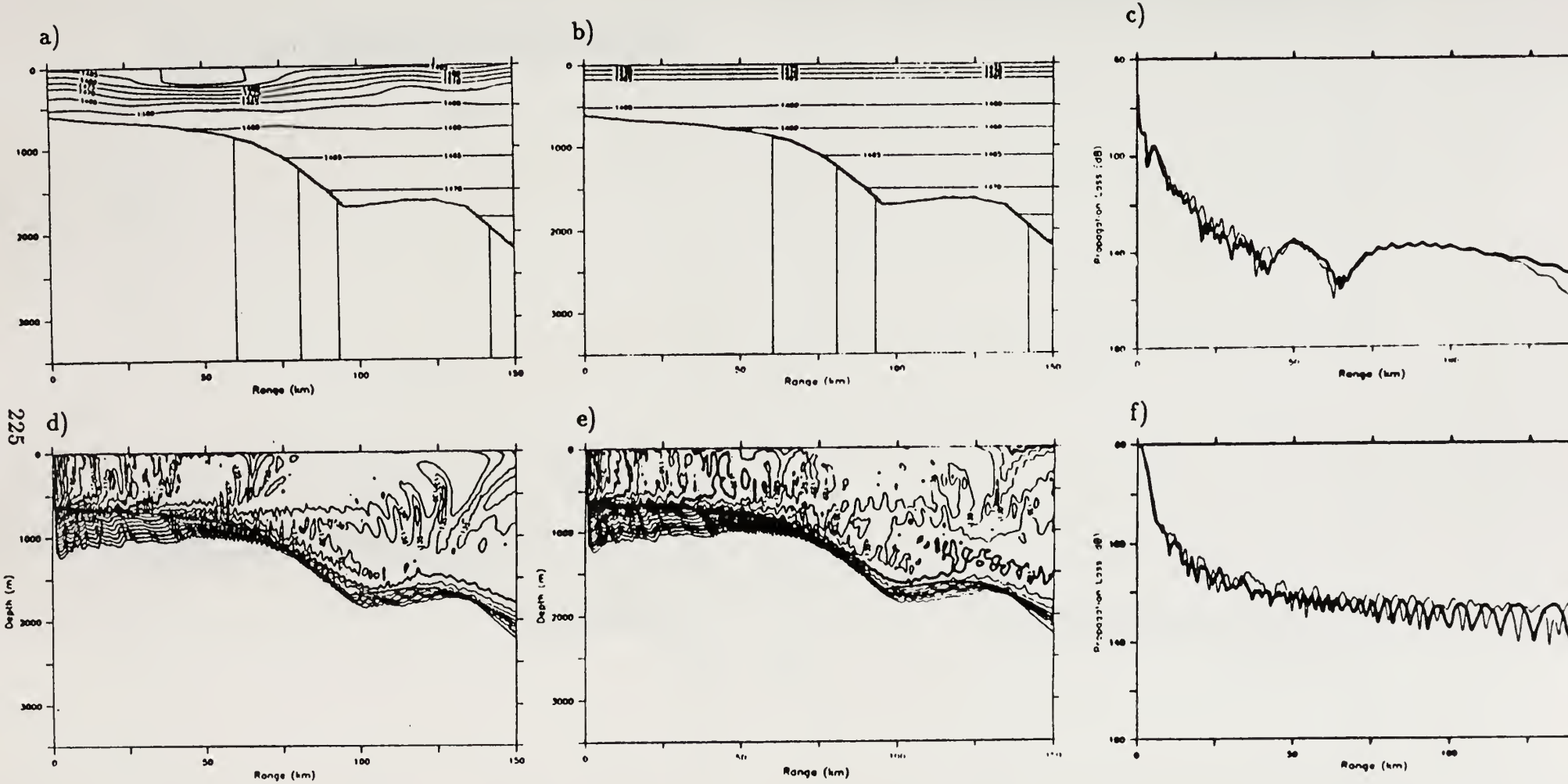

Figure 4.11) Comparison of propagation through eddy, with propagation through Arctic sound speed profile; realistic topography. z_s = 10 m, f = 50 Hz. a. Range dependent sound speed contours. b. Arctic profile sound speed contours. c. Propagation loss at 10 m receivers, eddy case bold. d. Range dependent contours of propagation loss. e. Range independent contours of propagation loss. f. Propagation loss at 600 m receivers, eddy case bold.

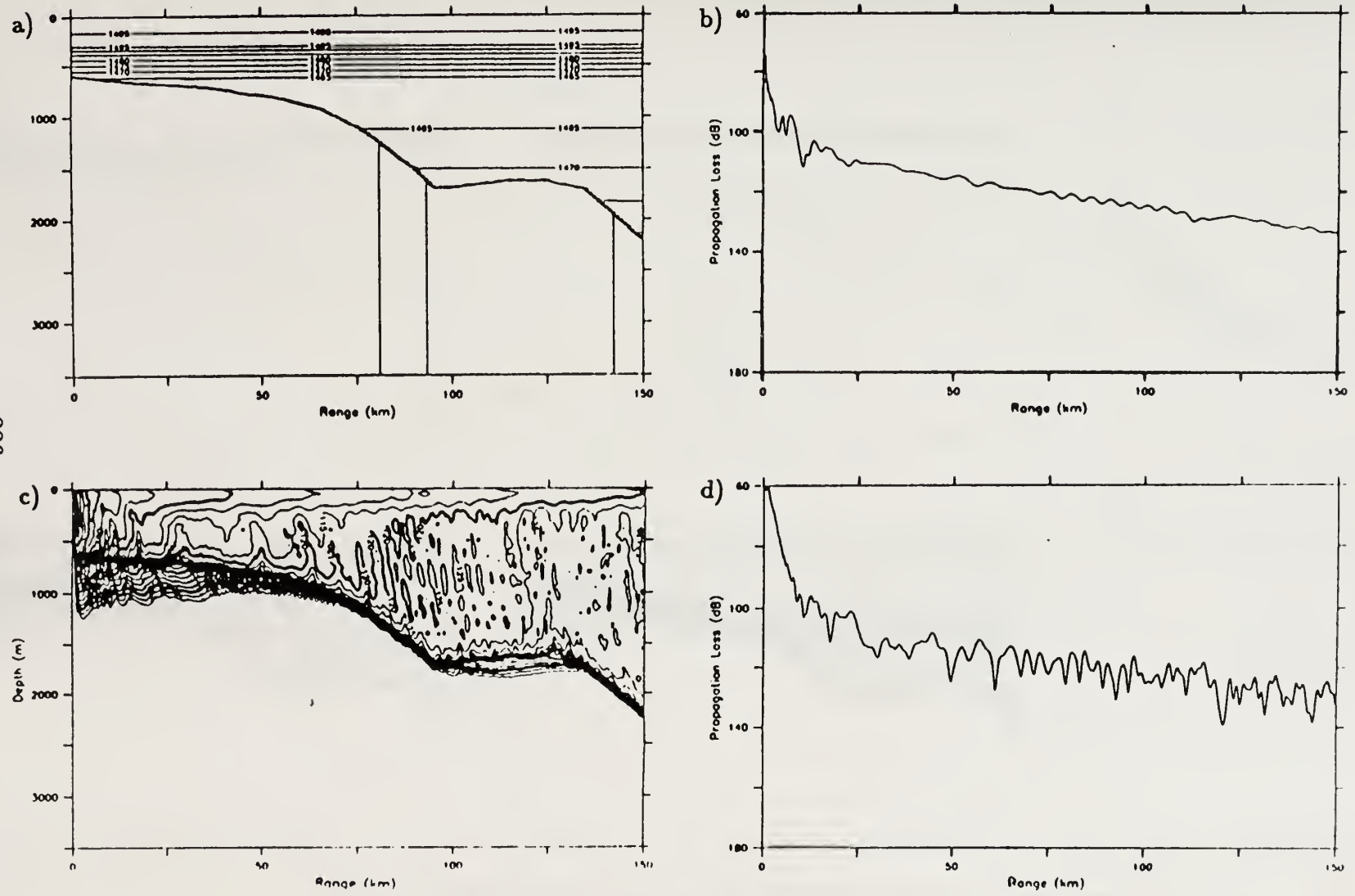

Figure 4.12) Propagation through Atlantic profile, realistic topography. $z_s = 10$ m, $f = 50$ Hz. a. Sound speed contours. b. Propagation loss at 10 m receiver. c. Contours of propagation loss. d. Propagation loss at 600 m receiver.

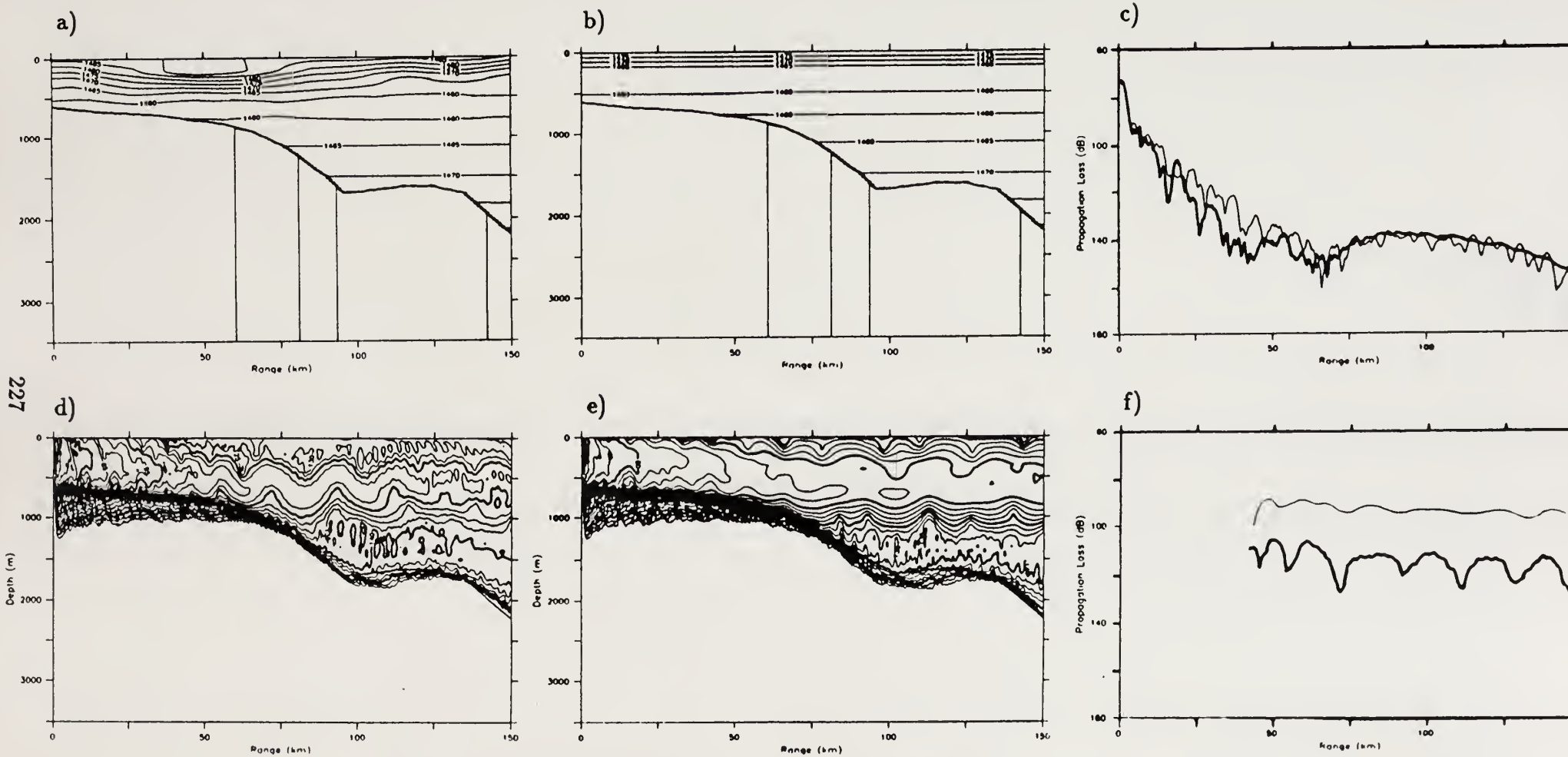

Figure 4.13) Comparison of propagation through eddy, with propagation through Arctic sound speed profile; realistic topography. z_s = 300 m, f = 50 Hz. a. Range dependent sound speed contours. b. Arctic profile sound speed contours. c. Propagation loss at 10 m receivers, eddy case bold. d. Range dependent contours of propagation loss. e. Range independent contours of propagation loss. f. Propagation loss at 750 m receivers, eddy case bold. Return blanked out prior to 42 km range as it is below the bottom.

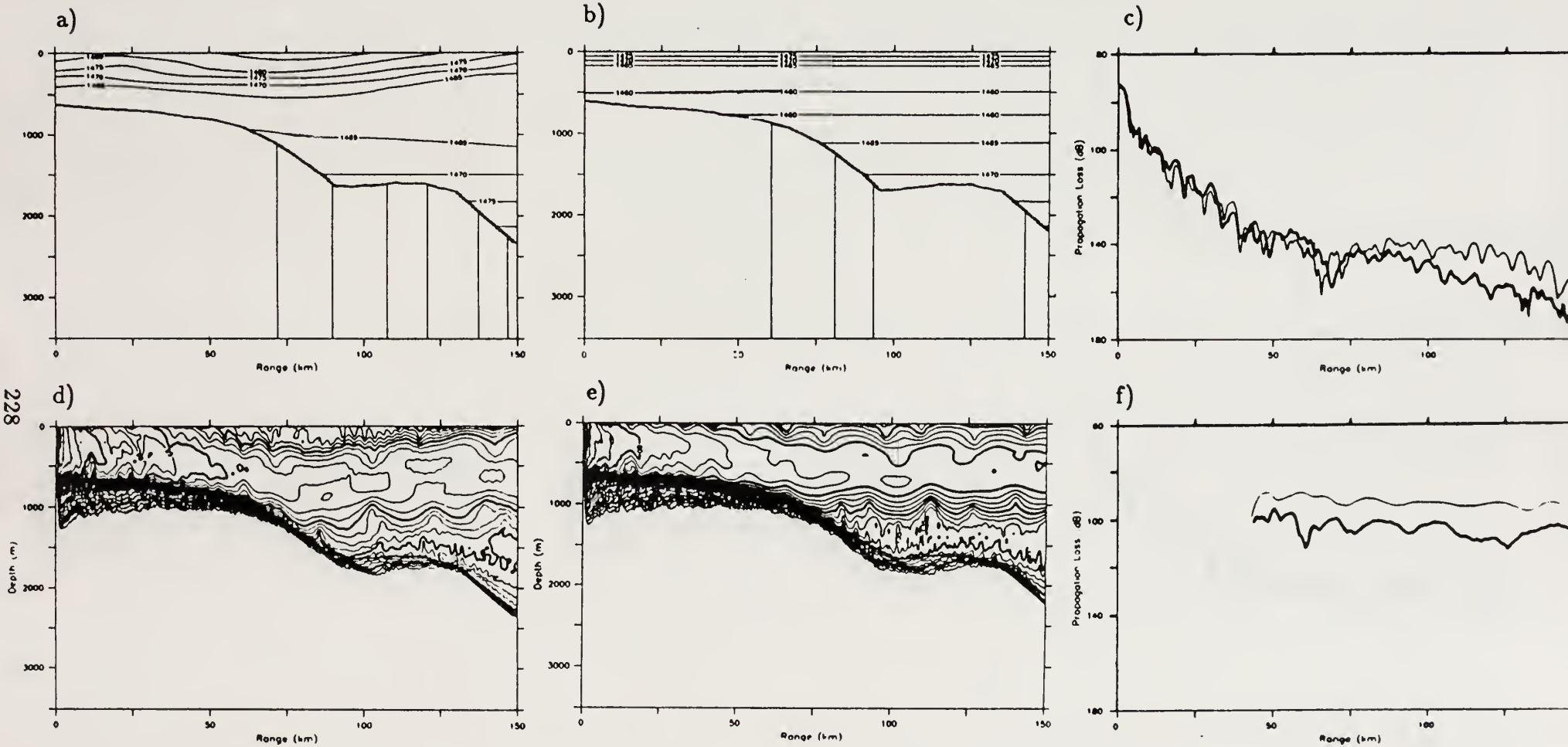

Figure 4.14) Comparison of propagation through eddy, PE model outputs, with propagation through Arctic sound speed profile; realistic topography. $z_s = 300$ m, $f = 50$ Hz. a. Range dependent sound speed contours. b. Arctic profile sound speed contours. c. Propagation loss at 10 m receivers, eddy case bold. d. Range dependent contours of propagation loss. e. Range independent contours of propagation loss. f. Propagation loss at 750 m receivers, eddy case bold. Return blanked out prior to 42 km range as it is below the bottom

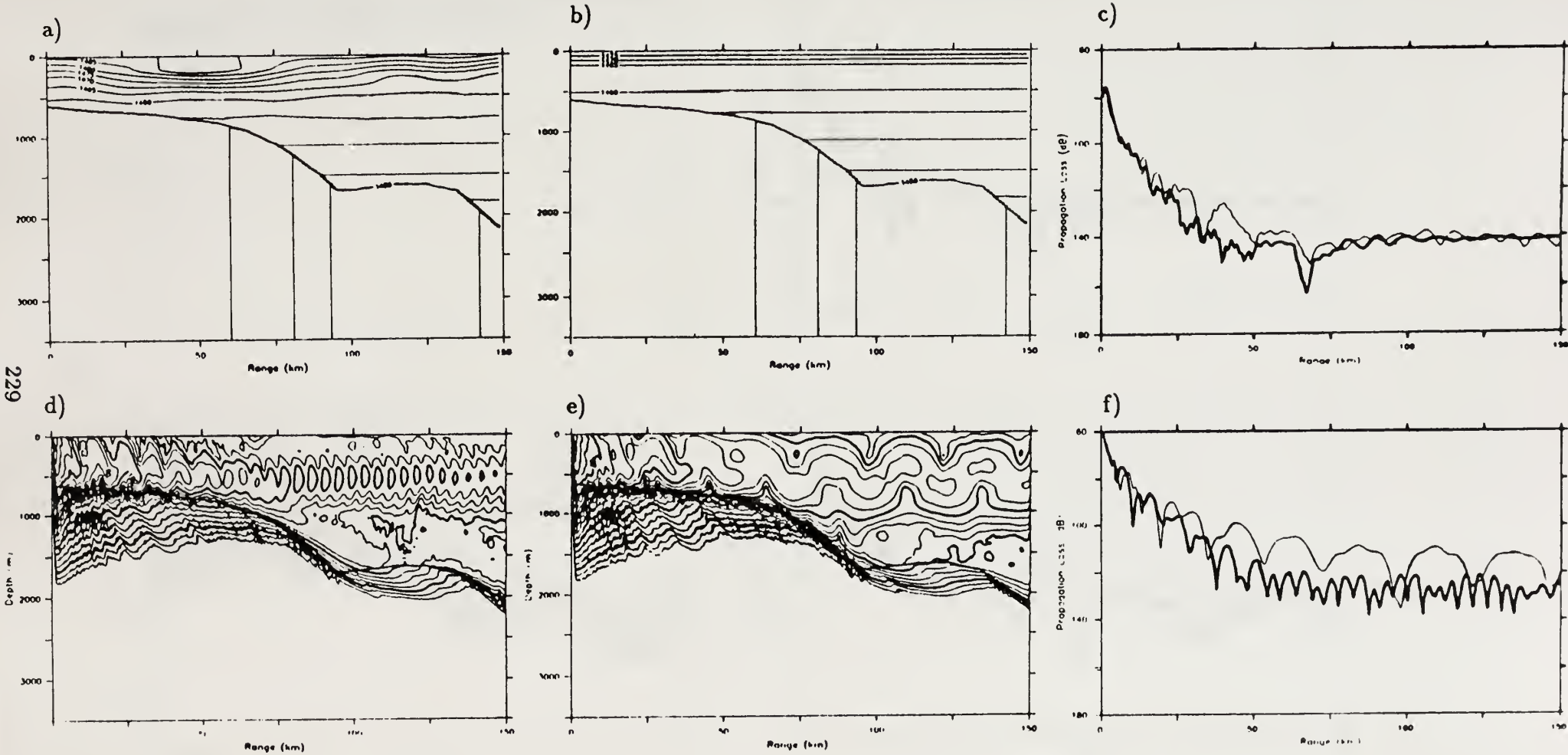

Figure 4.15) Comparison of propagation through eddy, QG model outputs, with propagation through Arctic sound speed profile; realistic topography. $z_s = 600$ m, $f = 25$ Hz. a. Range dependent sound speed contours. b. Arctic profile sound speed contours. c. Propagation loss at 10 m receivers, eddy case bold. d. Range dependent contours of propagation loss. e. Range independent contours of propagation loss. f. Propagation loss at 400 m receivers, eddy case bold.

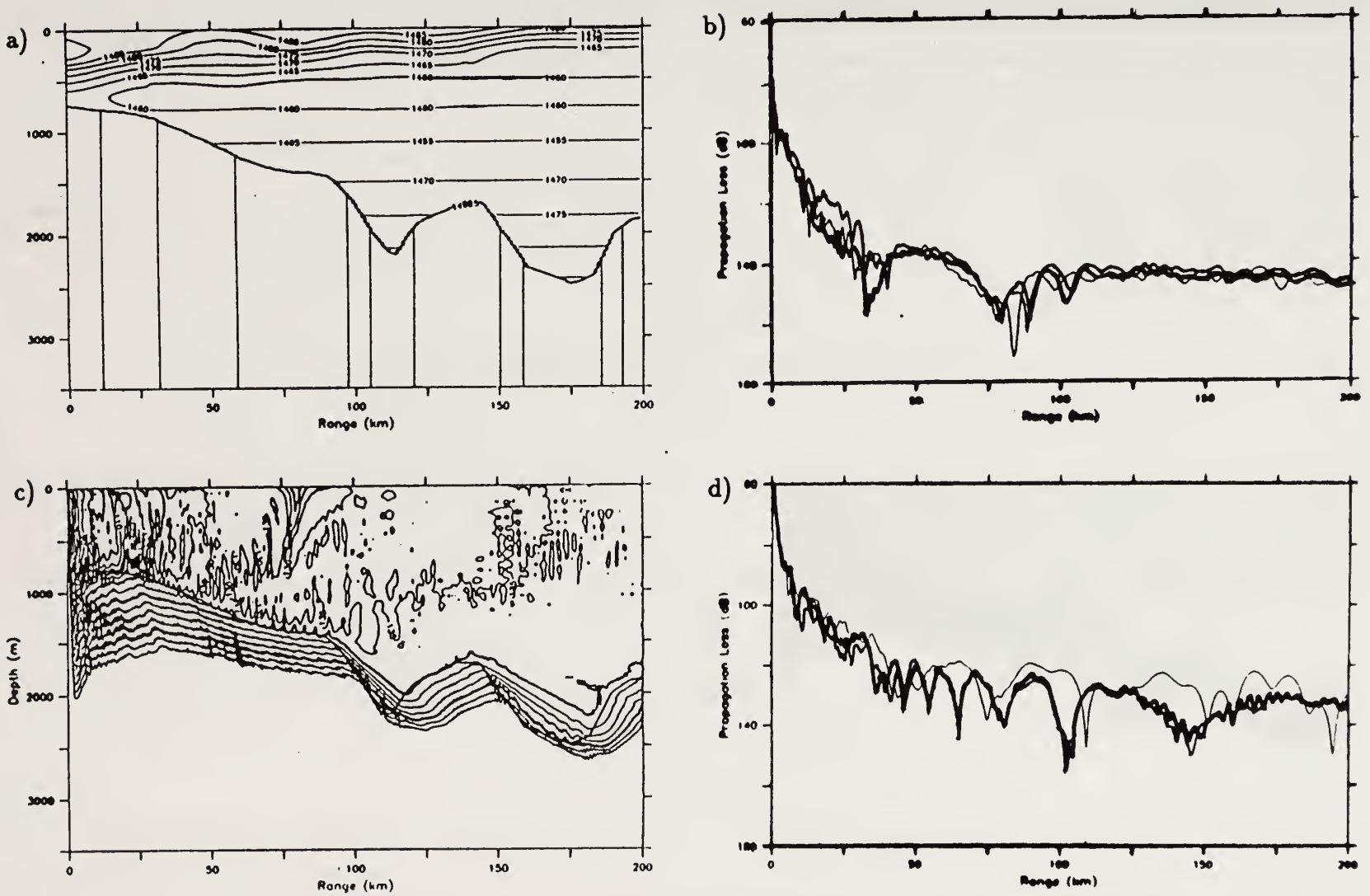

Figure 4.16) Propagation across front, realistic topography. $z_s = 10$ m, $f = 25$ Hz. a. Sound speed contours. b. Propagation loss at 10 m receivers, frontal case bold, Atlantic case medium, Arctic case light. c. Contours of propagation loss. d. Propagation loss at 250 m receivers, frontal case bold, Atlantic case medium, Arctic case light.

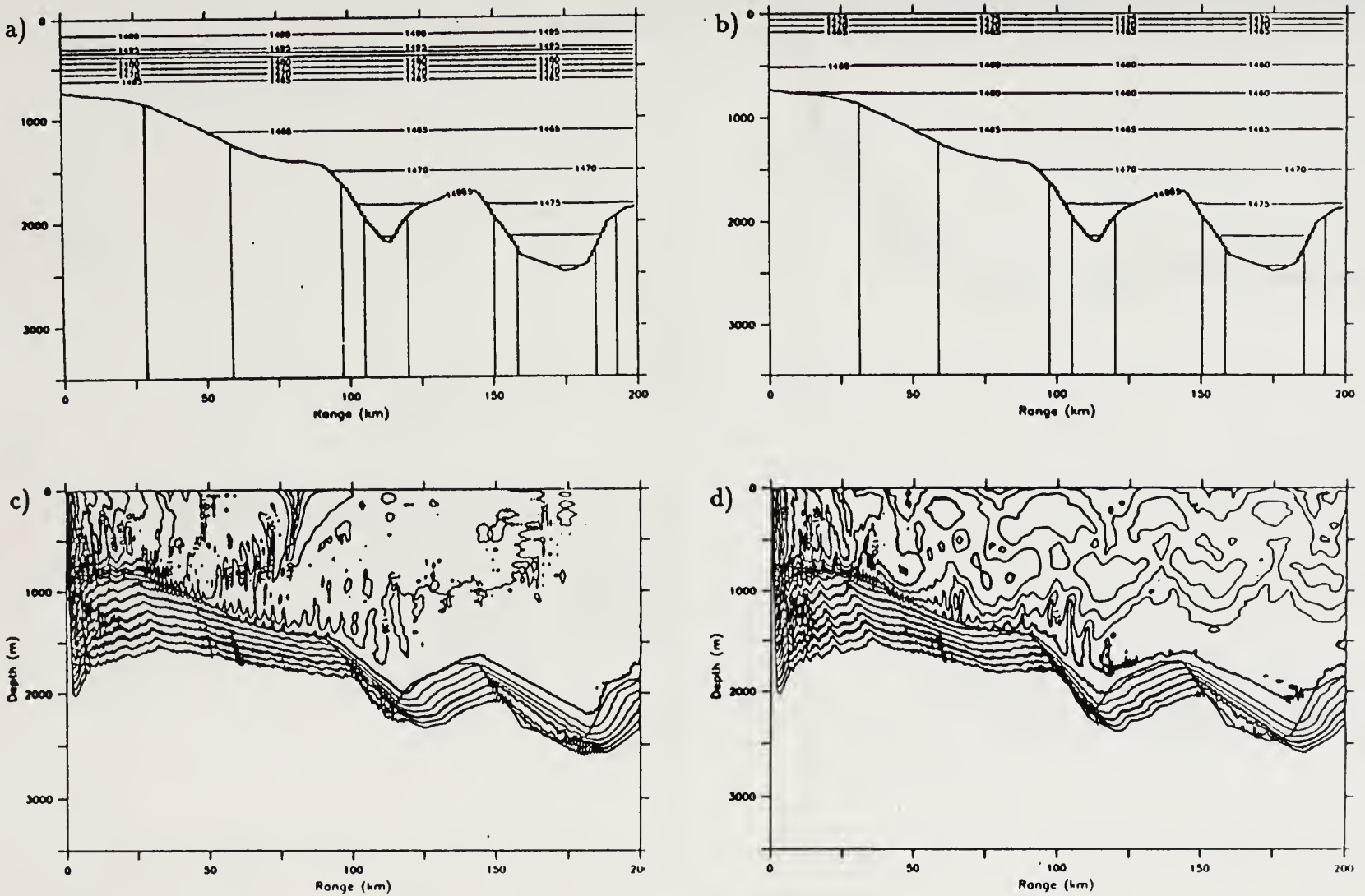

Figure 4.17) Propagation through Atlantic and Arctic profiles, realistic topography. $z_s = 10$ m, $f = 25$ Hz. a. Sound speed contours, Atlantic profile. b. Sound speed contours, Arctic profile. c. Contours of propagation loss, Atlantic profile. d. Contours of propagation loss, Arctic profile.

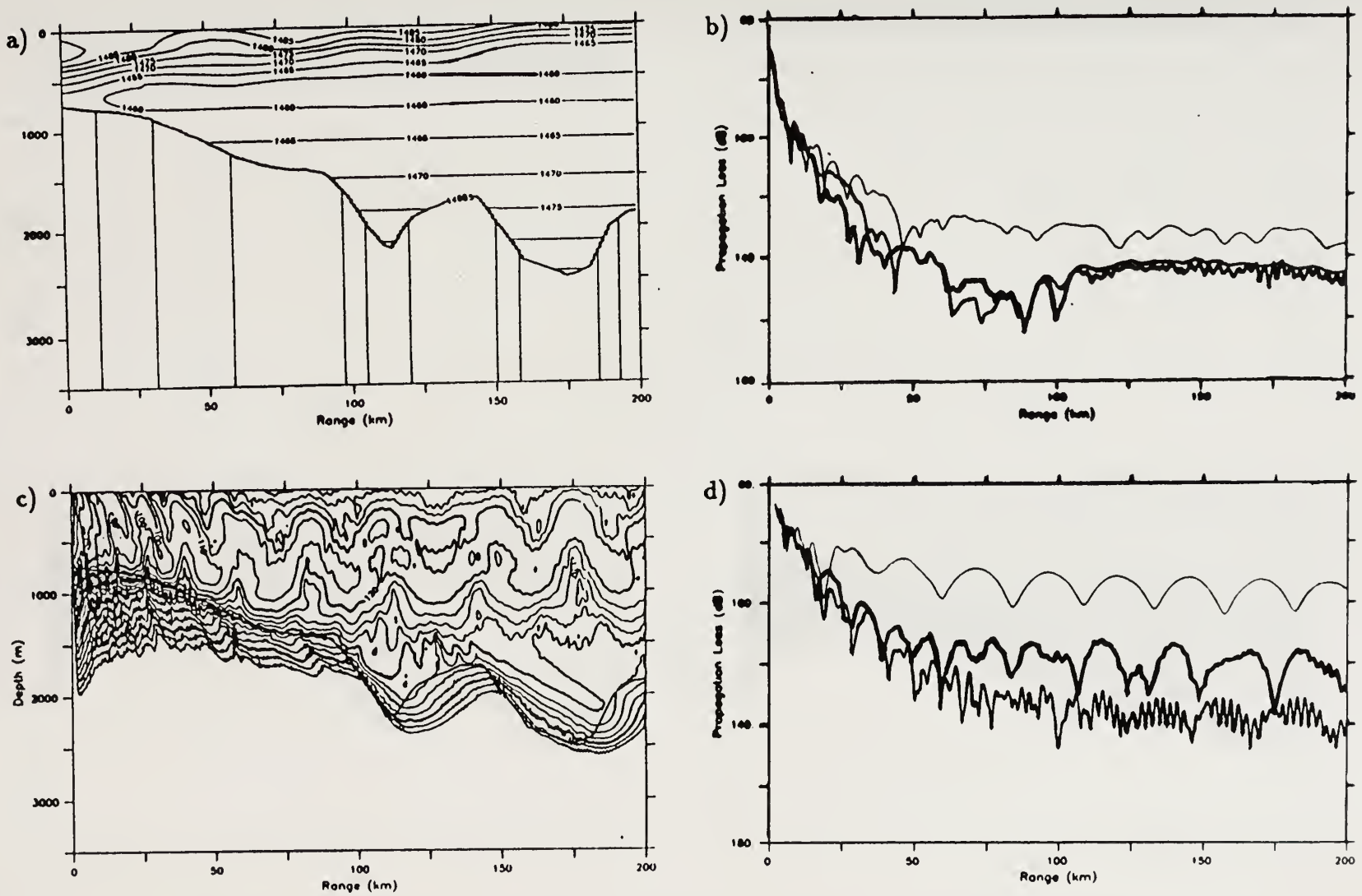

Figure 4.18) Propagation across front, realistic topography. $z_s = 300$ m, $f = 25$ Hz. a. Sound speed contours. b. Propagation loss at 10 m receivers, frontal case bold, Atlantic case medium, Arctic case light. c. Contours of propagation loss. d. Propagation loss at 750 m receivers, frontal case bold, Atlantic case medium, Arctic case light.

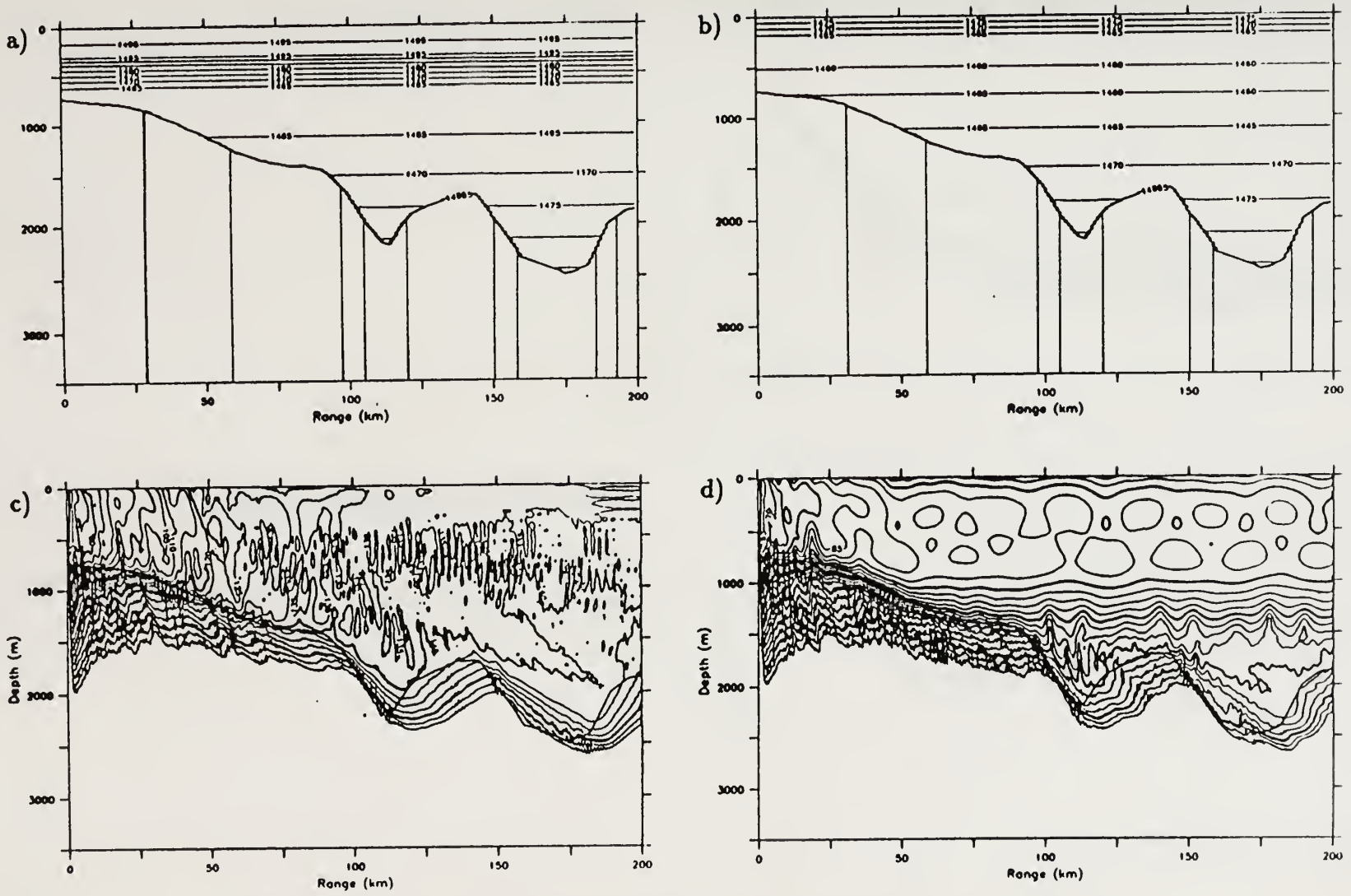

Figure 4.19) Propagation through Atlantic and Arctic profiles, realistic topography. $z_s = 300$ m, $f = 25$ Hz. a. Sound speed contours, Atlantic profile. b. Sound speed contours, Arctic profile. c. Contours of propagation loss, Atlantic profile. d. Contours of propagation loss, Arctic profile.

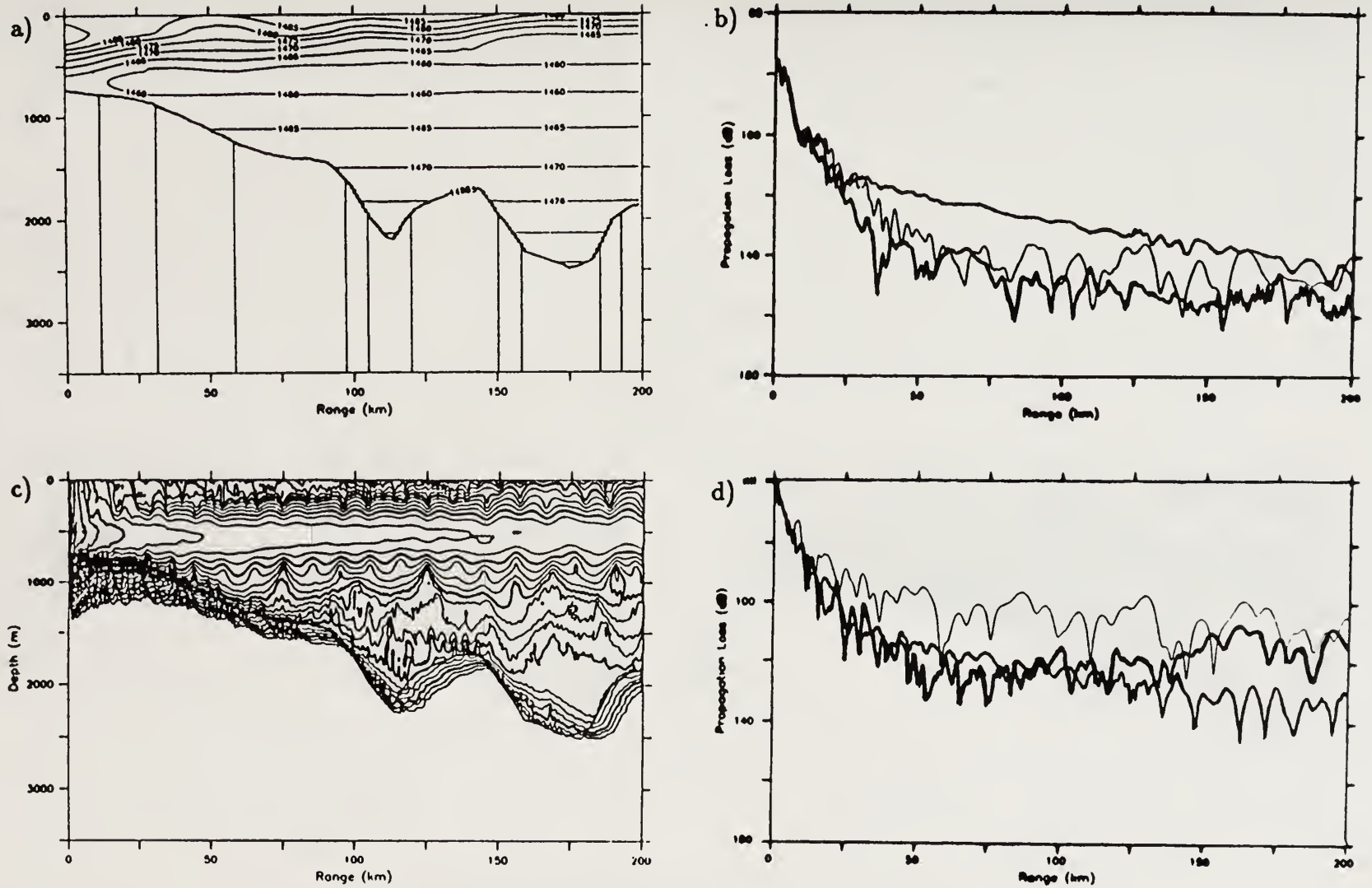

Figure 4.20) Propagation across front, realistic topography. $z_s = 600$ m, $f = 50$ Hz. a. Sound speed contours. b. Propagation loss at 10 m receivers, frontal case bold, Atlantic case medium, Arctic case light. c. Contours of propagation loss. d. Propagation loss at 300 m receivers, frontal case bold, Atlantic case medium, Arctic case light.

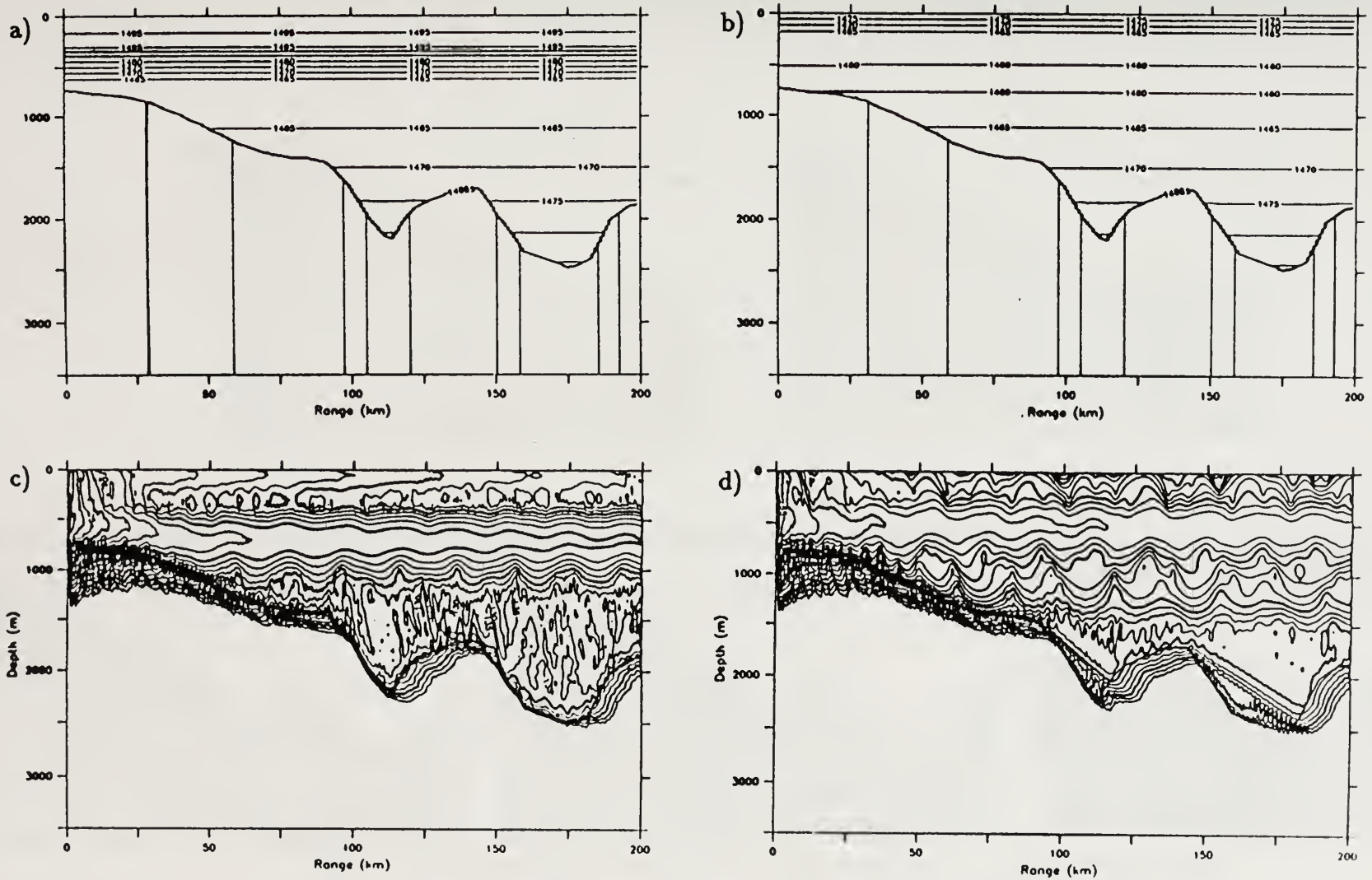

Figure 4.21) Propagation through Atlantic and Arctic profiles, realistic topography. $z_s = 600$ m, $f = 50$ Hz. a. Sound speed contours, Atlantic profile. b. Sound speed contours, Arctic profile. c. Contours of propagation loss, Atlantic profile. d. Contours of propagation loss, Arctic profile.

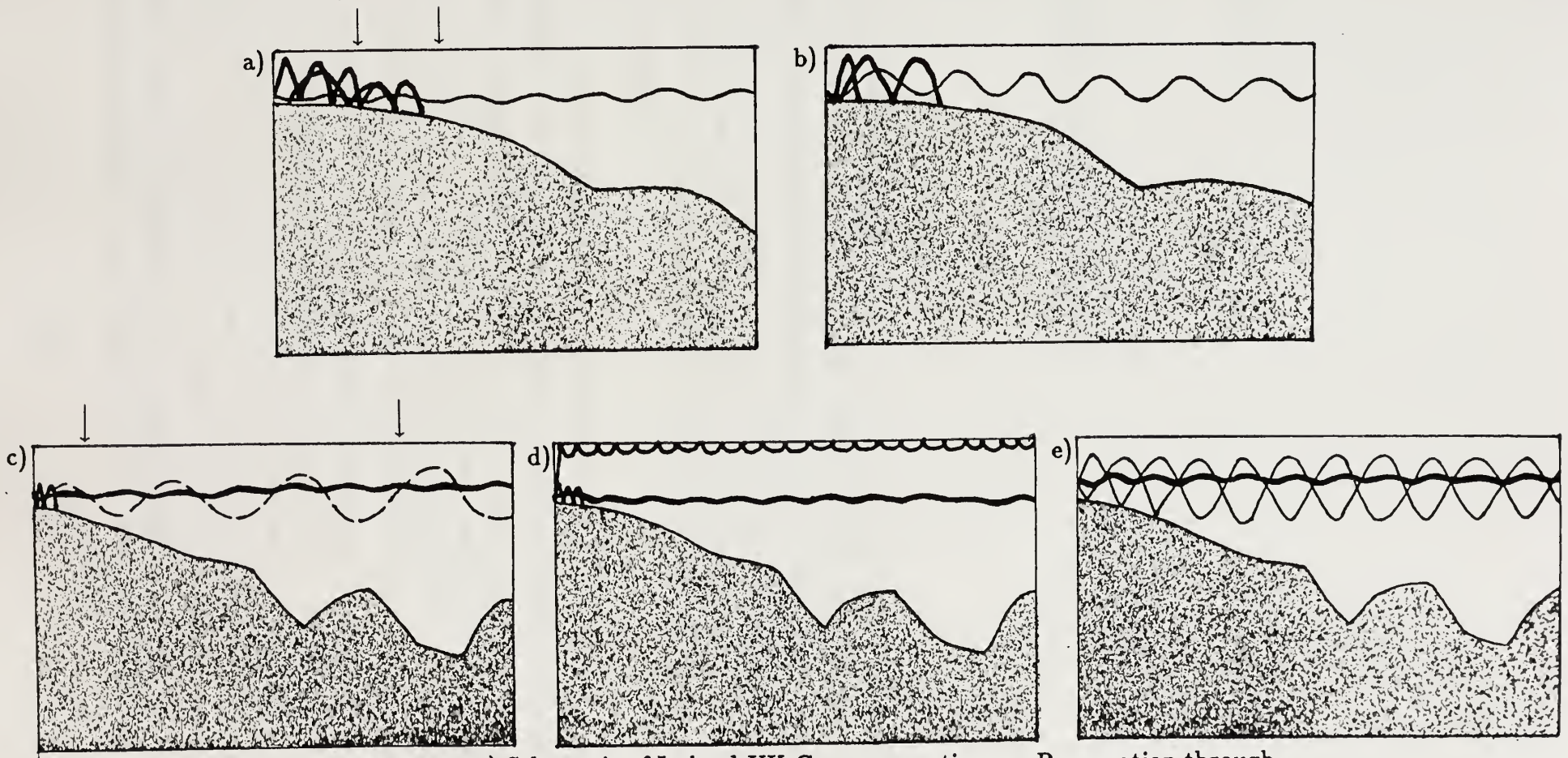

Figure 4.22) Schematic of Iceland-UK Gap propagation. a. Propagation through eddy. Arrows represent start and end of eddy. b. Propagation through Arctic water sound speed fields. c. Propagation across Iceland-Faeroes front. Arrows represent approximate locations of deep and surface front, respectively. d. Propagation through Atlantic water sound speed fields. e. Propagation through Arctic water sound speed fields.

Chapter 5

Summary and Conclusions

This thesis has studied underwater acoustic propagation at low frequencies in both deep oceanic regimes with slowly varying depths, and shallower regimes with rapidly varying topography. Effects of range dependence of the sound speed profile within the water column have been documented, and the interacting propagation effects when both the oceanography and topography vary. Additionally, this work has investigated the effects of a shallow surface mixed layer on water column propagation.

The primary contributions of this work are the detection of the dependence of propagation on the interaction of low-frequency source-image interference patterns and the angular dependence of the water-sediment interface reflection coefficient. This interaction provides an important classification of propagation regimes according to the relative magnitude of sediment interaction: whether bottom interacting propagation paths are dominant over purely water column paths, or vice versa. The different behaviors of propagation in these two regimes, when the oceanographic and topographic properties vary, has been thoroughly studied. Formation of shadow zones due to downward oceanographic refraction with a frontal crossing has been documented, as has the increase in surface ensonification or formation of convergence zones due to upward oceanographic refraction of sound. Additionally, long range convergence zone propagation for shallow sources via low frequency effects has been documented, increasing the

extent of permissible conditions for such propagation. Oceanographic and topographic interaction effects on propagation in regions of shallow and highly variable topography have been documented, showing the strong effects of the topography with significant modifications to propagation patterns by oceanographic variations. The inclusion of a thin surface mixed layer, at frequencies too low for duct trapping, has been shown to significantly modify propagation paths.

These phenomena have been identified by studying acoustic propagation in different regions under a wide variety of physical conditions. The Gulf Stream region represented a deep-water regime of strong oceanographic variation and slow topographic variation, where in general the oceanographic variations with range had a larger effect on acoustic propagation than did the topographic variations, although knowledge of the depth was crucial and variation of topography could produce important changes to propagation. The AthenA region demonstrated propagation patterns in another deep region which had weaker oceanographic variations with range; again changes to the oceanographic environment modified propagation more greatly than did changes to the topography. On the other hand, the shallow and highly variable topography in the Iceland-UK Gap region dominated the acoustic propagation in that region; the oceanographic variations provided significant but lesser modifications to the resulting field.

Throughout this work we have seen that the topographic depth and the sediment layer can have large and sometimes overwhelming effects on acoustic propagation within the waveguide. For a certain topographic configuration, a change in the sediment model parameters can totally transform propagation patterns; alternatively, a change in the topographic configuration can change the entire propagation regime. If again we think of the ocean sediment as the bottom boundary condition of the acoustic waveguide, the topography determines the distance to the boundary and the sediment model conceptually determines the boundary condition used. Considering the magnitude of sound speed gradient generally found in the water column (less than .1 sec^{-1}, in central depths) with that found in typical sediments (.5 to 1.5 sec^{-1}), as well as the sound speed and density discontinuities at the water-sediment interface, it is not surprising that the location and form of this bottom boundary condition can be the primary determination of oceanographic waveguide propagation properties. It becomes

useful to think of the topography and sediment as forming a set of constraints for propagation patterns, with the oceanographic variations modifying propagation patterns within those constraints. The amount of change which the oceanographic variations can produce varies with the type of topographic and sediment configuration.

In regions of shallow or very highly variable topography, such as the Iceland-UK Gap, the modifications possible by the oceanography were occasionally extremely limited; indeed, some cases where the propagation patterns were nearly invariant to topography appeared, such as cases with shallow source depth. In other examples with deeper source depth, the oceanographic variations could modify the entire propagation regime from one in which the sound was tightly constrained to the center of the sound channel, to one with greater vertical extent of propagation. Figure 5.1 schematizes such cases; figures 5.1a and 5.1b compare propagation across the eddy with propagation through the range-independent Arctic water profile. The strong sound speed gradient at the base of the eddy refracts sound down toward the sediment in figure 5.1a, and increases the horizontal frequency of bottom interactions. The increased loss due to these interactions decreases sound channel axis magnitudes 20 dB; since bottom reflections selectively filter out high-angle sound, the remaining propagation patterns are more closely confined to the sound channel axis. In figure 5.1b of propagation through the range-independent Arctic profile, the lesser amount of bottom interactions leaves a greater amount of higher angle sound in the channel.

Propagation across the Iceland-Faeroes front showed the same effect of oceanographic variations modifying propagation regime. Frequently the frontal interaction with topography resulted in patterns revealing the effects of both water masses, the Atlantic-type starting profile and the Arctic-type destination. Figure 5.1c schematizes propagation across the front, while figures 5.1d and 5.1e depict propagation in Atlantic and Arctic profiles, respectively. The strong deep gradient near the start of the frontal transect increases the sediment losses and confines sound near the axis of the sound channel as in the Atlantic profile, although the rapid loss of the surface duct in the realistic case prevents surface trapping. The frontal transition to Arctic type profile, with its shallower sound speed gradient, decreased the amount of bottom loss from that seen in the Atlantic profile, permitting a greater angular excursion of sound. Figure 5.1c

shows this propagation path with the dashed line, to indicate its lesser magnitude. Propagation across the front resulted in sound channel axis ensonification intermediate between that in the Arctic and Atlantic water masses; magnitudes were up to 20–25 dB less than in the Arctic profile, and 25–30 dB greater than in the Atlantic profile. The position of the front, with respect to the shallow topography, will adjust the amount of bottom loss that occurs, and thus must be known for accurate acoustic prediction.

These results confirm previous work in the area (Jensen et al., 1991) which showed that knowledge of the topography was paramount in producing acoustic forecasts for the region, and that oceanography produced significant but lesser modifications to the propagation patterns. That work illustrated overall propagation patterns using ray traces which did not explicitly show the loss of vertical propagation extent due to the selective filtering of bottom interactions as the contours of propagation loss do.

Thus the Iceland-UK Gap represents a region of shallow or highly variable topography where the bottom boundary condition forms a relatively tight constraint on possibilities for propagation patterns; oceanographic modification to propagation had a lesser but still quite significant effect. In such regions detailed knowledge of the topography and sediment conditions would clearly be crucial to accurate acoustic prediction.

In deep regions with flat or gently sloping topography, the range of modifications possible by the oceanography is relatively greater and can cause drastic changes to the propagation regime, either refracting sound upward or downward within the waveguide, or adjusting the horizontal refraction distance of the sound. At the same time, with the smoother topography, variations to the propagation patterns caused by the topography changes could be much less. As case in point, the abyssal hill seen in the AthenA region had an extremely small effect on propagation patterns, only shifting bottom-reflected returns approximately 5 km in range as schematized in figure 5.2a. Additionally, the upsloping or downsloping topography cases studied in the Gulf Stream region frequently only provided adjustments of 2–4 km to the radius of convergence zones, or affected ensonification levels 5–7 dB within those convergence zones. The modifications by the oceanographic variations with range in both the AthenA and Gulf Stream regions caused considerably greater changes to the propagation patterns than did

the topographic changes; in the AthenA region oceanographic range dependence shortened convergence zone radii enough to cause local changes in ensonification of 30–40 dB by the third convergence zone compared with ensonification in a range independent ocean. Figure 5.2a shows the modifications to long-range propagation paths that produce these ensonification changes; range dependent oceanographic propagation paths are drawn bold, range independent drawn light. In the Gulf Stream region, oceanographic variations with range could increase or decrease surface ensonification by 25–30 dB. In such regions of relatively flat topography, the changes in propagation caused by the oceanographic variations were much greater than the changes caused by the local topographic variations.

In that Gulf Stream study, however, other cases occurred in which the same gradual alterations to the bottom depth changed the entire propagation regime. The Sargasso profile cases with weak excitation of trapped water column modes showed that topographic effects could overwhelm oceanographic effects if the magnitude of the purely oceanographic perturbation to the propagation were weak enough; in the case of propagation from Sargasso to Slope water for a source near the surface and frequency of 100 Hz, acoustic propagation was nearly invariant to the changes in the water column. Additionally, changes of sediment parameters showed that under conditions with highly reflective sediments, propagation patterns were again nearly unaffected by modifications to the oceanographic sound speeds. Propagation patterns in deeper regions still seems to be limited by constraints determined by the topography and sediment, with those constraints considerably broader in deep water regions with gentle topographic variations.

This entire work was conducted with a range-independent fluid sediment model. In the Gulf Stream region, such a model could well be unrealistic in view of the horizontal extent of the calculation; in the Iceland-UK Gap region it is unrealistic in view of the widely varying topography, which experiences different sedimentation conditions. In view of the demonstrated importance of sediment and topographic interaction effects on the water column propagation patterns, a very important next step would be to include variation of the sediment properties with location.

In addition to considering the bottom boundary condition carefully, the surface boundary condition of the waveguide must be known. Surface rough-

ness was not considered in this work, and generally has lesser effects in the frequency range considered, but the surface mixed layer can frequently be considered a boundary condition to the waveguide due to its much smaller vertical scale. The thickness of the surface mixed layer is usually less than that of the sediment; sound speed gradients at the base of the mixed layer are frequently of order .6 sec^{-1}, comparable to the sound speed gradients in the bottom sediment. Sound trapping within a surface duct is generally considered a high-frequency phenomenon; however, the comparison studies in the AthenA region showed that the surface duct can also have a distinct effect on propagation patterns at frequencies too low for such ducting to occur. For sources within the deep sound channel, careful resolution of the sound speed profile and inclusion of a thin layer of high sound speed water near the surface of the ocean can significantly modify propagation paths in the deeper water, causing changes in local magnitudes of 20 dB or more in the vicinity of the modified sound paths. Figure 5.2b demonstrates these modified propagation paths due to the better-resolved QG-SBL sound speed profile; the QG-SBL case is drawn bold and has greater vertical extent. Figure 5.2c demonstrates the effect for a different source depth, where inclusion of the high sound speed layer refracted sound away from the surface. The thin layer of high sound speed water prevented sound in propagation paths just below the surface layer from penetrating into the near-surface regions, for 100 Hz sound; for sound too low for duct trapping, the surface layer can be an effective barrier. At lower frequencies diffraction effects permitted some lessened ensonification of that layer.

The Iceland-UK Gap region also demonstrated the effects of a surface duct. The 250 m deep layer on the Atlantic side of the front was capable of trapping sound at the higher frequency used (50 Hz). At 25 Hz the calculations with realistic topography showed too many topographic interaction effects to determine if sound was barred from the thick surface layer. The calculations with the Atlantic profile and deep flat bottom showed a significant decrease in surface ensonification over similar propagation in the Arctic profile. Thus for a source within the deep sound channel, a surface mixed layer can act to decrease near-surface ensonification for frequencies too low for duct trapping and too high for low frequency diffraction to permit significant sound penetration of the layer.

Previous work in surface boundary layer acoustics (Porter et al., 1990;

Urick, 1983) has concentrated on conditions for duct formation, strength, depth, and trapping, or on propagation effects of the duct for a source within the surface layer. This work has studied the effects of that duct for a source within the deep sound channel, and has shown that inclusion of the surface duct can produce distinct changes at frequencies too low for duct trapping, by both altering propagation paths and forming a barrier to sound in a certain middle frequency range determined by duct depth.

Within the oceanic waveguide, low frequency interference patterns had a very strong effect on propagation patterns in deep water regimes. The initial source-image interference patterns produced an angular distribution of sound striking the sediment which varies strongly with frequency; the interaction of this distribution of sound energy with the functional form of the Rayleigh reflection coefficient at the water-sediment interface determines the reflected sound intensity propagating back within the water column relative to the sound intensity refracting entirely within the water channel.

In the Gulf Stream region, an important classification of propagation regimes emerged according to the refraction characteristics of the initial Lloyd's Mirror interference pattern in the water. When the primary interference lobe refracts entirely within the waveguide, then a large percentage of the total sound energy never interacts with the sediment and propagation patterns were comparatively less sensitive to the form of the sediment model. Propagation with deep sources in both water masses, and with source at 100 m in the Slope profile at 100 Hz, fell into this group. Figure 5.3a schematizes propagation in this group.

When the primary interference lobe interacts with the sediment and additionally there are strongly excited trapped modes within the water column, then propagation patterns are more sensitive to the form of the sediment model than in the previous case, due to the increased percentage of sound energy interacting with the sediment layer relative to that propagating in the water column. Slope water propagation with the source at 10 m, and at 100 m at 25 and 50 Hz, fit into this group; figure 5.3b depicts propagation under these conditions. The bold line indicates the primary Lloyd's Mirror interference lobe interacting with the sediment. Within that sediment, density decreases of less than .5 gm/cm^3 caused increases of 3–7 dB in convergence zone minima, by modifying the functional form of the Rayleigh reflection coefficient. Alterations to the sediment sound speed

gradient modified the primary refracted return 5–7 dB; refracted sound sometimes interfered constructively, sometimes destructively with the water column propagation patterns. The sediment sound speed discontinuity alters the functional form of the reflection coefficient, altering the amount of grazing-incidence sound reflected back to interfere with water column propagation patterns. Only when the amount of such interference was extremely large ($c_w/c_b = .98$) did it overwhelm the water column propagation pattern.

The effects of downward topography differed between these two groups. In the first group, with the primary Lloyd's Mirror interference lobe refracting within the water column in the flat-bottom waveguide, the downward topography only affected the lesser interference maxima as schematized in figure 5.4a. The primary lobe defined the major convergence zones and remained unchanged, but the modification to the lesser lobe(s) can cause changes of 5–7 dB in deeper regions of lower ensonification.

In the second group, where the primary interference lobe interacted with the sediment, downsloping topography permitted a greater portion of that primary lobe to refract within the water column, as shown in figure 5.4b. The increase in sound refracting within the water column increased convergence zone magnitudes 7–10 dB; the deeper sound paths increased convergence zone radii 1–3 km.

It must be noted that these two groups differ only due to the effects caused by the main Lloyd's Mirror interference lobe interacting with the sediment: if more energy interacts with the sediment, then sediment changes affect a greater percentage of the total waveguide sound. Additionally, with downsloping topography, the additional sound refracting within the water column greatly affects convergence zone radius if the convergence zones are not already strongly determined by the large sound magnitude in the primary Lloyd's Mirror lobe.

Upsloping topography for both these groups had the same effect on propagation, as schematized in figure 5.4c. The upward topography truncated deep propagation paths; this truncation shortened convergence zone radii 1–3 km and decreased ensonification 15–20 dB. The magnitude of these topographic effects will, in general, depend on the propagation patterns in the water and on the topographic slope.

Oceanographic effects with flat topography were very similar for both these groups, whether the primary beam of sound interacted with the sediment or not. Figure 5.5a illustrates downward oceanographic refraction and subsequent increased bottom interactions; the downward refraction produced a shadow zone. Sound levels (for these flat bottom cases) decreased between 50 and 125 dB from their range-independent values, depending on frequency. At any one frequency, post-frontal shadow zone ensonification depended more strongly on the distance from the front to the observer than the source to the front.

Upward oceanographic refraction, as shown in figure 5.5b, caused an increase in surface ensonification of 20–25 dB and a decrease of bottom interactions. This change was largely independent of frequency.

Not all combinations of oceanography and topography were tested; only those two in which the oceanographic effects conteracted the topographic effects. Figure 5.5c depicts propagation patterns with the downward oceanographic refraction, which would increase bottom interactions, and the downward topography, which would decrease such interactions and include deeper sound paths in the water column. The net effect was formation of a shadow zone, whose ensonification levels were between 25 and 45 dB below the flat bottom, range independent propagation case, depending on frequency. Inclusion of the deep propagation paths prevented ensonification levels from dropping as low as in the flat bottom, range dependent oceanographic case.

Figure 5.5d schematizes upward oceanographic refraction, which would decrease bottom interactions, in conjunction with upward topography, which would increase those bottom interactions. The net result of these effects was an increase in surface ensonification of 20–25 dB, as in the flat-bottom case. The truncation of deep paths due to upward topography rearranged the small-scale maxima but did not affect overall magnitudes.

The case of upward oceanographic refraction with downward topography was not tested, but would probably result in increased surface ensonification, with modifications due to the topographic effects of inclusion of deeper paths. The case of downward oceanographic refraction with upward topography was also not tested, but would probably result in very low sound levels due to the increased losses from both oceanography and topography.

A third classification of propagation patterns emerged, consisting of propagation in the Sargasso profile with source at 10 and 100 m as schematized in figure 5.6a. In these cases, the primary interference lobe interacted with the sediment near grazing incidence where the magnitude of the Rayleigh reflection coefficient was relatively large, and the trapped water column modes were relatively weakly excited. The combination of these two factors permitted sound in bottom-glancing paths to dominate propagation patterns for mid to long ranges, before sediment reflection losses removed enough of the bottom-glancing sound for trapped modes to predominate. Due to the importance of these bottom-reflecting paths in the total propagation pattern, small changes in the parameters controlling the reflection coefficient (ρ, c_w/c_b) could produce dramatic changes to propagation patterns. Density decreases of less than .5 gm/cm^3 increased ensonification 7–10 dB throughout the range of calculation, by increasing the magnitude of the reflection coefficient for angles near grazing. Changes in the interface sound speed discontinuity of order .01 could cause large and qualitative changes to the propagation patterns by controlling the amount of sound reflecting at these bottom-glancing angles, in some cases causing these propagation paths to collapse.

Due to the amount of sound interacting with the sediment relative to the strength of the water column modes, the sediment sound speed gradient sometimes had a dramatic effect on propagation as well, modifying local sound magnitudes as much as 25 dB for changes of .5 sec^{-1} in $\partial c/\partial z$. This refracted return could interfere constructively or destructively with the water-propagating and bottom-glancing sound.

The relative weakness of the trapped water column modes caused propagation in this regime to react unusually to variations in topography and oceanography, as well. Downsloping topography (figure 5.6b) permitted the bottom-glancing sound to refract within the deeper water column, increasing resolution of convergence zones and magnitudes by up to 20 dB. Upsloping topography (figure 5.6c) truncated the bottom-glancing paths and weak trapped modes, causing bottom reflections and an unusual interference pattern if mode excitation were weak enough. Upsloping topography caused a general increase of ensonification of 15–20 dB, the opposite effect observed in the previous group of profiles.

Oceanographic refraction upward, schematized in figure 5.7a, permitted

water column refraction of the bottom-glancing sound, which reinforced the trapped modes and increased convergence zone ensonification 10–20 dB. Refraction downward was not tested but would increase bottom interactions for those weak trapped modes.

Only one oceanographic/topographic interaction case was tested for these profiles, that of upward refracting oceanography and upward topography. The results differed, depending on the strength of excitation of the trapped modes. For lower frequencies or when the source was closer to the sound channel axis, the trapped modes were excited more strongly, as schematized in figure 5.7b. The frontal interaction shifted trapped modes upward within the water; as the upward topography truncated these paths, others closer to the sound channel axis were excited with enough magnitude to permit convergence zone behavior to persist, although with magnitudes lessened by 10–15 dB over the flat bottom case. Propagation patterns for these examples appeared dominated by the oceanographic effects.

For higher frequencies or when the source was farther from the sound channel axis, the trapped modes were less strongly excited, as case is schematized in figure 5.7c. The frontal interaction refracted those trapped modes upward within the water column; as upward topography truncated the deeper paths, shallower ones closer to the sound channel axis were not excited with enough magnitude to permit convergence zone behavior to persist. In an extreme case ($f = 100$ Hz, $z_s = 10$ m), propagation patterns contain the odd beam pattern and were invariant to the oceanographic change. In other cases, propagation patterns in the final combined case qualitatively resembled neither the flat bottom, range dependent oceanographic case nor the upsloping topographic, range independent oceanographic case. These latter examples are thought to represent a transition state between propagation patterns dominated by oceanography and propagation patterns dominated by topography.

The other configurations of oceanographic/topographic interactions were not tested; however, upward oceanographic refraction in conjunction with downward topography would probably cause strong convergence zone behavior. The sound in bottom glancing paths would refract with depth within the deeper water column; the upward refraction of the front would shift sound maxima closer to the surface. The other combinations of downward oceanographic refraction with

upward or downward topography would both involve shifting the weakly-excited trapped modes deeper in the water column; the results are difficult to predict.

This third group of cases has demonstrated that under conditions of weak excitation of trapped water column modes, propagation patterns can be dominated for mid to long ranges by sound in bottom glancing paths. Such propagation patterns will depend greatly on the form of the sediment, especially the magnitude of the reflection coefficient for sound near grazing incidence. It must be noted again that inclusion of range dependence in the sediment model could have a strong effect on propagation in these paths, although for all realistic sediments the magnitude of the reflection coefficient approaches unity at angles approaching grazing. No previous work known has studied the dependence of these paths on exact sediment properties, nor the effects when the topographic and oceanographic conditions change.

The entire Gulf Stream study has demonstrated that the Lloyd's Mirror source-image interference pattern, interacting with the angular dependence of the Rayleigh reflection coefficient, controls the form and magnitude of sediment effects for deep water propagation. No previous work known has studied the question of sensitivity to, and form of, sediment effects using this representation of the sound fields showing low frequency interference effects.

It was additionally noted that long-range convergence zone propagation patterns were seen with shallow sources for which local sound speed exceeded that at the sediment; Snell's law refraction for these cases would indicate that all the sound leaving these sources with real propagation angle would strike the sediment. Previously this condition has been viewed as precluding convergence zone propagation, as all the sound would interact with the bottom. The long range convergence zone patterns seen consisted of trapped modes excited via the magnitudes of their exponential tails into the higher sound speed water near the source. Thus low-frequency effects increase the permissible range of propagation regimes beyond those which have been viewed as permitting convergence zone propagation.

Propagation with an initially shallow depth, such as in the Iceland-UK Gap region, did not show the same frequency dependence on bottom interactions since source-image interference patterns did not form. However, since frequency

determines the excitation of modes, propagation patterns within the deeper sound channel will depend on frequency via density of mode excitation. Diffraction down the sloping topography did appear in these calculations.

The governing condition in the Gap region was instead the shallow initial propagation range, which caused many interactions with the sediment and produced losses which varied according to propagation angle. The angular dependence of the reflection coefficient (small magnitude for steeper sound) preferentially filtered out all but the shallower propagation angles; thus when the topography deepened, propagation was limited to shallow-angle sound near the sound channel axis. The oceanographic variations strongly influenced the amount of loss that occurred over these shallow regions, causing decreases in ensonification of as much as 25 dB and strongly affecting the amounts of sound at various propagation angles. In several cases, losses were so selective that only a small number of modes with shallow equivalent ray-angle remained in the sound field.

Thus the underlying consideration in modeling underwater acoustic propagation in lower frequency ranges appears to be the inclusion of a parameterization of the sediment and the varying topography, and the frequency-dependent interactions that occur. The variations of the oceanographic medium with range additionally have such strong effects on propagation patterns within the constraints determined by the local topographic regime as to be indispensable to an accurate prediction of the acoustic fields. The Harvard Modeling System provides a useful tool for providing the requisite oceanographic environmental fields, for valid times both present and forecast, which can so profoundly affect the propagation patterns in both deep water and shallower variable-topographic regimes. The combination of a fast, effective method for providing realistic oceanographic environmental fields with a precise knowledge of the bottom conditions can result in accurate prediction of the underwater acoustic propagation fields.

Figure Captions, Chapter 5

Figure 5.1) Schematic of Iceland-UK Gap propagation. a. Propagation through eddy. Arrows represent start and end of eddy. b. Propagation through Arctic water sound speed fields. c. Propagation across Iceland-Faeroes front. Arrows represent approximate locations of deep and surface front, respectively. d. Propagation through Atlantic water sound speed fields. e. Propagation through Arctic water sound speed fields.

Figure 5.2) Schematic of AthenA region propagation effects. a. Range dependent (bold) vs. range-independent propagation. Arrows represent approximate locations of start and stop of sound speed change. b. QG-SBL vs. QG: refraction of sound away from surface in QG-SBL (bold) case, deeper refraction in QG-QBL case. c. QG-SBL vs. QG: shallower excursion of sound in QG-SBL (bold) case.

Figure 5.3) Schematic of sediment interaction effects, water modes dominant over bottom interactions. a. Principal sound path refracts with depth. b. Principal sound path interacts with sediment.

Figure 5.4) Schematic of topography effects, water modes dominant over bottom interactions. a. Principal sound path refracts within flat bottom waveguide, downsloping topography. b. Principal sound path interacts with sediment, downsloping topography. c. Upsloping topography.

Figure 5.5) Schematic of oceanographic effects and oceanographic/topographic interactions, water modes dominant over bottom interactions. Arrows represent approximate beginning and ending of Gulf Stream. a. Downward oceanographic refractions, flat bottom. b. Upward oceanographic refractions, flat bottom. c. Downward oceanographic refractions, downsloping bottom. d. Upward oceanographic refractions, upsloping bottom.

Figure 5.6) Schematic of sediment interaction effects, topography effects, bottom interactions dominant over water modes. a. Sediment interactions, bottom glancing path bold. b. Downsloping topography. c. Upsloping topography.

Figure 5.7) Schematic of oceanographic effects, oceanographic/topographic interactions, bottom interactions dominant over water modes. Arrows represent approximate beginning and ending of Gulf Stream. a. Upward oceanographic refractions, flat bottom. b. Upward oceanographic refractions, upsloping bottom, water modes relatively strongly excited. c. Upward oceanographic refractions, upsloping bottom, water modes weakly excited.

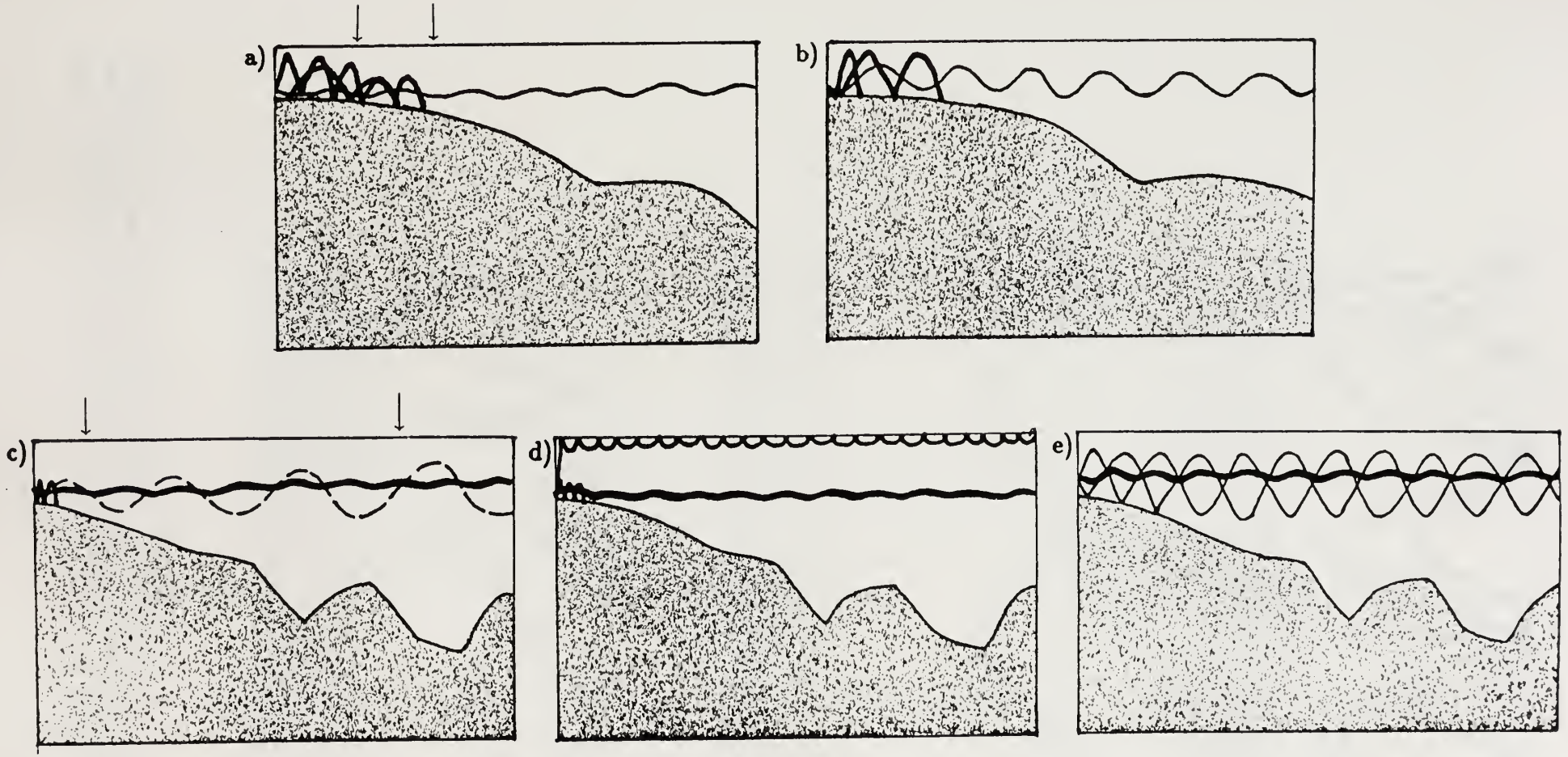

Figure 5.1) Schematic of Iceland-UK Gap propagation. a. Propagation through eddy. b. Propagation through Arctic water sound speed fields. c. Propagation across Iceland-Faeroes front. d. Propagation through Atlantic water sound speed fields. e. Propagation through Arctic water sound speed fields.

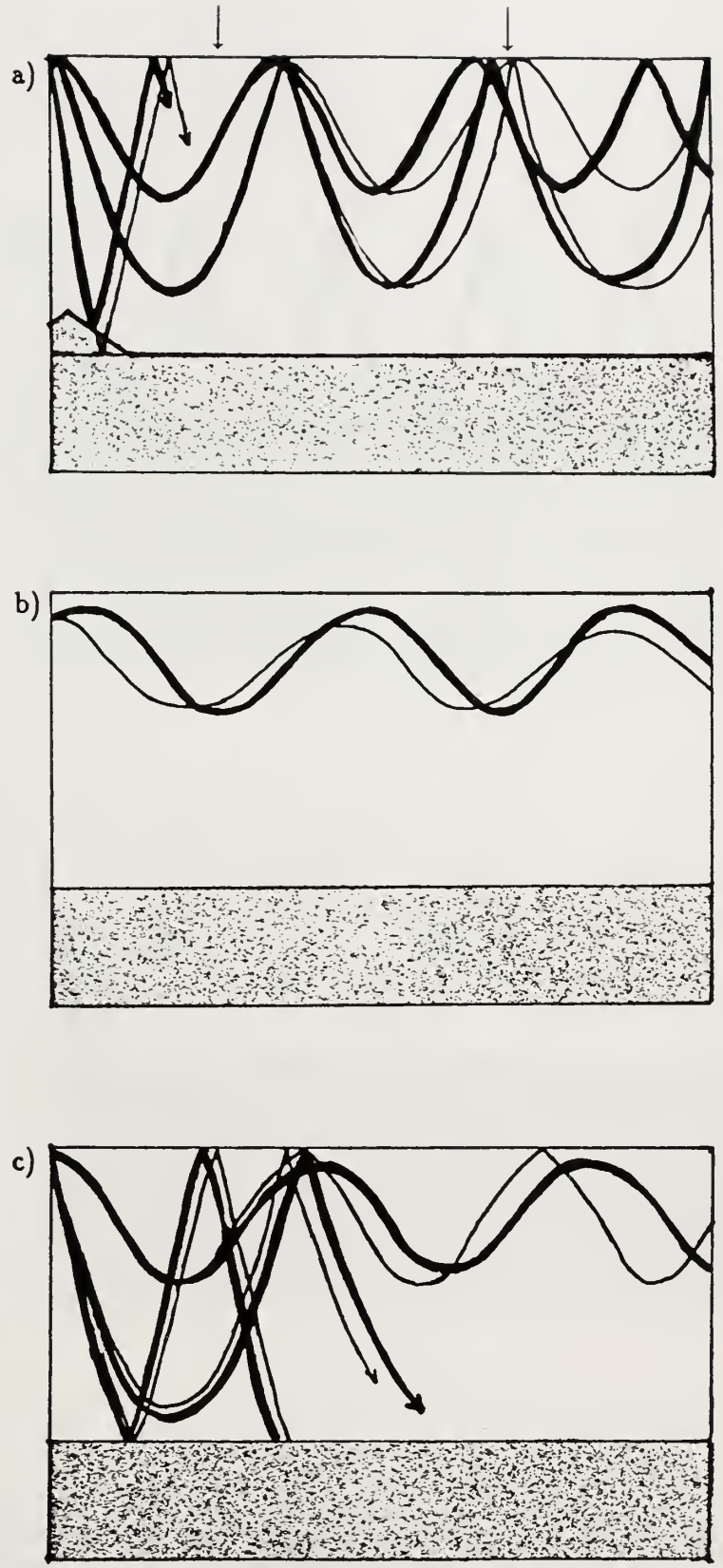

Figure 5.2) Schematic of AthenA region propagation effects. a. Range dependent (bold) vs. range-independent propagation. b. QG-SBL vs. QG: refraction of sound away from surface in QG-SBL (bold) case, deeper refraction in QG-QBL case. c. QG-SBL vs. QG: shallower excursion of sound in QG-SBL (bold) case.

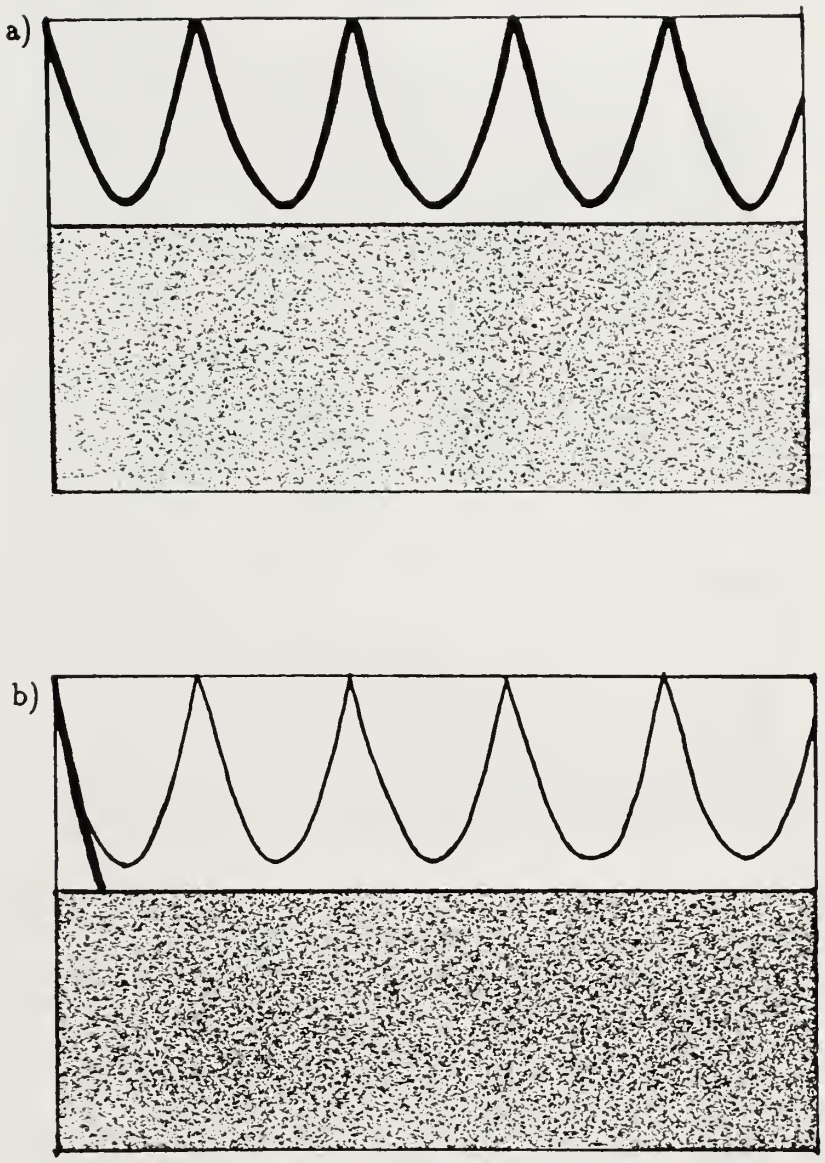

Figure 5.3) Schematic of sediment interaction effects, water modes dominant over bottom interactions. a. Principal sound path refracts with depth. b. Principal sound path interacts with sediment.

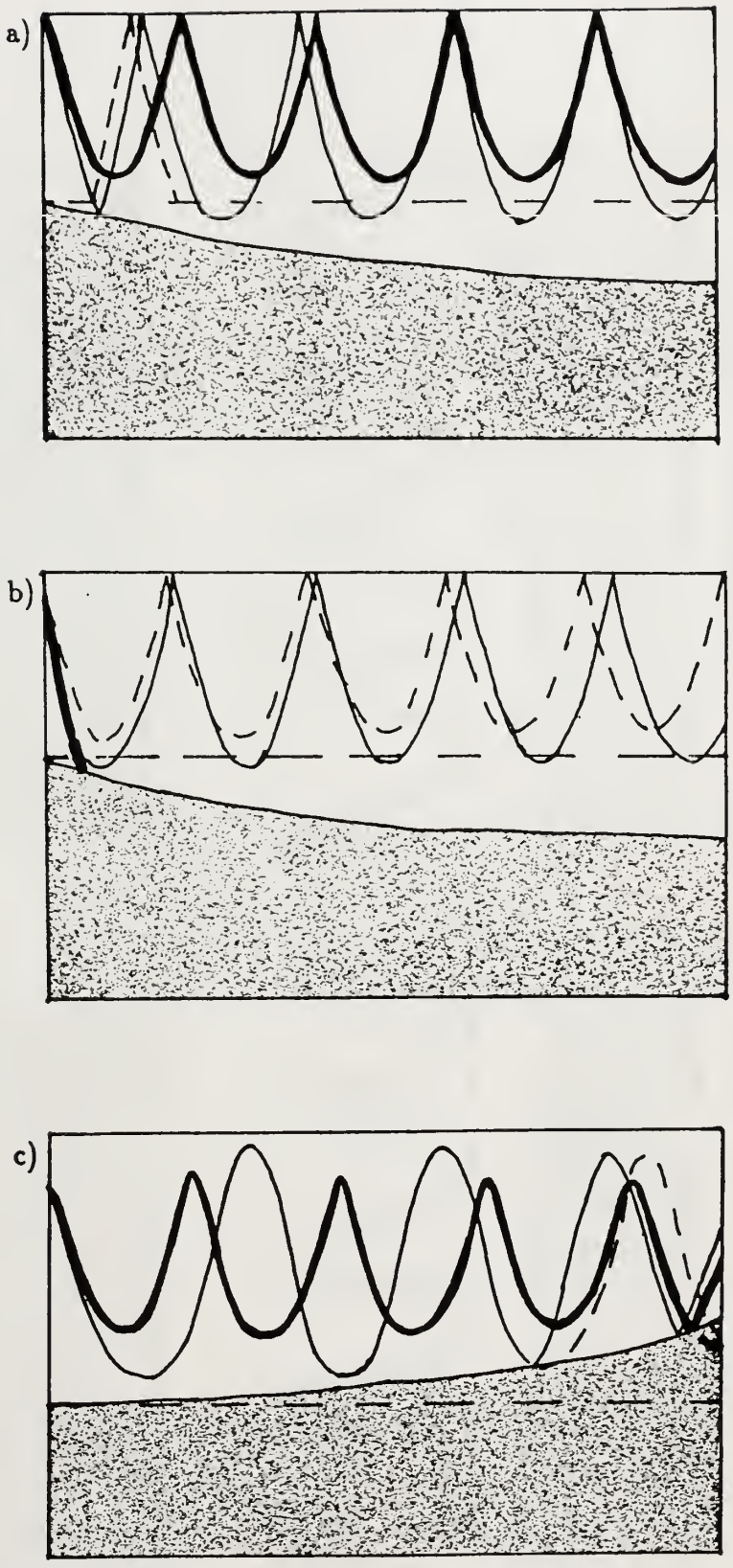

Figure 5.4) Schematic of topography effects, water modes dominant over bottom interactions. a. Principal sound path refracts within flat bottom waveguide, downsloping topography. b. Principal sound path interacts with sediment, downsloping topography. c. Upsloping topography.

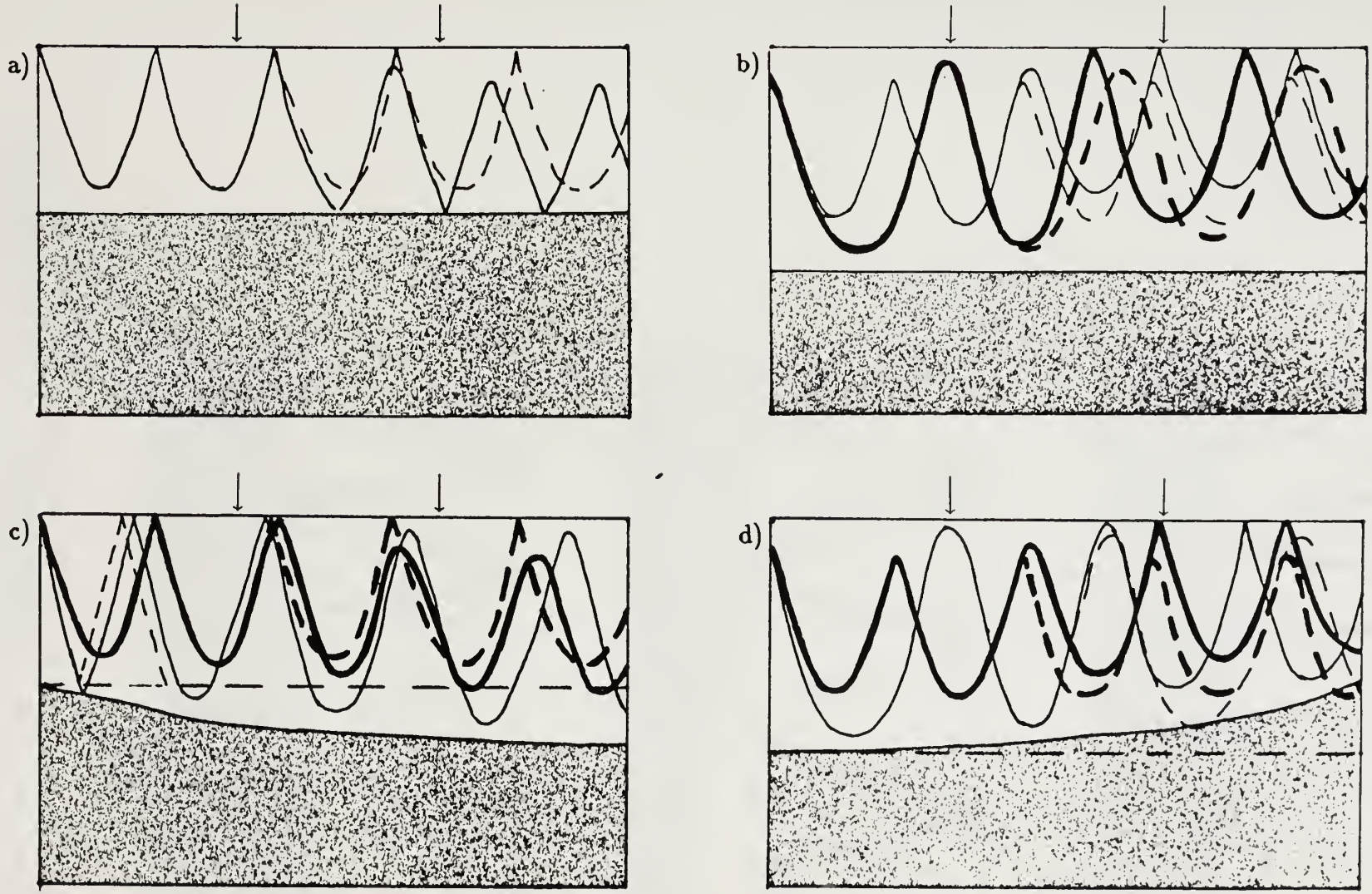

Figure 5.5) Schematic of oceanography effects and oceanographic/topographic interactions, water modes dominant over bottom interactions. a. Downward oceanographic refractions, flat bottom. b. Upward oceanographic refractions, flat bottom. c. Downward oceanographic refractions, downsloping bottom. d. Upward oceanographic refractions, upsloping bottom.

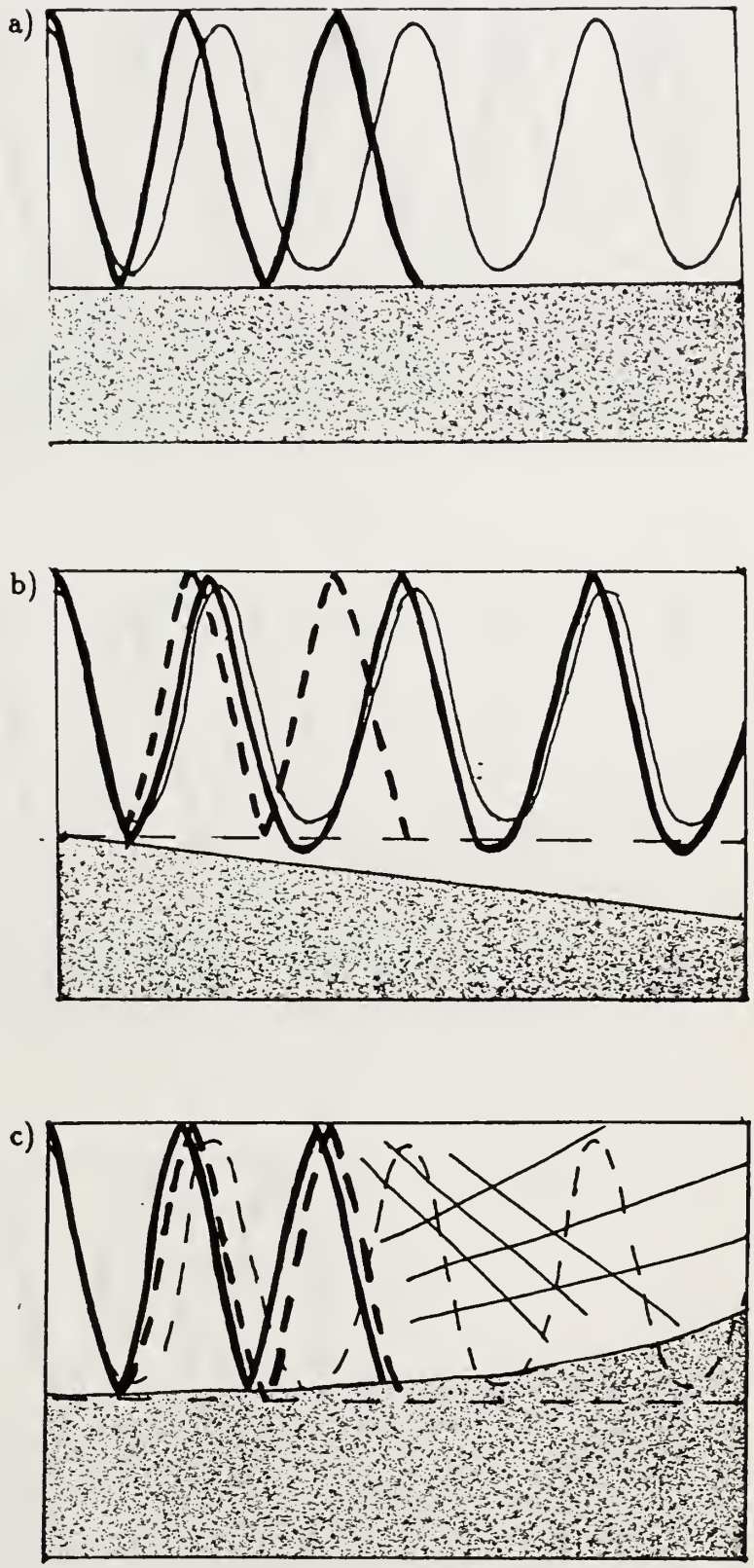

Figure 5.6) Schematic of sediment interaction effects, topography effects, bottom interactions dominant over water modes. a. Sediment interactions, bottom glancing path bold. b. Downsloping topography. c. Upsloping topography.

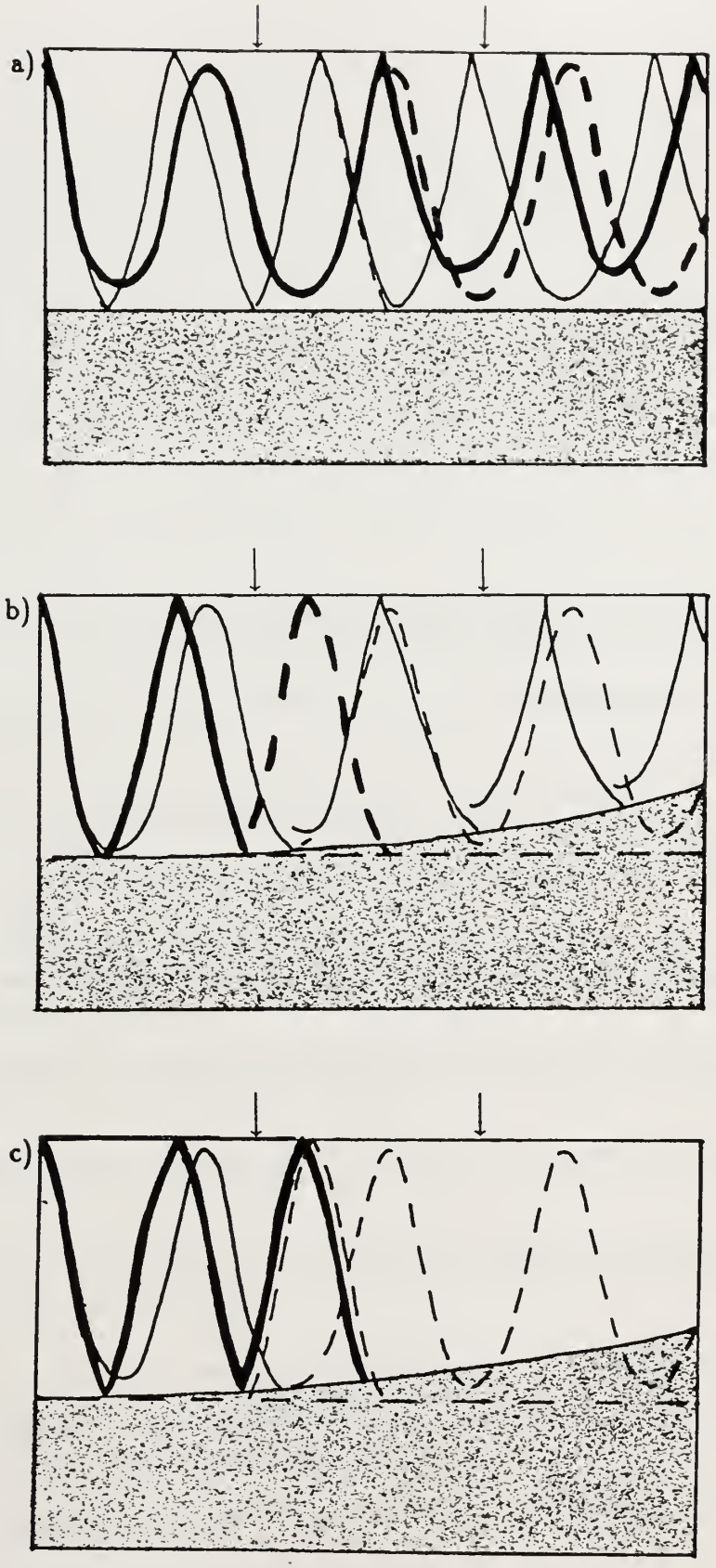

Figure 5.7) Schematic of oceanography effects, oceanographic/topographic interactions, bottom interactions dominant over water modes. a. Upward oceanographic refractions, flat bottom. b. Upward oceanographic refractions, upsloping bottom, water modes relatively strongly excited. c. Upward oceanographic refractions, upsloping bottom, water modes weakly excited.

References

H. Akima, "A New Method of Interpolation and Smooth Curve Fitting Based on Local Procedures," J. Assoc. Comp. Mach. **17**, 589–602 (1970).

G. Botseas, D. Lee, and K.E. Gilbert, "IFD: Wide Angle Capability," NUSC Technical Report 6905 (1983).

G. Botseas, D. Lee, and W.L. Siegmann, "IFD: Interfaced with Harvard Open Ocean Model Forecasts," NUSC Technical Report 8367 (1989).

L.M. Brekhovskikh, *Waves in Layered Media*, R.T. Beyer, trans. (Academic Press, Inc., Orlando, 1980).

K. Bryan and M.D. Cox, "A Numerical Investigation of the Oceanic General Circulation," Tellus **19** 54–80, (1967).

E.F. Carter and A.R. Robinson, "Analysis Models for the Estimation of Oceanic Fields," J. Atm. and Oceanic Technol. **4**, 49–74 (1987).

J.G. Charney, R. Fjortoft and J. von Neumann, "Numerical Integration of the Barotropic Vorticity Equation," Tellus **2**, 237–254 (1950).

J.G. Charney and G.R. Flierl, "Oceanic Analogues of Large Scale Atmospheric Motions," in: B.A. Warren and C. Wunsch, eds., *Evolution of Physical Oceanography* (MIT Press, Cambridge, MA, 1981).

C.S. Chiu and L.L. Ehret, "Computations of Sound Propagation in a Three-Dimensionally Varying Ocean: A Coupled Normal Mode Approach," in: D. Lee, A. Cakmak, and R. Vichnevetsky, eds., *Proc. Second IMACS Symposium on Computational Acoustics* (North-Holland, New York, 1990).

G. Choubert and A. Faure-Muret, gen. coords. *Geological World Atlas*, (UNESCO, 1976).

C.S. Clay and H. Medwin, *Acoustical Oceanography: Principles and Applications*, (John Wiley & Sons, New York, 1977).

M.D. Collins, H.B. Ali, M.J. Authement, A. Nagl, H. Überall, J.F. Miller, and

J.I. Arvelo, "Low-Frequency Sound Interaction with a Sloping, Refracting Ocean Bottom," IEEE J. Oceanic Engineering **13**, 235–244, (1988).

D.W. Denbo, A.R. Robinson, S.M. Glenn, L.J. Walstad, and C. Mooney, "Harvard Gapcasts—Dynamical Nowcasts and Forecasts of the East Iceland-Faeroe Front July 1987," Reports in *Meteorology and Oceanography 25* (1988).

S.E. Dosso and N.R. Chapman, "Measurement and Modeling of Downslope Acoustic Propagation Loss over a Continental Slope," J. Acoust. Soc. Am. **81**, 258–268 (1987).

N.P. Fofonoff and R.C. Millard, Jr., "Algorithms for Computation of Fundamental Properties of Seawater," *UNESCO Technical Papers in Marine Science* 44 (1983).

G.V. Frisk, J.A. Doutt, and E.E. Hays, "Geoacoustic Models for the Icelanding Basin," J. Acoust. Soc. Am. **80**, 591–600, 1986.

R.W. Garwood, "An Oceanic Mixed-Layer Model Capable of Simulating Cyclic States," J. Phys. Oceanog. **7**, 455–471, 1977.

S.M. Glenn and A.R. Robinson, "Nowcasting and Forecasting of Oceanic Dynamic and Acoustic Fields," in: D. Lee, A. Cakmak, and R. Vichnevetsky, eds., *Proc. Second IMACS Symposium on Computational Acoustics* (North-Holland, New York, 1990).

S.M. Glenn, A.R. Robinson, and M.A. Spall, "Recent Results from the Harvard Gulf Stream Forecasting Program," Oceanographic Monthly Summary **7**, 12–13 (1987).

K.M. Guthrie and C.T. Tindle, "Ray Effects in the Normal Mode Approach to Underwater Acoustics," J. Sound and Vibration **47**, 403–413 (1976).

E.L. Hamilton, "Sound Attenuation as a Function of Depth in the Sea Floor," J. Acoust. Soc. Am. **59**, 528–536 (1976).

E.L. Hamilton, "Geoacoustic Modeling of the Sea Floor," J. Acoust. Soc. Am. **68**, 1313–1340 (1980).

E.L. Hamilton and R.T. Bachman, "Sound Velocity and Related Properties of Marine Sediments," J. Acoust. Soc. Am. **72**, 1891–1904 (1982).

F.B. Jensen, G. Dreini, and M. Prior, "Acoustic Effects of the Iceland-Faeroe Front," in: J.R. Potter and A. Warn-Varnas, eds., *Ocean Variability and Acoustic Propagation* (Kluwer Academic Publishers, Dordrecht, Netherlands, 1991).

F.B. Jensen and W.A. Kuperman, "Range-Dependent Bottom-Limited Propagation Modelling with the Parabolic Equation," in: W.A. Kuperman, F.B. Jensen, eds. *Bottom-Interacting Ocean Acoustics,* (Plenum Press, NY, 1980a).

F.B. Jensen and W.A. Kuperman, "Sound Propagation in a Wedge-Shaped Ocean with a Penetrable Bottom," J. Acoust. Soc. Am. **67**, 1564–1566 (1980b).

R.M. Jones, J.P. Riley, and T.M. Georges, "HARPO—A Versatile Three-Dimensional Hamiltonian Ray-Tracing Program for Acoustic Waves in an Ocean with Irregular Bottom," NOAA Report, Environmental Research Laboratories, Boulder, CO (1986).

A.C. Kibblewhite, "Attenuation of Sound in Marine Sediments: A Review with Emphasis on New Low-Frequency Data," J. Acoust. Soc. Am. **86**, 716–738 (1989).

D.P. Knobles and P.J. Vidmar, "Simulation of Bottom Interacting Waveforms," J. Acoust. Soc. Am. **79**, 1760–1766 (1986).

D. Lee and G. Botseas, "IFD: An Implicit Finite-Difference Computer Model for Solving the Parabolic Equation," NUSC Technical Report 6659 (1982).

D. Lee, G. Botseas, and J.S. Papadakis, "Finite-Difference Solution to the Parabolic Wave Equation," J. Acoust. Soc. Am. **70**, 795–800 (1981).

D. Lee, G. Botseas, W.L. Siegmann, A.R. Robinson, "Numerical Computations of Acoustic Propagation through Three-Dimensional Ocean Eddies," in: W.F. Ames, ed, *Numerical and Applied Mathematics* (J.C. Baltzer AG, Scientific Publishing Co. 1989).

D. Lee and S.T. McDaniel, *Ocean Acoustic Propagation by Finite Difference Methods* (Pergamon Press, 1988).

D. Lee and J.S. Papadakis, "Numerical Solutions of Underwater Acoustic Wave Propagation Problems," NUSC Technical Report 5929 (1979).

S. Levitus, *Climatological Atlas of the World Ocean*, NOAA Professional Paper No. 13, Rockville, MD (1982).

K.V. MacKenzie, "Reflection of Sound from Coastal Bottoms," J. Acoust. Soc. Am. **32**, 221–231, (1960).

L.E. Mellberg, A.R. Robinson, and G. Botseas, "Modeled Time Variability of Acoustic Propagation through a Gulf Stream Meander and Eddies," J. Acoust. Soc. Am. **87**, 1044–1054, (1990).

R.N. Miller, A.R. Robinson, and D.B. Haidvogel, "A Baroclinic Quasigeostrophic Open Ocean Model," J. Comp. Phys. **50**, 38–70 (1981).

A.E. Newhall, J.F. Lynch, C.S. Chiu, and R. Dougherty, "Improvements in Three-Dimensional Raytracing Codes for Underwater Acoustics," in: D. Lee, A. Cakmak, and R. Vichnevetsky, eds., *Proc. Second IMACS Symposium on Computational Acoustics* (North-Holland, New York, 1990).

N.A. Phillips, *The Dynamics of the Upper Ocean* (Cambridge University Press, 1969).

N. Pinardi and A.R. Robinson, "Quasigeostrophic Energetics of Open Ocean Regions," Dyn. Atm. Oc. **10**, 185–219 (1986).

M. Porter, S. Piacsek, L. Henderson, and F. Jensen, "Acoustic Impact of Upper Ocean Models," in: D. Lee, A. Cakmak, and R. Vichnevetsky, eds., *Proc. Second IMACS Symposium on Computational Acoustics* (North-Holland, New York, 1990).

Lord Rayleigh (J.W. Strutt), *Theory of Sound*, (2nd Ed. Dover, New York, 1945).

A.R. Robinson, "Dynamical Forecasting of Mesoscale Fronts and Eddies for Acoustical Applications," J. Acoust. Soc. Am. Suppl. 1 **82**, S90 (1987).

A.R. Robinson, "Overview and Summary of Eddy Science," in: A.R. Robinson, ed., *Eddies in Marine Science* (Springer-Verlag Berlin Heidelberg 1983).

A.R. Robinson, J.A. Carton, N. Pinardi, and C.N.K. Mooers, "Dynamical Forecasting and Dynamical Interpolation: An Experiment in the California Current," J. Phys. Oc. **16**, 1561–1579 (1986).

A.R. Robinson, S.M. Glenn, W.L. Siegmann, D. Lee, and G. Botseas, "Environmental Sensitivity Studies with an Interfaced Ocean-Acoustics System," in: J.R. Potter and A. Warn-Varnas, eds., *Ocean Variability and Acoustic Propagation* (Kluwer Academic Publishers, Dordrecht, Netherlands, 1991).

A.R. Robinson and W.G. Leslie, "Estimation and Prediction of Oceanic Eddy Fields," Prog. Oceanog. **14**, 485–510 (1985).

A.R. Robinson, M.A. Spall, and N. Pinardi, "Gulf Stream Simulations and the Dynamics of Ring and Meander Processes," J. Phys. Oceanogr. **18**, 1811–1853 (1988).

A.R. Robinson and L.J. Walstad, "The Harvard Open Ocean Model: Calibration and Application to Dynamical Process, Forecasting, and Data Assimilation Studies," Applied Num. Mathemat. **3**, 89–131 (1987).

A.R. Robinson, L.J. Walstad, J. Calman, E.B. Dobson, D.W. Denbo, S.M. Glenn, D.L. Porter, and J. Goldhirsh, "Frontal Signals East of Iceland from the GEOSAT Altimeter," Geophys. Res. Letters **16**, 77–80 (1989).

S.R. Rutherford and K.E. Hawker, "Effects of Density Gradients on Bottom Reflection Loss for a Class of Marine Sediments," J. Acoust. Soc. Am. **63**, 750–757 (1978).

R. Shapiro, "The Use of Linear Filtering as a Parameterization for Atmospheric Diffusion," J. Atmospheric Sci. **29**, 523–531 (1971).

W.L. Siegmann, M.J. Jacobson, D. Lee, G. Botseas, A.R. Robinson, and S.M. Glenn, "Interfacing Mesoscale Ocean Prediction and Parabolic Acoustic Propagation Models Including Bottom Topography," in: D. Lee, A. Cakmak, and R. Vichnevetsky, eds., *Proc. Second IMACS Symposium on Computational Acoustics* (North-Holland, New York, 1990).

M.A. Spall and A.R. Robinson, "A New Open Ocean, Hybrid Coordinate Primitive Equation Model," Mathematics and Computers in Simulation **31**, 241–269,

(1989).

M.A. Spall and A.R. Robinson, "Regional Primitive Equation Studies of the Gulf Stream Meander and Ring Formation Region," J. Phys. Oceanogr. **20**, 985–1016, (1990).

R.C. Spindel and Y.J-F. Desaubies, "Eddies and Acoustics," in: A.R. Robinson, ed., *Eddies in Marine Science* (Springer-Verlag, Berlin, 1983).

B. le Squere, *Rapport sur le Traitement des Données de la Campagne AthenA88*, (CNRM/UDC Toulouse, 1989).

F.D. Tappert, "The Parabolic Approximation Method," in: J.B. Keller and J.S. Papadakis, eds., *Wave Propagation and Underwater Acoustics* (Springer-Verlag, Berlin, 1977).

C.T. Tindle and K.M. Guthrie, "Rays as Interfering Modes in Underwater Acoustics," J. Sound and Vibration **34**, 291–295, (1974).

R.J. Urick, *Principles of Underwater Sound* (McGraw-Hill, New York, 1983).

P.J. Vidmar, "The Effect of Sediment rigidity on Bottom Reflection Loss in a Typical Deep Sea Sediment," J. Acoust. Soc. Am. **68**, 634–638 (1980).

P.J. Vidmar and T.L. Foreman, "A Plane-Wave Reflection Loss Model Including Sediment Rigidity," J. Acoust. Soc. Am **66**, 1830–1835 (1979).

J.J. von Schwind, *Geophysical Fluid Dynamics for Oceanographers* (Prentice-Hall, Englewood Cliffs, NJ, 1980).

L.J. Walstad and A.R. Robinson, "Hindcasting and Forecasting of the POLYMODE Data Set with the Harvard Open-Ocean Model," J. Phys. Oceanog. **20**, 1682–1702, 1990.

L.J. Walstad and A.R. Robinson, "A Coupled Surface Boundary Layer—Quasi-geostrophic Model," (submitted manuscript).

A.O. Williams, Jr., "Hidden Depths: Acceptable Ignorance about Ocean Bottoms," J. Acoust. Soc. Am. **59**, 1175–1179 (1976).

A.O. Williams, Jr., "Normal-mode Propagation in Deep-Ocean Sediment Channels," J. Acoust. Soc. Am. **70**, 820–824 (1981).

A.O. Williams, Jr. and D.R. MacAyeal, "Acoustic Reflection from a Sea Bottom with Linearly Increasing Sound Speed," J. Acoust. Soc. Am. **66**, 1836–1841 (1979).

Appendix Contents

Due to the size of the appendices, they are contained on microfiche, held at Gordon McKay Library, Harvard University, Cambridge, MA 02138. For further information please contact the Division of Applied Sciences, Harvard University. Contents of each section are included on the following pages.

A.1.1 "Realistic" Sediment, 25 Hz

Calculations in this section were run with the "realistic" set of sediment parameters, $\rho = 1.352$ gm/cm^3, $\beta = .9$ dB/λ, $c_w/c_b = 1.017$, $\partial c/\partial z = 1.227$ sec^{-1}, and $z_{sed} = 100$ m, at a frequency $f = 25$ Hz.
Each page contains the following plots:

a. Sound speed contours.
b. Propagation loss at 100 m receiver.
c. Contours of propagation loss.
d. Propagation loss at 1000 m receiver.

Figure A.1.1.1) Slope to Sargasso water propagation, downsloping topography. z_s = 10 m.
Figure A.1.1.2) Slope to Sargasso water propagation, downsloping topography. z_s = 100 m.
Figure A.1.1.3) Slope to Sargasso water propagation, downsloping topography. z_s = 750 m.
Figure A.1.1.4) Slope to Sargasso water propagation, downsloping topography. z_s = 3000 m.
Figure A.1.1.5) Slope water profile, downsloping topography. z_s = 10 m.
Figure A.1.1.6) Slope water profile, downsloping topography. z_s = 100 m.
Figure A.1.1.7) Slope water profile, downsloping topography. z_s = 750 m.
Figure A.1.1.8) Slope water profile, downsloping topography. z_s = 3000 m.
Figure A.1.1.9) Slope to Sargasso water propagation, 3170 m bottom. z_s = 10 m.
Figure A.1.1.10) Slope to Sargasso water propagation, 3170 m bottom. z_s = 100 m.
Figure A.1.1.11) Slope to Sargasso water propagation, 3170 m bottom. z_s = 750 m.
Figure A.1.1.12) Slope to Sargasso water propagation, 3170 m bottom. z_s = 3000 m.
Figure A.1.1.13) Slope water profile, 3170 m bottom. z_s = 10 m.
Figure A.1.1.14) Slope water profile, 3170 m bottom. z_s = 100 m.
Figure A.1.1.15) Slope water profile, 3170 m bottom. z_s = 750 m.
Figure A.1.1.16) Slope water profile, 3170 m bottom. z_s = 3000 m.
Figure A.1.1.17) Sargasso to Slope water propagation, upsloping topography. z_s = 10 m.
Figure A.1.1.18) Sargasso to Slope water propagation, upsloping topography. z_s = 100 m.
Figure A.1.1.19) Sargasso to Slope water propagation, upsloping topography. z_s = 750 m.
Figure A.1.1.20) Sargasso to Slope water propagation, upsloping topography. z_s = 3000 m.
Figure A.1.1.21) Sargasso water profile, upsloping topography. z_s = 10 m.
Figure A.1.1.22) Sargasso water profile, upsloping topography. z_s = 100 m.
Figure A.1.1.23) Sargasso water profile, upsloping topography. z_s = 750 m.
Figure A.1.1.24) Sargasso water profile, upsloping topography. z_s = 3000 m.
Figure A.1.1.25) Sargasso to Slope water propagation, 4440 m bottom. z_s = 10 m.
Figure A.1.1.26) Sargasso to Slope water propagation, 4440 m bottom. z_s = 100 m.
Figure A.1.1.27) Sargasso to Slope water propagation, 4440 m bottom. z_s = 750 m.
Figure A.1.1.28) Sargasso to Slope water propagation, 4440 m bottom. z_s = 3000 m.
Figure A.1.1.29) Sargasso water profile, 4440 m bottom. z_s = 10 m.
Figure A.1.1.30) Sargasso water profile, 4440 m bottom. z_s = 100 m.
Figure A.1.1.31) Sargasso water profile, 4440 m bottom. z_s = 750 m.
Figure A.1.1.32) Sargasso water profile, 4440 m bottom. z_s = 3000 m.

A.1.2 Sediment Density Test, 25 Hz

Calculations in this section were run with the following set of sediment parameters, $\rho = 1.0$ gm/cm^3, $\beta = .9$ dB/λ, $c_w/c_b = 1.017$, $\partial c/\partial z = 1.227$ sec^{-1}, and $z_{sed} = 100$ m, at a frequency $f = 25$ Hz. Each page contains the following plots:

a. Sound speed contours.
b. Propagation loss at 100 m receiver.
c. Contours of propagation loss.
d. Propagation loss at 1000 m receiver.

Figure A.1.2.1) Slope to Sargasso water propagation, downsloping topography. z_s = 10 m.
Figure A.1.2.2) Slope to Sargasso water propagation, downsloping topography. z_s = 100 m.
Figure A.1.2.3) Slope to Sargasso water propagation, downsloping topography. z_s = 750 m.
Figure A.1.2.4) Slope to Sargasso water propagation, downsloping topography. z_s = 3000 m.
Figure A.1.2.5) Slope water profile, downsloping topography. z_s = 10 m.
Figure A.1.2.6) Slope water profile, downsloping topography. z_s = 100 m.
Figure A.1.2.7) Slope water profile, downsloping topography. z_s = 750 m.
Figure A.1.2.8) Slope water profile, downsloping topography. z_s = 3000 m.
Figure A.1.2.9) Slope to Sargasso water propagation, 3170 m bottom. z_s = 10 m.
Figure A.1.2.10) Slope to Sargasso water propagation, 3170 m bottom. z_s = 100 m.
Figure A.1.2.11) Slope to Sargasso water propagation, 3170 m bottom. z_s = 750 m.
Figure A.1.2.12) Slope to Sargasso water propagation, 3170 m bottom. z_s = 3000 m.
Figure A.1.2.13) Slope water profile, 3170 m bottom. z_s = 10 m.
Figure A.1.2.14) Slope water profile, 3170 m bottom. z_s = 100 m.
Figure A.1.2.15) Slope water profile, 3170 m bottom. z_s = 750 m.
Figure A.1.2.16) Slope water profile, 3170 m bottom. z_s = 3000 m.
Figure A.1.2.17) Sargasso to Slope water propagation, upsloping topography. z_s = 10 m.
Figure A.1.2.18) Sargasso to Slope water propagation, upsloping topography. z_s = 100 m.
Figure A.1.2.19) Sargasso to Slope water propagation, upsloping topography. z_s = 750 m.
Figure A.1.2.20) Sargasso to Slope water propagation, upsloping topography. z_s = 3000 m.
Figure A.1.2.21) Sargasso water profile, upsloping topography. z_s = 10 m.
Figure A.1.2.22) Sargasso water profile, upsloping topography. z_s = 100 m.
Figure A.1.2.23) Sargasso water profile, upsloping topography. z_s = 750 m.
Figure A.1.2.24) Sargasso water profile, upsloping topography. z_s = 3000 m.
Figure A.1.2.25) Sargasso to Slope water propagation, 4440 m bottom. z_s = 10 m.
Figure A.1.2.26) Sargasso to Slope water propagation, 4440 m bottom. z_s = 100 m.
Figure A.1.2.27) Sargasso to Slope water propagation, 4440 m bottom. z_s = 750 m.
Figure A.1.2.28) Sargasso to Slope water propagation, 4440 m bottom. z_s = 3000 m.
Figure A.1.2.29) Sargasso water profile, 4440 m bottom. z_s = 10 m.
Figure A.1.2.30) Sargasso water profile, 4440 m bottom. z_s = 100 m.
Figure A.1.2.31) Sargasso water profile, 4440 m bottom. z_s = 750 m.
Figure A.1.2.32) Sargasso water profile, 4440 m bottom. z_s = 3000 m.

A.1.3 Sediment Attenuation Test, 25 Hz

Calculations in this section were run with the following set of sediment parameters, $\rho = 1.352$ gm/cm^3, $c_w/c_b = 1.017$, $\partial c/\partial z = 1.227$ sec^{-1}, and $z_{sed} = 100$ m, at a frequency $f = 25$ Hz. Various values of β were used

Each page contains the following plots:

a. Sound speed contours.
b. Propagation loss at 100 m receiver.
c. Contours of propagation loss.
d. Propagation loss at 1000 m receiver.

Figure A.1.3.1) Slope water profile, 3170 m bottom. z_s = 10 m, $\beta = 0.0$ dB/λ.
Figure A.1.3.2) Slope water profile, 3170 m bottom. z_s = 100 m, $\beta = 0.0$ dB/λ.
Figure A.1.3.3) Slope water profile, 3170 m bottom. z_s = 750 m, $\beta = 0.0$ dB/λ.
Figure A.1.3.4) Slope water profile, 3170 m bottom. z_s = 3000 m, $\beta = 0.0$ dB/λ.
Figure A.1.3.5) Sargasso water profile, 4440 m bottom. z_s = 10 m, $\beta = 0.0$ dB/λ.
Figure A.1.3.6) Sargasso water profile, 4440 m bottom. z_s = 100 m, $\beta = 0.0$ dB/λ.
Figure A.1.3.7) Sargasso water profile, 4440 m bottom. z_s = 750 m, $\beta = 0.0$ dB/λ.
Figure A.1.3.8) Sargasso water profile, 4440 m bottom. z_s = 3000 m, $\beta = 0.0$ dB/λ.
Figure A.1.3.9) Slope water profile, 3170 m bottom. z_s = 10 m, $\beta = 0.25$ dB/λ.
Figure A.1.3.10) Slope water profile, 3170 m bottom. z_s = 100 m, $\beta = 0.25$ dB/λ.
Figure A.1.3.11) Slope water profile, 3170 m bottom. z_s = 750 m, $\beta = 0.25$ dB/λ.
Figure A.1.3.12) Slope water profile, 3170 m bottom. z_s = 3000 m, $\beta = 0.25$ dB/λ.
Figure A.1.3.13) Sargasso water profile, 4440 m bottom. z_s = 10 m, $\beta = 0.25$ dB/λ.
Figure A.1.3.14) Sargasso water profile, 4440 m bottom. z_s = 100 m, $\beta = 0.25$ dB/λ.
Figure A.1.3.15) Sargasso water profile, 4440 m bottom. z_s = 750 m, $\beta = 0.25$ dB/λ.
Figure A.1.3.16) Sargasso water profile, 4440 m bottom. z_s = 3000 m, $\beta = 0.25$ dB/λ.
Figure A.1.3.17) Slope water profile, 3170 m bottom. z_s = 10 m, $\beta = 0.5$ dB/λ.
Figure A.1.3.18) Slope water profile, 3170 m bottom. z_s = 100 m, $\beta = 0.5$ dB/λ.
Figure A.1.3.19) Slope water profile, 3170 m bottom. z_s = 750 m, $\beta = 0.5$ dB/λ.
Figure A.1.3.20) Slope water profile, 3170 m bottom. z_s = 3000 m, $\beta = 0.5$ dB/λ.
Figure A.1.3.21) Sargasso water profile, 4440 m bottom. z_s = 10 m, $\beta = 0.5$ dB/λ.
Figure A.1.3.22) Sargasso water profile, 4440 m bottom. z_s = 100 m, $\beta = 0.5$ dB/λ.
Figure A.1.3.23) Sargasso water profile, 4440 m bottom. z_s = 750 m, $\beta = 0.5$ dB/λ.
Figure A.1.3.24) Sargasso water profile, 4440 m bottom. z_s = 3000 m, $\beta = 0.5$ dB/λ.
Figure A.1.3.25) Slope water profile, 3170 m bottom. z_s = 10 m, $\beta = 1.96$ dB/λ.
Figure A.1.3.26) Slope water profile, 3170 m bottom. z_s = 100 m, $\beta = 1.96$ dB/λ.
Figure A.1.3.27) Slope water profile, 3170 m bottom. z_s = 750 m, $\beta = 1.96$ dB/λ.
Figure A.1.3.28) Slope water profile, 3170 m bottom. z_s = 3000 m, $\beta = 1.96$ dB/λ.
Figure A.1.3.29) Sargasso water profile, 4440 m bottom. z_s = 10 m, $\beta = 1.96$ dB/λ.
Figure A.1.3.30) Sargasso water profile, 4440 m bottom. z_s = 100 m, $\beta = 1.96$ dB/λ.
Figure A.1.3.31) Sargasso water profile, 4440 m bottom. z_s = 750 m, $\beta = 1.96$ dB/λ.
Figure A.1.3.32) Sargasso water profile, 4440 m bottom. z_s = 3000 m, $\beta = 1.96$ dB/λ.

A.1.4 Sediment Sound Speed Gradient Test, 25 Hz

Calculations in this section were run with the following set of sediment parameters, $\rho = 1.352$ gm/cm^3, $\beta = .9$ dB/λ, $c_w/c_b = 1.017$, and $z_{sed} = 100$ m, at a frequency $f = 25$ Hz. Various values of $\partial c/\partial z$ were used Each page contains the following plots:

a. Sound speed contours.
b. Propagation loss at 100 m receiver.
c. Contours of propagation loss.
d. Propagation loss at 1000 m receiver.

Figure A.1.4.1) Slope water profile, 3170 m bottom. z_s = 10 m, $\partial c/\partial z = 0.0$.
Figure A.1.4.2) Slope water profile, 3170 m bottom. z_s = 100 m, $\partial c/\partial z = 0.0$.
Figure A.1.4.3) Slope water profile, 3170 m bottom. z_s = 750 m, $\partial c/\partial z = 0.0$.
Figure A.1.4.4) Slope water profile, 3170 m bottom. z_s = 3000 m, $\partial c/\partial z = 0.0$.
Figure A.1.4.5) Sargasso water profile, 4440 m bottom. z_s = 10 m, $\partial c/\partial z = 0.0$.
Figure A.1.4.6) Sargasso water profile, 4440 m bottom. z_s = 100 m, $\partial c/\partial z = 0.0$.
Figure A.1.4.7) Sargasso water profile, 4440 m bottom. z_s = 750 m, $\partial c/\partial z = 0.0$.
Figure A.1.4.8) Sargasso water profile, 4440 m bottom. z_s = 3000 m, $\partial c/\partial z = 0.0$.
Figure A.1.4.9) Slope water profile, 3170 m bottom. z_s = 10 m, $\partial c/\partial z = 0.75$.
Figure A.1.4.10) Slope water profile, 3170 m bottom. z_s = 100 m, $\partial c/\partial z = 0.75$.
Figure A.1.4.11) Slope water profile, 3170 m bottom. z_s = 750 m, $\partial c/\partial z = 0.75$.
Figure A.1.4.12) Slope water profile, 3170 m bottom. z_s = 3000 m, $\partial c/\partial z = 0.75$.
Figure A.1.4.13) Sargasso water profile, 4440 m bottom. z_s = 10 m, $\partial c/\partial z = 0.75$.
Figure A.1.4.14) Sargasso water profile, 4440 m bottom. z_s = 100 m, $\partial c/\partial z = 0.75$.
Figure A.1.4.15) Sargasso water profile, 4440 m bottom. z_s = 750 m, $\partial c/\partial z = 0.75$.
Figure A.1.4.16) Sargasso water profile, 4440 m bottom. z_s = 3000 m, $\partial c/\partial z = 0.75$.
Figure A.1.4.17) Slope water profile, 3170 m bottom. z_s = 10 m, $\partial c/\partial z = 1.5$.
Figure A.1.4.18) Slope water profile, 3170 m bottom. z_s = 100 m, $\partial c/\partial z = 1.5$.
Figure A.1.4.19) Slope water profile, 3170 m bottom. z_s = 750 m, $\partial c/\partial z = 1.5$.
Figure A.1.4.20) Slope water profile, 3170 m bottom. z_s = 3000 m, $\partial c/\partial z = 1.5$.
Figure A.1.4.21) Sargasso water profile, 4440 m bottom. z_s = 10 m, $\partial c/\partial z = 1.5$.
Figure A.1.4.22) Sargasso water profile, 4440 m bottom. z_s = 100 m, $\partial c/\partial z = 1.5$.
Figure A.1.4.23) Sargasso water profile, 4440 m bottom. z_s = 750 m, $\partial c/\partial z = 1.5$.
Figure A.1.4.24) Sargasso water profile, 4440 m bottom. z_s = 3000 m, $\partial c/\partial z = 1.5$.

A.1.6 Sediment Interface Sound Speed Discontinuity $c_w/c_b = .98$, 25 Hz

Calculations in this section were run with the following set of sediment parameters, $\rho = 1.352$ gm/cm^3, $\beta = .9$ dB/λ, $c_w/c_b = 0.98$, $\partial c/\partial z = 1.227$ sec^{-1}, and $z_{sed} = 100$ m, at a frequency $f = 25$ Hz. Each page contains the following plots:

a. Sound speed contours.
b. Propagation loss at 100 m receiver.
c. Contours of propagation loss.
d. Propagation loss at 1000 m receiver.

Figure A.1.6.1) Slope to Sargasso water propagation, downsloping topography. z_s = 10 m.
Figure A.1.6.2) Slope to Sargasso water propagation, downsloping topography. z_s = 100 m.
Figure A.1.6.3) Slope to Sargasso water propagation, downsloping topography. z_s = 750 m.
Figure A.1.6.4) Slope to Sargasso water propagation, downsloping topography. z_s = 3000 m.
Figure A.1.6.5) Slope water profile, downsloping topography. z_s = 10 m.
Figure A.1.6.6) Slope water profile, downsloping topography. z_s = 100 m.
Figure A.1.6.7) Slope water profile, downsloping topography. z_s = 750 m.
Figure A.1.6.8) Slope water profile, downsloping topography. z_s = 3000 m.
Figure A.1.6.9) Slope to Sargasso water propagation, 3170 m bottom. z_s = 10 m.
Figure A.1.6.10) Slope to Sargasso water propagation, 3170 m bottom. z_s = 100 m.
Figure A.1.6.11) Slope to Sargasso water propagation, 3170 m bottom. z_s = 750 m.
Figure A.1.6.12) Slope to Sargasso water propagation, 3170 m bottom. z_s = 3000 m.
Figure A.1.6.13) Slope water profile, 3170 m bottom. z_s = 10 m.
Figure A.1.6.14) Slope water profile, 3170 m bottom. z_s = 100 m.
Figure A.1.6.15) Slope water profile, 3170 m bottom. z_s = 750 m.
Figure A.1.6.16) Slope water profile, 3170 m bottom. z_s = 3000 m.
Figure A.1.6.17) Sargasso to Slope water propagation, upsloping topography. z_s = 10 m.
Figure A.1.6.18) Sargasso to Slope water propagation, upsloping topography. z_s = 100 m.
Figure A.1.6.19) Sargasso to Slope water propagation, upsloping topography. z_s = 750 m.
Figure A.1.6.20) Sargasso to Slope water propagation, upsloping topography. z_s = 3000 m.
Figure A.1.6.21) Sargasso water profile, upsloping topography. z_s = 10 m.
Figure A.1.6.22) Sargasso water profile, upsloping topography. z_s = 100 m.
Figure A.1.6.23) Sargasso water profile, upsloping topography. z_s = 750 m.
Figure A.1.6.24) Sargasso water profile, upsloping topography. z_s = 3000 m.
Figure A.1.6.25) Sargasso to Slope water propagation, 4440 m bottom. z_s = 10 m.
Figure A.1.6.26) Sargasso to Slope water propagation, 4440 m bottom. z_s = 100 m.
Figure A.1.6.27) Sargasso to Slope water propagation, 4440 m bottom. z_s = 750 m.
Figure A.1.6.28) Sargasso to Slope water propagation, 4440 m bottom. z_s = 3000 m.
Figure A.1.6.29) Sargasso water profile, 4440 m bottom. z_s = 10 m.
Figure A.1.6.30) Sargasso water profile, 4440 m bottom. z_s = 100 m.
Figure A.1.6.31) Sargasso water profile, 4440 m bottom. z_s = 750 m.
Figure A.1.6.32) Sargasso water profile, 4440 m bottom. z_s = 3000 m.

A.1.7 Sediment Interface Sound Speed Discontinuity $c_w/c_b = 1.0$, 25 Hz

Calculations in this section were run with the following set of sediment parameters, $\rho = 1.352$ gm/cm^3, $\beta = .9$ dB/λ, $c_w/c_b = 1.0$, $\partial c/\partial z = 1.227$ sec^{-1}, and $z_{sed} = 100$ m, at a frequency $f = 25$ Hz. Each page contains the following plots:

a. Sound speed contours.
b. Propagation loss at 100 m receiver.
c. Contours of propagation loss.
d. Propagation loss at 1000 m receiver.

Figure A.1.7.1) Slope to Sargasso water propagation, downsloping topography. z_s = 10 m.
Figure A.1.7.2) Slope to Sargasso water propagation, downsloping topography. z_s = 100 m.
Figure A.1.7.3) Slope to Sargasso water propagation, downsloping topography. z_s = 750 m.
Figure A.1.7.4) Slope to Sargasso water propagation, downsloping topography. z_s = 3000 m.
Figure A.1.7.5) Slope water profile, downsloping topography. z_s = 10 m.
Figure A.1.7.6) Slope water profile, downsloping topography. z_s = 100 m.
Figure A.1.7.7) Slope water profile, downsloping topography. z_s = 750 m.
Figure A.1.7.8) Slope water profile, downsloping topography. z_s = 3000 m.
Figure A.1.7.9) Slope to Sargasso water propagation, 3170 m bottom. z_s = 10 m.
Figure A.1.7.10) Slope to Sargasso water propagation, 3170 m bottom. z_s = 100 m.
Figure A.1.7.11) Slope to Sargasso water propagation, 3170 m bottom. z_s = 750 m.
Figure A.1.7.12) Slope to Sargasso water propagation, 3170 m bottom. z_s = 3000 m.
Figure A.1.7.13) Slope water profile, 3170 m bottom. z_s = 10 m.
Figure A.1.7.14) Slope water profile, 3170 m bottom. z_s = 100 m.
Figure A.1.7.15) Slope water profile, 3170 m bottom. z_s = 750 m.
Figure A.1.7.16) Slope water profile, 3170 m bottom. z_s = 3000 m.
Figure A.1.7.17) Sargasso to Slope water propagation, upsloping topography. z_s = 10 m.
Figure A.1.7.18) Sargasso to Slope water propagation, upsloping topography. z_s = 100 m.
Figure A.1.7.19) Sargasso to Slope water propagation, upsloping topography. z_s = 750 m.
Figure A.1.7.20) Sargasso to Slope water propagation, upsloping topography. z_s = 3000 m.
Figure A.1.7.21) Sargasso water profile, upsloping topography. z_s = 10 m.
Figure A.1.7.22) Sargasso water profile, upsloping topography. z_s = 100 m.
Figure A.1.7.23) Sargasso water profile, upsloping topography. z_s = 750 m.
Figure A.1.7.24) Sargasso water profile, upsloping topography. z_s = 3000 m.
Figure A.1.7.25) Sargasso to Slope water propagation, 4440 m bottom. z_s = 10 m.
Figure A.1.7.26) Sargasso to Slope water propagation, 4440 m bottom. z_s = 100 m.
Figure A.1.7.27) Sargasso to Slope water propagation, 4440 m bottom. z_s = 750 m.
Figure A.1.7.28) Sargasso to Slope water propagation, 4440 m bottom. z_s = 3000 m.
Figure A.1.7.29) Sargasso water profile, 4440 m bottom. z_s = 10 m.
Figure A.1.7.30) Sargasso water profile, 4440 m bottom. z_s = 100 m.
Figure A.1.7.31) Sargasso water profile, 4440 m bottom. z_s = 750 m.
Figure A.1.7.32) Sargasso water profile, 4440 m bottom. z_s = 3000 m.

A.1.8 Sediment Interface Sound Speed Discontinuity $c_w/c_b = 1.1$, 25 Hz

Calculations in this section were run with the following set of sediment parameters, $\rho = 1.352$ gm/cm^3, $\beta = .9$ dB/λ, $c_w/c_b = 1.1$, $\partial c/\partial z = 1.227$ sec^{-1}, and $z_{sed} = 150$ m, at a frequency $f = 25$ Hz.
Each page contains the following plots:

a. Sound speed contours.
b. Propagation loss at 100 m receiver.
c. Contours of propagation loss.
d. Propagation loss at 1000 m receiver.

Figure A.1.8.1) Slope to Sargasso water propagation, downsloping topography. z_s = 10 m.
Figure A.1.8.2) Slope to Sargasso water propagation, downsloping topography. z_s = 100 m.
Figure A.1.8.3) Slope to Sargasso water propagation, downsloping topography. z_s = 750 m.
Figure A.1.8.4) Slope to Sargasso water propagation, downsloping topography. z_s = 3000 m.
Figure A.1.8.5) Slope water profile, downsloping topography. z_s = 10 m.
Figure A.1.8.6) Slope water profile, downsloping topography. z_s = 100 m.
Figure A.1.8.7) Slope water profile, downsloping topography. z_s = 750 m.
Figure A.1.8.8) Slope water profile, downsloping topography. z_s = 3000 m.
Figure A.1.8.9) Slope to Sargasso water propagation, 3170 m bottom. z_s = 10 m.
Figure A.1.8.10) Slope to Sargasso water propagation, 3170 m bottom. z_s = 100 m.
Figure A.1.8.11) Slope to Sargasso water propagation, 3170 m bottom. z_s = 750 m.
Figure A.1.8.12) Slope to Sargasso water propagation, 3170 m bottom. z_s = 3000 m.
Figure A.1.8.13) Slope water profile, 3170 m bottom. z_s = 10 m.
Figure A.1.8.14) Slope water profile, 3170 m bottom. z_s = 100 m.
Figure A.1.8.15) Slope water profile, 3170 m bottom. z_s = 750 m.
Figure A.1.8.16) Slope water profile, 3170 m bottom. z_s = 3000 m.
Figure A.1.8.17) Sargasso to Slope water propagation, upsloping topography. z_s = 10 m.
Figure A.1.8.18) Sargasso to Slope water propagation, upsloping topography. z_s = 100 m.
Figure A.1.8.19) Sargasso to Slope water propagation, upsloping topography. z_s = 750 m.
Figure A.1.8.20) Sargasso to Slope water propagation, upsloping topography. z_s = 3000 m.
Figure A.1.8.21) Sargasso water profile, upsloping topography. z_s = 10 m.
Figure A.1.8.22) Sargasso water profile, upsloping topography. z_s = 100 m.
Figure A.1.8.23) Sargasso water profile, upsloping topography. z_s = 750 m.
Figure A.1.8.24) Sargasso water profile, upsloping topography. z_s = 3000 m.
Figure A.1.8.25) Sargasso to Slope water propagation, 4440 m bottom. z_s = 10 m.
Figure A.1.8.26) Sargasso to Slope water propagation, 4440 m bottom. z_s = 100 m.
Figure A.1.8.27) Sargasso to Slope water propagation, 4440 m bottom. z_s = 750 m.
Figure A.1.8.28) Sargasso to Slope water propagation, 4440 m bottom. z_s = 3000 m.
Figure A.1.8.29) Sargasso water profile, 4440 m bottom. z_s = 10 m.
Figure A.1.8.30) Sargasso water profile, 4440 m bottom. z_s = 100 m.
Figure A.1.8.31) Sargasso water profile, 4440 m bottom. z_s = 750 m.
Figure A.1.8.32) Sargasso water profile, 4440 m bottom. z_s = 3000 m.

A.1.9 Test of Distance to Gulf Stream, 25 Hz

Calculations in this section were run with the "realistic" set of sediment parameters, $\rho = 1.352$ gm/cm^3, $\beta = .9$ dB/λ, $c_w/c_b = 1.017$, $\partial c/\partial z = 1.227$ sec^{-1}, and $z_{sed} = 100$ m, at a frequency $f = 25$ Hz.

Various source locations were used, to test the effects of relative closeness of the Gulf Stream. To choose the source locations, cycle distances for propagation in each of the water masses were calculated by looking at the range-independent propagation calculations; measuring the distance to the nth convergence zone, and dividing by the number of convergence zones. Cycle distances were thus determined at 25 Hz to be approximately 49.5 km for slope water and 65 km for Sargasso water. Source positions were found up close to the Gulf Stream on each side, as well as .75 cycle distance away in each water mass.

Each page contains the following plots:

a. Sound speed contours.
b. Propagation loss at 100 m receiver.
c. Contours of propagation loss.
d. Propagation loss at 1000 m receiver.

Figure A.1.9.1) Slope to Sargasso water propagation, 3170 m bottom. Starting position 37.07 N 72.11 W. $z_s = 10$ m.
Figure A.1.9.2) Slope to Sargasso water propagation, 3170 m bottom. Starting position 37.07 N 72.11 W. $z_s = 100$ m.
Figure A.1.9.3) Slope to Sargasso water propagation, 3170 m bottom. Starting position 37.07 N 72.11 W. $z_s = 750$ m.
Figure A.1.9.4) Slope to Sargasso water propagation, 3170 m bottom. Starting position 37.07 N 72.11 W. $z_s = 3000$ m.
Figure A.1.9.5) Slope to Sargasso water propagation, 3170 m bottom. Starting position 36.82 N 71.80 W. $z_s = 10$ m.
Figure A.1.9.6) Slope to Sargasso water propagation, 3170 m bottom. Starting position 36.82 N 71.80 W. $z_s = 100$ m.
Figure A.1.9.7) Slope to Sargasso water propagation, 3170 m bottom. Starting position 36.82 N 71.80 W. $z_s = 750$ m.
Figure A.1.9.8) Slope to Sargasso water propagation, 3170 m bottom. Starting position 36.82 N 71.80 W. $z_s = 3000$ m.
Figure A.1.9.9) Sargasso to Slope water propagation, 4440 m bottom. Starting position 35.95 N 70.67 W. $z_s = 10$ m.
Figure A.1.9.10) Sargasso to Slope water propagation, 4440 m bottom. Starting position 35.95 N 70.67 W. $z_s = 100$ m.
Figure A.1.9.11) Sargasso to Slope water propagation, 4440 m bottom. Starting position 35.95 N 70.67 W. $z_s = 750$ m.
Figure A.1.9.12) Sargasso to Slope water propagation, 4440 m bottom. Starting position 35.95 N 70.67 W. $z_s = 3000$ m.
Figure A.1.9.13) Sargasso to Slope water propagation, 4440 m bottom. Starting position 36.26 N 71.05 W. $z_s = 10$ m.
Figure A.1.9.14) Sargasso to Slope water propagation, 4440 m bottom. Starting position 36.26 N 71.05 W. $z_s = 100$ m.
Figure A.1.9.15) Sargasso to Slope water propagation, 4440 m bottom. Starting position 36.26 N 71.05 W. $z_s = 750$ m.
Figure A.1.9.16) Sargasso to Slope water propagation, 4440 m bottom. Starting position 36.26 N 71.05 W.

$z_s = 3000$ m.

A.2.1 "Realistic" Sediment, 50 Hz

Calculations in this section were run with the "realistic" set of sediment parameters, $\rho = 1.352$ gm/cm^3, $\beta = .9$ dB/λ, $c_w/c_b = 1.017$, and $\partial c/\partial z = 1.227$ sec^{-1}, at a frequency $f = 50$ Hz. Due to typographical error, some runs were conducted with z_{sed} set deeper than necessary.
Each page contains the following plots:

a. Sound speed contours.
b. Propagation loss at 100 m receiver.
c. Contours of propagation loss.
d. Propagation loss at 1000 m receiver.

Figure A.2.1.1) Slope to Sargasso water propagation, downsloping topography. $z_s = 10$ m. $z_{sed} = 100$ m.
Figure A.2.1.2) Slope to Sargasso water propagation, downsloping topography. $z_s = 100$ m. $z_{sed} = 100$ m.
Figure A.2.1.3) Slope to Sargasso water propagation, downsloping topography. $z_s = 750$ m. $z_{sed} = 100$ m.
Figure A.2.1.4) Slope to Sargasso water propagation, downsloping topography. $z_s = 3000$ m. $z_{sed} = 100$ m.
Figure A.2.1.5) Slope to Sargasso water propagation, 3170 m bottom. $z_s = 10$ m. $z_{sed} = 250$ m.
Figure A.2.1.6) Slope to Sargasso water propagation, 3170 m bottom. $z_s = 100$ m. $z_{sed} = 250$ m.
Figure A.2.1.7) Slope to Sargasso water propagation, 3170 m bottom. $z_s = 750$ m. $z_{sed} = 250$ m.
Figure A.2.1.8) Slope to Sargasso water propagation, 3170 m bottom. $z_s = 3000$ m. $z_{sed} = 250$ m.
Figure A.2.1.9) Slope water profile, 3170 m bottom. $z_s = 10$ m. $z_{sed} = 100$ m.
Figure A.2.1.10) Slope water profile, 3170 m bottom. $z_s = 100$ m. $z_{sed} = 100$ m.
Figure A.2.1.11) Slope water profile, 3170 m bottom. $z_s = 750$ m. $z_{sed} = 100$ m.
Figure A.2.1.12) Slope water profile, 3170 m bottom. $z_s = 3000$ m. $z_{sed} = 100$ m.
Figure A.2.1.13) Sargasso to Slope water propagation, upsloping topography. $z_s = 10$ m. $z_{sed} = 100$ m.
Figure A.2.1.14) Sargasso to Slope water propagation, upsloping topography. $z_s = 100$ m. $z_{sed} = 100$ m.
Figure A.2.1.15) Sargasso to Slope water propagation, upsloping topography. $z_s = 750$ m. $z_{sed} = 100$ m.
Figure A.2.1.16) Sargasso to Slope water propagation, upsloping topography. $z_s = 3000$ m. $z_{sed} = 100$ m.
Figure A.2.1.17) Sargasso water profile, upsloping topography. $z_s = 10$ m. $z_{sed} = 100$ m.
Figure A.2.1.18) Sargasso water profile, upsloping topography. $z_s = 100$ m. $z_{sed} = 100$ m.
Figure A.2.1.19) Sargasso to Slope water propagation, 4440 m bottom. $z_s = 10$ m. $z_{sed} = 250$ m.
Figure A.2.1.20) Sargasso to Slope water propagation, 4440 m bottom. $z_s = 100$ m. $z_{sed} = 250$ m.
Figure A.2.1.21) Sargasso to Slope water propagation, 4440 m bottom. $z_s = 750$ m. $z_{sed} = 250$ m.
Figure A.2.1.22) Sargasso to Slope water propagation, 4440 m bottom. $z_s = 3000$ m. $z_{sed} = 250$ m.
Figure A.2.1.23) Sargasso water profile, 4440 m bottom. $z_s = 10$ m. $z_{sed} = 100$ m.
Figure A.2.1.24) Sargasso water profile, 4440 m bottom. $z_s = 100$ m. $z_{sed} = 100$ m.
Figure A.2.1.25) Sargasso water profile, 4440 m bottom. $z_s = 750$ m. $z_{sed} = 100$ m.
Figure A.2.1.26) Sargasso water profile, 4440 m bottom. $z_s = 3000$ m. $z_{sed} = 100$ m.

A.2.2 Sediment Sound Speed Gradient Test, 50 Hz

Calculations in this section were run with the following set of sediment parameters, $\rho = 1.352$ gm/cm^3, $\beta = .9$ dB/λ, $c_w/c_b = 1.017$, and $z_{sed} = 100$ m, at a frequency $f = 25$ Hz. Various values of $\partial c/\partial z$ were used Each page contains the following plots:

a. Sound speed contours.
b. Propagation loss at 100 m receiver.
c. Contours of propagation loss.
d. Propagation loss at 1000 m receiver.

Figure A.2.2.1) Sargasso water profile, 4440 m bottom. $z_s = 10$ m, $\partial c/\partial z = 0.0$.
Figure A.2.2.2) Sargasso water profile, 4440 m bottom. $z_s = 100$ m, $\partial c/\partial z = 0.0$.

A.2.3 Sediment Depth Test, 50 Hz

Calculations in this section were run with the following set of sediment parameters, $\rho = 1.352$ gm/cm^3, $\beta = .9$ dB/λ, $c_w/c_b = 1.017$, and $\partial c/\partial z = 1.227$ sec^{-1}, at a frequency $f = 50$ Hz. Various values of z_{sed} were used.

Each page contains the following plots:

a. Sound speed contours.
b. Propagation loss at 100 m receiver.
c. Contours of propagation loss.
d. Propagation loss at 1000 m receiver.

Figure A.2.3.1) Slope water profile, 3170 m bottom. $z_s = 10$ m, $z_{sed} = 50$ m.
Figure A.2.3.2) Slope water profile, 3170 m bottom. $z_s = 10$ m, $z_{sed} = 40$ m.
Figure A.2.3.3) Slope water profile, 3170 m bottom. $z_s = 10$ m, $z_{sed} = 30$ m.
Figure A.2.3.4) Slope water profile, 3170 m bottom. $z_s = 10$ m, $z_{sed} = 20$ m.
Figure A.2.3.5) Slope water profile, 3170 m bottom. $z_s = 10$ m, $z_{sed} = 10$ m.
Figure A.2.3.6) Slope water profile, 3170 m bottom. $z_s = 10$ m, $z_{sed} = 0$ m.

A.2.4 Sediment Interface Sound Speed Discontinuity Test, 50 Hz

Calculations in this section were run with sediment parameters, $\rho = 1.352$ gm/cm^3, $\beta = .9$ dB/λ, $\partial c/\partial z = 1.227$ sec^{-1}, and $z_{sed} = 100$ m. Frequency $f = 50$ Hz.
Each page contains the following plots:

a. Contours of sound speed.
b. Propagation loss at 100 m receiver.
c. Contours of propagation loss.
d. Propagation loss at 1000 m receiver.

Figure A.2.4.1) Slope water sound speed profile, 3170 m bottom. $z_s = 10$ m, $c_w/c_b = 1.00$.
Figure A.2.4.2) Slope water sound speed profile, 3170 m bottom. $z_s = 100$ m, $c_w/c_b = 1.00$.
Figure A.2.4.3) Slope water sound speed profile, 3170 m bottom. $z_s = 750$ m, $c_w/c_b = 1.00$.
Figure A.2.4.4) Slope water sound speed profile, 3170 m bottom. $z_s = 3000$ m, $c_w/c_b = 1.00$.
Figure A.2.4.5) Sargasso water sound speed profile, 4440 m bottom. $z_s = 10$ m, $c_w/c_b = 1.00$.
Figure A.2.4.6) Sargasso water sound speed profile, 4440 m bottom. $z_s = 100$ m, $c_w/c_b = 1.00$.
Figure A.2.4.7) Sargasso water sound speed profile, 4440 m bottom. $z_s = 750$ m, $c_w/c_b = 1.00$.
Figure A.2.4.8) Sargasso water sound speed profile, 4440 m bottom. $z_s = 3000$ m, $c_w/c_b = 1.00$.
Figure A.2.4.9) Slope water sound speed profile, 3170 m bottom. $z_s = 10$ m, $c_w/c_b = 0.98$.
Figure A.2.4.10) Slope water sound speed profile, 3170 m bottom. $z_s = 100$ m, $c_w/c_b = 0.98$.
Figure A.2.4.11) Slope water sound speed profile, 3170 m bottom. $z_s = 750$ m, $c_w/c_b = 0.98$.
Figure A.2.4.12) Slope water sound speed profile, 3170 m bottom. $z_s = 3000$ m, $c_w/c_b = 0.98$.
Figure A.2.4.13) Sargasso water sound speed profile, 4440 m bottom. $z_s = 10$ m, $c_w/c_b = 0.98$.
Figure A.2.4.14) Sargasso water sound speed profile, 4440 m bottom. $z_s = 100$ m, $c_w/c_b = 0.98$.
Figure A.2.4.15) Sargasso water sound speed profile, 4440 m bottom. $z_s = 750$ m, $c_w/c_b = 0.98$.
Figure A.2.4.16) Sargasso water sound speed profile, 4440 m bottom. $z_s = 3000$ m, $c_w/c_b = 0.98$.
Figure A.2.4.17) Slope water sound speed profile, 3170 m bottom. $z_s = 10$ m, $c_w/c_b = 1.10$.
Figure A.2.4.18) Slope water sound speed profile, 3170 m bottom. $z_s = 100$ m, $c_w/c_b = 1.10$.
Figure A.2.4.19) Slope water sound speed profile, 3170 m bottom. $z_s = 750$ m, $c_w/c_b = 1.10$.
Figure A.2.4.20) Slope water sound speed profile, 3170 m bottom. $z_s = 3000$ m, $c_w/c_b = 1.10$.
Figure A.2.4.21) Sargasso water sound speed profile, 4440 m bottom. $z_s = 10$ m, $c_w/c_b = 1.10$.
Figure A.2.4.22) Sargasso water sound speed profile, 4440 m bottom. $z_s = 100$ m, $c_w/c_b = 1.10$.
Figure A.2.4.23) Sargasso water sound speed profile, 4440 m bottom. $z_s = 750$ m, $c_w/c_b = 1.10$.
Figure A.2.4.24) Sargasso water sound speed profile, 4440 m bottom. $z_s = 3000$ m, $c_w/c_b = 1.10$.

A.2.5 Test of Distance to Gulf Stream, 50 Hz

Calculations in this section were run with the "realistic" set of sediment parameters, $\rho = 1.352$ gm/cm^3, $\beta = .9$ dB/λ, $c_w/c_b = 1.017$, $\partial c/\partial z = 1.227$ sec^{-1}, and $z_{sed} = 250$ m, at a frequency $f = 50$ Hz. Typographic error caused the sediment depth to be set deeper than in other cases; this error was permitted to persist in view of the discussion of chapter 3. Various source locations were used. To choose the source locations, cycle distances for propagation in each of the water masses were calculated from the range-independent propagtion calculations; measuring the distance to the nth convergence zone, and dividing by the number of convergence zones, giving figures of 49.5 km for slope water and 65 km for Sargasso water, at 25 Hz. Source positions were found up close to the Gulf Stream on each side, as well as .75 cycle distance away in each water mass.
Each page contains the following plots:

a. Sound speed contours.
b. Propagation loss at 100 m receiver.
c. Contours of propagation loss.
d. Propagation loss at 1000 m receiver.

Figure A.2.5.1) Slope to Sargasso water propagation, 3170 m bottom. Starting position 37.07 N 72.11 W. $z_s = 10$ m.
Figure A.2.5.2) Slope to Sargasso water propagation, 3170 m bottom. Starting position 37.07 N 72.11 W. $z_s = 100$ m.
Figure A.2.5.3) Slope to Sargasso water propagation, 3170 m bottom. Starting position 37.07 N 72.11 W. $z_s = 750$ m.
Figure A.2.5.4) Slope to Sargasso water propagation, 3170 m bottom. Starting position 37.07 N 72.11 W. $z_s = 3000$ m.
Figure A.2.5.5) Slope to Sargasso water propagation, 3170 m bottom. Starting position 36.82 N 71.80 W. $z_s = 10$ m.
Figure A.2.5.6) Slope to Sargasso water propagation, 3170 m bottom. Starting position 36.82 N 71.80 W. $z_s = 100$ m.
Figure A.2.5.7) Slope to Sargasso water propagation, 3170 m bottom. Starting position 36.82 N 71.80 W. $z_s = 750$ m.
Figure A.2.5.8) Slope to Sargasso water propagation, 3170 m bottom. Starting position 36.82 N 71.80 W. $z_s = 3000$ m.
Figure A.2.5.9) Sargasso to Slope water propagation, 4440 m bottom. Starting position 35.95 N 70.67 W. $z_s = 10$ m.
Figure A.2.5.10) Sargasso to Slope water propagation, 4440 m bottom. Starting position 35.95 N 70.67 W. $z_s = 100$ m.
Figure A.2.5.11) Sargasso to Slope water propagation, 4440 m bottom. Starting position 35.95 N 70.67 W. $z_s = 750$ m.
Figure A.2.5.12) Sargasso to Slope water propagation, 4440 m bottom. Starting position 35.95 N 70.67 W. $z_s = 3000$ m.
Figure A.2.5.13) Sargasso to Slope water propagation, 4440 m bottom. Starting position 36.26 N 71.05 W. $z_s = 10$ m.
Figure A.2.5.14) Sargasso to Slope water propagation, 4440 m bottom. Starting position 36.26 N 71.05 W. $z_s = 100$ m.
Figure A.2.5.15) Sargasso to Slope water propagation, 4440 m bottom. Starting position 36.26 N 71.05 W. $z_s = 750$ m.
Figure A.2.5.16) Sargasso to Slope water propagation, 4440 m bottom. Starting position 36.26 N 71.05 W. $z_s = 3000$ m.

A.3.1 "Realistic" Sediment, 100 Hz

Calculations in this section were run with the "realistic" set of sediment parameters, $\rho = 1.352$ gm/cm^3, $\beta = .9$ dB/λ, $c_w/c_b = 1.017$, $\partial c/\partial z = 1.227$ sec^{-1}, and $z_{sed} = 100$ m, at a frequency $f = 100$ Hz. Each page contains the following plots:

a. Sound speed contours.
b. Propagation loss at 100 m receiver.
c. Contours of propagation loss.
d. Propagation loss at 1000 m receiver.

Figure A.3.1.1) Slope to Sargasso water propagation, downsloping topography. z_s = 10 m.
Figure A.3.1.2) Slope to Sargasso water propagation, downsloping topography. z_s = 100 m.
Figure A.3.1.3) Slope to Sargasso water propagation, downsloping topography. z_s = 750 m.
Figure A.3.1.4) Slope to Sargasso water propagation, downsloping topography. z_s = 3000 m.
Figure A.3.1.5) Slope water profile, downsloping topography. z_s = 10 m.
Figure A.3.1.6) Slope water profile, downsloping topography. z_s = 100 m.
Figure A.3.1.7) Slope water profile, downsloping topography. z_s = 750 m.
Figure A.3.1.8) Slope water profile, downsloping topography. z_s = 3000 m.
Figure A.3.1.9) Slope to Sargasso water propagation, 3170 m bottom. z_s = 10 m.
Figure A.3.1.10) Slope to Sargasso water propagation, 3170 m bottom. z_s = 100 m.
Figure A.3.1.11) Slope to Sargasso water propagation, 3170 m bottom. z_s = 750 m.
Figure A.3.1.12) Slope to Sargasso water propagation, 3170 m bottom. z_s = 3000 m.
Figure A.3.1.13) Slope water profile, 3170 m bottom. z_s = 10 m.
Figure A.3.1.14) Slope water profile, 3170 m bottom. z_s = 100 m.
Figure A.3.1.15) Slope water profile, 3170 m bottom. z_s = 750 m.
Figure A.3.1.16) Slope water profile, 3170 m bottom. z_s = 3000 m.
Figure A.3.1.17) Sargasso to Slope water propagation, upsloping topography. z_s = 10 m.
Figure A.3.1.18) Sargasso to Slope water propagation, upsloping topography. z_s = 100 m.
Figure A.3.1.19) Sargasso to Slope water propagation, upsloping topography. z_s = 750 m.
Figure A.3.1.20) Sargasso to Slope water propagation, upsloping topography. z_s = 3000 m.
Figure A.3.1.21) Sargasso water profile, upsloping topography. z_s = 10 m.
Figure A.3.1.22) Sargasso water profile, upsloping topography. z_s = 100 m.
Figure A.3.1.23) Sargasso water profile, upsloping topography. z_s = 750 m.
Figure A.3.1.24) Sargasso water profile, upsloping topography. z_s = 3000 m.
Figure A.3.1.25) Sargasso to Slope water propagation, 4440 m bottom. z_s = 10 m.
Figure A.3.1.26) Sargasso to Slope water propagation, 4440 m bottom. z_s = 100 m.
Figure A.3.1.27) Sargasso to Slope water propagation, 4440 m bottom. z_s = 750 m.
Figure A.3.1.28) Sargasso to Slope water propagation, 4440 m bottom. z_s = 3000 m.
Figure A.3.1.29) Sargasso water profile, 4440 m bottom. z_s = 10 m.
Figure A.3.1.30) Sargasso water profile, 4440 m bottom. z_s = 100 m.
Figure A.3.1.31) Sargasso water profile, 4440 m bottom. z_s = 750 m.
Figure A.3.1.32) Sargasso water profile, 4440 m bottom. z_s = 3000 m.

A.3.2 Sediment Density Test, 100 Hz

Calculations in this section were run with the following set of sediment parameters, $\rho = 1.0$ gm/cm^3, $\beta = .9$ dB/λ, $c_w/c_b = 1.017$, $\partial c/\partial z = 1.227$ sec^{-1}, and $z_{sed} = 100$ m, at a frequency $f = 100$ Hz.
Each page contains the following plots:

a. Sound speed contours.
b. Propagation loss at 100 m receiver.
c. Contours of propagation loss.
d. Propagation loss at 1000 m receiver.

Figure A.3.2.1) Slope to Sargasso water propagation, downsloping topography. $z_s = 10$ m.
Figure A.3.2.2) Slope to Sargasso water propagation, downsloping topography. $z_s = 100$ m.
Figure A.3.2.3) Slope to Sargasso water propagation, downsloping topography. $z_s = 750$ m.
Figure A.3.2.4) Slope to Sargasso water propagation, downsloping topography. $z_s = 3000$ m.
Figure A.3.2.5) Slope water profile, downsloping topography. $z_s = 10$ m.
Figure A.3.2.6) Slope water profile, downsloping topography. $z_s = 100$ m.
Figure A.3.2.7) Slope water profile, downsloping topography. $z_s = 750$ m.
Figure A.3.2.8) Slope water profile, downsloping topography. $z_s = 3000$ m.
Figure A.3.2.9) Slope to Sargasso water propagation, 3170 m bottom. $z_s = 10$ m.
Figure A.3.2.10) Slope to Sargasso water propagation, 3170 m bottom. $z_s = 100$ m.
Figure A.3.2.11) Slope to Sargasso water propagation, 3170 m bottom. $z_s = 750$ m.
Figure A.3.2.12) Slope to Sargasso water propagation, 3170 m bottom. $z_s = 3000$ m.
Figure A.3.2.13) Slope water profile, 3170 m bottom. $z_s = 10$ m.
Figure A.3.2.14) Slope water profile, 3170 m bottom. $z_s = 100$ m.
Figure A.3.2.15) Slope water profile, 3170 m bottom. $z_s = 750$ m.
Figure A.3.2.16) Slope water profile, 3170 m bottom. $z_s = 3000$ m.
Figure A.3.2.17) Sargasso to Slope water propagation, upsloping topography. $z_s = 10$ m.
Figure A.3.2.18) Sargasso to Slope water propagation, upsloping topography. $z_s = 100$ m.
Figure A.3.2.19) Sargasso to Slope water propagation, upsloping topography. $z_s = 750$ m.
Figure A.3.2.20) Sargasso to Slope water propagation, upsloping topography. $z_s = 3000$ m.
Figure A.3.2.21) Sargasso water profile, upsloping topography. $z_s = 10$ m.
Figure A.3.2.22) Sargasso water profile, upsloping topography. $z_s = 100$ m.
Figure A.3.2.23) Sargasso water profile, upsloping topography. $z_s = 750$ m.
Figure A.3.2.24) Sargasso water profile, upsloping topography. $z_s = 3000$ m.
Figure A.3.2.25) Sargasso to Slope water propagation, 4440 m bottom. $z_s = 10$ m.
Figure A.3.2.26) Sargasso to Slope water propagation, 4440 m bottom. $z_s = 100$ m.
Figure A.3.2.27) Sargasso to Slope water propagation, 4440 m bottom. $z_s = 750$ m.
Figure A.3.2.28) Sargasso to Slope water propagation, 4440 m bottom. $z_s = 3000$ m.
Figure A.3.2.29) Sargasso water profile, 4440 m bottom. $z_s = 10$ m.
Figure A.3.2.30) Sargasso water profile, 4440 m bottom. $z_s = 100$ m.
Figure A.3.2.31) Sargasso water profile, 4440 m bottom. $z_s = 750$ m.
Figure A.3.2.32) Sargasso water profile, 4440 m bottom. $z_s = 3000$ m.

A.3.3 Sediment Attenuation Test, 100 Hz

Calculations in this section were run with the following set of sediment parameters, $\rho = 1.352$ gm/cm^3, $c_w/c_b = 1.017$, $\partial c/\partial z = 1.227$ sec^{-1}, and $z_{sed} = 100$ m, at a frequency $f = 100$ Hz. Various values of β were used

Each page contains the following plots:

a. Sound speed contours.
b. Propagation loss at 100 m receiver.
c. Contours of propagation loss.
d. Propagation loss at 1000 m receiver.

Figure A.3.3.1) Slope water profile, 3170 m bottom. z_s = 10 m, $\beta = 0.0$ dB/λ.
Figure A.3.3.2) Slope water profile, 3170 m bottom. z_s = 100 m, $\beta = 0.0$ dB/λ.
Figure A.3.3.3) Slope water profile, 3170 m bottom. z_s = 750 m, $\beta = 0.0$ dB/λ.
Figure A.3.3.4) Slope water profile, 3170 m bottom. z_s = 3000 m, $\beta = 0.0$ dB/λ.
Figure A.3.3.5) Slope water profile, 3170 m bottom. z_s = 10 m, $\beta = 0.25$ dB/λ.
Figure A.3.3.6) Slope water profile, 3170 m bottom. z_s = 100 m, $\beta = 0.25$ dB/λ.
Figure A.3.3.7) Slope water profile, 3170 m bottom. z_s = 750 m, $\beta = 0.25$ dB/λ.
Figure A.3.3.8) Slope water profile, 3170 m bottom. z_s = 3000 m, $\beta = 0.25$ dB/λ.
Figure A.3.3.9) Slope water profile, 3170 m bottom. z_s = 10 m, $\beta = 0.5$ dB/λ.
Figure A.3.3.10) Slope water profile, 3170 m bottom. z_s = 100 m, $\beta = 0.5$ dB/λ.
Figure A.3.3.11) Slope water profile, 3170 m bottom. z_s = 750 m, $\beta = 0.5$ dB/λ.
Figure A.3.3.12) Slope water profile, 3170 m bottom. z_s = 3000 m, $\beta = 0.5$ dB/λ.
Figure A.3.3.13) Slope water profile, 3170 m bottom. z_s = 10 m, $\beta = 2.0$ dB/λ.
Figure A.3.3.14) Slope water profile, 3170 m bottom. z_s = 100 m, $\beta = 2.0$ dB/λ.
Figure A.3.3.15) Slope water profile, 3170 m bottom. z_s = 750 m, $\beta = 2.0$ dB/λ.
Figure A.3.3.16) Slope water profile, 3170 m bottom. z_s = 3000 m, $\beta = 2.0$ dB/λ.

A.3.4 Sediment Sound Speed Gradient Test, 100 Hz

Calculations in this section were run with the following set of sediment parameters, $\rho = 1.352$ gm/cm^3, $\beta = .9$ dB/λ, $c_w/c_b = 1.017$, and $z_{sed} = 100$ m, at a frequency $f = 100$ Hz. Various values of $\partial c/\partial z$ were used Each page contains the following plots:

a. Sound speed contours.
b. Propagation loss at 100 m receiver.
c. Contours of propagation loss.
d. Propagation loss at 1000 m receiver.

Figure A.3.4.1) Slope water profile, 3170 m bottom. $z_s = 10$ m, $\partial c/\partial z = 0.0$.
Figure A.3.4.2) Slope water profile, 3170 m bottom. $z_s = 750$ m, $\partial c/\partial z = 0.0$.
Figure A.3.4.3) Slope water profile, 3170 m bottom. $z_s = 3000$ m, $\partial c/\partial z = 0.0$.
Figure A.3.4.4) Sargasso water profile, 4440 m bottom. $z_s = 10$ m, $\partial c/\partial z = 0.0$.
Figure A.3.4.5) Sargasso water profile, 4440 m bottom. $z_s = 750$ m, $\partial c/\partial z = 0.0$.
Figure A.3.4.6) Sargasso water profile, upsloping topography. $z_s = 10$ m, $\partial c/\partial z = 0.0$.
Figure A.3.4.7) Slope water profile, 3170 m bottom. $z_s = 10$ m, $\partial c/\partial z = 0.75$.
Figure A.3.4.8) Slope water profile, 3170 m bottom. $z_s = 10$ m, $\partial c/\partial z = 1.50$.

A.3.5 Sediment Depth Test, 100 Hz

Calculations in this section were run with the following set of sediment parameters, $\rho = 1.352$ gm/cm^3, $\beta = .9$ dB/λ, $c_w/c_b = 1.017$, and $\partial c/\partial z = 1.227$ sec^{-1}, at a frequency $f = 100$ Hz. Various values of z_{sed} were used.

Each page contains the following plots:

a. Sound speed contours.
b. Propagation loss at 100 m receiver.
c. Contours of propagation loss.
d. Propagation loss at 1000 m receiver.

Figure A.3.5.1) Slope water profile, 3170 m bottom. $z_s = 10$ m, $z_{sed} = 20$ m.
Figure A.3.5.2) Slope water profile, 3170 m bottom. $z_s = 750$ m, $z_{sed} = 20$ m.
Figure A.3.5.3) Slope water profile, 3170 m bottom. $z_s = 10$ m, $z_{sed} = 10$ m.
Figure A.3.5.4) Slope water profile, 3170 m bottom. $z_s = 750$ m, $z_{sed} = 10$ m.
Figure A.3.5.5) Slope water profile, 3170 m bottom. $z_s = 10$ m, $z_{sed} = 5$ m.
Figure A.3.5.6) Slope water profile, 3170 m bottom. $z_s = 750$ m, $z_{sed} = 5$ m.
Figure A.3.5.7) Slope water profile, 3170 m bottom. $z_s = 10$ m, $z_{sed} = 2.5$ m.
Figure A.3.5.8) Slope water profile, 3170 m bottom. $z_s = 750$ m, $z_{sed} = 2.5$ m.
Figure A.3.5.9) Slope water profile, 3170 m bottom. $z_s = 10$ m, $z_{sed} = 0$ m.
Figure A.3.5.10) Slope water profile, 3170 m bottom. $z_s = 750$ m, $z_{sed} = 0$ m.

A.3.6 Sediment Interface Sound Speed Discontinuity $c_w/c_b = .98$, 100 Hz

Calculations in this section were run with the following set of sediment parameters, $\rho = 1.352$ gm/cm^3, $\beta = .9$ dB/λ, $c_w/c_b = 0.98$, $\partial c/\partial z = 1.227$ sec^{-1}, and $z_{sed} = 100$ m, at a frequency $f = 100$ Hz.
Each page contains the following plots:

a. Sound speed contours.
b. Propagation loss at 100 m receiver.
c. Contours of propagation loss.
d. Propagation loss at 1000 m receiver.

Figure A.3.6.1) Slope to Sargasso water propagation, downsloping topography. z_s = 10 m.
Figure A.3.6.2) Slope to Sargasso water propagation, downsloping topography. z_s = 100 m.
Figure A.3.6.3) Slope to Sargasso water propagation, downsloping topography. z_s = 750 m.
Figure A.3.6.4) Slope to Sargasso water propagation, downsloping topography. z_s = 3000 m.
Figure A.3.6.5) Slope water profile, downsloping topography. z_s = 10 m.
Figure A.3.6.6) Slope water profile, downsloping topography. z_s = 750 m.
Figure A.3.6.7) Slope to Sargasso water propagation, 3170 m bottom. z_s = 10 m.
Figure A.3.6.8) Slope to Sargasso water propagation, 3170 m bottom. z_s = 100 m.
Figure A.3.6.9) Slope to Sargasso water propagation, 3170 m bottom. z_s = 750 m.
Figure A.3.6.10) Slope to Sargasso water propagation, 3170 m bottom. z_s = 3000 m.
Figure A.3.6.11) Slope water profile, 3170 m bottom. z_s = 10 m.
Figure A.3.6.12) Slope water profile, 3170 m bottom. z_s = 100 m.
Figure A.3.6.13) Slope water profile, 3170 m bottom. z_s = 750 m.
Figure A.3.6.14) Slope water profile, 3170 m bottom. z_s = 3000 m.
Figure A.3.6.15) Sargasso to Slope water propagation, upsloping topography. z_s = 10 m.
Figure A.3.6.16) Sargasso to Slope water propagation, upsloping topography. z_s = 100 m.
Figure A.3.6.17) Sargasso to Slope water propagation, upsloping topography. z_s = 750 m.
Figure A.3.6.18) Sargasso to Slope water propagation, upsloping topography. z_s = 3000 m.
Figure A.3.6.19) Sargasso water profile, upsloping topography. z_s = 10 m.
Figure A.3.6.20) Sargasso water profile, upsloping topography. z_s = 750 m.
Figure A.3.6.21) Sargasso to Slope water propagation, 4440 m bottom. z_s = 10 m.
Figure A.3.6.22) Sargasso to Slope water propagation, 4440 m bottom. z_s = 100 m.
Figure A.3.6.23) Sargasso to Slope water propagation, 4440 m bottom. z_s = 750 m.
Figure A.3.6.24) Sargasso to Slope water propagation, 4440 m bottom. z_s = 3000 m.
Figure A.3.6.25) Sargasso water profile, 4440 m bottom. z_s = 10 m.
Figure A.3.6.26) Sargasso water profile, 4440 m bottom. z_s = 100 m.
Figure A.3.6.27) Sargasso water profile, 4440 m bottom. z_s = 750 m.
Figure A.3.6.28) Sargasso water profile, 4440 m bottom. z_s = 3000 m.

A.3.7 Sediment Interface Sound Speed Discontinuity $c_w/c_b = 1.0$, 100 Hz

Calculations in this section were run with the following set of sediment parameters, $\rho = 1.352$ gm/cm^3, $\beta = .9$ dB/λ, $c_w/c_b = 1.0$, $\partial c/\partial z = 1.227$ sec^{-1}, and $z_{sed} = 100$ m, at a frequency $f = 100$ Hz.
Each page contains the following plots:

a. Sound speed contours.
b. Propagation loss at 100 m receiver.
c. Contours of propagation loss.
d. Propagation loss at 1000 m receiver.

Figure A.3.7.1) Slope to Sargasso water propagation, downsloping topography. z_s = 10 m.
Figure A.3.7.2) Slope to Sargasso water propagation, downsloping topography. z_s = 100 m.
Figure A.3.7.3) Slope to Sargasso water propagation, downsloping topography. z_s = 750 m.
Figure A.3.7.4) Slope to Sargasso water propagation, downsloping topography. z_s = 3000 m.
Figure A.3.7.5) Slope water profile, downsloping topography. z_s = 10 m.
Figure A.3.7.6) Slope water profile, downsloping topography. z_s = 100 m.
Figure A.3.7.7) Slope water profile, downsloping topography. z_s = 750 m.
Figure A.3.7.8) Slope water profile, downsloping topography. z_s = 3000 m.
Figure A.3.7.9) Slope to Sargasso water propagation, 3170 m bottom. z_s = 10 m.
Figure A.3.7.10) Slope to Sargasso water propagation, 3170 m bottom. z_s = 100 m.
Figure A.3.7.11) Slope to Sargasso water propagation, 3170 m bottom. z_s = 750 m.
Figure A.3.7.12) Slope to Sargasso water propagation, 3170 m bottom. z_s = 3000 m.
Figure A.3.7.13) Slope water profile, 3170 m bottom. z_s = 10 m.
Figure A.3.7.14) Slope water profile, 3170 m bottom. z_s = 100 m.
Figure A.3.7.15) Slope water profile, 3170 m bottom. z_s = 750 m.
Figure A.3.7.16) Slope water profile, 3170 m bottom. z_s = 3000 m.
Figure A.3.7.17) Sargasso to Slope water propagation, upsloping topography. z_s = 10 m.
Figure A.3.7.18) Sargasso to Slope water propagation, upsloping topography. z_s = 100 m.
Figure A.3.7.19) Sargasso to Slope water propagation, upsloping topography. z_s = 750 m.
Figure A.3.7.20) Sargasso to Slope water propagation, upsloping topography. z_s = 3000 m.
Figure A.3.7.21) Sargasso water profile, upsloping topography. z_s = 10 m.
Figure A.3.7.22) Sargasso water profile, upsloping topography. z_s = 100 m.
Figure A.3.7.23) Sargasso water profile, upsloping topography. z_s = 750 m.
Figure A.3.7.24) Sargasso water profile, upsloping topography. z_s = 3000 m.
Figure A.3.7.25) Sargasso to Slope water propagation, 4440 m bottom. z_s = 10 m.
Figure A.3.7.26) Sargasso to Slope water propagation, 4440 m bottom. z_s = 100 m.
Figure A.3.7.27) Sargasso to Slope water propagation, 4440 m bottom. z_s = 750 m.
Figure A.3.7.28) Sargasso to Slope water propagation, 4440 m bottom. z_s = 3000 m.
Figure A.3.7.29) Sargasso water profile, 4440 m bottom. z_s = 10 m.
Figure A.3.7.30) Sargasso water profile, 4440 m bottom. z_s = 100 m.
Figure A.3.7.31) Sargasso water profile, 4440 m bottom. z_s = 750 m.
Figure A.3.7.32) Sargasso water profile, 4440 m bottom. z_s = 3000 m.

A.3.8 Sediment Interface Sound Speed Discontinuity $c_w/c_b = 1.1$, 100 Hz

Calculations in this section were run with the following set of sediment parameters, $\rho = 1.352$ gm/cm^3, $\beta = .9$ dB/λ, $c_w/c_b = 1.1$, $\partial c/\partial z = 1.227$ sec^{-1}, and $z_{sed} = 100$ m, at a frequency $f = 100$ Hz.
Each page contains the following plots:

a. Sound speed contours.
b. Propagation loss at 100 m receiver.
c. Contours of propagation loss.
d. Propagation loss at 1000 m receiver.

Figure A.3.8.1) Slope to Sargasso water propagation, downsloping topography. z_s = 10 m.
Figure A.3.8.2) Slope to Sargasso water propagation, downsloping topography. z_s = 100 m.
Figure A.3.8.3) Slope to Sargasso water propagation, downsloping topography. z_s = 750 m.
Figure A.3.8.4) Slope to Sargasso water propagation, downsloping topography. z_s = 3000 m.
Figure A.3.8.5) Slope water profile, downsloping topography. z_s = 10 m.
Figure A.3.8.6) Slope water profile, downsloping topography. z_s = 750 m.
Figure A.3.8.7) Slope to Sargasso water propagation, 3170 m bottom. z_s = 10 m.
Figure A.3.8.8) Slope to Sargasso water propagation, 3170 m bottom. z_s = 100 m.
Figure A.3.8.9) Slope to Sargasso water propagation, 3170 m bottom. z_s = 750 m.
Figure A.3.8.10) Slope to Sargasso water propagation, 3170 m bottom. z_s = 3000 m.
Figure A.3.8.11) Slope water profile, 3170 m bottom. z_s = 10 m.
Figure A.3.8.12) Slope water profile, 3170 m bottom. z_s = 100 m.
Figure A.3.8.13) Slope water profile, 3170 m bottom. z_s = 750 m.
Figure A.3.8.14) Slope water profile, 3170 m bottom. z_s = 3000 m.
Figure A.3.8.15) Sargasso to Slope water propagation, upsloping topography. z_s = 10 m.
Figure A.3.8.16) Sargasso to Slope water propagation, upsloping topography. z_s = 100 m.
Figure A.3.8.17) Sargasso to Slope water propagation, upsloping topography. z_s = 750 m.
Figure A.3.8.18) Sargasso to Slope water propagation, upsloping topography. z_s = 3000 m.
Figure A.3.8.19) Sargasso water profile, upsloping topography. z_s = 10 m.
Figure A.3.8.20) Sargasso water profile, upsloping topography. z_s = 100 m.
Figure A.3.8.21) Sargasso water profile, 4440 m bottom. z_s = 10 m.
Figure A.3.8.22) Sargasso water profile, 4440 m bottom. z_s = 100 m.
Figure A.3.8.23) Sargasso water profile, 4440 m bottom. z_s = 750 m.
Figure A.3.8.24) Sargasso water profile, 4440 m bottom. z_s = 3000 m.

A.4.1 Upsloping "Realistic" Sediment, Sargasso and Slope Sound Speed Profiles

Calculations in this section were run with the "realistic" set of sediment parameters, $\rho = 1.352$ gm/cm^3, $\beta = .9$ dB/λ, $c_w/c_b = 1.017$, $\partial c/\partial z = 1.227$ sec^{-1}, and $z_{sed} = 100$ m. Runs were computed with sloping topography having various constant values of $\Delta z/\Delta r$.
Each page contains the following plots:

a. Sound speed contours.
b. Propagation loss at 100 m receiver.
c. Contours of propagation loss.
d. Propagation loss at 1000 m receiver.

Figure A.4.1.1) Sargasso sound speed profile, $z_s = 10$ m, $f = 100$ Hz, $\Delta z/\Delta r = .001$.
Figure A.4.1.2) Sargasso sound speed profile, $z_s = 10$ m, $f = 100$ Hz, $\Delta z/\Delta r = .002$.
Figure A.4.1.3) Sargasso sound speed profile, $z_s = 10$ m, $f = 100$ Hz, $\Delta z/\Delta r = .003$.
Figure A.4.1.4) Sargasso sound speed profile, $z_s = 10$ m, $f = 100$ Hz, $\Delta z/\Delta r = .004$.
Figure A.4.1.5) Sargasso sound speed profile, $z_s = 10$ m, $f = 50$ Hz, $\Delta z/\Delta r = .001$.
Figure A.4.1.6) Sargasso sound speed profile, $z_s = 10$ m, $f = 50$ Hz, $\Delta z/\Delta r = .002$.
Figure A.4.1.7) Sargasso sound speed profile, $z_s = 10$ m, $f = 50$ Hz, $\Delta z/\Delta r = .003$.
Figure A.4.1.8) Sargasso sound speed profile, $z_s = 10$ m, $f = 50$ Hz, $\Delta z/\Delta r = .004$.
Figure A.4.1.9) Sargasso sound speed profile, $z_s = 10$ m, $f = 50$ Hz, $\Delta z/\Delta r = .005$.
Figure A.4.1.10) Sargasso sound speed profile, $z_s = 10$ m, $f = 50$ Hz, $\Delta z/\Delta r = .006$.
Figure A.4.1.11) Sargasso sound speed profile, $z_s = 10$ m, $f = 50$ Hz, $\Delta z/\Delta r = .007$.
Figure A.4.1.12) Slope sound speed profile, $z_s = 10$ m, $f = 50$ Hz, $\Delta z/\Delta r = .002$.
Figure A.4.1.13) Slope sound speed profile, $z_s = 10$ m, $f = 50$ Hz, $\Delta z/\Delta r = .003$.
Figure A.4.1.14) Slope sound speed profile, $z_s = 10$ m, $f = 50$ Hz, $\Delta z/\Delta r = .004$.
Figure A.4.1.15) Slope sound speed profile, $z_s = 10$ m, $f = 50$ Hz, $\Delta z/\Delta r = .005$.
Figure A.4.1.16) Slope sound speed profile, $z_s = 10$ m, $f = 50$ Hz, $\Delta z/\Delta r = .006$.
Figure A.4.1.17) Slope sound speed profile, $z_s = 10$ m, $f = 50$ Hz, $\Delta z/\Delta r = .007$.

A.4.2 Downsloping "Realistic" Sediment, Sargasso Sound Speed Profile

Calculations in this section were run with the "realistic" set of sediment parameters, $\rho = 1.352$ gm/cm^3, $\beta = .9$ dB/λ, $c_w/c_b = 1.017$, $\partial c/\partial z = 1.227$ sec^{-1}, and $z_{sed} = 100$ m. Range-independent Sargasso water sound speed profile; downsloping topography with various constant values of $\Delta z/\Delta r$.
Each page contains the following plots:

a. Sound speed contours.
b. Propagation loss at 100 m receiver.
c. Contours of propagation loss.
d. Propagation loss at 1000 m receiver.

Figure A.4.2.1) $z_s = 10$ m, $f = 25$ Hz, $\Delta z/\Delta r = .002$.
Figure A.4.2.2) $z_s = 10$ m, $f = 25$ Hz, $\Delta z/\Delta r = .003$.
Figure A.4.2.3) $z_s = 10$ m, $f = 25$ Hz, $\Delta z/\Delta r = .004$.
Figure A.4.2.4) $z_s = 10$ m, $f = 25$ Hz, $\Delta z/\Delta r = .005$.
Figure A.4.2.5) $z_s = 10$ m, $f = 25$ Hz, $\Delta z/\Delta r = .006$.
Figure A.4.2.6) $z_s = 100$ m, $f = 25$ Hz, $\Delta z/\Delta r = .005$.
Figure A.4.2.7) $z_s = 750$ m, $f = 25$ Hz, $\Delta z/\Delta r = .005$.
Figure A.4.2.8) $z_s = 3000$ m, $f = 25$ Hz, $\Delta z/\Delta r = .005$.
Figure A.4.2.9) $z_s = 10$ m, $f = 50$ Hz, $\Delta z/\Delta r = .005$.
Figure A.4.2.10) $z_s = 100$ m, $f = 50$ Hz, $\Delta z/\Delta r = .005$.
Figure A.4.2.11) $z_s = 750$ m, $f = 50$ Hz, $\Delta z/\Delta r = .005$.
Figure A.4.2.12) $z_s = 3000$ m, $f = 50$ Hz, $\Delta z/\Delta r = .005$.
Figure A.4.2.13) $z_s = 10$ m, $f = 100$ Hz, $\Delta z/\Delta r = .005$.
Figure A.4.2.14) $z_s = 100$ m, $f = 100$ Hz, $\Delta z/\Delta r = .005$.
Figure A.4.2.15) $z_s = 750$ m, $f = 100$ Hz, $\Delta z/\Delta r = .005$.
Figure A.4.2.16) $z_s = 3000$ m, $f = 100$ Hz, $\Delta z/\Delta r = .005$.

A.4.3 Test of Sensitivity to c_w/c_b, Sargasso Sound Speed Profile, Flat Topography

Calculations in this section were run with sediment parameters, $\rho = 1.352$ gm/cm^3, $\beta = .9$ dB/λ, and $\partial c/\partial z = 1.227$ sec^{-1}. Typographical error caused z_{sed} to be set more deeply than necessary, in view of the discussion in chapter 3. Various values of c_w/c_b were used, frequencies of 25 and 50 Hz, source depths of 10 and 100 m. Range-independent Sargasso water sound speed profile; downsloping topography with various constant values of $\Delta z/\Delta r$.

Each page contains the following plots:

a. Contours of propagation loss over the first 50 km.
b. Propagation loss at 100 m receiver.
c. Contours of propagation loss.
d. Propagation loss at 1000 m receiver.

Figure A.4.3.1) $z_s = 100$ m, $f = 25$ Hz, $c_w/c_b = 1.01$.
Figure A.4.3.2) $z_s = 100$ m, $f = 25$ Hz, $c_w/c_b = 1.02$.
Figure A.4.3.3) $z_s = 100$ m, $f = 25$ Hz, $c_w/c_b = 1.03$.
Figure A.4.3.4) $z_s = 100$ m, $f = 25$ Hz, $c_w/c_b = 1.04$.
Figure A.4.3.5) $z_s = 100$ m, $f = 25$ Hz, $c_w/c_b = 1.05$.
Figure A.4.3.6) $z_s = 100$ m, $f = 50$ Hz, $c_w/c_b = 1.01$.
Figure A.4.3.7) $z_s = 100$ m, $f = 50$ Hz, $c_w/c_b = 1.02$.
Figure A.4.3.8) $z_s = 100$ m, $f = 50$ Hz, $c_w/c_b = 1.03$.
Figure A.4.3.9) $z_s = 100$ m, $f = 50$ Hz, $c_w/c_b = 1.04$.
Figure A.4.3.10) $z_s = 100$ m, $f = 50$ Hz, $c_w/c_b = 1.05$.
Figure A.4.3.11) $z_s = 10$ m, $f = 25$ Hz, $c_w/c_b = 1.02$.
Figure A.4.3.12) $z_s = 10$ m, $f = 25$ Hz, $c_w/c_b = 1.03$.
Figure A.4.3.13) $z_s = 10$ m, $f = 25$ Hz, $c_w/c_b = 1.04$.
Figure A.4.3.14) $z_s = 10$ m, $f = 25$ Hz, $c_w/c_b = 1.05$.

A.4.4 Sound Speed Gradient Discontinuity Test, Sargasso Sound Speed Profile

Calculations in this section were run in the Sargasso profile with bottom at 4440 m and $f = 100$ Hz, with range 50 km. Various highly artificial sediment parameters were used, to test the origins of odd reflected sound beams obtained with a so-called "absorbing" bottom, which has $\rho = 1.0$ gm/cm^3, $\beta = 0$ dB/λ, $c_w/c_b = 1.0$, $\partial c/\partial z = 0$ sec^{-1}, and $z_{sed} = 0$ m. Source depths were $z_s = 10$ and 100 m. Tests with the sediment layer thick but acoustically transparent, to prove that there was no unusual interaction with the exponential field damping in the artificial absorbing layer applied below the fluid sediment layer, showed no change in the reflected returns. Such a layer is formed with the above parameters the same, except $z_{sed} = 250$ m. Normal step size for these 100 Hz calculations is $dz = 1.25$ m, $dr = 2.5$ m; tests with smaller step size ($dz = 1.0$ m, $dr = 2.0$ m) showed that the effect is not dependent on step size. Tests with a negative gradient within the sediment $\partial c/\partial z = -.5$ showed a dramatic increase of approximately 25 dB in the reflected returns. These phenomena are discussed in Brekhovskikh (1980, section 20.5) and Rayleigh (1945, section 148b).
Each page contains the following plots:

a. Sound speed contours.
b. Propagation loss at 100 m receiver.
c. Contours of propagation loss.
d. Propagation loss at 1000 m receiver.

Figure A.4.4.1) $z_s = 10$ m, $\partial c/\partial z = 0$ sec^{-1}, $z_{sed} = 0$ m.
Figure A.4.4.2) $z_s = 10$ m, $\partial c/\partial z = 0$ sec^{-1}, $z_{sed} = 250$ m.
Figure A.4.4.3) $z_s = 10$ m, $\partial c/\partial z = -.5$ sec^{-1}, $z_{sed} = 125$ m.
Figure A.4.4.4) $z_s = 10$ m, $\partial c/\partial z = -.5$ sec^{-1}, $z_{sed} = 250$ m.
Figure A.4.4.5) $z_s = 100$ m, $\partial c/\partial z = 0$ sec^{-1}, $z_{sed} = 0$ m.
Figure A.4.4.6) $z_s = 100$ m, $\partial c/\partial z = 0$ sec^{-1}, $z_{sed} = 250$ m.
Figure A.4.4.7) $z_s = 100$ m, $\partial c/\partial z = 0$ sec^{-1}, $z_{sed} = 250$ m. Smaller step size.
Figure A.4.4.8) $z_s = 100$ m, $\partial c/\partial z = -.5$ sec^{-1}, $z_{sed} = 125$ m.
Figure A.4.4.9) $z_s = 100$ m, $\partial c/\partial z = -.5$ sec^{-1}, $z_{sed} = 250$ m.

B.1 AthenA QG Calculations

Calculations in this section were run with the following set of sediment parameters, $\rho = 1.404$ gm/cm^3, $\beta = 1.35$ dB/λ, $c_w/c_b = 0.996$, $\partial c/\partial z = 1.71$ sec^{-1}, and $z_{sed} = 300$ m. Sound speed fields were supplied by the quasigeostrophic model alone, at depths of 125, 325, 675, 1375, 2175, and 2975 m.
Each page contains the following plots:

a. Sound speed contours.
b. Propagation loss at 10 m receiver.
c. Contours of propagation loss.
d. Propagation loss at 200 m receiver.

Figure B.1.1) Range dependent oceanography, realistic topography. $z_s = 10$ m. $f = 25$ Hz.
Figure B.1.2) Range dependent oceanography, realistic topography. $z_s = 150$ m. $f = 25$ Hz.
Figure B.1.3) Range dependent oceanography, realistic topography. $z_s = 500$ m. $f = 25$ Hz.
Figure B.1.4) Range dependent oceanography, realistic topography. $z_s = 750$ m. $f = 25$ Hz.
Figure B.1.5) Range independent oceanography, 3300 m bottom. $z_s = 10$ m. $f = 25$ Hz.
Figure B.1.6) Range independent oceanography, 3300 m bottom. $z_s = 150$ m. $f = 25$ Hz.
Figure B.1.7) Range independent oceanography, 3300 m bottom. $z_s = 500$ m. $f = 25$ Hz.
Figure B.1.8) Range independent oceanography, 3300 m bottom. $z_s = 750$ m. $f = 25$ Hz.
Figure B.1.9) Range dependent oceanography, realistic topography. $z_s = 10$ m. $f = 50$ Hz.
Figure B.1.10) Range dependent oceanography, realistic topography. $z_s = 150$ m. $f = 50$ Hz.
Figure B.1.11) Range dependent oceanography, realistic topography. $z_s = 500$ m. $f = 50$ Hz.
Figure B.1.12) Range dependent oceanography, realistic topography. $z_s = 750$ m. $f = 50$ Hz.
Figure B.1.13) Range independent oceanography, 3300 m bottom. $z_s = 10$ m. $f = 50$ Hz.
Figure B.1.14) Range independent oceanography, 3300 m bottom. $z_s = 150$ m. $f = 50$ Hz.
Figure B.1.15) Range independent oceanography, 3300 m bottom. $z_s = 500$ m. $f = 50$ Hz.
Figure B.1.16) Range independent oceanography, 3300 m bottom. $z_s = 750$ m. $f = 50$ Hz.
Figure B.1.17) Range dependent oceanography, realistic topography. $z_s = 150$ m. $f = 100$ Hz.
Figure B.1.18) Range dependent oceanography, realistic topography. $z_s = 500$ m. $f = 100$ Hz.
Figure B.1.19) Range independent oceanography, 3300 m bottom. $z_s = 150$ m. $f = 100$ Hz.
Figure B.1.20) Range independent oceanography, 3300 m bottom. $z_s = 500$ m. $f = 100$ Hz.

B.2 AthenA QG-SBL Calculations

Calculations in this section were run with the following set of sediment parameters, $\rho = 1.404$ gm/cm^3, $\beta = 1.35$ dB/λ, $c_w/c_b = 0.996$, $\partial c/\partial z = 1.71$ sec^{-1}, and $z_{sed} = 300$ m. Sound speed fields were provided by the six-level quasigeostrophic model at depths of 125, 325, 675, 1375, 2175, and 2975 m; the surface boundary layer model provided values at depths of 6, 19, 33, 49, 66, 85, 107, and 130 m. Where the SBL level was deeper than the QG level, the SBL output was accepted in preference to the QG value.
Each page contains the following plots:

a. Sound speed contours.
b. Propagation loss at 10 m receiver.
c. Contours of propagation loss.
d. Propagation loss at 200 m receiver.

Figure B.2.1) Range dependent oceanography, realistic topography. $z_s = 10$ m. $f = 25$ Hz.
Figure B.2.2) Range dependent oceanography, realistic topography. $z_s = 150$ m. $f = 25$ Hz.
Figure B.2.3) Range dependent oceanography, realistic topography. $z_s = 500$ m. $f = 25$ Hz.
Figure B.2.4) Range dependent oceanography, realistic topography. $z_s = 750$ m. $f = 25$ Hz.
Figure B.2.5) Range independent oceanography, 3330 m bottom. $z_s = 10$ m. $f = 25$ Hz.
Figure B.2.6) Range independent oceanography, 3330 m bottom. $z_s = 150$ m. $f = 25$ Hz.
Figure B.2.7) Range independent oceanography, 3330 m bottom. $z_s = 500$ m. $f = 25$ Hz.
Figure B.2.8) Range independent oceanography, 3330 m bottom. $z_s = 750$ m. $f = 25$ Hz.
Figure B.2.9) Range dependent oceanography, realistic topography. $z_s = 10$ m. $f = 50$ Hz.
Figure B.2.10) Range dependent oceanography, realistic topography. $z_s = 150$ m. $f = 50$ Hz.
Figure B.2.11) Range dependent oceanography, realistic topography. $z_s = 500$ m. $f = 50$ Hz.
Figure B.2.12) Range dependent oceanography, realistic topography. $z_s = 750$ m. $f = 50$ Hz.
Figure B.2.13) Range independent oceanography, 3330 m bottom. $z_s = 10$ m. $f = 50$ Hz.
Figure B.2.14) Range independent oceanography, 3330 m bottom. $z_s = 150$ m. $f = 50$ Hz.
Figure B.2.15) Range independent oceanography, 3330 m bottom. $z_s = 500$ m. $f = 50$ Hz.
Figure B.2.16) Range independent oceanography, 3330 m bottom. $z_s = 750$ m. $f = 50$ Hz.
Figure B.2.17) Range dependent oceanography, realistic topography. $z_s = 150$ m. $f = 100$ Hz.
Figure B.2.18) Range dependent oceanography, realistic topography. $z_s = 500$ m. $f = 100$ Hz.
Figure B.2.19) Range independent oceanography, 3330 m bottom. $z_s = 150$ m. $f = 100$ Hz.
Figure B.2.20) Range independent oceanography, 3330 m bottom. $z_s = 500$ m. $f = 100$ Hz.

C.1 Iceland-U.K. Gap Region, Propagation through Eddy

Calculations in this section were run with the following set of sediment parameters, $\rho = 1.60$ gm/cm^3, $\beta = 4.8$ dB/λ, $c_w/c_b = 1.031$, $\partial c/\partial z = 0.5$ sec^{-1}, and $z_{sed} = 5$ m.
Each page contains the following plots:

a. Sound speed contours.
b. Propagation loss at 10 m receiver.
c. Contours of propagation loss.
d. Propagation loss at 600 m receiver.

Figure C.1.1) Range dependent QG oceanography, 607 m bottom. $z_s = 10$ m. $f = 25$ Hz.
Figure C.1.2) Atlantic sound speed profile, 607 m bottom. $z_s = 10$ m. $f = 25$ Hz.
Figure C.1.3) Arctic sound speed profile, 607 m bottom. $z_s = 10$ m. $f = 25$ Hz.
Figure C.1.4) Range dependent QG oceanography, 3000 m bottom. $z_s = 10$ m. $f = 25$ Hz.
Figure C.1.5) Range dependent QG oceanography, realistic topography. $z_s = 10$ m. $f = 25$ Hz.
Figure C.1.6) Range dependent QG oceanography, realistic topography. $z_s = 300$ m. $f = 25$ Hz.
Figure C.1.7) Range dependent QG oceanography, realistic topography. $z_s = 600$ m. $f = 25$ Hz.
Figure C.1.8) Atlantic sound speed profile, realistic topography. $z_s = 10$ m. $f = 25$ Hz.
Figure C.1.9) Atlantic sound speed profile, realistic topography. $z_s = 300$ m. $f = 25$ Hz.
Figure C.1.10) Atlantic sound speed profile, realistic topography. $z_s = 600$ m. $f = 25$ Hz.
Figure C.1.11) Arctic sound speed profile, realistic topography. $z_s = 10$ m. $f = 25$ Hz.
Figure C.1.12) Arctic sound speed profile, realistic topography. $z_s = 300$ m. $f = 25$ Hz.
Figure C.1.13) Arctic sound speed profile, realistic topography. $z_s = 600$ m. $f = 25$ Hz.
Figure C.1.14) Range dependent QG oceanography, realistic topography. $z_s = 10$ m. $f = 50$ Hz.
Figure C.1.15) Range dependent QG oceanography, realistic topography. $z_s = 300$ m. $f = 50$ Hz.
Figure C.1.16) Range dependent QG oceanography, realistic topography. $z_s = 600$ m. $f = 50$ Hz.
Figure C.1.17) Atlantic sound speed profile, realistic topography. $z_s = 10$ m. $f = 50$ Hz.
Figure C.1.18) Atlantic sound speed profile, realistic topography. $z_s = 300$ m. $f = 50$ Hz.
Figure C.1.19) Atlantic sound speed profile, realistic topography. $z_s = 600$ m. $f = 50$ Hz.
Figure C.1.20) Arctic sound speed profile, realistic topography. $z_s = 10$ m. $f = 50$ Hz.
Figure C.1.21) Arctic sound speed profile, realistic topography. $z_s = 300$ m. $f = 50$ Hz.
Figure C.1.22) Arctic sound speed profile, realistic topography. $z_s = 600$ m. $f = 50$ Hz.

C.2 Iceland-U.K. Gap Region, Propagation across Front

Calculations in this section were run with the following set of sediment parameters, $\rho = 1.60$ gm/cm^3, $\beta = 4.8$ dB/λ, $c_w/c_b = 1.031$, $\partial c/\partial z = 0.5$ sec^{-1}, and $z_{sed} = 5$ m.
Each page contains the following plots:

a. Sound speed contours.
b. Propagation loss at 10 m receiver.
c. Contours of propagation loss.
d. Propagation loss at 600 m receiver.

Figure C.2.1) Range dependent QG oceanography, 734 m bottom. $z_s = 10$ m. $f = 25$ Hz.
Figure C.2.2) Atlantic sound speed profile, 734 m bottom. $z_s = 10$ m. $f = 25$ Hz.
Figure C.2.3) Arctic sound speed profile, 734 m bottom. $z_s = 10$ m. $f = 25$ Hz.
Figure C.2.4) Range dependent QG oceanography, 3000 m bottom. $z_s = 10$ m. $f = 25$ Hz.
Figure C.2.5) Atlantic sound speed profile, 3000 m bottom. $z_s = 10$ m. $f = 25$ Hz.
Figure C.2.6) Atlantic sound speed profile, 3000 m bottom. $z_s = 300$ m. $f = 25$ Hz.
Figure C.2.7) Atlantic sound speed profile, 3000 m bottom. $z_s = 600$ m. $f = 25$ Hz.
Figure C.2.8) Arctic sound speed profile, 3000 m bottom. $z_s = 10$ m. $f = 25$ Hz.
Figure C.2.9) Arctic sound speed profile, 3000 m bottom. $z_s = 300$ m. $f = 25$ Hz.
Figure C.2.10) Arctic sound speed profile, 3000 m bottom. $z_s = 600$ m. $f = 25$ Hz.
Figure C.2.11) Range dependent QG oceanography, realistic topography. $z_s = 10$ m. $f = 25$ Hz.
Figure C.2.12) Range dependent QG oceanography, realistic topography. $z_s = 300$ m. $f = 25$ Hz.
Figure C.2.13) Range dependent QG oceanography, realistic topography. $z_s = 600$ m. $f = 25$ Hz.
Figure C.2.14) Atlantic sound speed profile, realistic topography. $z_s = 10$ m. $f = 25$ Hz.
Figure C.2.15) Atlantic sound speed profile, realistic topography. $z_s = 300$ m. $f = 25$ Hz.
Figure C.2.16) Atlantic sound speed profile, realistic topography. $z_s = 600$ m. $f = 25$ Hz.
Figure C.2.17) Arctic sound speed profile, realistic topography. $z_s = 10$ m. $f = 25$ Hz.
Figure C.2.18) Arctic sound speed profile, realistic topography. $z_s = 300$ m. $f = 25$ Hz.
Figure C.2.19) Arctic sound speed profile, realistic topography. $z_s = 600$ m. $f = 25$ Hz.
Figure C.2.20) Range dependent QG oceanography, realistic topography. $z_s = 10$ m. $f = 50$ Hz.
Figure C.2.21) Range dependent QG oceanography, realistic topography. $z_s = 300$ m. $f = 50$ Hz.
Figure C.2.22) Range dependent QG oceanography, realistic topography. $z_s = 600$ m. $f = 50$ Hz.
Figure C.2.23) Atlantic sound speed profile, realistic topography. $z_s = 10$ m. $f = 50$ Hz.
Figure C.2.24) Atlantic sound speed profile, realistic topography. $z_s = 300$ m. $f = 50$ Hz.
Figure C.2.25) Atlantic sound speed profile, realistic topography. $z_s = 600$ m. $f = 50$ Hz.
Figure C.2.26) Arctic sound speed profile, realistic topography. $z_s = 10$ m. $f = 50$ Hz.
Figure C.2.27) Arctic sound speed profile, realistic topography. $z_s = 300$ m. $f = 50$ Hz.
Figure C.2.28) Arctic sound speed profile, realistic topography. $z_s = 600$ m. $f = 50$ Hz.